Universidad Autónoma de Madrid

Departamento de Química Orgánica

Instituto de Ciencia de Materiales de Madrid

NEW MULTI STIMULI-RESPONSIVE ORGANIC SEMICONDUCTORS FOR SMART MATERIALS

Marcelo A. Echeverri Muñoz

Directora:

Dr. Berta Gomez-Lor Perez

Madrid 2021

La presente tesis ha sido realizada en el Instituto de Ciencias de Materiales de Madrid, en el departamento de Nuevas Arquitecturas en Química de Materiales, bajo la supervisión de la Doctora Berta Gomez-Lor. La financiación de este trabajo ha provenido del Ministerio de Economía y Competitividad (CTQ2016-78557-R y PID2019-104125RB-I00)

La tesis se presenta como un compendio de artículos. El idioma en el que está escrita la tesis es el inglés. Conforme con la normativa, la introducción y las conclusiones finales están redactadas en español.

AGRADECIMIENTOS

Me gustaría agradecer a mi directora, la Dr. Berta Gómez-Lor por su valiosa dirección y dedicación durante estos años. También me gustaría agradecer a mi tutor académico Dr. Gunther Hennrich, y a todos los colaboradores que han participado en el desarrollo de esta tesis doctoral. Especialmente a la profesora M. Ángeles Monge Bravo y al profesor Enrique Gutiérrez Puebla por sus aportaciones, su indispensable ayuda y amistad. A Dr. Eva María Maya y a Dr. Marta Iglesias por todos sus consejos y soporte.

Especialmente agradezco a mis padres, por su constante apoyo y comprensión, por siempre creer en mí a pesar de todos los baches. A mis hermanos, que han sido siempre un ejemplo de dedicación y profesionalidad. A Vivi, que siempre me motiva para ser mejor cada día y me ayuda a superar cualquier obstáculo.

Muchas gracias a Álvaro, Raúl, Yisus, Carla, Mar, Oscar, Avi, Paloma, Pablo, Vero, David y a todos aquellos amigos que han estado ahí siempre para compartir momentos y echar unas risas (algunos como Alvarito, juntos por más de 14 años).

También quería dar las gracias a Dori, Amparo, Ana María, Leticia y Ana del departamento de química inorgánica de la UAM, ya que han sido parte esencial de mi formación.

En el instituto, quería agradecer a Antonio, Samar, Afsar, Huan, Celia, Dani, Ralu, Clara… por ser buenos amigos y compañeros, por compartir esta experiencia juntos y apoyarnos mutuamente. En especial quería agradecer a Ángela y Lina por ser como mis hermanas mayores, siendo un apoyo incondicional y fuente de sabiduría. También he de agradecer a Ana, Silvia, Cristina, Lucia, Mario, María, Eli, Pablo, Helena, Ángela, Laura, Victor, Remy, Linda y a todos los que han pasado por el laboratorio haciendo prácticas o TFGs/TFMs, porque han sido parte de mi preparación.

En general muchas gracias a toda mi familia, amigos y compañeros, porque sin ellos no tendría sentido ningún logro.

INDICE/INDEX

1. INTRODUCCION GENERAL

En los últimos años el campo de la electrónica orgánica ha experimentado una gran evolución, pasando en muy pocos años de un nivel de investigación básica al desarrollo de dispositivos ya comercialmente viables. Este contundente aumento ha estado motivado por las interesantes ventajas que presentan las moléculas orgánicas para generar dispositivos, entre ellas su compatibilidad con variedad de sustratos que posibilita la obtención de dispositivos flexibles, de amplia área y su fácil procesado desde disolución. Otra gran ventaja de los materiales orgánicos es la gran versatilidad que ofrece la síntesis orgánica, que permite acceder a gran variedad de estructuras moleculares proporcionando de esta manera materiales con propiedades prediseñadas, así como materiales multifuncionales (combinando propiedades magnéticas, ópticas, eléctricas, etc)

A pesar de todas estas ventajas, los semiconductores orgánicos son significativamente menos eficientes en términos de transporte de carga que sus homólogos inorgánicos y, por tanto, no se espera que los sustituyan, sino que los complementen. La posible sustitución de los semiconductores inorgánicos en otros campos de aplicación como la detección de analitos de interés, presión, temperatura..., parece mucho más cercana.

En este contexto uno de los retos actuales en el campo de los semiconductores orgánicos es el diseño de "materiales inteligentes", capaces de ordenarse y autoensamblarse para obtener propiedades diseñadas "a la carta", que sean capaces de reaccionar a estímulos externos como la temperatura, la presión, los campos eléctricos o magnéticos, el pH, la presencia de analitos, la humedad, etc. produciendo cambios en su forma, color, propiedades físicas o produciendo un voltaje.

Especialmente interesante en este contexto son los cambios que ocurren en la luminiscencia, la emisión de luz de cualquier sustancia excitada que libera un fotón al volver al estado fundamental. Los fenómenos de luminiscencia son apropiados para el diseño de materiales inteligentes, ya que los niveles de energía se ven fácilmente perturbados por ligeros cambios estructurales o supramoleculares o por la presencia de otras moléculas. De este modo, se puede influir en la propiedad fotolumínica, generando un cambio de absorción o emisión.

La presente tesis doctoral se ha desarrollado en el Laboratorio de Química Orgánica del Instituto de Ciencia de Materiales de Madrid, dirigido por la Dra. Berta Gómez-Lor. El grupo de investigación lleva trabajando desde hace varios años en el campo de la

electrónica orgánica en el desarrollo de semiconductores orgánicos altamente competitivos que han podido ser incorporados en distintos dispositivos tales como OLEDs y OFETs. Asimismo, el grupo trabaja en el desarrollo de eficientes sistemas emisores de luz, cuyas propiedades pueden ser moduladas variando la estructura química y la organización molecular de sus constituyentes.

Esta tesis, se ha centrado en el diseño, síntesis, caracterización y aplicación de semiconductores orgánicos en el campo de los materiales inteligentes, siguiendo dos enfoques distintos: El primero, mediante una aproximación tanto molecular como supramolecular, desarrollando moléculas capaces de autoensamblarse basadas en la molécula de benzotiadiazol (BTD). Para ello se tratará de establecer claras relaciones estructura-propiedad con el fin de entender el papel fundamental de los sustituyentes en las propiedades electrónicas de estos sistemas, así como en sus interacciones supramoleculares.

Los derivados del benzotiadiazol (BTD) presentan propiedades electrónicas muy interesantes. Este heterociclo es un eficiente fluoróforo y su alta deficiencia electrónica le confiere propiedades semiconductoras tipo n. Además, tiene una fuerte tendencia a imponer geometrías "quinoidales" cuando son incorporados en sistemas conjugados facilitando la transferencia de carga entre sustituyentes y posibilitando la fácil sintonización de sus propiedades electrónicas. Esto lo hace un candidato idóneo para obtener materiales inteligentes que posean propiedades como mesomorfismo (propiedades cristal líquido), mecanocromismo (cambio de color o emision mediante estímulos físicos) y termocromismo (cambio de color o emisión por medio de cambios de temperatura).

Este trabajo quedó plasmado en tres publicaciones diferentes que se presentan en esta tesis doctoral.

- Echeverri, M.; Martín, I.; Concellón, A.; Ruiz, C.; Anselmo, M. S.; Gutiérrez-Puebla, E.; Serrano, J. L.; Gómez-Lor, B. Fluorescent and Electroactive Monoalkyl BTD-Based Liquid Crystals with Tunable Self-Assembling and Electronic Properties. *ACS Omega* **2018**, *3*, 11857–11864.
- Echeverri, M.; Ruiz, C.; Gámez-Valenzuela, S.; Martín, I.; Delgado, M. C. R.; Gutiérrez-Puebla, E.; Monge, M. Á.; Aguirre-Díaz, L. M.; Gómez-Lor, B. Untangling the Mechanochromic Properties of Benzothiadiazole- Based Luminescent Polymorphs through Supramolecular Organic Framework Topology. *J. Am. Chem. Soc.* **2020**, *142*, 17147–17155.
- Echeverri, M.; Ruiz, C.; Gámez-Valenzuela, S.; Alonso-Navarro, M.; Gutierrez-

Puebla, E.; Serrano, J. L.; Ruiz Delgado, M. C.; Gómez-Lor, B. Stimuli-Responsive Benzothiadiazole Derivative as a Dopant for Rewritable Polymer Blends. *ACS Appl. Mater. Interfaces* **2020**, *12,* 10929–10937.

El segundo enfoque, ha sido el diseño y desarrollo de polímeros orgánicos porosos (POPs) basados en semiconductores capaces de interaccionar y detectar explosivos y compuestos nitroaromaticos. Para ello se han utilizado la inhibición de fluorescencia "quenching" como señal en la detección. Este fenómeno puede ser causado por variedad de mecanismos tales como interacciones moleculares, reacciones en el estado excitado, reordenamientos moleculares, transferencia de energía, formación de complejos en el estado fundamental .... En el caso de la detección de analitos (explosivos, metales, contaminantes, etc,) la alta sensibilidad y la enorme diversidad de posibles inhibidores confiere al fenómeno de "quenching" un especial interés para futuras aplicaciones.

En esta tesis, se han utilizado semiconductores basados en truxeno para el diseño, síntesis y aplicación de POPs en la detección de explosivos. El truxeno (10,15-dihidro-5*H*-diindeno [1,2-*a*; 1',2'-*c*] fluoreno) es una molécula heptacíclica poliaromática que contiene un eje de simetría C_3 y una estructura rígida y plana. Esta molécula posee interesantes propiedades ópticas (es un eficiente emisor en azul) y propiedades semiconductoras tipo p. El truxeno es un material con una alta estabilidad térmica y química, lo que junto con sus propiedades optoelectrónicas lo hace adecuado para su introducción en diferentes tipos de dispositivos, como el desarrollo de nuevos transistores orgánicos de efecto de campo (OFETs), absorción de los fotones (TPA), células fotovoltaicas orgánicas (OPVs), diodos orgánicos de emisión de luz (OLEDs), sondas fluorescentes,etc. También se han estudiado las posibles aplicaciones de análogos del truxeno tales como el triindol y la diazatruxenona (Figura 1.1), compuestos con la misma geometría que el truxeno pero propiedades redox y semiconductoras completamente diferentes. Así, mientras que el truxeno y el triindol son semiconductores de tipo p, la truxenona se presenta como un semiconductor de tipo n de alta movilidad. La estructura trigonal π-conjugada de estas moléculas ha despertado interés como unidades de construcción de materiales moleculares y poliméricos.

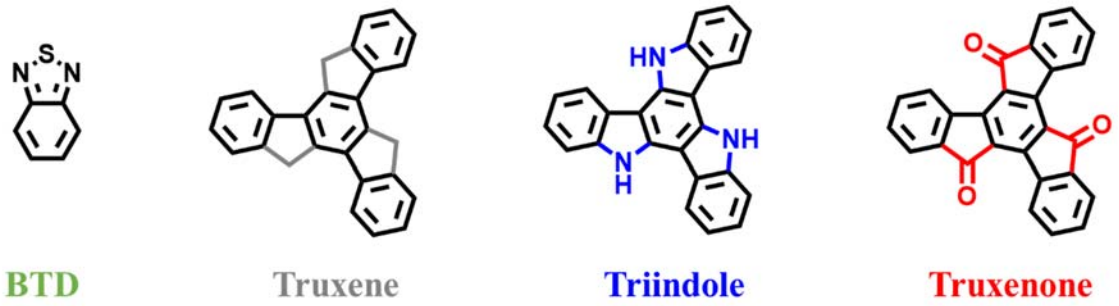

Figura 1.1. Estructura química de los semiconductores orgánicos utilizados en esta tesis doctoral.

Este parte del trabajo quedó plasmado en dos publicaciones diferentes que se presentan en esta tesis doctoral.

- Echeverri, M.; Gámez-Valenzuela, S.; González-Cano, R. C.; Guadalupe, J.; Cortijo-Campos, S.; López Navarrete, J. T.; Iglesias, M.; Ruiz Delgado, M. C.; Gómez-Lor, B. Effect of the Linkage Position on the Conjugation Length of Truxene-Based Porous Polymers: Implications for Their Sensing Performance of Nitroaromatics. *Chem. Mater.* **2019**, *31*, 6971–6978.
- Gámez-Valenzuela, S.; Echeverri, M.; Gómez-Lor, B.; Martínez, J. I.; Ruiz Delgado, M. C. In Silico Design of 2D Polymers Containing Truxene-Based Platforms: Insights into Their Structural and Electronic Properties. *J. Mater. Chem. C* **2020**, *8*, 15416–15425.

A continuación, se presenta un resumen de cada publicación obtenida durante esta tesis doctoral.

2. SUMMARY OF RESULTS

- **Fluorescent and Electroactive Monoalkyl BTD-Based Liquid Crystals with Tunable Self-Assembling and Electronic Properties**

Marcelo Echeverri, Irene Martín, Alberto Concellón, Constanza Ruiz, María San Anselmo, Enrique Gutiérrez-Puebla, José L. Serrano, and Berta Gómez-Lor*

The first step of the research was to synthesize a series of redox active benzothiadiazole (BTD) derivatives in order to establish clear structure-properties relationships. These compounds were functionalized on one edge with a phenyl-nonyl substituent, which confers these molecules a rod-like shape and a tendency to self-assemble into layered superstructures. On the other edge, the molecules are endowed with different p-substituted phenyl rings, which allows the modulation of their redox and optical properties on the base of the electronic nature of the terminal substituents.

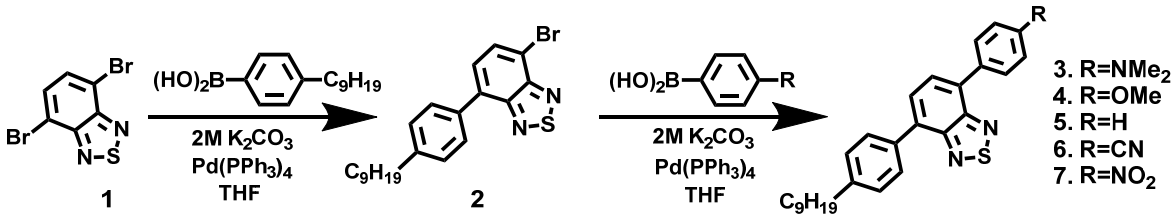

Scheme 2.1. Synthesis of compounds 2-7 of "Fluorescent and Electroactive Monoalkyl BTD-Based Liquid Crystals with Tunable Self-Assembling and Electronic Properties" publication.

We have shown that attaching only one terminal alkyl chain to the 4,7-diphenyl BTD core is enough to induce mesomorphism in these systems. The other terminal position can be used to fine-tune not only the electronic properties (by modulating the intramolecular charge transfer in the system) but also their mesomorphic behaviour and crystal packing by participating in different intermolecular interactions, which stabilize the bulk structure.

The results of this study have allowed us to understand the strong influence that the substituents have not only in the electronic properties of these molecules but also in their crystallographic packing, of interest to design of new stimuli response materials.

- **Untangling the mechanochromic properties of benzothiadiazole- based luminescent polymorphs through supramolecular organic framework topology**

Marcelo Echeverri, Constanza Ruiz, Sergio Gámez-Valenzuela, Irene Martín, M. Carmen Ruiz Delgado, Enrique Gutiérrez-Puebla, M. Ángeles Monge, Lina M. Aguirre-Díaz*, and Berta Gómez-Lor*

This publication presents a study of two polymorphs (**1α** and **1β**) of a BTD-based luminophore (compound **2** in previous publication) exhibiting different color emission, which switch into each other in response to shear force and solvent vapors. Single crystals of both polymorphs were grown and their crystal structure solved, which allowed us to study the mechanism responsible of the phase transition. (see Figure 2.1)

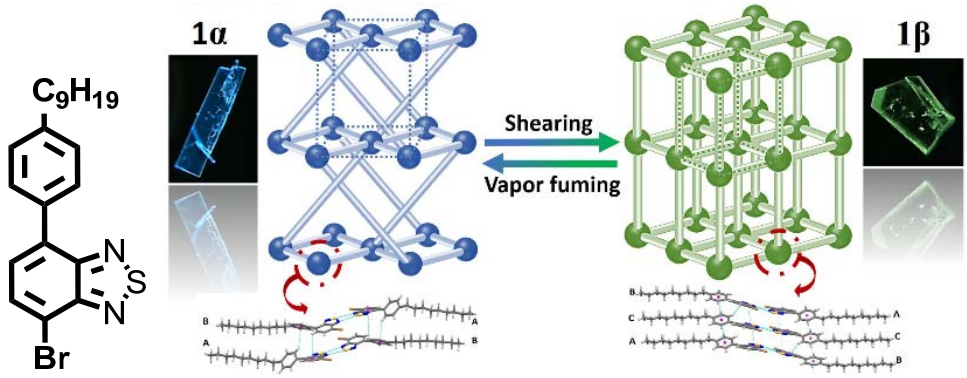

Figure 2.1. Table of contents of publication "Untangling the mechanochromic properties of benzothiadiazole- based luminescent polymorphs through supramolecular organic framework topology" where is represented the two different polymorphs structure of BTD derivative.

The interconversion between **1α** and **1β** polymorphs upon mechanical stress or solvent vapors was successfully followed by Raman spectroscopy, demonstrating similar conjugation lengths but different intermolecular interactions operating in both phases, in good agreement with the X-Ray data. TD-DFT calculations on representative aggregates extracted from **1α** and **1β** crystals predict a lower energy difference between the ground and the first excited electronic states in **1β** polymorph when compared to **1α**, thus explaining the different colors observed.

Additionally, in this paper Supramolecular Organic Framework Analysis (SOFA) and Supramolecular Organic Framework Topology (SOFT), was performed in collaboration of Dr. Lina M. Aguirre-Díaz and Porf. M. Ángeles Monge. This study allowed us to conclude that the mechanochromic phase transformation can be explained on the base of

modifications in their respective topological nets: **mab** and **pcu** for **1α** and **1β** respectively because of the breaking and restoration of a number of weak supramolecular interactions.

- **Stimuli-Responsive Benzothiadiazole Derivative as a Dopant for Rewritable Polymer Blends**

Marcelo Echeverri, Constanza Ruiz, Sergio Gámez-Valenzuela, Matias Alonso-Navarro, Enrique Gutierrez-Puebla, José L. Serrano, M. Carmen Ruiz Delgado*, and Berta Gómez-Lor*

In this publication, a new rod-shaped benzothiadiazole fluorophore which emits strongly both in solution and in solid state is presented. This molecule crystallizes in two distinct light emitting crystalline phases, which can be interconverted in response to pressure, temperature and solvent vapors. Powder X-ray diffraction indicates that in both polymorphs molecules adopt a lamellar packing, being the main difference between the two structures the different interlayer spacing. The study of crystal structure, DRX and Raman spectroscopic, suggests that the different emission colors observed are due different intermolecular aromatic interactions owing to the displacement of the molecules with respect to the layer normal. To obtain a "smart material", blending this molecule with a biodegradable polymer such as polyvinylalcohol gives rise to a thermal activated reversible switchable fluorescent system, which entitles this material as an attractive candidate for technological applications, such as thermal sensors, security inks or rewritable paper. (Figure 2.2)

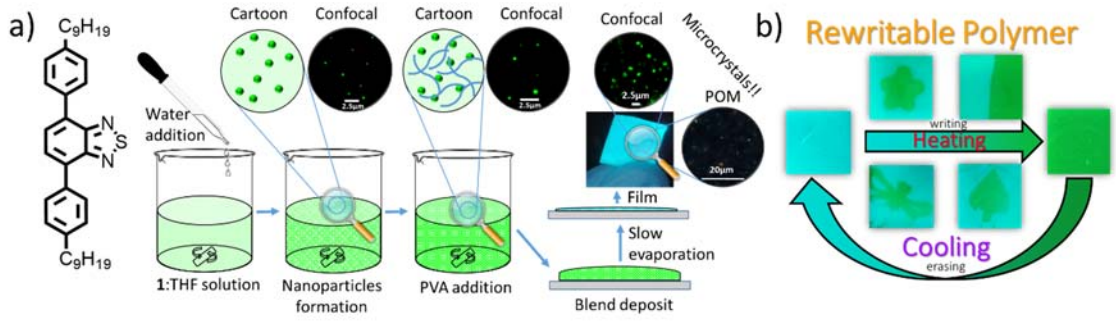

Figure 2.2. a) Schematic representation of the preparation **1**:polyvinylalcohol films. b) Different motifs stamped on a sole **1**:PVA blend thin film following a written-erasing procedure.

- **Effect of the Linkage Position on the Conjugation Length of Truxene-Based Porous Polymers: Implications for Their Sensing Performance of Nitroaromatics**

Marcelo Echeverri, Sergio Gámez-Valenzuela, Rafael C. González-Cano, Jordy Guadalupe, Sandra Cortijo-Campos, Juan Teodomiro López Navarrete, Marta Iglesias*, M. Carmen Ruiz Delgado*, and Berta Gómez-Lor*

In this publication, we explore the use of organic semiconductors (truxene) as monomer to obtain Porous Organic Polymers with optical activity. These truxene-based organic polymers have been synthesized via C-C cross coupling methodologies under Yamamoto and Suzuki-Miyaura conditions in two different functionalization position (2,7,12 and 3,8,13) and with or without a phenylene spacer. (Scheme 2.2) rendering porosity materials (SA_{BET} 520-1167 $m^2.g^{-1}$).

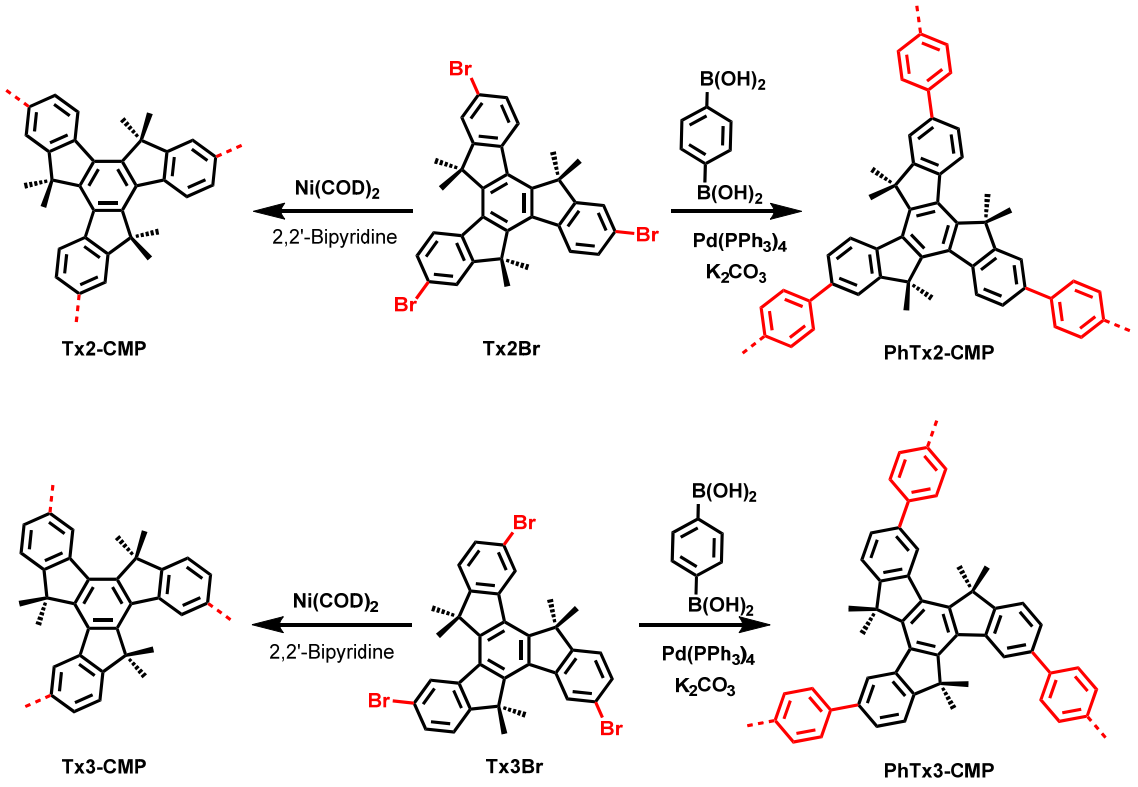

Scheme 2.2. Synthesis of Tx2-CMP, Tx3-CMP, PhTx2-CMP and PhTx3-CMP based on heptacylic truxene (in black).

Both experimental (UV-vis absorption, fluorescence and Raman spectroscopy) and theoretical results point to the fact that connecting the truxene monomers through the 2,7,12 positions results in a better electronic communication between the covalently

linked building units, thus strongly affecting the extension of the conjugation, lowering the HOMO-LUMO gap and influencing the energy levels of the final materials.

On the other hand, we have evaluated the potential use of the truxene-based polymers for the detection of electron deficient nitroaromatics (analytes of relevance for sectors that go from security to human health) in order to determine the implication of the different linkage position on their sensing performance. Interestingly the strong influence that the positional connectivity exerts on the LUMO level of these polymers explain the different sensing behaviour of these polymers towards nitroaromatic compounds. The results of this work highlight the importance of the linkage position as a new design tool to tune the electronic properties of electroactive porous polymers for emerging real-life applications.

- **In silico design of 2D polymers containing truxene-based platforms: Insights into their structural and electronic properties**

Sergio Gámez-Valenzuela, Marcelo Echeverri, Berta Gómez-Lor*, José I. Martínez* and M. Carmen Ruiz Delgado*

In this last publication, we explore more deeply the structural dependency of electronic properties of truxene and other truxene-related (triindole and truxenone) polymers. A computational study was performed in collaboration with Dr. M. Carmen Ruiz Delgado and Dr. José I. Martínez in order predict structure-property relationships of 2D truxene-based conjugated polymers (Figure 2.3) and provide interesting guidelines to design novel 2D materials with applications ranging from sensing to electronics.

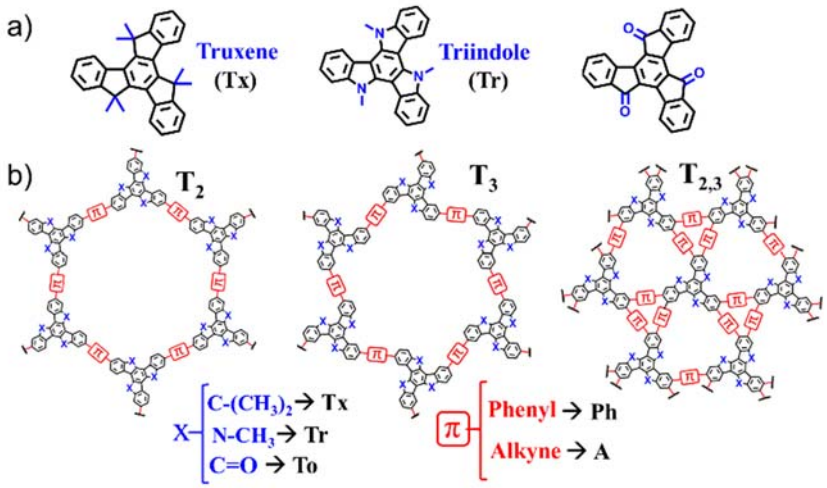

Figure 2.3. General chemical structures of the conjugated cores (a) and 2D- polymers (b) examined in this study with the notation used throughout the text. Note that **T_2** and **T_3** polymers

are referred to tri-substituted materials with different linkage positions (2,7,12 in $\mathbf{T_2}$ and 3,8,13 in $\mathbf{T_3}$) while $\mathbf{T_{2,3}}$ corresponds to hexa-substituted materials in 2,3,7,8,12 and 13 positions.

Our results show that a wide tuning of the structural (i.e, geometry or pore size) and electronic (*i.e*., band-gap or band dispersion) properties can be achieved in these truxene-based 2D polymers by suitable structural design of the organic building blocks. Band-gap values in the range between 1.17 and 3.13 eV are predicted, which correspond to semiconductor band-gaps. In the same line, a strong modulation of the absorption spectral response from the UV to the near infrared is found through suitable chemical modification. These results make these materials attractive for optoelectronics, photovoltaics or sensing.

This computational first-principle-based strategy emerges as a powerful tool towards the in silico pre-filtering of future similar 2D materials, through an adequate and careful selection of the building block.

3. INTRODUCTION

3.1. Organic Smart Materials

Organic chemistry has advanced rapidly for almost 200 years, from the first artificial synthesis of urea by Friedrich Wöhler in 1828,[1] up to today, where the petrochemical, pharmaceutical, technological and materials industries set the pace of modern society and take an integral part of our lives. Along these years, organic chemistry has become more complex and multidisciplinary, getting increasingly interconnected with others sciences like physics, biology and computational science.

In recent decades, organic chemistry has emerged as a very important research area in materials science. The versatility, diversity and constant evolution of organic synthesis has allowed the development of new materials such as polymers, fabric, composites, dyes, catalyst, sensors and devices.

One of the current challenges is the design of “smart materials”, capable of ordering and self-assembling to obtain designed "a la carte" properties, which are capable of reacting to external stimuli such as temperature, pressure, electric or magnetic fields, pH, presence of analytes, humidity, etc. producing changing their shape, color, physical properties, or producing voltage.

To accomplish this goal, it is not only necessary to control the chemistry behind the creation of the new materials, but also, and much more important, it is to understand the close relationship between structure-properties, which allow to create strategies to control it. The properties of organic materials are not only governed by the molecular units, but also by the way in which they organize and interact with neighboring molecules in the material. This close relationship between the properties of a material and the organization of the building blocks at the nano level, offers many opportunities to synthesize materials that can respond to external stimuli.

3.2. Semiconductors for smart materials

Organic semiconductors represent an expanding market as their versatility, soft character, and substrates compatibility, render them very attractive in the development of flexible, lightweight, large area devices. In the past decade, research in the field of organic electronics has progressed to the extent that desirable charge transport properties in the

[1] Wöhler, F. *Ann. Phys.* **1828**, *88*, 253–256.

organic semiconductor materials can be achieved through an adequate design both at the molecular and supramolecular level. In only a few years, this area of research has progressed from a basic research level to the commercialization of the light emitting devices based on organic semiconductors (OLEDs).

In spite of all these advantages, organic semiconductors are significantly less efficient in terms of charge transport than their inorganic counterparts and therefore they are not expected to replace but complement them. The potential replacement of inorganic semiconductors in other fields of applications such as sensing, recording or photocatalysts seems to be much closer. The interesting advantage of these materials, is the possibility of design their (opto)electronics properties thanks to the broad knowledge that has been acquired through numerous structure-properties studies.

Organic semiconductors are usually based on molecules with extended π-conjugated aromatics systems. This allows high delocalization of electrons through the structure and the generation of interesting electronics properties. These properties are influenced by their electronic structure and frontier molecular orbitals: the highest occupied molecular orbital (HOMO) and the lowest unoccupied molecular orbital (LUMO) (Figure 3.2.1a). The HOMO and LUMO orbitals are analogous to the inorganic semiconductor valence band maximum and conduction band minimum (Figure 3.2.1b). In both cases, organic and inorganic semiconductors, present an energy gap between orbitals or bands that control the energy necessary to excite one electron from the HOMO to the LUMO level or from the valence to conduction bands. This difference of energy is called bandgap and determines the conducting properties of the materials: In the case of metals, exist an overlap between conduction and valence band. It is usually accepted that bandgaps energy less than 3.2 eV corresponds to semiconducting properties, higher that this value it is consider as an insulator (Figure 3.2.1b). There are two types of semiconductors, n-type and p-type. P-type semiconductors are electron-rich molecules, they conduct holes and have high energy levels HOMO. On the other hand, n-type semiconductors are electron-deficient molecules. These molecules possess low LUMO energy levels.

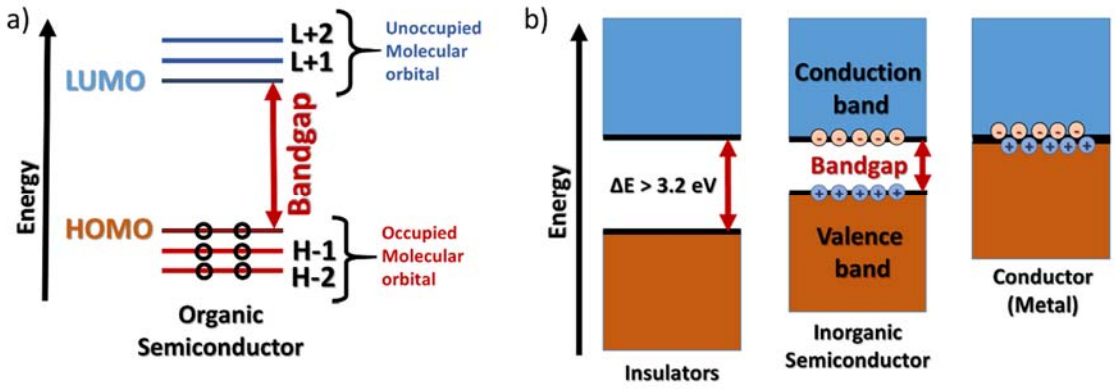

Figure 3.2.1. a) Band diagram of insulators, inorganic semiconductor and conductor. b) Schematic representation of the HOMO and LUMO bands for organic semiconductors.

The bandgap energy also determines the UV transitions from fundamental to excite states, this represent the electronic absorption in the UV-Visible spectra, determination macroscopically the color of the material.

3.3. Luminescence: Fluorescence and Phosphorescence

In organic semiconductors, electronic configurations and lowers bandgaps favors the appearance of luminescence phenomena. Luminescence is the emission of light from any excited substance that release a photon upon return to ground state. Fluorescence and phosphorescence are two particular cases of luminescence, and differ on the nature of the excited state from which they are produced. In the case of fluorescence, the excited state is a singlet state (electron paired, by opposite spin than ground state spin); while the phosphorescence present an excited triplet state (electron with the same ground state spin) (Figure 3.3.1a). The Jablonski diagram shows the various molecular processes that can occur between ground state and excited states (Figure 3.3.1b).

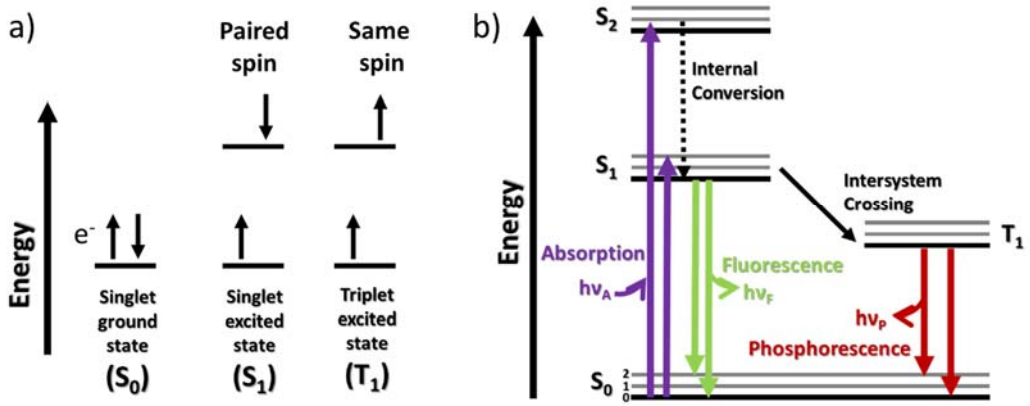

Figure 3.3.1. a) Electron spin configuration in singlet and triplet excited state. b) Jablonski diagram of fluorescence and phosphorescence mechanism.

The molecule in its fundamental electronic state (S_0) absorbs a photon of electromagnetic radiation ($h\nu_A$), promoting an electron to excited singlets states of higher energy (S_1, S_2,..., S_n) by the same amount of absorbed photon`s energy. Immediately after absorption, excited molecule relax to lower energetic vibrational levels in excited state. In the excited state, a molecule is energetically unstable and must return to its ground state. The loss of energy takes place through radiative processes. In the case of a transition from excited state S_1 to ground state S_0 called fluorescence, this luminescence phenomena has low lifetimes (10^{-8} s) and high emission rates (10^8 s^{-1}). On the other hand, molecules in the S_1 excited state can also undergo a spin conversion to the first triplet state T_1, producing an intersystem crossing. The emission from this T_1 is called phosphorescence, the transitions to ground state is forbidden (T_1 to S_0) and this cause a slowdown in the emission rates (10^3 to 1 s^{-1}), so the phosphorescence lifetimes are typically milliseconds to seconds.

Fluorophores are substances with fluorescence properties, some typical examples are show in Figure 3.3.2. There is a great variety of fluorophores; with very diverse structures and emission colors that cover the entire UV-Visible spectrum. After the first description of fluorescence in quinine solutions by Sir Herschel in 1845, fluorescence has arose great interest because of its high detection sensitivity. This high sensibility was used in 1877 to demonstrate that the rivers Danube and Rhine where connected by underground streams, placing fluorescein into the Danube and detecting green fluorescence in the Rhine water. The use of fluorescein is still used as an emergency marker for locating individuals at sea. Organic fluorophores find multiple application, for example 1,4.bis-(5-phenyloxazol-2-yl)benzene (POPOP) is used in scintillation counting to detect radioactive activity; acridine orange in DNA stain in bioimaging; Pyridine 1 and rhodamine are use in lasers as dyes, etc.

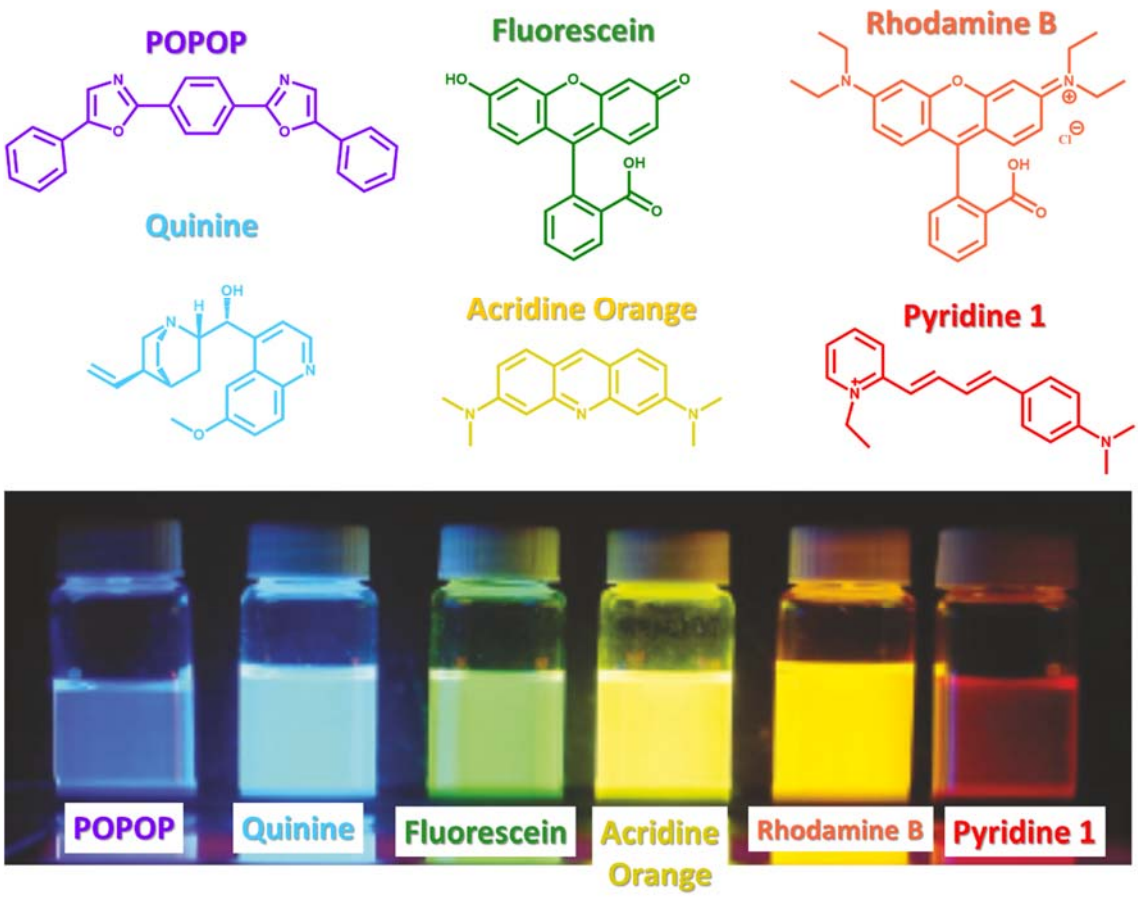

Figure 3.3.2. Structures of typical fluorescent substances and emission photographs.

The design of new organic fluorophores and applications are extended, because the capacity of organic chemistry to switching and tuning the emission properties of new materials by structural changes. On the other hand, today we know that the electronic properties of organic materials depend not only on the building unit, but also on how the molecules are related among each other. Thus, the supramolecular interactions are as important as the chemical structure for tune the opto-electronic properties. This high dependence of the final properties of the materials from the organization of the molecular building blocks at the nanometer level, offers many opportunities to synthesize materials that can respond to external stimuli by varying their supramolecular arrangement.

The fluorescence and phosphorescence phenomena are appropriate for smart materials design, since energy levels are easily disturbed by slight structural or supramolecular changes or by the presence of other molecules. In this way, the photoluminic property can be influenced, generating a change in absorption or emission color.

3.4. Mecanochromic and Thermochromic behaviour

Mechanochromic materials, i.e. solids that changes optical properties upon mechanical stimulation (grinding, crushing, pressing) arouse much interest for rewritable paper,[2] recording[3] or stress sensing.[4] On the other hand, thermochromics materials are materials that response to temperature changes has been used in different applications such as temperature sensors,[5] smart windows,[6] smart packaging[7] and displays.[8]

Even though most of mechanochromic and thermochromic organic materials have been discover by serendipity or as a consequence of screening of compounds, extensive studies has been carried to relate structural and properties relationship. In brief, the requirements to obtain these phenomena seem to be three:

- At least two stable states with different molecular order. This is the more important requirement. It means two or more thermodynamically stable or metastable states with different arrangement (Figure 3.4.1).
- Arrangement or packing of π-conjugated moieties in the assembly states must be sufficient different, enough to generate a relevant influences in the photophysical properties.
- Low energy barrier between the states. The energy necessary to obtain the transformation must be enough by mechanical force or heating.

[2] Khazi, M. I.; Jeong, W.; Kim, J. M. *Adv. Mater.* **2018**, *30*, 1–22.
[3] Genovese, D.; Aliprandi, A.; Prasetyanto, E. A.; Mauro, M.; Hirtz, M.; Fuchs, H.; Fujita, Y.; Uji-I, H.; Lebedkin, S.; Kappes, M.; De Cola, L. *Adv. Funct. Mater.* **2016**, *26*, 5271–5278.
[4] Roberts, D. R. T.; Holder, S. J. *J. Mater. Chem.* **2011**, *21*, 8256–8268.
[5] a)Yu, S.-S.; Zhao, H.-R.; Zhang, H.; Duan, H.-B. *Dalt. Trans.* **2020**, *49*, 16643–16648. b) Mehta, S.; Kushwaha, A.; Kisannagar, R. R.; Gupta, D. *RSC Adv.* **2020**, *10*, 21270–21276.
[6] a) Bi, S.; Feng, C.; Wang, M.; Kong, M.; Liu, Y.; Cheng, X.; Wang, X.; Chen, X. *Carbohydr. Polym.* **2020**, *229*, 115557. b) Zhang, Y.; Tso, C. Y.; Iñigo, J. S.; Liu, S.; Miyazaki, H.; Chao, C. Y. H.; Yu, K. M. *Appl. Energy* **2019**, *254*.
[7] Torrico, D. D.; Fuentes, S.; Viejo, C. G.; Ashman, H.; Gurr, P. A.; Dunshea, F. R. *LWT - Food Sci. Technol.* **2018**, *89*, 475–481.
[8] Kavčič, U.; Mraović, M.; Bračko, S.; Muck, D. *Color. Technol.* **2019**, *135*, 60–66.

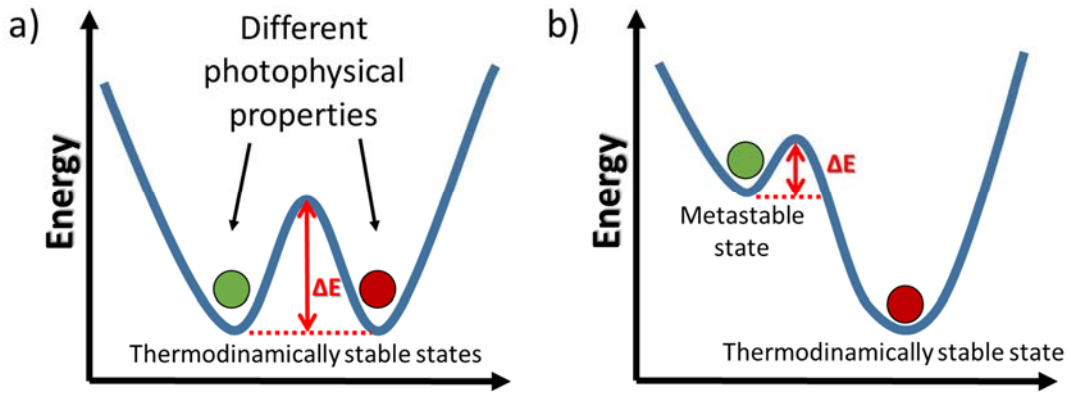

Figure 3.4.1. Gibbs free energy representation of mechanochromic material with a) two thermodynamic stable states, or b) with a metastable state.

Diverse intramolecular and intermolecular interactions, such as conformational rotations, hydrogen bonding, π–π stacking, ionic interactions, and van der Waals forces have a key role in the stability of each state. The competition between these interactions define the arrangements of molecules to metastable or thermodynamically stable states. Moreover, these interactions determine the necessary energy to accomplish a reversible or irreversible transformation and the final photophysical properties.

Some examples of organic mechanochromic and thermochromic molecules are represented in Scheme 3.4.1.[9] In the case of 1,3,6,8-tetraphenylpyrene derivative **1** (see Scheme 3.4.2),[10] crystallize in two different states (B-form and G-form) with distinct absorption and emission properties. The role of interactions is clear in the two states: in B-form hydrogen bonds between amide groups and weak π-π stacking produce a crystalline blue emitting columnar phase; while in G-form (metastable) which is obtained after grinding, linear hydrogen bonds are disturbed and the cores approach to each other becoming amorphous, leadeing to a redshifting to green emission. The transformation is reversed by heating, returning to the blue crystalline phase.

[9] Sagara, Y.; Yamane, S.; Mitani, M.; Weder, C.; Kato, T. *Adv. Mater.* **2016**, *28*, 1073–1095.
[10] Sagara, Y.; Mutai, T.; Yoshikawa, I.; Araki, K. *J. Am. Chem. Soc.* **2007**, *129*, 1520–1521.

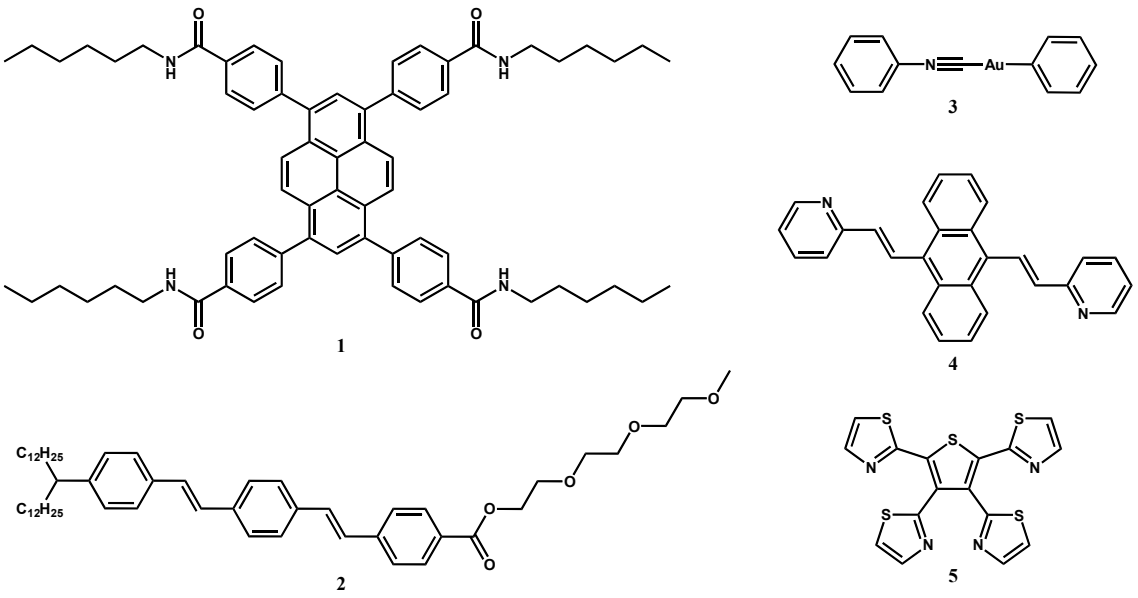

Scheme 3.4.1. Structure of examples of mechanochromic and thermochromic molecules.

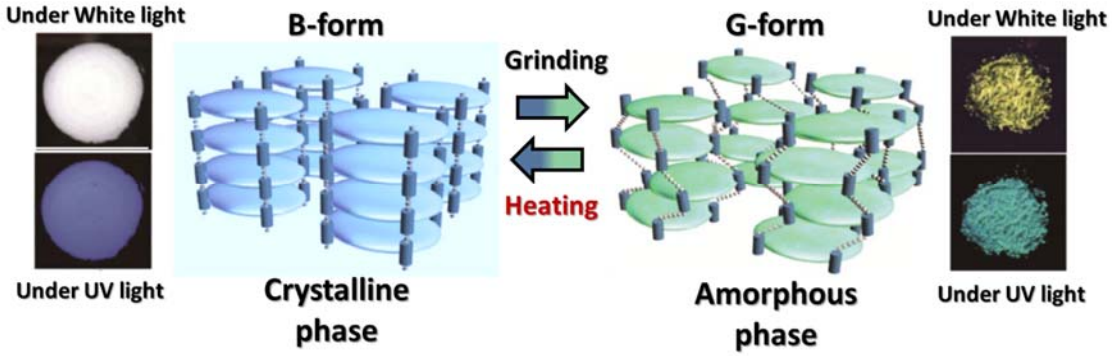

Figure 3.4.2. Molecular assembled structures and photographs under room light and UV light of B-form and G-form of 1. Adapted with permission from Ref. 9. Copyright 2016 JohnWiley and Sons.

Figure 3.4.3 shows another example, the amphiphilic oligo(*p*-phenylenevinylene) derivarive **2**[11] which presents also mechanochromic and thermochromic behavior related to intermolecular interactions. The structure of molecule induces a dipole repulsion force and a strong tendency to form segregated molecular laminar structures, generated by the action of different interactions involving the functional groups in the molecule, which generates different sublayers for aliphatic, aromatic and triethylenglicol (TEG) groups (See Figure 3.4.3a). This compound has four stable states that changes depending oon the treatment performed: Through drop-casting, this material forms a crystal phase

[11] Yagai, S.; Okamura, S.; Nakano, Y.; Yamauchi, M.; Kishikawa, K.; Karatsu, T.; Kitamura, A.; Ueno, A.; Kuzuhara, D.; Yamada, H.; Seki, T.; Ito, H. *Nat. Commun.* **2014**, *5*, 1–10.

characterized by tilted bilayers with yellow emission **2Y** (See Figure 3.4.3b). After pressing or shearing, it turns into a liquid crystal phase (LC) with orange emission **2O**, where molecules adopt a twisted arrangement of the π-conjugated groups. This LC phase can be reversed to **2Y** by exposing it to CH_3CN vapors. Instead, when **2O** is rubbed, crystallization occurs and produce a new green phase **2G***. Finally, thermal annealing at 50°C generates a more crystalline phase **2G** with bluish-green emission.

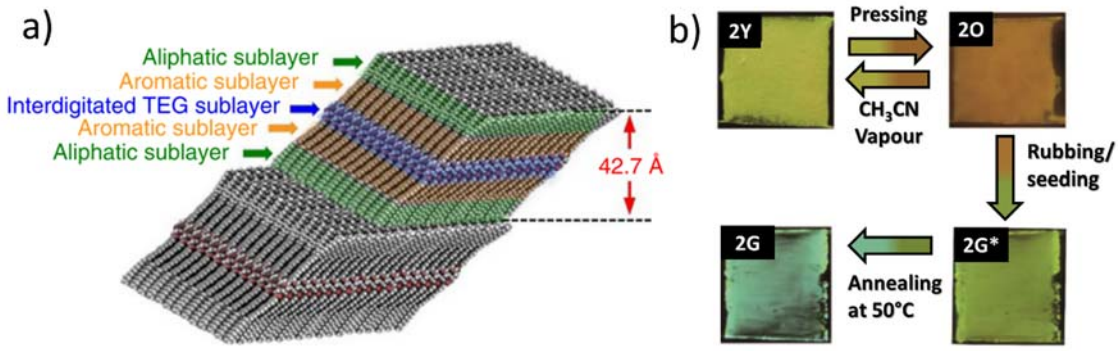

Figure 3.4.3. a) Molecular assembled structures of **2**. b) Photograph of the interconversion of **2** under UV light. Adapted with permission from Ref. 9. Copyright 2016 JohnWiley and Sons.

Other examples of mechanochromic materials can be found in metalorganic and complex molecules.[12] In particular, the compound **3** is a gold complex with interesting metal-metal interactions (see Figure 3.4.4.a).[13] This Au-Au (aurophilic) interactions stabilize two crystalline phases with different emission under UV irradiation. phase I_b is obtained by rapid crystallization and exhibit blue photoluminescence while phase II_y is obtained upon slow crystallization and presents yellow emission. The phase I_b shows Au-Au distances of 5.733 Å while in phase II_y the Au-Au distance is 3.177 Å. This aurophilic interaction in phase II_y causes red shifting of the emission band to yellow color. A crystal to crystal transformation from phase I_b to phase II_y occurs by grinding, mechanical stimuli or solid seeding, via a "molecular domino effect" (see figure 3.4.4.b and c). Triggered by the strong bonding character of aurophilics interactions.

[12] Zhang, X.; Chi, Z.; Zhang, Y.; Liu, S.; Xu, J. *J. Mater. Chem. C* **2013**, *1*, 3376–3390.
[13] Ito, H.; Muromoto, M.; Kurenuma, S.; Ishizaka, S.; Kitamura, N.; Sato, H.; Seki, T. *Nat. Commun.* **2013**, *4*, 1–5.

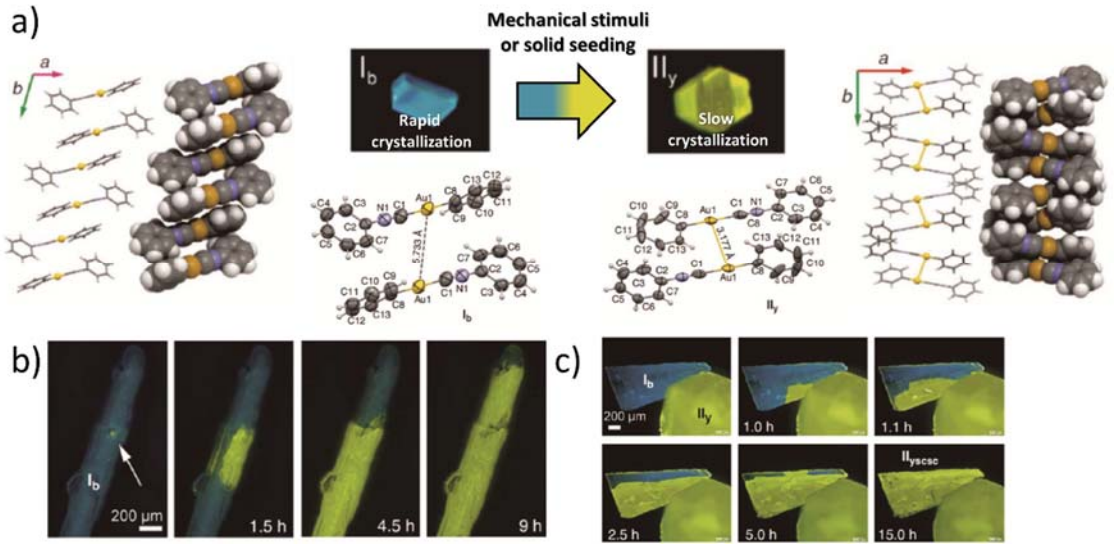

Figure 3.4.4. a) Crystal structures of 3 polymorphs and photographs phase Ib and phase IIy under UV-light. Crystal transformation of phase Ib tophase IIy under UV-light after b) mechanical stumili, c) solid seeding. Adapted with permission from Ref. 9. Copyright 2016 JohnWiley and Sons.

In another example, anthracene derivative **4** was reported to show gradual mechanochromic transformation by grinding or hydrostatic pressure.[14] The emission changes occurs by modification of assembled structure from J-type aggregation (green emission, no π-π interaction) to H-type aggregration (orange, weak π-π interaction) and then to aggregated dimers (red, strong π-π interaction) (Figure 3.4.5.a), this transformation can be reversed by heating. Last but not least, compound **5** presents different mechanochromic behavior by mechanical grinding or hydrostatic pressure.[15] Grinding lead to green emission state but applying hydrostatic pressure produce a higher red shitting in emission (see figure 3.4.5.b). This molecule forms face-to-face dimers and grinding cause transformation from a crystalline phase to amorphous state, while high hydrostatic pressure causes the reversible compression of crystal structure, the distance between dimers get shorter and emission turns to red emission.

In conclusion, mechanochromic and thermochromic phenomena are completely related to molecular and supramolecular interactions. In general, this behavior occurs by crystal-to-crystal, crystal-to-amorphous or crystal-to-liquid crystals transformation. In special,

[14] Dong, Y.; Xu, B.; Zhang, J.; Tan, X.; Wang, L.; Chen, J.; Lv, H.; Wen, S.; Li, B.; Ye, L.; Zou, B.; Tian, W. *Angew. Chem. Int. Ed.* **2012**, *51*, 10782–10785.
[15] Nagura, K.; Saito, S.; Yusa, H.; Yamawaki, H.; Fujihisa, H.; Sato, H.; Shimoikeda, Y.; Yamaguchi, S. *J. Am. Chem. Soc.* **2013**, *135*, 10322–10325.

polymorphism offers an excellent opportunity to establish optimal relationship between structure-properties and drives to the design of this smart materials. Crystallographic packing strongly influences exciton migration and light emitting properties of optically active materials. This high dependence of the final properties of the materials from the organization of the molecules at the nanometer level, offers many opportunities to synthesize materials that can respond to external stimuli by varying their supramolecular arrangement.

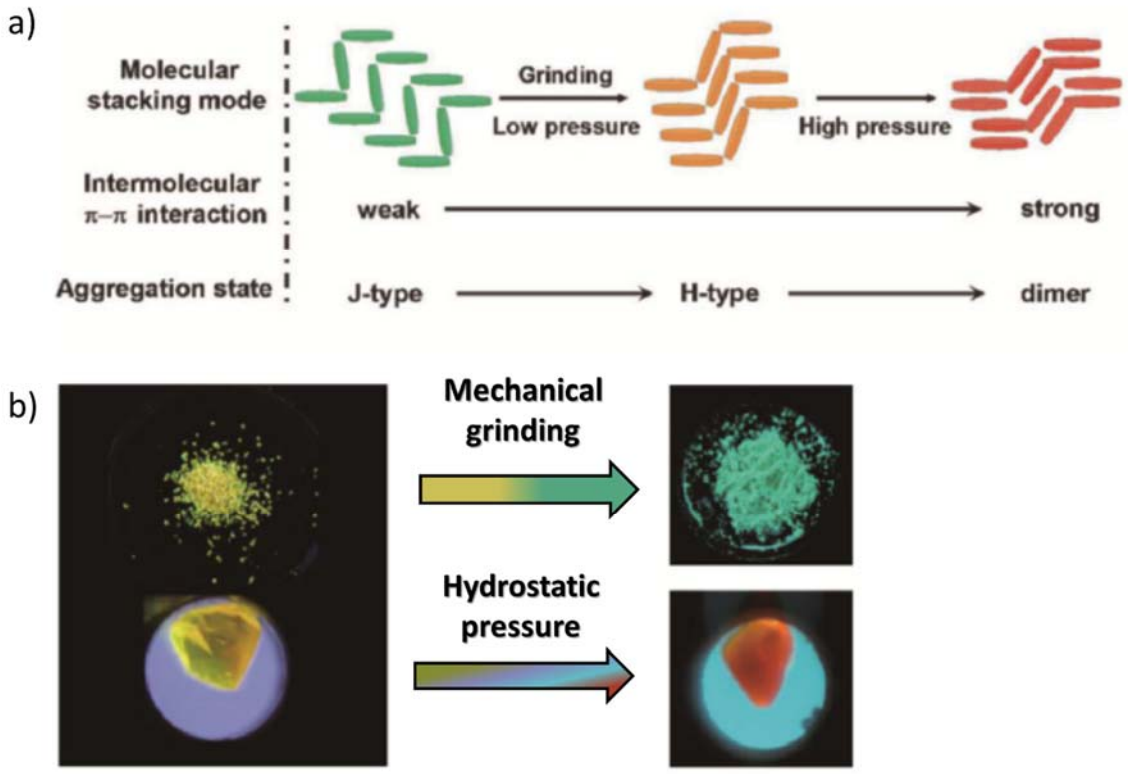

Figure 3.4.5. a) Schematic representation of molecular stacking changes in compound **4**. b) Photographs under UV light of compound **5** before and after mechanical grinding and hidrystatic pressure. Adapted with permission from Ref. 9. Copyright 2016 JohnWiley and Sons.

3.5. Quenching, Sensing and Porous Polymers

Another useful phenomenon involving fluorescence is its intensity decrease "quenching" under certain circumstances. This phenomenon can be caused by molecular interactions such as excited-state reactions, molecular rearrangements, energy transfer, ground-state complex formation, and collisional quenching.[16,] In spite of the diversity and complexity of this mechanism, this phenomenon is suitable for the design and development of multi-stimuli materials, for example, some applications have been developed in biotechnology[17], sensing and detection of explosives,[18] metals,[19] contaminants, etc. In the case of sensing, the high sensibility and huge diversity of possible inhibitors confers as quenching phenomena special interest for future applications.

The relationship between quenching and concentration of inhibitor can be quantify by the Stern-Volmer equation(Equation 3.5.1).[20]

$$I_q = I_0 + \frac{I_{final}-I_0}{2} \cdot \left\{1 + \frac{[Q]}{[F]} + \frac{1}{K_{SV}[F]} - \left[\left(1 + \frac{[Q]}{[F]} + \frac{1}{K_{SV}[F]}\right)^2 - 4\frac{[Q]}{[F]}\right]^{1/2}\right\} \quad \text{Equation 3.5.1}$$

Where I_0 is the initial fluorescent intensity of the fluorophore and I_{final} is the final intensity; Iq is the fluorescent intensity with the inhibitor, [F] is the concentration of the fluorophore and [Q] is the total concentration of the added inhibitor Q and K_{sv} the Stern-Volmer constant.

The Stern-Volmer constant K_{sv} can be calculated by linearizing the simplified equation (Equation 3.5.2) where [Q] is the total concentration of the added inhibitor Q.

$$\frac{I_0}{I} = 1 + K_{SV} \cdot [Q] \quad \text{Equation 3.5.2.}$$

By adding increasing amounts of an analyte to a fluorophore solution or dispersion, this constant can be readily calculated, analyzing the decrease in the intensity of the emission maximum. Representation of I_0/I-1 versus [Q] provides the Stern-Volmer constant from the slope of the plot obtained (Figure 3.5.1a). A higher value means that the interaction

---

[16] a) Wilkinson, F. Mechanism of Fluorescence Quenching in Solution. *East* **1964**, No. C, 620–630; b) Zu, F.; Yan, F.; Bai, Z.; Xu, J.; Wang, Y.; Huang, Y.; Zhou, X. *Microchim. Acta* **2017**, *184*, 1899–1914. b) McPhie, P. *Principles of Fluorescence Spectroscopy, Second Ed. Joseph R. Lakowicz*; 2000; Vol. 287.

[17] Anand, U.; Jash, C.; Boddepalli, R. K.; Shrivastava, A.; Mukherjee, S. *J. Phys. Chem. B*

[18] a) Banerjee, D.; Hu, Z.; Li, J. Royal Society of Chemistry July 28, 2014, pp 10668–10685. b) lw molecular weight gelator: Nath, S.; Pathak, S. K.; Pradhan, B.; Gupta, R. K.; Reddy, K. A.; Krishnamoorthy, G.; Achalkumar, A. S. *New J. Chem.* **2018**, *42*, 5382–5394.

[19] Fabbrizzi, L.; Licchelli, M.; Pallavicini, P.; Sacchi, D.; Taglietti, A. *Analyst* **1996**, *121*, 1763–1768.

[20] Boaz, H.; Rollefson, G. *J. Am. Chem. Soc.* **1950,** *72*, 3435-3443.

is stronger. The Stern-Volmer constant is a great way to evaluate the possible application of a material as a sensor and it is strongly dependent on the nature of fluorophore and the nature of analyte.

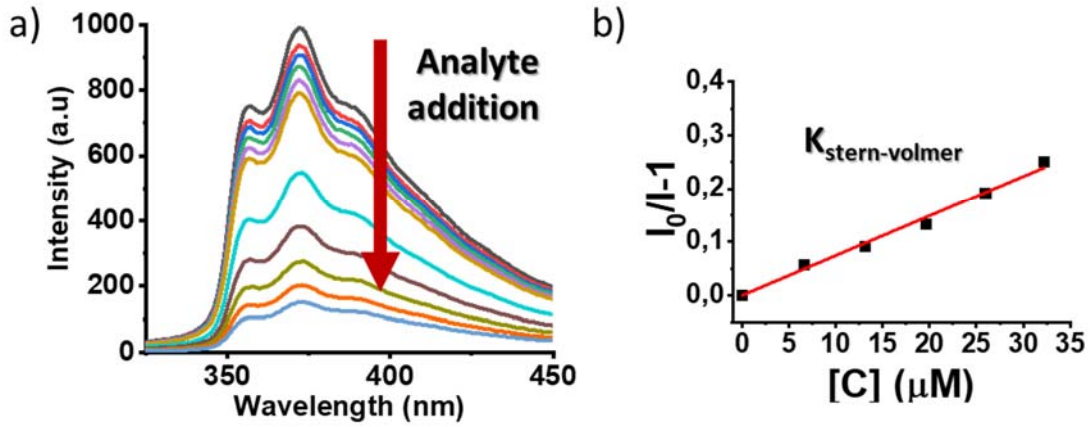

Figure 3.5.1. a) Typical fluorescence spectral changes of a fluorophore upon addition of increasing amounts of analytes. b) Stern-Volmer plots of 5 additions in a typical quenching experiment.

The two most common quenching mechanisms for sensing of aromatic analytes are Photoinduced Electron Transfer (PET) and Resonance Energy Transfer (RET). In the PET mechanism the quencher causes the transfer of electrons from excited states of fluorophore (LUMO) to excited states of quencher (LUMO) (Figure 3.5.2a), causing the loss of emission of the fluorophore through non-radiative transitions. Therefore, the larger the difference between the fluorophore and the analyte LUMO levels, the most favorable the electron transfer process will be.

The RET mechanism occurs when fluorophore confers the energy to the quencher to excite it. Contrary to what occurs in the PET mechanism, in this case, the excited fluorophore returns to ground state without any system change. This mechanism happens in the case where that spectra of fluorophores and absorption spectra of quenchers overlap (Figure3.5.2b).

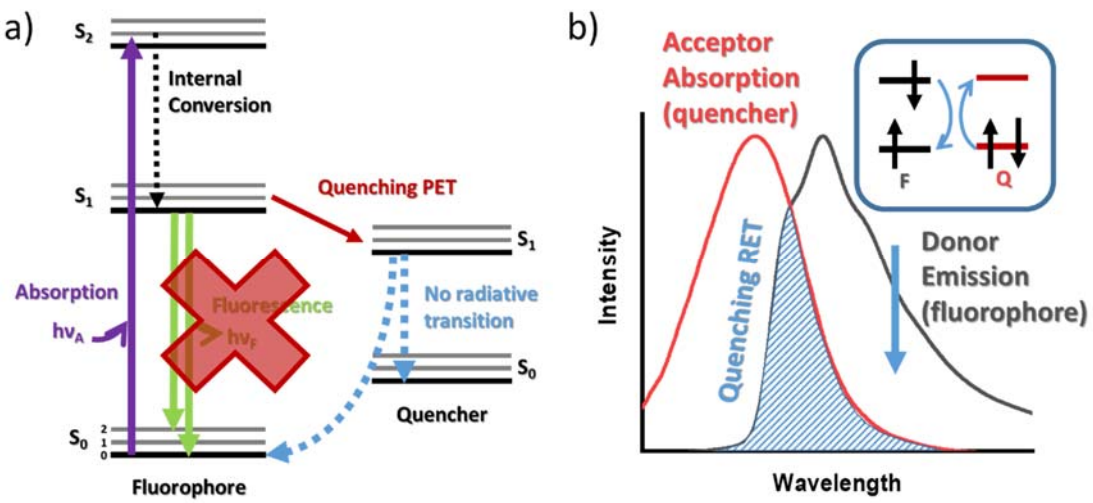

Figure 3.5.2. a) Photoinduced electron transfer (PET) mechanism. b) Resonance energy transfer (RET) mechanism.

Nitroaromatics are widely used as intermediates in many sectors such as pharmaceutical, dyes or pesticides and therefore they are frequent toxic contaminants in the effluvia of these industries. In addition, they are common raw materials in the preparation of explosives. Due to their importance in sectors that go from security to human health, there is an enormous interest in the reliable and selective detection of these compounds. Following the pioneering work by T. Swager on the use of linear π-conjugated polymers for the detection of nitroaromatic compounds,[21] electron rich light emitting microporous conjugated polymers, have emerged as an attractive platform for sensing these electron deficient compounds.[22] Interestingly the persistent porosity that characterize these polymers, facilitate the confinement and close contact of the analytes with the photofunctional organic moieties, thus resulting in enhanced optical responses.

In the last decades, Porous Organic Polymers (POPs) have been aroused great interest due to their multiple applications in fields as varied as sensing, adsorption[23], separation, catalysis[24] or energy storage[25]. Such applications take advantage of the persistent porosity that characterize these materials but also of the flexibility of the design "*a la carte*" that offer organic chemistry. In fact, there is a broad variety of available building units that,

[21] Yang, J. S.; Swager, T. M. *J. Am. Chem. Soc.* **1998**, *120*, 11864–11873.
[22] Liu, X.; Xu, Y.; Jiang, D. *J. Am. Chem. Soc.* **2012**, *134*, 8738–8741.
[23] Sadak, A. E.; Karakuş, E.; Chumakov, Y. M.; Dogan, N. A.; Yavuz, C. T. *ACS Appl. Energy Mater.* **2020**, *3*, 4983–4994.
[24] Byun, J.; Zhang, K. A. I. *Mater. Horizons* **2020**, *7*, 15–31.
[25] Cheng, Z.; Pan, H.; Zhong, H.; Xiao, Z.; Li, X.; Wang, R. *Advanced Functional Materials*. Wiley-VCH Verlag September 19, 2018, p 1707597.

when incorporated in polymeric backbones, usually maintains the functionality of the constituent units allowing the development of porous materials with predesigned properties.[26] This make these materials perfect candidates to use it for design of materials sensible to nitro aromatic and explosive compounds.

Some examples of fluorescent POPs are show in the Scheme 3.5.1 that have been used to detect the presence of different nitroaromatic compounds.

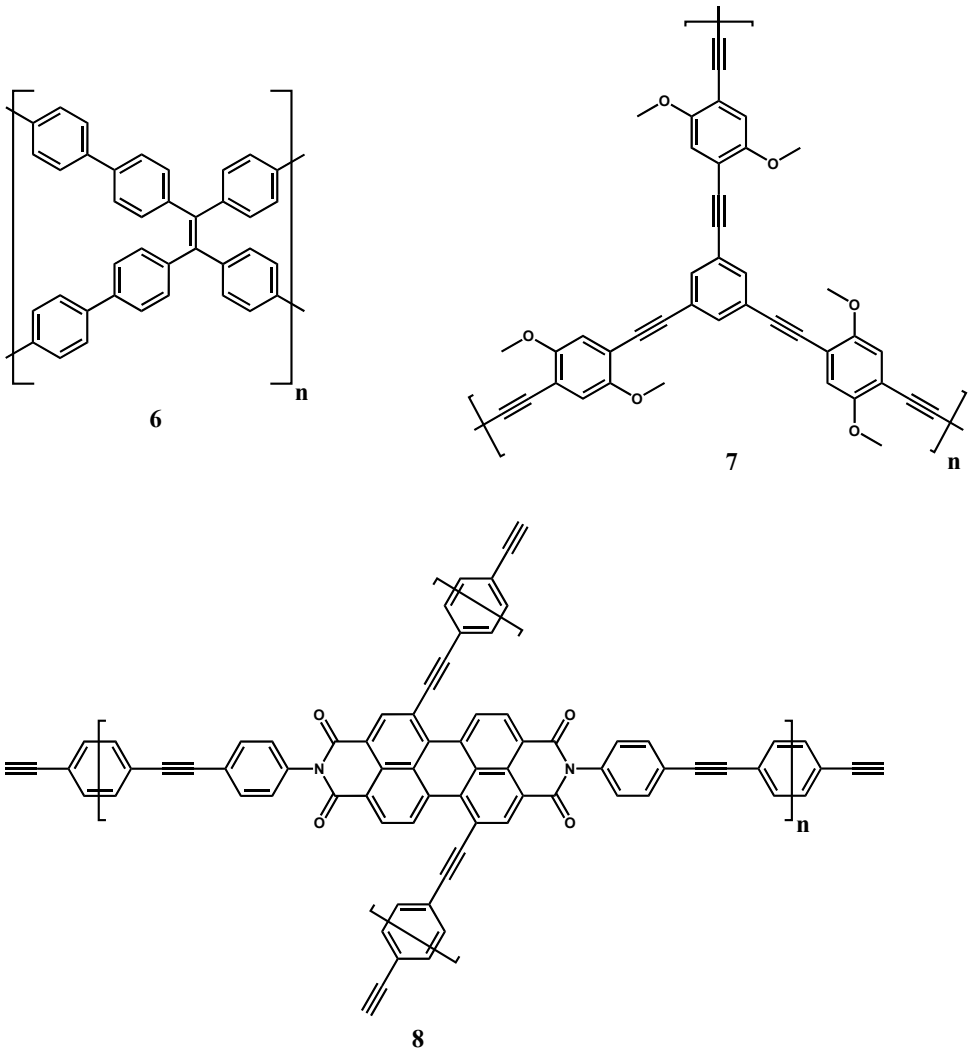

Scheme 3.5.1. Chemical structures of some examples of Porous Organic Polymers (POPs) used in sensing of nitroaromatic compounds.

In the case of **6**,[27] polymerization of tetraphenylethylene gives rise to a highly porous π-extended polymer, with a BET surface of 680 m^2g^{-1}. This polymer is able to detect 2,4-

[26] Xu, Y.; Jin, S.; Xu, H.; Nagai, A.; Jiang, D., *Chem. Soc. Rev.* **2013**, *42*, 8012–8031.
[27] Namgung, H.; Lee, J. J.; Gwon, Y. J.; Lee, T. S., *RSC Adv.* **2018**, *8*, 34291–34296.

dinitrotoluene (2,4-DNT), 2,6- dinitrotoluene (2,6-DNT), picric acid (PA), and 2,3-dinitro-2,3-dimethylethane (2,3-DN-2,3DM) through a PET quenching mechanism. Higher sensibility was found for PA with a K_{SV} constant of 3.53 $x10^2$ M^{-1}.

Compound **7** with a BET surface of 259 m^2g^{-1} was obtained by polymerization of 1,4-dialkoxybenzene subunits. This unit was chosen because of its electronic complementarity to TNT.[28] The porosity of this material vas determinate by. The sensibility to TNT was measures by film exposure to TNT vapors for 1 hour. It demonstrates the high sensibility of this polymer to TNT and the importance of the material design to optimize the sensing performance.

In another example, polymer **8** was made by perylene tetraanhydride bisimide derivative polymerization.[29] The BET surface was 378 m^2g^{-1}. Experiments with different nitroaromatics as o-nitrophenol (o-NP), picric acid (PA), dinitrotoluene (DNT), nitrobencene (NB), etc. shows typical PET mechanism quenching, where the quenching efficiencies are enhanced with the increase of such electron withdrawing groups ($-NO_2$) in analytes. However, this material shows higher sensitivity for o-NP and PA than expected, which has been ascribed to hydrogen-bonding interactions between the hydroxy units of the analytes that form with the open nitrogen and oxygen atoms in the perylene units on the pore walls. This present high sensitivity and selectivity to tracing o-nitrophenol in THF with a K_{SV} constant of 2.0 $x10^4$ M^{-1}.

The above examples demonstrate the versatility and selectivity of POPs in explosives and nitroaromatics compounds, the possibility of develop these polymers by design and their possible applications in suspension, film or solid.

[28] Novotney, J. L.; Dichtel, W. R., *ACS Macro Lett.* **2013**, *2*, 423–426.
[29] Geng, T. M.; Li, D. K.; Zhu, Z. M.; Zhang, W. Y.; Ye, S. N.; Zhu, H.; Wang, Z. Q., *Anal. Chim. Acta* **2018**, *1011*, 77–85.

3.6. Semicondutors moieties: Benzothiadiazol and Truxene derivatives

To date a great variety of π-conjugated molecules have been used as moieties in the construction of light emitting π-conjugated molecules and polymers. Among them, in the research group have a vast experience and special interest in the structures shown in Scheme 3.6.1. (Benzothiadiazole, Truxene, Triindol, and Truxenone).[30]

Benzothiadiazole (BTD) is one of the preferred moieties in the quest for efficient light emitting compounds.[31] This electron deficient heterocycle presents high fluorescence quantum efficiencies and has a strong propensity to adopt quinoid conformations, thus facilitating charge transfer between attached substituents and enabling the tuning of its emission properties. These properties have made possible their application as markers in biological studies,[32] OLEDs,[33] OPVS,[34] etc. This demonstrates the potential of these systems and their possible application in all the aforementioned fields. Moreover, this moieties present an important interaction between S and N, this is called chalcogen bonding.[35] The S-N interactions present great potential for supramolecular interactions, capable of induce intermolecular order.

On the other hand, Truxene (10,15-dihydro-5H-diindeno[1,2-*a*:1',2'-*c*] fluorene) is a molecule that contains a C_3 axis of symmetry and a rigid, planar, heptacyclic and polyaromatic structure. This molecule has interesting optical properties (it is an efficient blue emitter) due to the delocalization of the π electrons in its structure. In addition, it has p-type semiconductor properties. Truxene is a material with high thermal and chemical stability, which together with its optoelectronic properties makes it suitable for its use in different types of devices, such as the development of new organic field effect transistors

---

[30] a) García-Frutos, E. M.; Pandey, U. K.; Termine, R.; Omenat, A.; Barberá, J.; Serrano, J. L.; Golemme, A.; Gomez-Lor, B., *Angewandte Chemie - International Edition* **2011,** *50* (32), 7399-7402. b) Coya, C.; Ruiz, C.; Álvarez, Á. L.; Álvarez-García, S.; García-Frutos, E. M.; Gómez-Lor, B.; De Andrés, A., *Organic Electronics: physics, materials, applications* **2012,** *13* (10), 2138-2148. c) Ruiz, C.; Pandey, U. K.; Termine, R.; García-Frutos, E. M.; López-Espejo, G.; Ortiz, R. P.; Huang, W.; Marks, T. J.; Facchetti, A.; Ruiz Delgado, M. C.; Golemme, A.; Gómez-Lor, B., *ACS Applied Materials and Interfaces* **2016,** *8* (40), 26964-26971.

[31] Ito, S.; Yamada, T.; Taguchi, T.; Yamaguchi, Y.; Asami, M., *Chem. Asian J.* **2016,** *11*, 1963-1970.

[32] Neto, B. A. D.; Lapis, A. A. M.; Mancilha, F. S.; Vasconcelos, I. B.; Thum, C.; Basso, L. A.; Santos, D. S.; Dupont, J., *Organic Letters* **2007,** *9* (20), 4001-4004.

[33] Yan, B. P.; Cheung, C. C. C.; Kui, S. C. F.; Xiang, H. F.; Roy, V. A. L.; Xu, S. J.; Che, C. M., *Advanced Materials* **2007,** *19* (21), 3599-3603.

[34] Ogawa, T.; Yanai, N.; Monguzzi, A.; Kimizuka, N., *Scientific Reports* **2015,** *5*, 10882.

[35] Ams, M. R.; Trapp, N.; Schwab, A.; Milić, J. V.; Diederich, F., *Chem. Eur. J.* **2019**, *25*, 323–333.

(OFETs),[36] absorption of photons (TPA),[37] organic photovoltaic cells (OPVs), [38] organic light emitting diodes (OLEDs), fluorescent probes, etc.

Truxene, can be considered as a 1,3,5,-triphenylbenzene planarized through three bridging methylenes (Figure 3.6.1). These methylene groups give rise to three additional fused 5 membered rings thus enhancing the delocalization of the π-system, which confers this molecule interesting photoactive properties and excellent electron-donating capabilities. Changing the methylene units (gray) to amino (blue) or ketone groups (red), allow us to obtain isostructural molecules but with completely different redox and semiconducting properties. Therefore, while truxene[39] and triindole[40] are p-type semiconductors, truxenone[41] present as a high-mobility n-type semiconductor. Trigonal π-conjugated structure of this moieties have aroused interest as building units for molecular and polymeric materials.

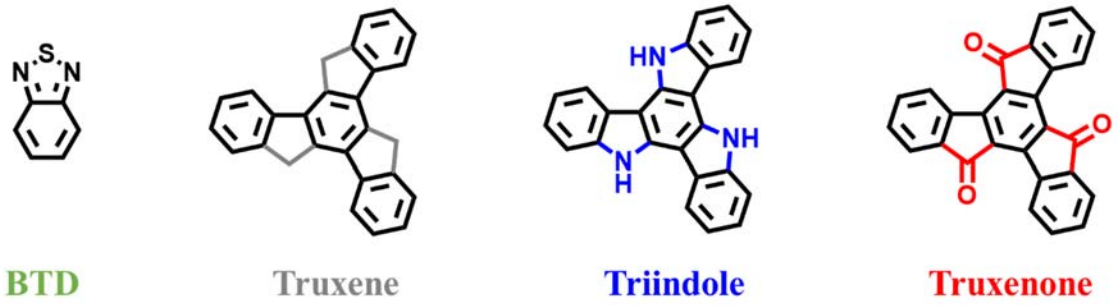

Scheme 3.6.1. Chemical structure of Benzothiadiazole, Truxene, Triindole and Truxenone.

Triindole (10,15-dihydro-5H-diindolo[3,2-*a*:3',2'-*c*]carbazole) can be considered as a flat π-conjugated system formed by the union of three carbazole units (known gap transporter) sharing a ring. This discotic platform has three N-H units that can be easily functionalized by the introduction of alkyl chains. The triindole presents a high versatility of

[36] Sun, Y. M.; Xiao, K.; Liu, Y. Q.; Wang, J. L.; Pei, J.; Yu, G.; Zhu, D. B., *Adv. Funct. Mater.* **2005,** *15*, 818-822.
[37] Xie, Y.; Zhang, X.; Xiao, Y.; Zhang, Y.; Zhou, F.; Qi, J.; Qu, J., *Chem. Commun.* **2012,** *48*, 4338-4340.
[38] Ke, S.; Jie-Yu, W.; Jian, P., *The Chemical Record* **2015,** *15*, 52-72.
[39] Goubard, F.; Dumur, F., *RSC Adv.* **2015,** *5*, 3521-3551..
[40] a) Ruiz, C.; Pandey, U. K.; Termine, R.; García-Frutos, E. M.; López-Espejo, G.; Ortiz, R. P.; Huang, W.; Marks, T. J.; Facchetti, A.; Ruiz Delgado, M. C.; Golemme, A.; Gómez-Lor, B., *ACS Appl. Mater. Interfaces* **2016**, *8*, 26964–26971. b) Benito-Hernández, A.; Pandey, U. K.; Cavero, E.; Termine, R.; García-Frutos, E. M.; Serrano, J. L.; Golemme, A.; Gómez-Lor, B., *Chem. Mater.* **2013**, *25*, 117–121.
[41] Gómez-Esteban, S.; Benito-Hernandez, A.; Termine, R.; Hennrich, G.; Navarrete, J. T. L.; Ruiz Delgado, M. C.; Golemme, A.; Gómez-Lor, B., *Chem. Eur. J.* **2018**, *24*, 3576–3583.

functionalization that allows multiple possibilities when tuning its optical and electronic properties, as well as its supramolecular organization for its subsequent implementation in different fields.

Last but not least, truxenone (5H-diindeno[1,2-*a*:1',2'-*c*]fluorene-5,10,15-trione) can be described as a polyaromatic heptacyclic system formed by the union of three fluorenone units sharing a central aromatic ring with C_3 symmetry. The structure of this molecule is also planar and is characterized by carbonyl groups, which makes truxenone electron-deficient, making it an n-type semiconductor.

All four moieties present tunable fluorescence, interesting supramolecular interactions (π-π staking, dipole-dipole, H-bonding, chalcogen, etc) and high quantum fields. This make these molecules perfect candidates for the design of fluorescence "smart materials" that respond to external stimuli.

To sum up, in this thesis we have explored two possible approaches to the design of smart materials: First, molecular design of mechanochromic and thermochromic materials capable of response to pressure, mechanical stimuli or temperature. This transformation only is possible by stabilizing at least two states/phases with different emission properties and requiring a low amount of energy to be transformed. Intermolecular and intramolecular interactions as conformational rotations, hydrogen bonding, chalcogen bonding, π–π stacking, ionic interactions, and van der Waals forces plays a key role in this design.

Second, the design of photoactive Porous Organic Polymers (POPs) to detection and sensing of nitroaromatic compounds. Using semiconductors monomers, we can transfer their properties to the final material and tune their interactions with nitroaromatics. By PET mechanism we can rationalize the relation POP-LUMO levels with analyte LUMO levels , making it possible to generate selectivity of polymer-analyte.

4. OBJECTIVES

Smart materials which switch their optical spectroscopic properties (*i.e.*, color, fluorescence) upon physical external stimulation (*i.e.*, pressure, temperature) arouse enormous interest and have found applications in fields as varied as sensing, construction, recording, display technologies or rewritable paper.

The main objective of this thesis aims to the development of "smart materials" capable of reacting to external stimuli such as temperature, pressure or presence of analytes producing changing their shape, color or emission properties.

To achieve these objectives, was used organic semiconductor such as benzothiadiazole, truxene, triindol and truxenone because the versatility and easy tuning of their electronic properties. In addition to the high luminescent properties of the moieties.

The specific objectives of this thesis are:

- Synthesis and characterization of a series of benzothiadiazole derivatives. Changing the functional group to tune the electronic and luminescence properties.
- Study of supramolecular interactions and properties as liquid crystal phases, mechanochromic and thermochromic phenomena.
- Development of BTD-based "smart materials". Taking advantage of the properties of liquid crystal phases, mechanochromic and thermochromic phenomena to obtain rewritable materials.
- Synthesis and characterization of truxene-based porous organic polymers. Study of variation of electronic and optical properties with the structure changes.
- Study of sensing properties of truxene-based porous organic polymers against nitroaromatic and explosives molecules in suspension.
- Design of new truxene-derivatives-based porous organic polymers to the overall understanding of the structure-electronic property relationships.

5. PUBLICATIONS

The work done in this doctoral thesis are described in these publications. They will appear in this order:

1. **Fluorescent and Electroactive Monoalkyl BTD-Based Liquid Crystals with Tunable Self-Assembling and Electronic Properties**

Marcelo Echeverri, Irene Martín, Alberto Concellón, Constanza Ruiz, María San Anselmo, Enrique Gutiérrez-Puebla, José L. Serrano, and Berta Gómez-Lor*

2. **Untangling the mechanochromic properties of benzothiadiazole- based luminescent polymorphs through supramolecular organic framework topology**

Marcelo Echeverri, Constanza Ruiz, Sergio Gámez-Valenzuela, Irene Martín, M. Carmen Ruiz Delgado, Enrique Gutiérrez-Puebla, M. Ángeles Monge, Lina M. Aguirre-Díaz*, and Berta Gómez-Lor*

3. **Stimuli-Responsive Benzothiadiazole Derivative as a Dopant for Rewritable Polymer Blends**

Marcelo Echeverri, Constanza Ruiz, Sergio Gámez-Valenzuela, Matias Alonso-Navarro, Enrique Gutierrez-Puebla, José L. Serrano, M. Carmen Ruiz Delgado*, and Berta Gómez-Lor*

4. **Effect of the Linkage Position on the Conjugation Length of Truxene-Based Porous Polymers: Implications for Their Sensing Performance of Nitroaromatics**

Marcelo Echeverri, Sergio Gámez-Valenzuela, Rafael C. González-Cano, Jordy Guadalupe, Sandra Cortijo-Campos, Juan Teodomiro López Navarrete, Marta Iglesias*, M. Carmen Ruiz Delgado*, and Berta Gómez-Lor*

5. **In silico design of 2D polymers containing truxene-based platforms: Insights into their structural and electronic properties**

Sergio Gámez-Valenzuela, Marcelo Echeverri, Berta Gómez-Lor*, José I. Martínez* and M. Carmen Ruiz Delgado*

ACS OMEGA

Article

Cite This: ACS Omega 2018, 3, 11857−11864

http://pubs.acs.org/journal/acsodf

Fluorescent and Electroactive Monoalkyl BTD-Based Liquid Crystals with Tunable Self-Assembling and Electronic Properties

Marcelo Echeverri,[†] Irene Martín,[†] Alberto Concellon,[‡] Constanza Ruiz,[†] María San Anselmo,[‡] Enrique Gutierrez-Puebla,[†] Jose L. Serrano,[‡] and Berta Gomez-Lor*[,†]

[†]Material Science Factory, Instituto de Ciencia de Materiales de Madrid, Cantoblanco, 20849 Madrid, Spain

[‡]Dpto. Química Organica, Instituto de Nanociencia de Aragon, Universidad de Zaragoza, 50009, Zaragoza, Spain

Supporting Information

ABSTRACT: We report here on a series of redox active benzothiadiazole-based luminophores functionalized on one edge with a phenyl-nonyl substituent, which confers these molecules a rodlike shape and a tendency to self-assemble into layered superstructures. On the other edge, the molecules are endowed with different p-substituted phenyl rings, which allows the modulation of their redox and optical properties on the basis of the electronic nature of the terminal substituents. We have found that just one lateral alkyl chain is sufficient to induce mesomorphism in these molecules, which present nematic or smectic mesophases upon thermal treatment. Single-crystal analysis allows us to get an insight into the nature of the forces responsible for different supramolecular assemblies in these derivatives, and point to a strong contribution of the terminal groups in the different arrangements observed. The interesting redox and optical properties together with their self-assembling tendencies render these new materials interesting candidates for optoelectronics.

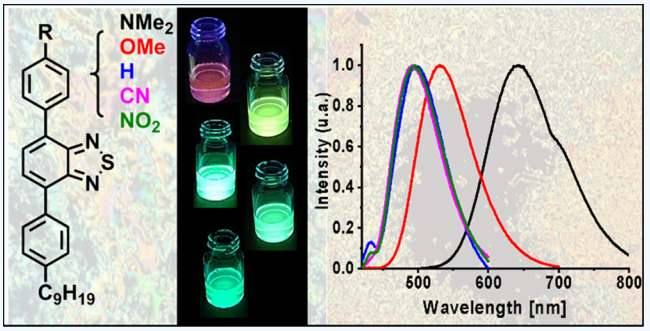

INTRODUCTION

The area of organic electronics has evolved in only a few years from basic research to the development of devices such as organic light emitting diodes (OLEDs), which are already being massively commercialized.[1,2] Organic active layers can be usually implemented in devices by different solution-processing techniques in contrast to the expensive lithography and vacuum techniques required for silicon-based materials offering interesting opportunities to obtain low-cost devices.

On the other hand, the high versatility of organic chemistry allows the rational development of organic materials, with a high control of their final properties. Fundamental parameters for the development of molecules for their incorporation in (opto)electronic devices, such as light emission or absorption properties, energy levels, etc., can be designed "a la carte", thanks to the deep knowledge that has been acquired in the last few years through numerous structure−properties studies.[3] Unfortunately, our ability to predict/control the supramolecular arrangement of electro/photoactive molecules is still very limited, although the electronic properties of organic materials depend not only on those of the building units but also on how the molecules are organized in the bulk.

Thus, in the search of device-oriented molecular systems, self-assembling materials,[4] able to self-organize, through the cooperation of different intramolecular forces, represent interesting candidates in the area. In this context, liquid crystalline ordering has emerged as an attractive concept in the development of materials for (opto)electronic applications.[5,6] The dynamic character of the mesophases confers to them interesting self-healing properties and facilitates their processing as highly ordered thin films from solution or melt. The design principles to induce liquid-crystalline phases are well established and usually require a molecular disk-shaped (discotic liquid crystals) or rod-shaped (calamitic liquid crystals) π-conjugated core, functionalized with alkyl chains on their periphery to induce microphase segregation upon thermal heating.[7] Discotic liquid crystals, with their highly anisotropic columnar organization, have been long identified as one-dimensional semiconductors,[8−11] exhibiting, in some cases, remarkable hole[12,13] and electron[14,15] mobility values. However, the anisotropic character of charge transport in these systems and the difficult alignment of the columns on substrates with an edge-on configuration have hampered their incorporation in devices[16−18] Although less explored in this area, calamitic liquid crystals that are much more fluid and easy to align have emerged as interesting alternatives.[19−22] Particularly, the smectic mesophases found in different monoalkyl rod-shaped molecules have been demonstrated to be promising vehicles to obtain homogeneous films with reduced grain boundaries and a favorable layered arrangement for charge transport.[20,22]

Received: July 18, 2018
Accepted: September 11, 2018
Published: September 25, 2018

DOI: 10.1021/acsomega.8b01696
ACS Omega 2018, 3, 11857−11864

Scheme 1. Synthesis of Compounds 2−7

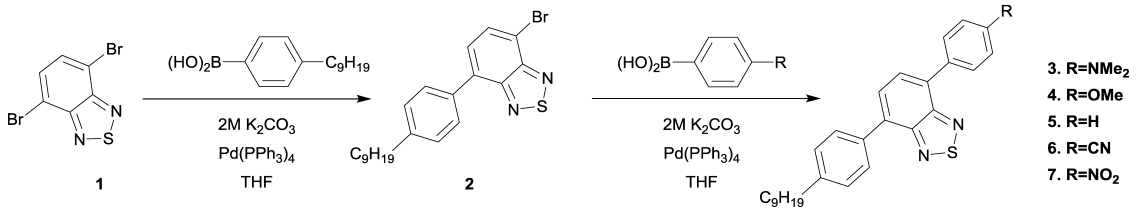

Table 1. Thermal Stability and Mesogenic Properties of 3−7

compounds	$T_{2\%}$ (°C)[a]	phase transitions[b]
3	220	I 88 (0.5) N 22 (2.9)[c] N + Cr; N + Cr 32 (−9.8) Cr 100 (28.5) I
4	284	I 112 (0.5) N 48 (20.4) N + Cr; N + Cr 70 (−10.5) Cr 101 (37.2) N 114 (0.5) I
5	272	I 26 (24.3) Cr; Cr 62 (31.1) I
6	302	I 114 (1.3) SmA 52 (27.7) Cr_1; Cr_1 69 (4.9) Cr_2 92 (19.5) SmA 117 (0.7) I
7	274	I 74 (0.5) N 32 (28.5)[c] Cr; Cr 106 (42.6) I

[a]Temperature at which 2% mass lost is detected in the thermogravimetric curve. [b]DSC data of the first cooling process and the second heating process at a rate of 10 °C min^{-1}. Temperatures are read at the maximum of the corresponding peaks, and enthalpies (kJ mol^{-1}) are in brackets. Cr: crystal, N: nematic mesophase, SmA: smectic A mesophase, I: isotropic liquid. [c]Monotropic liquid crystals, data obtained in the second cooling process.

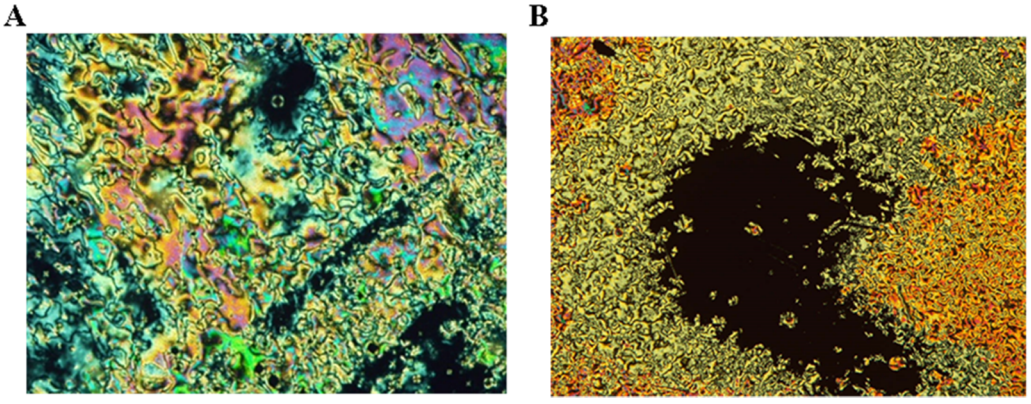

Figure 1. Micrograph of the textures observed by POM for (A) **4** at 90 °C (cooling, 20×) and (B) **6** at 90 °C (cooling, 20×).

In the last few years, the benzothiadiazole (BTD) core has emerged as a promising molecular design motif in the development of device-oriented small molecule and polymeric materials. This electron-deficient moiety presents interesting n-type semiconducting properties and high fluorescence quantum efficiencies and has a strong propensity to adopt quinoid conformations, thus facilitating charge transfer (CT) between attached substituents and enabling the tuning of its electronic properties. Because of these attractive properties, this molecule has been extensively incorporated as an active layer in electronic devices.[23−26] By symmetrical functionalization with two aryl groups endowed with flexible chains, several BTD-based nematic and smectic liquid crystals[27] have been synthesized and incorporated as an active layer in organic field effect transistors (OFETs)[24] or as highly dichroic fluorescent dyes for liquid crystal displays.[28] However, to our knowledge, asymmetric monoalkyl liquid crystalline BTD derivatives have not yet been reported.

In this manuscript, we describe the synthesis and the electronic and self-assembling properties of a series of asymmetrically functionalized rod-shaped electroactive benzothiadiazole derivatives, presenting interesting redox and light-emitting properties. These molecules are endowed on one edge with a phenyl-nonyl substituent and on the other edge with different p-substituted phenyl rings. Interestingly, we have found that just one lateral alkyl chain is enough to induce mesomorphism in these molecules that present nematic or smectic mesophases upon thermal treatment, which allows us to use the other terminal substituent to modulate their electronic properties. Thus, by systematic variation of the electronic nature of these substituents, we could fine-tune the redox and optical properties of these derivatives. The attached substituents also play a key role in how these molecules self-assemble in crystalline or liquid crystalline phases by participating in different intermolecular interactions, as could be unequivocally determined through single-crystal analysis.

RESULTS AND DISCUSSION

The synthesis of compounds **3**−**7** was performed in two steps of palladium-catalyzed Suzuki cross-coupling reactions (Scheme 1). Initially 4,7-dibromo-2,1,3-benzothiadiazole **1** was reacted with 1 equiv of 4-nonylphenylboronic acid. Under thermal heating conditions, compound **2** is obtained, along with some byproduct of double coupling and unreacted dibrominated benzothiadiazole. Monocoupling can be favored by using microwave heating conditions, which provides compound **2** in good yield in just 3 h. Starting from **2**, compounds **3**−**7** were synthesized straightforwardly in the

DOI: 10.1021/acsomega.8b01696
ACS Omega 2018, 3, 11857−11864

second step by Suzuki cross-coupling with the corresponding p-substituted phenyl boronic acid under microwave heating. All new compounds were purified by silica gel column chromatography, using a mixture of hexane/CH_2Cl_2 (3:1) as eluent and characterized by ^{1}H NMR, ^{13}C NMR, and mass spectrometry.

Study of the Self-Assembling Properties. *Liquid Crystalline Properties.* With the aim of investigating the propensity of these compounds to organize in smectic/nematic mesophases, we studied their thermal properties. Please note that although several rod-shaped BTD-based nematic and smectic liquid crystals have been reported, to our knowledge, all of them exhibit a C_2 symmetry.[24,27,28]

The thermal transitions and mesomorphic properties were studied by polarizing optical microscopy (POM), differential scanning calorimetry (DSC), and X-ray diffraction (XRD). With the exception of **5**, all of these derivatives showed mesomorphic properties (see Table 1 and the Supporting Information).

Derivatives **4** and **6** displayed enantiotropic liquid crystalline mesophases, whereas **3** and **7** exhibited monotropic liquid crystalline behavior. Schlieren textures with homeotropic domains were obtained by POM for all four compounds, indicating that the mesophases have an orthogonal character (Figure 1).

To determine the nature of the mesophases and the structural parameters, we performed the XRD studies. The diffractograms recorded for **3**, **4**, and **7** only contains broad diffuse maxima, suggesting the absence of a long-range positional order in the liquid crystal phase. These types of patterns are typical of nematic mesophases, which have only orientational order.

In contrast, the diffractogram of compound **6** is in agreement with a smectic phase, which has been assigned as a smectic A organization, given the orthogonal character of the mesophases deduced from the presence of homeotropic domains in the textures observed by POM. Its X-ray diffraction pattern shows a sharp, strong maximum in the small-angle region (assigned to the first-order reflection of the smectic layer) and a diffuse halo (related to the conformational disorder of the liquid-like chain in the high-angle region). A layer spacing of 39.4 Å was deduced by applying the Bragg's law to the small-angle maximum. This spacing is significantly larger than the molecular length in its most extended conformation (25.2 Å), which suggests that the mesophase adopts a bilayer structure.

This bilayer arrangement is reminiscent of that observed in cyanobiphenyl liquid crystals,[29,30] the first liquid crystals with technological applications, and points to an important contribution of the nitrile groups in the smectic behavior of this compound via dipole−dipole interactions. Please note that the use of promesogenic cyanobiphenyl core continues to play a fundamental role in the liquid crystals arena.[31−35]

Crystal Structure. To shed light on the influence of the substituents on the different arrangements observed, we attempted to grow single crystals of different compounds. Single crystals of sufficient quality for structure determination were obtained for **4**, **6**, and **7** by slow evaporation of 1:1 CH_2Cl_2/CH_3CN solutions at room temperature. We found that the terminal substituents also significantly affect the self-assembling trends of these molecules, as they are involved in intermolecular interactions with the BTD core, or in the case of the cyano groups by establishing dipolar interactions among the terminal nitriles.

Compound **4** crystallizes in the triclinic space group *P*1, with two independent molecules in the asymmetric unit. The main difference between the two independent units is derived from different torsion angles between the BTD unit and the phenyl linkers, which, in each molecule, are rotated in opposite directions (by 39.44 and 31.88° in one of the molecules and by 33.73 and 27.42° in the other).

The compound crystallizes to form dimers, which are stabilized by O···S (2.964 Å) and CH···N (2.877 Å) interactions (Figure 2a). These dimers form layers driven by

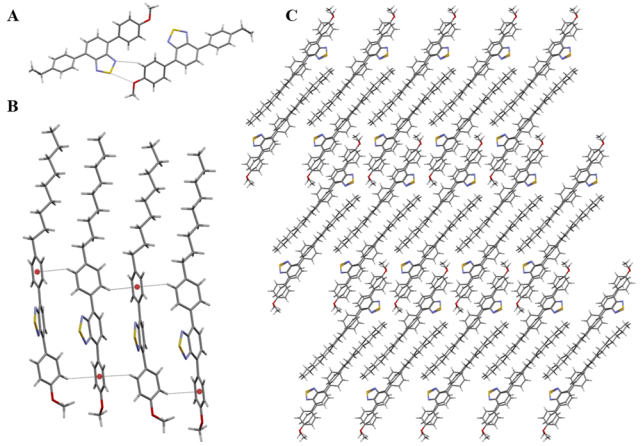

Figure 2. Depiction of the intermolecular interactions of **4** (A) between dimers and (B) between molecules of the same layer. (C) Crystal packing view along (a).

C−H···π interactions involving the neighboring phenyl rings (Figure 2b), whereas the BTD rings are situated in a parallel-displaced arrangement. The long alkyl chains are strongly interdigitated (Figure 2c).

Compound **6** crystallizes in the monoclinic space group *C*2/*c*, with two independent molecules in the asymmetric unit. Again the main difference between two independent units is derived from different torsion angles between the BTD unit and the phenyl linkers, which, in this case, are rotated in the same directions (by 48.36 and 44.88° in one of the molecules and by 46.32 and 45.73° in the other).

The analysis of the crystal packing shows that **6** is organized in a bilayered structure, as previously observed in the mesophases (Figure 3). An analysis of the close contacts in the structure evidences the antiparallel coupling of the cyano end groups, demonstrating the leading role of the nitrile groups in the attained bimolecular arrangement, via dipolar interactions. No interdigitation of the alkyl chains can be detected in this case.

Compound **7** crystallizes in the monoclinic space group $P2_1/c$ and has one independent molecule in the asymmetric unit. Both phenyl rings are rotated in the same directions by 31.69 and 37.90° with respect to the BTD unit.

The molecules adopt an extended conformation and arrange in a highly compact superstructure, in which the molecules grow with their long axis nearly parallel to the *a*-axis of the unit cell (Figure 4). The analysis of the short contacts in the crystal packing shows a nonbonded interaction between the sulfur atom and one of the oxygen atoms of the nitro group situated at an interatomic distance of 3.0 Å. This indicates that again

DOI: 10.1021/acsomega.8b01696
ACS Omega 2018, 3, 11857−11864

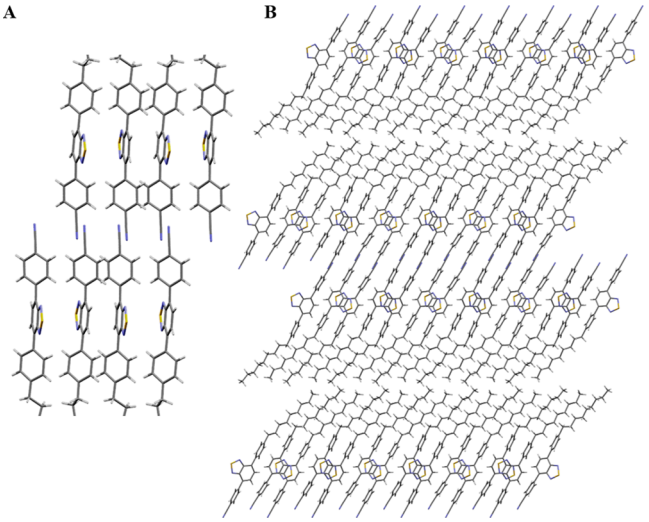

Figure 3. Depiction of the intermolecular interactions of **6** (A) between molecules of the same layer. (B) Crystal packing view along (b).

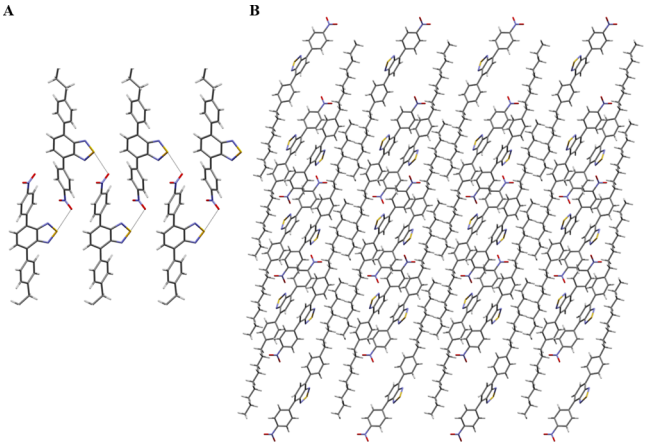

Figure 4. Depiction of the intermolecular interactions of **7** (A) between molecules of the same layer. (B) Crystal packing view along (b).

the stabilization of this structure involves the attached functional groups.

Electronic Properties. The tendency of these molecules to self-assemble into layered arrangements, as shown above, render them very attractive for the easy formation of ordered thin films to be implemented in devices. In the search for molecules that can be incorporated in the devices, it is also highly desirable to be able to fine tune their electronic properties. With this in mind, we have investigated how the electronic nature of the terminal groups influence the optical and redox properties of these molecules by means of optical (UV−vis absorption and fluorescence) spectroscopy and cyclic voltammetry (CV).

The absorption properties of the BTD derivatives **3**−**7** were recorded in a 10^{-5} M dichloromethane solution by UV−vis spectroscopy at room temperature. All of the derivatives show two absorption bands: one at high energies associated with the $\pi \rightarrow \pi^*$ transitions of the molecule and other at lower energies assigned to charge transfer (CT) transition involving the end groups. In compounds **3** and **4**, which are substituted with electron-donor groups, the CT band is red-shifted. This behavior is more notable for **3** functionalized with the strongest dimethylamine donor (Table 2 and Figure 5a).

The electrochemical properties of the compounds **3**−**7** were investigated by cyclic voltammetry (CV). All of the compounds can be easily reduced to stable radical anions, thus reflecting the strong acceptor character of the BTD core. The reduction potential of the derivatives substituted with electron donors is nearly identical; however, the reduction potentials move to less negative values as the electron-acceptor character of the substituents is increased and therefore the electron density in the π system is lowered.

Interestingly, derivatives **3**−**5** present an amphoteric redox character, as they can be also easily oxidized in the accessible solvent window and the oxidation potentials shifts anodically with increase in the acceptor character of the substituent. Compound **3** presents a second oxidation wave because of the oxidation of the NMe_2 group (Table 2 and Figure 5b).

The energy of the HOMO−LUMO levels of compounds **3**−**5** was estimated from their first oxidation and the reduction potentials respectively, by referring the potentials to the ferrocene/ferrocenium redox couple and considering a value of −4.8 eV for ferrocene with respect to zero vacuum level. In compounds **6** and **7**, which show only a reduction process, the HOMO level was calculated by subtracting the value of the optical gap from that of the LUMO level, estimated electrochemically.

The position of the HOMO and LUMO levels calculated for **3** and **4** are adequate for the easy injection of electrons and holes from common electrodes of much relevance for potential electronic applications. Conversely, those of **5**−**7** are more appropriate for the easy injection of electrons (see Table 2).

All of these compounds emit intensely in a solution and their emission wavelengths are also strongly influenced by the electronic nature of the substituents. In 10^{-5} M dichloromethane solutions, compounds **5**−**7** emit cyan fluorescence, with maxima being barely affected by the electron-withdrawing character of the substituents. Conversely, the emission of compounds **3** and **4** is significantly red-shifted as a result of their increased intramolecular charge transfer.

Compound **3** presents an orange-red fluorescence at 644 nm, whereas **4** exhibits a maximum at 532 nm with the emission of a shiny yellow color (Table 2 and Figure 5a). High

Table 2. UV−Vis and Fluorescence Spectroscopic and Redox Properties of 3−7 in CH_2Cl_2 and Estimated Highest Occupied Molecular Orbital (HOMO) and Lowest Unoccupied Molecular Orbital (LUMO) Energies

compounds	λ_{max}^{abs}(nm)	λ_{max}^{em}(nm)	E_{gap}^{opt}(eV)	$E_{1/2}^{red}$	$E_{1/2}^{ox}$	HOMO(eV)	LUMO(eV)
3	446	644	2.33	−1.49	0.80	5.17	2.87
4	399	532	2.70	−1.46	1.41	5.74	2.88
5	385	496	2.86	−1.44	1.64	6.01	2.94
6	384	494	2.83	−1.32		5.88	3.05
7	388	496	2.83	−1.03		6.18	3.35

DOI: 10.1021/acsomega.8b01696
ACS Omega 2018, 3, 11857−11864

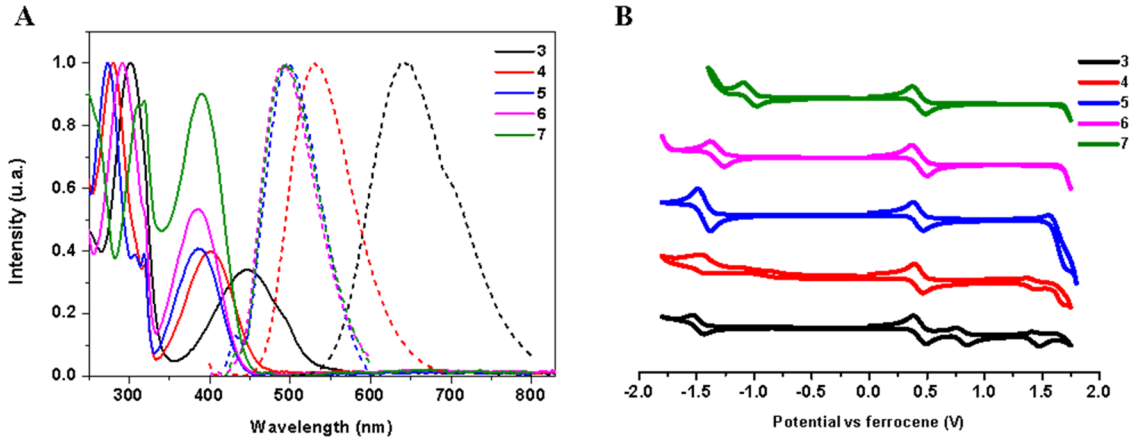

Figure 5. (A) Normalized UV−vis (lines) and fluorescence (dots) spectra of compounds **3**−**7** in CH_2Cl_2, $c = 5 \times 10^{-6}$ M solutions and (B) cyclic voltammograms of compounds **3**−**7** at $c = 1 \times 10^{-3}$ M recorded at a scan rate 100 mV s^{-1} in CH_2Cl_2/0.1 M $TBAPF_6$ measured versus Ag/AgCl and using ferrocene as an internal reference.

Stokes shifts are observed in all of the cases, which again show a strong dependence of the nature of the terminal substituents; **5**−**7** present Stokes shifts around 110 nm and **3** and **4** show Stokes shifts of 198 and 133 nm, respectively.

We have investigated the light-emitting properties of these compounds in different environments. The fluorescence spectra of compounds **3**−**7** show a strong solvent dependence. The emission bands shift bathochromically as the solvent polarity is increased. This behavior is more significant in compound **3**, with a higher charge-transfer character, whose emission maximum shows a remarkable shift of more than 100 nm from cyclohexane (541 nm) to CH_2Cl_2 (645 nm) and fluorescence is completely quenched in MeOH. The strong influence of the polarity of the solvent in the emission properties of **3** is probably related to the formation of twisted intramolecular charge-transfer states in this compound.[36] The environmental sensitivity of the light-emitting properties of this compound represents a promising property toward its application in sensing/bioimaging.

Interestingly, all of these compounds emit intensely also in solid state and mesophase. Please note that strong intermolecular interaction and close packing usually lead to quenching of emission. In the condensed states, the maximum emission wavelengths are slightly blue-shifted when compared to the fluorescence in CH_2Cl_2 solution (Table 3). The observed hypsochromism is probably associated with higher dihedral angles between the phenyl rings and the benzothiadiazole cores in the more constrained environments of the crystalline and liquid crystalline phases, which would reduce the extent of π-delocalization in these rod-shaped compounds.

Table 3. Maximum Emission Wavelength in Different Solvent Systems

compounds	cyclohexane	CH_2Cl_2	THF	MeOH	crystal	mesophase
3	541	645	635		580	612
4	494	532	523	554	509	528
5	475	497	492	512	488	
6	471	494	487	499	484	503
7	470	496	488	501	487	506

CONCLUSIONS

In conclusion, a new series of redox active monoalkyl liquid crystalline BTD fluorophores functionalized on one edge with a phenyl-nonyl substituent and on the other edge with different p-substituted phenyl rings have been synthesized and characterized with the aim of finding molecules of potential interest for electronic applications.

We have found that attaching only one terminal alkyl chain to the 4,7-diphenyl BTD core is enough to induce mesomorphism in these molecules and to prompt their self-assembly into layered supramolecular arrangements, as could be determined by the single-crystal analysis. The other terminal groups allow fine-tuning of the electronic properties of these molecules (by influencing the intramolecular charge transfer in the system) and the modulation of their mesomorphic behavior and crystal packing by participating in different intermolecular interactions.

The easy reversible oxidation/reductions of these BTD derivatives and adequate HOMO−LUMO levels for the easy injection of charge carriers, together with their efficient light-emitting properties and tendency to self-assemble to form layered arrangements (highly favorable for charge/exciton migration transport), make these derivatives promising candidates for incorporation in devices such as OLEDs and OFETs. Compound **6** especially has a remarkable bilayer arrangement, which together with its favorable amphoteric redox properties renders it a promising candidate for ambipolar OFETs. Work along these lines is in progress.

EXPERIMENTAL SECTION

Materials Synthesis. *Synthesis of 4-Bromo-7-(4-nonylphenyl)benzo[c][1,2,5]thiadiazole (**2**).* A solution of 4,7-dibromo[*c*][1,2,5]thiadiazole (250 mg, 0.85 mmol), Pd-$(PPh_3)_4$ (59.0 mg, 0.051 mmol), and 4-nonylphenyl boronic acid (221 mg, 0.89 mmol) in a mixture of 2 M aqueous K_2CO_3 (0.5 mL) and dry tetrahydrofuran (THF, 5 mL) was degassed and irradiated with an Anton Paar microwave irradiator (CEM) at 150 °C (80 W) for 180 min. After cooling to room temperature, the reaction mixture was concentrated. The solid was diluted with CH_2Cl_2, washed with water, and dried over $MgSO_4$ anhydrous. The solvent was evaporated and the residue was purified by column chromatography with CH_2Cl_2/hexane (1:3) to give a pale yellow solid (**2**) (333.7 mg, 94%).

DOI: 10.1021/acsomega.8b01696
ACS Omega 2018, 3, 11857−11864

^{1}H NMR (300 MHz, $CDCl_3$) δ 7.82 (d, J = 7.5 Hz, 1H), 7.78 (d, J = 8.1 Hz, 2H), 7.48 (d, J = 7.5 Hz, 1H), 7.32 (d, J = 8.0 Hz, 2H), 2.88−2.47 (m, 2H), 1.76−1.63 (m, 2H), 1.43−1.23 (m, 12H), 1.00−0.84 (m, 3H); ^{13}C NMR (50 MHz, $CDCl_3$) δ 153.9, 153.3, 143.8, 134.1, 133.9, 132.3, 129.0, 128.8, 127.9, 112.7, 35.8, 31.9, 31.4, 29.53, 29.3, 22.7, 14.1; UV−vis (CH_2Cl_2, 25 °C): λ_{max} (nm) 244, 307, 377; MS (FAB, m/z): 417.41 (M^+). HRMS (FAB) calcd for $C_{21}H_{25}N_2SBr$: 416.0922, found: 416.0923.

*Synthesis of N,N-Dimethyl-4-(7-(4-nonylphenyl)benzo[c][1,2,5]thiadiazol-4-yl)aniline (**3**).* A solution of 4,7-dibromo[c][1,2,5]thiadiazole (150 mg, 0.36 mmol), $Pd(PPh_3)_4$ (35.4 mg, 0.031 mmol), and (4-(dimethylamino)phenyl)boronic acid (59.4 mg, 0.36 mmol) in a mixture of 2 M aqueous K_2CO_3 (0.3 mL) and dry THF (2 mL) was degassed and irradiated with an Anton Paar microwave irradiator (CEM) at 150 °C (80 W) for 180 min. After cooling to room temperature, the reaction mixture was diluted with CH_2Cl_2, washed with water, and dried over $MgSO_4$ anhydrous. Then, the solvent was evaporated and the residue was purified by column chromatography with hexane/CH_2Cl_2 (1:1) to give a red solid (**3**) (45 mg, 28%).

^{1}H NMR (200 MHz, $CDCl_3$) δ 7.92 (d, J = 8.8 Hz, 2H), 7.87 (d, J = 8.1 Hz, 2H), 7.72 (d, J = 1.2 Hz, 2H), 7.35 (d, J = 8.0 Hz, 2H), 6.90 (d, J = 8.9 Hz, 2H), 3.05 (s, 6H), 2.73−2.63 (m, 2H), 1.77−1.59 (m, 2H), 1.39−1.23 (m, 12H), 0.88 (t, J = 6.3 Hz, 3H); ^{13}C NMR (75 MHz, $CDCl_3$) δ 162.3, 154.5, 143.2, 135.1, 133.1, 132.2, 130.55, 130.3, 129.1, 128.8, 128.2, 126.7, 122.3, 113.2, 41.1, 36.0, 32.0, 31.6, 31.4, 29.7, 29.6, 29.6, 29.5, 22.8, 14.3; UV (CH_2Cl_2, 25 °C): λ_{max} (nm) 300, 400; MS (FAB, m/z): 457.1 (M^+). HRMS (ESI) calcd for $C_{29}H_{35}N_3S$: 457.25675, found: 457.25517.

*Synthesis of 4-(4-Methoxyphenyl)-7-(4-nonylphenyl)benzo[c][1,2,5]thiadiazole (**4**).* A solution of 4,7-dibromo[c][1,2,5]thiadiazole (150 mg, 0.36 mmol), $Pd(PPh_3)_4$ (58.1 mg, 0.050 mmol), and 4-methoxyphenyl boronic acid (54.7 mg, 0.36 mmol) in a mixture of 2 M aqueous K_2CO_3 (0.3 mL) and dry THF (2 mL) was degassed and irradiated with an Anton Paar microwave irradiator (CEM) at 150 °C (80 W) for 180 min. After cooling to room temperature, the reaction mixture was diluted with CH_2Cl_2, washed with water, and dried over $MgSO_4$ anhydrous. Then, the solvent was evaporated and the residue was purified by column chromatography with hexane/CH_2Cl_2 (3:1) to give a fluorescent greenish-yellow solid (**4**) (95.2 mg, 68%).

^{1}H NMR (200 MHz, $CDCl_3$) δ 7.93 (d, J = 9.1 Hz, 2H), 7.87 (d, J = 8.1 Hz, 2H), 7.74 (s, 2H), 7.36 (d, J = 8.1 Hz, 2H), 7.09 (d, J = 9.1 Hz, 2H), 3.90 (s, 3H), 2.70 (t, J = 7.5 Hz, 2H), 1.77−1.60 (m, 2H), 1.31 (m, 12H), 0.98−0.80 (m, 3H); ^{13}C NMR (50 MHz, $CDCl_3$) δ 160.0, 154.4, 143.4, 135.0, 132.9, 130.6, 130.2, 129.2, 128.9, 128.0, 127.5, 114.3, 55.6, 36.0, 32.1, 31.6, 29.7, 29.6, 29.5, 22.8, 14.3; UV (CH_2Cl_2, 25 °C) λ_{max} (nm) 246, 280, 399; MS (MALDI, m/z): 444.3 (M^+), HRMS (ESI) calcd for $C_{28}H_{32}N_2OS$: 444.22262, found: 444.22353.

*Synthesis of 4-(4-Nonylphenyl)-7-phenylbenzo[c][1,2,5]thiadiazole (**5**).* A solution of 4,7-dibromo[c][1,2,5]thiadiazole (150 mg, 0.36 mmol), $Pd(PPh_3)_4$ (58.9 mg, 0.050 mmol) and phenylboronic acid (43.9 mg, 0.36 mmol) in a mixture of 2 M aqueous K_2CO_3 (0.3 mL) and dry THF (2 mL) was degassed and irradiated with an Anton Paar microwave irradiator (CEM) at 150 °C (80 W) for 180 min. After cooling to room temperature, the reaction mixture was diluted with CH_2Cl_2, washed with water, and dried over $MgSO_4$ anhydrous. Then, the solvent was evaporated and the residue was purified by column chromatography with hexane/CH_2Cl_2 (4:1) to give a pale yellow solid (**5**) (80.5 mg, 54%).

^{1}H NMR (300 MHz, $CDCl_3$) δ 7.97 (d, J = 7.0 Hz, 2H), 7.89 (d, J = 8.3 Hz, 2H), 7.78 (s, 2H), 7.55 (t, J = 7.4 Hz, 2H), 7.46 (t, J = 7.3 Hz, 1H), 7.37 (d, J = 8.4 Hz, 2H), 2.76−2.62 (m, 2H), 1.83−1.59 (m, 2H), 1.44−1.17 (m, 12H), 0.94−0.80 (m, 3H); ^{13}C NMR (75 MHz, $CDCl_3$) δ 154.3, 154.2, 143.5, 137.6, 134.8, 133.5, 133.1, 129.3, 129.2, 128.8, 128.7, 128.4, 128.3, 127.9, 36.0, 32.0, 31.9, 31.6, 29.7, 29.6, 29.5, 22.8, 14.3; UV (CH_2Cl_2, 25 °C) λ_{max} (nm) 273, 318, 385. MS (FAB, m/z): 414.2 (M^+). HRMS (ESI) calcd for $C_{27}H_{30}N_2S$: 414.21377, found: 414.21297.

*Synthesis of 4-(7-(4-Nonylphenyl)benzo[c][1,2,5]thiadiazol-4-yl)benzonitrile (**6**).* A solution of 4,7-dibromo[c][1,2,5]thiadiazole (150 mg, 0.36 mmol), $Pd(PPh_3)_4$ (58.8 mg, 0.050 mmol), 4-cyanophenylboronic acid (52.8 mg, 0.36 mmol) in a mixture of 2 M aqueous K_2CO_3 (0.3 mL) and dry THF (2.0 mL) was degassed and irradiated with an Anton Paar microwave irradiator (CEM) at 150 °C (80 W) for 180 min. After cooling to room temperature, the reaction mixture was diluted with CH_2Cl_2, washed with water, and dried over $MgSO_4$ anhydrous. Then, the solvent was evaporated and the residue was purified by column chromatography with hexane/CH_2Cl_2 (3:1) to give a pale light yellow solid (**6**) (88.5 mg, 56%).

^{1}H NMR (200 MHz, $CDCl_3$) δ 8.12 (d, J = 8.1 Hz, 2H), 7.95−7.77 (m, 6H), 7.38 (d, J = 7.9 Hz, 2H), 2.70 (t, J = 7.6 Hz, 2H), 1.78−1.60 (m, 2H), 1.46−1.13 (m, 12H), 1.07−0.70 (m, 3H); ^{13}C NMR (75 MHz, $CDCl_3$) δ 154.19, 153.64, 143.95, 141.91, 134.97, 134.34, 132.40, 130.66, 129.85, 129.24, 128.97, 128.88, 127.57, 118.92, 111.79, 35.91, 32.00, 31.51, 31.01, 29.79, 29.67, 29.65, 29.51, 29.44, 22.78, 14.23; UV (CH_2Cl_2, 25 °C) λ_{max} (nm) 291, 384; MS (MALDI, m/z): 439.2 (M^+). HRMS (ESI) calcd for $C_{28}H_{29}N_3S$: 439.20805, found: 439.20822.

*Synthesis of 4-(4-Nitrophenyl)-7-(4-nonylphenyl)benzo[c][1,2,5]thiadiazole (**7**).* A solution of 4,7-dibromo[c][1,2,5]-thiadiazole (150 mg, 0.36 mmol), $Pd(PPh_3)_4$ (58.7 mg, 0.050 mmol), and 4-(4-nitrophenyl)-phenylboronic acid (60.1 mg, 0.36 mmol) in a mixture of 2 M aqueous K_2CO_3 (0.3 mL) and dry THF (2 mL) was degassed and irradiated with an Anton Paar microwave irradiator (CEM) at 150 °C (80 W) for 180 min. After cooling to room temperature, the reaction mixture was diluted with CH_2Cl_2, washed with water, and dried over $MgSO_4$ anhydrous. Then, the solvent was evaporated and the residue was purified by column chromatography with hexane/CH_2Cl_2 (1:1) to give a pale greenish yellow solid (**7**) (97.3 mg, 59%).

^{1}H NMR (300 MHz, $CDCl_3$) δ 8.41 (d, J = 9.0 Hz, 2H), 8.19 (d, J = 9.1 Hz, 2H), 7.90 (d, J = 8.2 Hz, 2H), 7.88 (d, J = 7.3 Hz, 1H), 7.82 (d, J = 7.3 Hz, 1H), 7.38 (d, J = 8.3 Hz, 2H), 2.71 (d, J = 15.4 Hz, 2H), 1.75−1.61 (m, 2H), 1.50−1.21 (m, 12H), 0.89 (m, 3H). ^{13}C NMR (75 MHz, $CDCl_3$) δ 154.2, 153.7, 147.5, 144.1, 143.8, 135.2, 134.3, 130.2, 130.0, 129.3, 129.2, 128.9, 127.5, 123.9, 35.9, 32.0, 31.5, 29.7, 29.7, 29.5, 29.5, 22.8, 14.2; UV (CH_2Cl_2, 25 °C) λ_{max} (nm) 315, 520; MS (MALDI, m/z): 460.2 ($M + H^+$). HRMS (ESI) calcd for $C_{27}H_{29}N_3O_2S$: 459.19877, found: 459.19805.

X-ray Structure Determinations. Crystals of **4**, **6**, and **7** were mounted on a Bruker four circle kappa-diffractometer equipped with a Cu INCOATED microsource, operated at 30

DOI: 10.1021/acsomega.8b01696
ACS Omega 2018, 3, 11857−11864

W power (45 kV, 0.60 mA) to generate Cu Kα radiation (λ = 1.54178 Å), and a Bruker VANTEC 500 area detector (microgap technology). Crystals of **4** and **7** showed well-defined faces, while crystals of **6** growed as polysynthetic twins. Diffraction data were collected exploring more than a hemisphere of the reciprocal space using a combination of φ and ω scans to reach a resolution of 0.86 Å. The structures were solved by the Multan and Fourier methods. Most of the calculations were carried out with APEXII software for data collection and reduction, and OLEX2[37] for structure solution and refinements. CCDC 1834993, CCDC 1834974, and CCDC 1834997 contain the supporting crystallographic data of **4**, **6**, and **7**, respectively.

Crystal data for **4**: $C_{28}H_{32}N_2OS$, M = 444.61 crystal dimensions: 0.35 × 0.04 × 0.02 mm^3, triclinic, $P1$ space group, unit cell dimensions: a = 9.7091(8), b = 10.9090(7), c = 23.3387(16) Å, α = 100.685(5)°, β = 98.924(5)°, γ = 95.706(5)°, V = 2378.7(3) Å^3, T = 250 K, Z = 4, ρ_{calcd} = 1.242 g cm^{-3}. The structure was refined anisotropically $R_1(F)$ = 0.0685 for observed data ($I > 2\sigma(I)$), final R values (all data) $R_1(F)$ = 0.1663, w$R_2(F)$ = 0.2451 for all data.

Crystal data for **6**: $C_{28}H_{29}N_3S$, M = 439.60 crystal dimensions: 0.50 × 0.10 × 0.04 mm^3, monoclinic, $C12/c1$ space group, unit cell dimensions: a = 82.379(9), b = 7.9627(9), c = 14.7427(13) Å, α = 90°, β = 93.622(7)°, γ = 90°, V = 9651.3(17) Å^3, T = 200 K, Z = 16, ρ_{calcd} = 1.210 g cm^{-3}. The structure was refined anisotropically $R_1(F)$ = 0.1466 for observed data ($I > 2\sigma(I)$), final R values (all data) $R_1(F)$ = 0.1859, w$R_2(F)$ = 0.3417 for all data. Two independent molecules are present in the structure showing one of them thermal noresolvable disorder. Seven soft restrictions (4 DFIX, 3 DELU) have been applied to the disordered molecule.

Crystal data for **7**: $C_{27}H_{29}N_3O_2S$, M = 459.59 crystal dimensions: 0.4 × 0.2 × 0.2 mm^3, monoclinic, $P12_1/c1$ space group, unit cell dimensions: a = 11.228(2), b = 8.077(2), c = 26.434(5) Å, α = 90°, β = 93.70(3)°, γ = 90°, V = 2392.4(9) Å^3, T = 250 K, Z = 4, ρ_{calcd} = 1.276 g cm^{-3}. The structure was refined anisotropically $R_1(F)$ = 0.0583 for observed data ($I > 2\sigma(I)$), final R values (all data) $R_1(F)$ = 0.0866, w$R_2(F)$ = 0.1323 for all data.

Crystal data for **6**. Explanation to checkcifs: The crystal diffracts poorly and some reflexions are weak and missing. Because of the theta-full value is slightly lower than 0.95.

Mesomorphic Properties. The optical textures of the mesophases were studied with an Olympus polarizing microscope BX51 equipped with a Linkam hot-stage and Linkam TMS 91 central processor. The transition temperatures and enthalpies were measured by differential scanning calorimetry with a TA Instruments Q20 instrument operated at a scanning rate of 10 °C min^{-1} on both heating and cooling. The apparatus was calibrated with indium (156.6 °C; 28.71 J g^{-1}) as the standard. The thermogravimetric analysis (TGA) was carried out in a TGA-Q5000 apparatus at a heating rate of 10° min^{-1} under nitrogen up to 600 °C and under air from 600 to 750 °C. The XRD patterns at the mesophases were obtained with a pinhole camera (Anton-Paar) operating with a point-focused Ni-filtered Cu Kα beam. The sample was held in Lindemann glass capillary (1 mm diameter) and heated, when necessary, in a variable-temperature oven. The capillary axis is perpendicular to the X-ray beam and the pattern is collected on flat photographic film perpendicular to the X-ray beam. Spacing was obtained via Bragg's law.

Linear Spectroscopy. The UV−vis studies were carried out on a PrekinElmer Lambda XLS+ spectrometer. The fluorescence spectra were recorded on an Aminco SLM 8000 spectrophotometer.

Electrochemistry. Cyclic voltammetry (CV) experiments were performed on a Bioanalytical System Inc. (BASI) Epsilon electrochemical workstation in a three-electrode cell at room temperature under nitrogen atmosphere. Electrochemical measurements were carried out in dichloromethane solutions (c = 1 × 10^{-3} M) containing 0.1 M tetra-*n*-butylammonium hexafluorophosphate ($TBAPF_6$) of supporting electrolyte at a scan rate 100 mV s^{-1}. A three-electrode setup was used, including a platinum working electrode, a Ag/AgCl (3 M NaCl) reference electrode, and a platinum wire auxiliary electrode. Ferrocene was used as an internal standard, and all potentials were referenced to the ferrocene/ferrocenium redox couple.

■ ASSOCIATED CONTENT

Supporting Information

The Supporting Information is available free of charge on the ACS Publications website at DOI: 10.1021/acsomega.8b01696.

Copy of the ^{1}H NMR and ^{13}C NMR spectra of compounds **2**−**7**, mesomorphic properties of compounds **3**−**6**, linear spectroscopy: UV−vis and fluorescence studies of compounds **3**−**7** (PDF)

■ AUTHOR INFORMATION

Corresponding Author

*E-mail: bgl@icmm.csic.es. Tel: 913349031. Fax: (+34) 913720623.

ORCID

Alberto Concellon: 0000-0002-8932-9085

Jose L. Serrano: 0000-0001-9866-6633

Berta Gomez-Lor: 0000-0002-2995-9624

Notes

The authors declare no competing financial interest.

■ ACKNOWLEDGMENTS

This work was funded by the Spanish Government MINECO CTQ2016-78557-R grant and the Comunidad de Madrid S2013/MIT-2740 (PHAMA_2.0).

■ REFERENCES

(1) Klauk, H. *Organic Electronics: Materials, Manufacturing and Applications*; Wiley- VCH: Weinheim, 2006.

(2) Klauk, H. *Organic Electronics: More Materials and Applications*; Wiley- VCH: Weinheim, 2012.

(3) Ostroverkhova, O. Organic Optoelectronic Materials: Mechanisms and Applications. *Chem. Rev.* **2016**, *116*, 13279−13412.

(4) Stupp, S. I.; Palmer, L. C. Supramolecular Chemistry and Self-Assembly in Organic Materials Design. *Chem. Mater.* **2014**, *26*, 507−518.

(5) Fleischmann, E.-K.; Zentel, R. Liquid-Crystalline Ordering as a Concept in Materials Science: From Semiconductors to Stimuli-Responsive Devices. *Angew. Chem., Int. Ed.* **2013**, *52*, 8810−8827.

(6) O'Neill, M.; Kelly, S. M. Liquid Crystals for Charge Transport, Luminescence, and Photonics. *Adv. Mater.* **2003**, *15*, 1135−1146.

(7) Collings, P. J.; Hird, M. *Introduction to Liquid Crystals: Chemistry and Physics*; Taylor & Francis, 1997.

(8) Sergeyev, S.; Pisula, W.; Geerts, Y. H. Discotic Liquid Crystals: A New Generation of Organic Semiconductors. *Chem. Soc. Rev.* **2007**, *36*, 1902−1929.
(9) Kaafarani, B. R. Discotic Liquid Crystals for Opto-Electronic Applications. *Chem. Mater.* **2011**, *23*, 378−396.
(10) Ruiz, C.; García Frutos, E.; Hennrich, G.; Gomez Lor, B. Organic Semiconductors toward Electronic Devices: High Mobility and Easy Processability. *J. Phys. Chem. Lett.* **2012**, *3*, 1428−1436.
(11) Wohrle, T.; Wurzbach, I.; Kirres, J.; Kostidou, A.; Kapernaum, N.; Litterscheidt, J.; Haenle, J. C.; Staffeld, P.; Baro, A.; Giesselmann, F.; Laschat, S. Discotic Liquid Crystals. *Chem. Rev.* **2016**, *116*, 1139−1241.
(12) Benito-Hernandez, A.; Pandey, U. K.; Cavero, E.; Termine, R.; García-Frutos, E. M.; Serrano, J. L.; Golemme, A.; Gomez-Lor, B. High Hole Mobility in Triindole-Based Columnar phases: Removing the Bottleneck of Homogeneous Macroscopic Orientation. *Chem. Mater.* **2013**, *25*, 117−121.
(13) García-Frutos, E. M.; Pandey, U. K.; Termine, R.; Omenat, A.; Barbera, J.; Serrano, J. L.; Golemme, A.; Gomez-Lor, B. High Charge Mobility in Discotic Liquid-Crystalline Triindoles: Just a Core Business? *Angew. Chem., Int. Ed.* **2011**, *50*, 7399−7402.
(14) An, Z.; Yu, J.; Domercq, B.; Jones, S. C.; Barlow, S.; Kippelen, B.; Marder, S. R. Room-temperature discotic liquid-crystalline coronene diimides exhibiting high charge-carrier mobility in air. *J. Mater. Chem.* **2009**, *19*, 6688−6698.
(15) Gomez-Esteban, S.; Benito-Hernandez, A.; Termine, R.; Hennrich, G.; Navarrete, J. T. L.; Ruiz Delgado, M. C.; Golemme, A.; Gomez-Lor, B. High-Mobility Self-Assembling Truxenone-Based n-Type Organic Semiconductors. *Chem. - Eur. J.* **2018**, *24*, 3576−3583.
(16) Mobilities which may differ several orders of magnitude are usually encountered when compared mobility values with different alignment requirements: Ruiz, C.; Pandey, U. K.; Termine, R.; García-Frutos, E. M.; Lopez-Espejo, G.; Ortiz, R. P.; Huang, W.; Marks, T. J.; Facchetti, A.; Ruiz Delgado, M. C.; Golemme, A.; Gomez-Lor, B. Mobility versus Alignment of a Semiconducting π-Extended Discotic Liquid-Crystalline Triindole. *ACS Appl. Mater. Interfaces* **2016**, *8*, 26964−26971.
(17) Eccher, J.; Zajaczkowski, W.; Faria, G. C.; Bock, H.; von Seggern, H.; Pisula, W.; Bechtold, I. H. Thermal Evaporation versus Spin-Coating: Electrical Performance in Columnar Liquid Crystal OLEDs. *ACS Appl. Mater. Interfaces* **2015**, *7*, 16374−16381.
(18) Shklyarevskiy, I. O.; Jonkheijm, P.; Stutzmann, N.; Wasserberg, D.; Wondergem, H. J.; Christianen, P. C. M.; Schenning, A. P. H. J.; de Leeuw, D. M.; Tomovic, Z.; Wu, J.; Mullen, K.; Maan, J. C. High Anisotropy of the Field-Effect Transistor Mobility in Magnetically Aligned Discotic Liquid-Crystalline Semiconductors. *J. Am. Chem. Soc.* **2005**, *127*, 16233−16237.
(19) Iino, H.; Hanna, Ji Availability of Liquid Crystallinity in Solution Processing for Polycrystalline Thin Films. *Adv. Mater.* **2011**, *23*, 1748−1751.
(20) Iino, H.; Usui, T.; Hanna, J. I. Liquid crystals for organic thin-film transistors. *Nat. Commun.* **2015**, *6*, No. 6828.
(21) Yaowu, H.; Melda, S.; Dongwei, Z.; Aiyuan, L.; Lijia, Y.; Hongtao, Y.; Chao, H.; Osamu, G.; Yueh-Lin, L.; Hong, M. High Performance OTFTs Fabricated Using a Calamitic Liquid Crystalline Material of 2-(4-Dodecyl phenyl)[1]benzothieno[3,2-b][1]-benzothiophene. *Adv. Electron. Mater.* **2016**, *2*, No. 1600179.
(22) He, K.; Li, W.; Tian, H.; Zhang, J.; Yan, D.; Geng, Y.; Wang, F. Asymmetric Conjugated Molecules Based on [1]Benzothieno[3,2-b][1]benzothiophene for High-Mobility Organic Thin-Film Transistors: Influence of Alkyl Chain Length. *ACS Appl. Mater. Interfaces* **2017**, *9*, 35427−35436.
(23) Sonar, P.; Singh, S. P.; Sudhakar, S.; Dodabalapur, A.; Sellinger, A. High-Mobility Organic Thin Film Transistors Based on Benzothiadiazole-Sandwiched Dihexylquaterthiophenes. *Chem. Mater.* **2008**, *20*, 3184−3190.
(24) Sonar, P.; Singh, S. P.; Leclere, P.; Surin, M.; Lazzaroni, R.; Lin, T. T.; Dodabalapur, A.; Sellinger, A. Synthesis, characterization and comparative study of thiophene-benzothiadiazole based donor-acceptor-donor (D-A-D) materials. *J. Mater. Chem.* **2009**, *19*, 3228−3237.
(25) Du, J.; Biewer, M. C.; Stefan, M. C. Benzothiadiazole building units in solution-processable small molecules for organic photovoltaics. *J. Mater. Chem. A* **2016**, *4*, 15771−15787.
(26) Findlay, N. J.; Breig, B.; Forbes, C.; Inigo, A. R.; Kanibolotsky, A. L.; Skabara, P. J. High brightness solution-processed OLEDs employing linear, small molecule emitters. *J. Mater. Chem. C* **2016**, *4*, 3774−3780.
(27) Aguiar, L. d. O.; Regis, E.; Tuzimoto, P.; Girotto, E.; Bechtold, I. H.; Gallardo, H.; Vieira, A. A. Investigation of thermal and luminescent properties in 4,7-diphenylethynyl-2,1,3-benzothiadiazole systems. *Liq. Cryst.* **2018**, *45*, 49−58.
(28) Zhang, X.; Yamaguchi, R.; Moriyama, K.; Kadowaki, M.; Kobayashi, T.; Ishi-i, T.; Thiemann, T.; Mataka, S. Highly dichroic benzo-2,1,3-thiadiazole dyes containing five linearly [small pi]-conjugated aromatic residues, with fluorescent emission ranging from green to red, in a liquid crystal guest-host system. *J. Mater. Chem.* **2006**, *16*, 736−740.
(29) Dunmur, D. A. The magic of cyanobiphenyls: celebrity molecules. *Liq. Cryst.* **2015**, *42*, 678−687.
(30) Gray, G. W.; Lydon, J. E. New type of smectic mesophase? *Nature* **1974**, *252*, 221.
(31) Paterson, D. A.; Abberley, J. P.; Harrison, W. T. A.; Storey, J. M. D.; Imrie, C. T. Cyanobiphenyl-based liquid crystal dimers and the twist-bend nematic phase. *Liq. Cryst.* **2017**, *44*, 127−146.
(32) Huitorel, B.; Benito, Q.; Fargues, A.; Garcia, A.; Gacoin, T.; Boilot, J.-P.; Perruchas, S.; Camerel, F. Mechanochromic Luminescence and Liquid Crystallinity of Molecular Copper Clusters. *Chem. Mater.* **2016**, *28*, 8190−8200.
(33) Sadati, M.; Ramezani-Dakhel, H.; Bu, W.; Sevgen, E.; Liang, Z.; Erol, C.; Rahimi, M.; Taheri Qazvini, N.; Lin, B.; Abbott, N. L.; Roux, B.; Schlossman, M. L.; de Pablo, J. J. Molecular Structure of Canonical Liquid Crystal Interfaces. *J. Am. Chem. Soc.* **2017**, *139*, 3841−3850.
(34) Prabhu, R.; Yelamaggad, C. V. Structure−Property Correlations in Cyanobiphenyl-Based Dimer-Like Mesogens. *J. Phys. Chem. B* **2015**, *119*, 11935−11952.
(35) Kim, Y.-K.; Wang, X.; Mondkar, P.; Bukusoglu, E.; Abbott, N. L. Self-reporting and self-regulating liquid crystals. *Nature* **2018**, *557*, 539−544.
(36) Grabowski, Z. R.; Rotkiewicz, K.; Rettig, W. Structural Changes Accompanying Intramolecular Electron Transfer: Focus on Twisted Intramolecular Charge-Transfer States and Structures. *Chem. Rev.* **2003**, *103*, 3899−4032.
(37) Dolomanov, O. V.; Bourhis, L. J.; Gildea, R. J.; Howard, J. A. K.; Puschmann, H. OLEX2: a complete structure solution, refinement and analysis program. *J. Appl. Crystallogr.* **2009**, *42*, 339−341.

DOI: 10.1021/acsomega.8b01696
ACS Omega 2018, 3, 11857−11864

JACS
JOURNAL OF THE AMERICAN CHEMICAL SOCIETY
pubs.acs.org/JACS
Article

Untangling the Mechanochromic Properties of Benzothiadiazole-Based Luminescent Polymorphs through Supramolecular Organic Framework Topology

Marcelo Echeverri, Constanza Ruiz, Sergio Gamez-Valenzuela, Irene Martín, M. Carmen Ruiz Delgado, Enrique Gutierrez-Puebla, M. Angeles Monge, Lina M. Aguirre-Díaz,* and Berta Gomez-Lor*

Cite This: J. Am. Chem. Soc. 2020, 142, 17147−17155

Read Online

ACCESS | Metrics & More | Article Recommendations | Supporting Information

ABSTRACT: Two new luminophore polymorphs of 4-bromo-7-(4-nonylphenyl)benzo[*c*][1,2,5]thiadiazole (**1α** and **1β**) exhibiting different color emissions, which switch into each other in response to shear force and solvent vapors, are presented and their X-ray structure is determined. Supramolecular organic framework topology (SOFT) studies on the two polymorphic structures led us to conclude that the mechanochromic phase transformation can be explained on the basis of modifications in their respective topological nets: **mab** and **pcu** for **1α** and **1β**, respectively, as a result of the breaking and restoration of a number of weak supramolecular interactions. The color changes accompanying this transformation have been rationalized with the help of time-dependent density functional theory. We firmly believe that our findings will inspire future research on the design of novel stimuli-responsive organic materials with switchable properties based on their supramolecular interactions by establishing clear SOFT-property relationships.

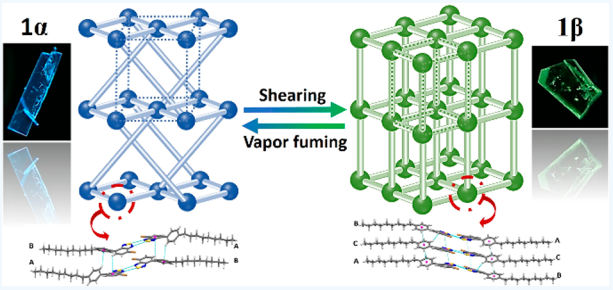

INTRODUCTION

Mechanochromic materials, possessing solid-state light-emitting properties that vary upon mechanical grinding or pressing, arouse much interest in recording or sensing applications that involve luminescent detection. A number of metal complexes and purely organic compounds have been found to exhibit this interesting phenomenon;[1−6] however, only in a few of them is the underlying mechanism properly understood, despite the obvious importance of such knowledge in the development of new mechanochromic compounds. In this context, the emission switching between polymorphs is especially interesting.[7−15] By allowing the understanding of how molecules are self-associated in the solid state through a deep supramolecular analysis, we can use single crystals to help us realize how intermolecular interactions operate among each other, either separately or cooperatively, thus providing accurate information on the key factors that govern the correspondig solid-state light-emitting properties.[6,16−19] Unfortunately, although several mechanochromic luminophores have been reported to date, in most examples crystal-to-amorphous transitions originate in the differences of color observed.

Topological analysis of crystalline structures provide an excellent tool to assess the origin of intermolecular interactions operating in crystals. The construction of a topological net is carried out considering the initial geometrical data, as well as the chemically relevant interactions of the material under study; so, as the reliability of the information increases, the resulting net can be the strongest topological reference for the structure.[20] To date, topological analysis has been extensively applied to simplify complex inorganic and hybrid covalent and supramolecular frameworks,[21−24] but its application to purely organic crystals is only very incipient.[25−28] On the other hand, although previous work has already unveiled the line from spectroscopy to property passing through synthon and crystal structure recognition within synthons,[29−31] the use of topological analysis to explain in a simple manner the correlation between the supramolecular framework and the physical properties for a specific system has not yet been realized.

Chalcogen bondings, that is, the interaction between group VI elements (O, S, Se, Te, and Po) and a Lewis-base partner atom,[32] has emerged as a key motif for controling supramolecular frameworks growth. The close contact of chalcogens and oxygen or nitrogen atoms is observed in many organic crystals, where this interaction enhances the intermolecular ordering and play important roles in determining the

Received: July 27, 2020
Published: September 11, 2020

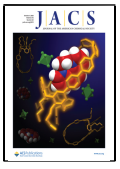

https://dx.doi.org/10.1021/jacs.0c08059
J. Am. Chem. Soc. 2020, 142, 17147−17155

orientation of molecules[33] with important implications in applications in materials science, medicinal chemistry, and crystal engineering.[34,35]

In this article we report on a new benzothiadiazole-based luminophore, 4-bromo-7-(4-nonylphenyl)benzo[*c*][1,2,5]-thiadiazole (**1**), which crystallize in two distinctive polymorphs with different color emissions. Interestingly, the interconversion between the two phases can be reversibly induced by mechanical stress or solvent vapors. We have determined the X-ray structures of both polymorphs and performed a deep supramolecular analysis that allowed us to rationalize the observed mechanochromic transformations on the basis of their topological nets, as follows: synthesis of a supramolecular organic framework (SOF) using the 2S−2N square chalcogen interaction (synthon) → crystal structure → supramolecular organic framework analysis (SOFA) → topology (SOFT) → mechanochromic phenomenom explanation. Additionally, time-dependent density functional theory (TD-DFT) calculations provide us with a clear picture of the origin of the different emission colors that accompanies the phase transformation.

RESULTS AND DISCUSSION

Synthesis and Characterization of Compound 1. 4-Bromo-7-(4-nonylphenyl)benzo[*c*][1,2,5]thiadiazole was obtained by palladium-catalyzed Suzuki cross-coupling reaction between 4,7-dibromo-2,1,3-benzothiadiazole and 1 equiv of 4-nonylphenylboronic acid. Under thermal heating conditions, compound **1** is obtained, along with some byproduct of double coupling and unreacted dibrominated benzothiadiazole. Monocoupling can be favored by using microwave heating conditions, which provides compound **1** in good yield in just 3 h. The optical properties of **1** were initially investigated in solution by UV−vis absorption and fluorescence spectroscopy (see the Supporting Information, Figure S3). In a 10^{-5} M CH_2Cl_2 solution, compound **1** exhibits characteristic absorption bands at 230 and 330 nm because of the benzothiadiazole unit (BTD). A lower energy absorption band centered at 376 nm is attributed to a charge-transfer transition between the moderate donor alkylphenyl group and the BTD strong electron acceptor moiety. The fluorescence spectrum at this concentration is characterized by an emission band peaking at 489 nm. It should be noted that the emission spectrum is highly concentration-dependent, showing a significant red shift and loss of vibronic resolution as the concentration is increased from 10^{-7} to 10^{-5} M, thus suggesting the presence of aggregates at higher concentrations.

Crystal Growth, Structure Determination, and Mechanochromic Polymorphic Transformation. Upon slow evaporation of a CH_2Cl_2 solution of **1**, two different colored platelike crystals (colorless **1*α*** and pale yellow **1*β*** crystals) were obtained, which can be easily differentiated upon irradiation with a 365 nm lamp showing blue (λ_{max} = 456 nm) and green emissions (λ_{max} = 486 nm), respectively (Figure 1). Photoluminescence quantum yields of ϕ_F = 0.15 and ϕ_F = 0.02 were determined for polymorphs **1*α*** and **1*β***, respectively. The significantly lower quantum yield measured for polymorph **1*β*** points to stronger intermolecular interactions in this polymorph, and thus increased nonradiative decay processes. Similar lifetimes are observed for both polymorphs ($\tau_F \approx 2-6$ ns, see Figure S4).

The selective formation of the blue-emitting polymorph could be achieved by blowing nitrogen on the dichloromethane (DCM) solution, thus increasing the solvent evaporation rate. Single-crystal structure determination shows that crystals with a blue emission (**1*α***) crystallize in the monoclinic $P2_1/c$ group and contain two independent molecules per unit cell. In the case of the green-emitting crystals (**1*β***), they crystallize in the triclinic $P1$ space group and contain three independent molecules per unit cell.

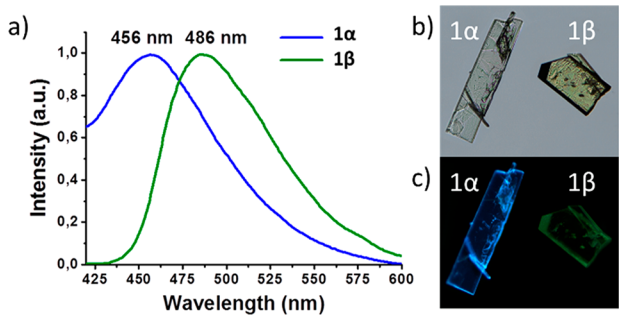

Figure 1. Solid fluorescence spectra of **1*α*** and **1*β*** (a), photograph of crystals under visible light (b) and illuminated with a 365 nm UV lamp (c).

The analysis of the single-crystal structures of the two polymorphs indicates that in both phases molecules crystallize, forming dimers, stabilized by S···N interactions that organize in stacks. As can be clearly observed by comparing parts (a) and (b) of Figure 2, in polymorph **1*β*** the torsion angle between the

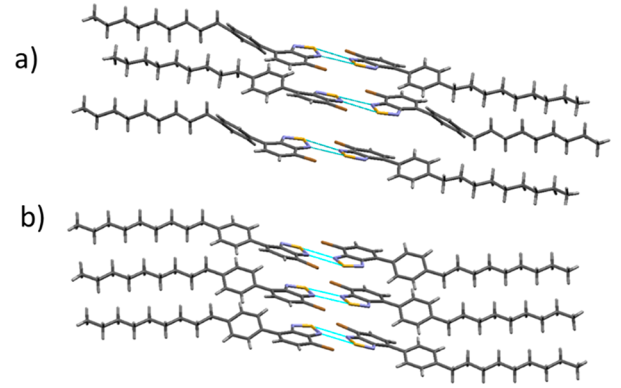

Figure 2. (a) Packing of polymorphs **1*α*** and (b) **1*β*** showing the arrangement of dimers in stacks.

BTD moiety and the attached phenyl ring is oriented in the same direction in the stacks, while in polymorph **1*α*** there is an alternation in the sign of these torsion angles along the stacks. Therefore, at a molecular level the main structural difference between both polymorphs relies on the rotation of a phenyl ring by nearly 180° in half of the crystal molecules while the other half remain nonrotated.

Interestingly, we observed that these two polymorphs can be interconverted by mechanical stress or exposition to solvent vapors. As monitored by powder X-ray diffraction, the shearing of blue-emitting crystals of **1*α*** on a substrate renders exclusively **1*β*** crystals. Although the mechanical action transforming **1*α*** into **1*β*** is irreversible, it is possible to reverse the whole process by exposing **1*β*** crystalline material to CH_2Cl_2 vapors. In this case a highly aligned film of **1*α*** polymorph is obtained (Figure 3 and Figure S5). This reversible recovery from **1*β*** to **1*α*** polymorph requires the restoration of the original supramolecular interactions of **1*α***

https://dx.doi.org/10.1021/jacs.0c08059
J. Am. Chem. Soc. 2020, 142, 17147−17155

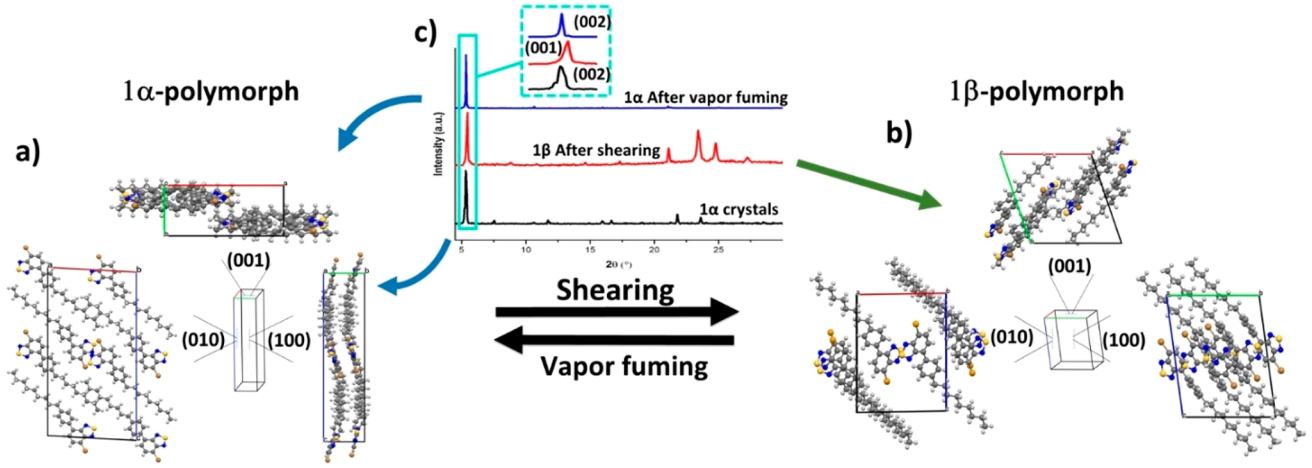

Figure 3. Packing diagrams of **1*α*** (a) and **1*β*** (b) polymorphs viewed down the major faces of the crystals and (c) mechanochromic transformation followed by PDXR.

polymorph and probably involves the solution of **1*β*** by the action of solvent vapors followed by a recrystallization process to the **1*α*** polymorph.

Conversely, no thermal polymorphic transformation could be observed. Polymorphs **1*β*** and **1*α*** melt at 34.6° and 40.4°, respectively, as could be determined in a hot stage microscope (their DSC thermograms show no phase transition); thus, no interconversion between the two phases can be observed (see the Supporting Information, Figures S8 and S9).[36]

When considering the different luminescent properties shown by these polymorphs, one could determine that the dihedral angles between the BTD moiety and the attached phenyl rings may play a role, as this angle will determine the intramolecular conjugation length, with obvious implications in the resulting color emission. A close inspection of the two structures shows that molecules in both polymorphs present similar dihedral angles (in the range of 30.4°−36.6°), even though differences in the sign of the rotation degree can be observed. Consequently, one should expect similar conjugation lengths, which points to a supramolecular origin of the different colors observed, in agreement with the large differences in quantum yield observed between the two polymophs.

The interconversion process between the two polymorphs was followed by FT-Raman spectroscopy (λ_{exc} = 1064 nm). Raman spectroscopy has been demonstrated to be of great utility to analyze π-conjugated systems, providing precise structural information such as π-electrons delocalization degree,[37−41] molecular order,[42−49] or supramolecular arrangement.[50−53] As seen in Figure 4, an intense band at 1531 cm^{-1}, which is assigned to a collective C−C/C=C stretching vibration, dominates Raman spectra of both polymorphs. In addition, another two intense bands appear at 1612 and 1363 cm^{-1}, which correspond to C−C/C=C stretching vibrations mainly localized on the outer phenyl rings and the BTD unit, respectively (see the theoretical Raman spectrum in Figure S10). No frequency shifts for the three C−C/C=C vibrational modes are observed when comparing the Raman of the two polymorphs. However, a decrease in intensity of the three bands is found when going from the blue-emitting (**1*α***) to the green-emitting (**1*β***) crystals after shearing, whereas the **1*α*** spectral profile is recovered upon exposing **1*β*** crystals to vapor fuming. These spectral changes suggest similar intramolecular

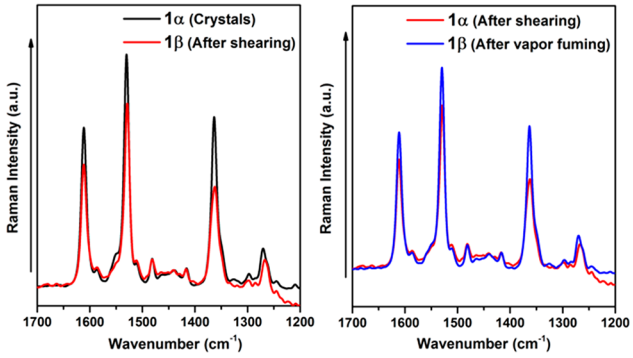

Figure 4. Mechanochromic transformation followed by Raman spectroscopy of **1*α*** and **1*β*** polymorphs.

conjugation lengths but different intermolecular interactions operating in both polymorphs. Note that a significant Raman frequency shifting is expected to occur upon twisting between the BTD and phenyl rings, as can be observed in Figure S11. A modulation of Raman intensity by intermolecular interaction has already been demonstrated by Milani et al.,[50] revealing that higher intermolecular interactions from a more effective packing can induce "pinning effects" that reduce the π-electrons delocalization and consequently the Raman intensity. Thus, the Raman spectral changes between the two polymorphs suggest an increased $\pi-\pi$ overlap in the **1*β*** phase with respect to that in the **1*α*** phase, in consonance with the experimental photophysical and X-ray data.

Supramolecular Organic Framework Analysis (SOFA). In an attempt to elucidate the mechanism of the mechanochromic phase transformation between both polymorphs, we have studied the intermolecular interactions responsible for the self-association of the molecules in the crystals through a Supramolecular Organic Framework Analysis (SOFA). To this goal, we have to first identify the existence of the basic structural motif (BSM) and the subsequent secondary structural motifs (SSMs). The importance of each type of motifs manifests itself on the different levels of organization of the molecular crystals.[29,30]

2S−2N Square Chalcogen Interaction Synthon. Crystals of both polymorphs contain the 2S−2N square synthon, which can be considered as the BSM, and the two polymorph modification differs by the geometry of these BSMs, which

https://dx.doi.org/10.1021/jacs.0c08059
J. Am. Chem. Soc. 2020, 142, 17147−17155

Table 1. Summary of Intermolecular Hydrogen Bonds and Weak Interactions Found for 1α and 1β Polymorphs

Interaction	$d_{H\cdots A}$(Å)	$D_{X\cdots A}$(Å)	Angle(°)	Motif
1α polymorph				
S2 ··· N1	-	2.992	75.10 and 108.40	BSM (synthon) I and Motif II 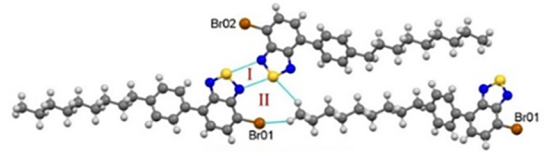
S1 ··· N4	-	3.091	72.09 and 103.89	
C_{sp^3}-H··· Br	3.037	3.762	132.60	
C_{sp^3}-H··· S	2.955	3.765	141.60	
$\pi_{5\text{-ring}} \cdots \pi_{Ar}$	3.367	3.822	offset: 21.28	Motif III and IV 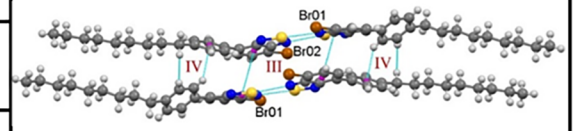
C_{sp^2}-H ··· π_{ph}	2.763	3.534	140.02	
C_{sp^2}-H ··· H-C_{sp^3}	2.397	3.046	123.19	
C_{sp^2}-H ···H-C_{sp^3}	2.336	3.011	125.34	Motif V 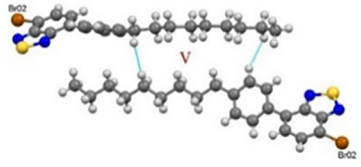
C_{sp^3}-H ··· H-C_{sp^3}	2.326	3.089	134.03	
C_{sp^2}-H ··· π_{Ar}	2.835	3.443	123.42	Motif VI 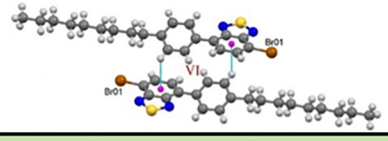
1β polymorph				
S4···N7	-	3.013	69.39 and 105.65	BSM (synthon) I and motif II 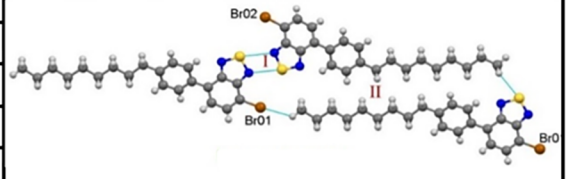
S5···N9	-	3.146	73.58 and 111.37	
S6···NB	-	3.140	74.32 and 105.68	
C_{sp^3}-H ··· S	2.842	3.674	145.99	
C_{sp^3}-H ··· Br	3.003	3.583	120.07	
$\pi_{5\text{-ring}}$B···$\pi_{5\text{-ring}}$C	3.563	3.787	20.31	Motif III and IV 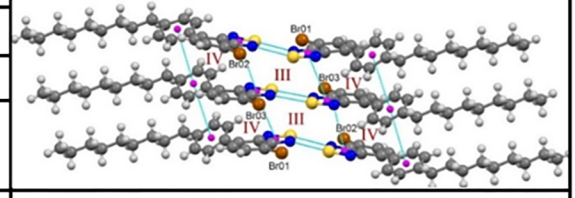
$\pi_{5\text{-ring}}$C ··· $\pi_{5\text{-ring}}$A	3.516	3.694	20.81	
π_{ph}B ··· π_{ph}C	3.815	4.041	19.86	
π_{ph}C ··· π_{ph}A	3.644	4.061	19.57	
$\pi_{5\text{-ring}} \cdots \pi_{ph}$	3.456	3.915	20.17	Motif V 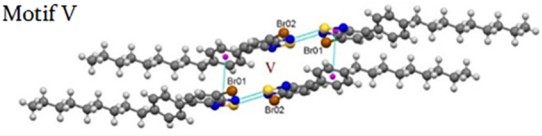
C_{sp^2}-H ··· Br	3.054	3.903	152.80	Motif VI 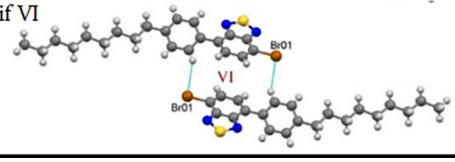

forces different supramolecular packings via weaker interactions. Although the energetic origin of the 2S−2N square dimer interaction is complex and because of the especial nature of its components, it has not been defined as synthon before; well-defined noncovalent interactions of this nature have been identified in both **1**α and **1**β polymorphs. The distances and

https://dx.doi.org/10.1021/jacs.0c08059
J. Am. Chem. Soc. 2020, 142, 17147−17155

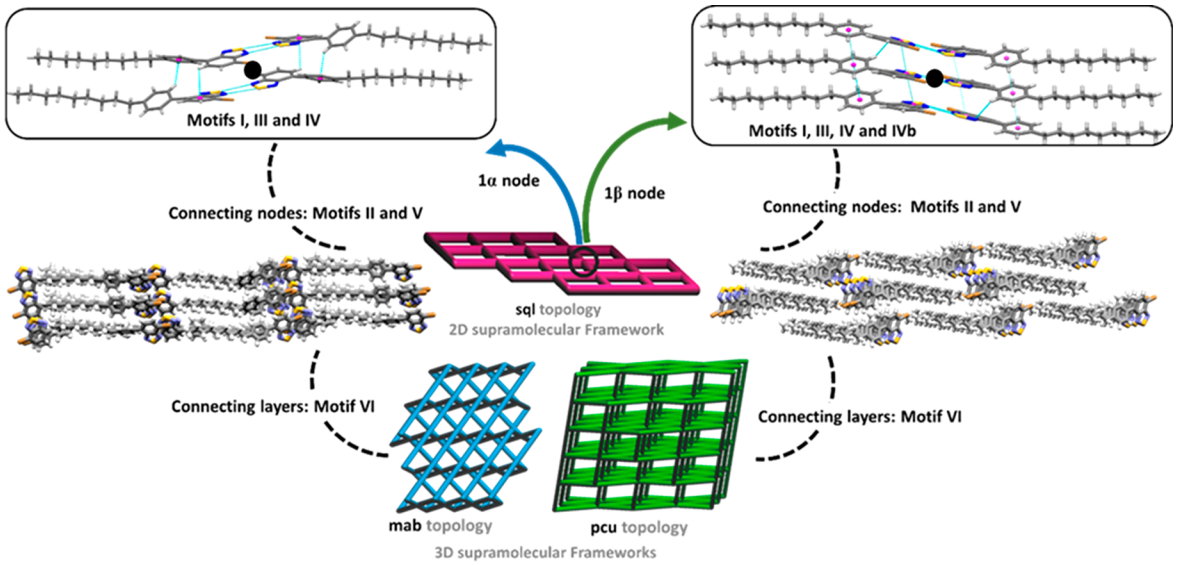

Figure 5. Definition of nodes and topology representation of the 2D and 3D frameworks in **1*α*** and **1*β*** polymorphs. The black circle represents the center of the nodes.

angles corresponding to these interactions (Table 1) fit in the shorter distances compared to the media values among benzothiadiazole rings containing S···N short distances published in the CCDC database (Figures S17 and S18 in the Supporting Information).[54]

Secondary Structural Motifs (SSMs). Continuing the analysis of both materials in the plane (010), we observed an additional motif (motif II) formed by C_{sp^3}–H···Br and C_{sp^3}–H···S interactions (Table 1), which involves the molecules containing the BSM (motif I) and the terminal methyl group, a neighboring molecule.

In the case of **1*α*** polymorph, this methyl group interacts with the Br and S atoms of the molecules that contain motif I. Conversely, in the case of **1*β*** polymorph, while the C_{sp^3}–H···Br interaction is similar to that found in polymorph **1*α***, the C_{sp^3}–H···S involves the terminal methyl group of one of the molecules that constitute motif I and the S of the BTD moiety of the neighboring molecule.

Along the *b* direction, motifs III, IV, and V are found in the case of **1*α*** (Table 1). Motif III is formed by $\pi\cdots\pi$ interactions involving the five- and six-membered rings of the BTD moieties, connecting two dimers generated by motif I. The resulting aggregate is additionally stabilized by C–H···π and C_{sp^2}–H···H–C_{sp^3} weak interactions (motifs IV and V) that probably avoid the crystallographic disorder of the long alkyl chains.

In the case of **1*β***, motif III shows a double square formed by double $\pi\cdots\pi$ interactions involving the five-membered rings of the BTDs that build an aggregate of six molecules by connecting three dimers generated by motif I. Additionally, $\pi\cdots\pi$ interactions between the attached phenyl rings (motif IV) reinforce the formation of this aggregate. Finally, the aggregates containing motifs III and IV are connected to each other through $\pi\cdots\pi$ interactions (motif V, Table 1) involving the five-membered ring of the BTD and the attached phenyl ring.

So, along the *b* axis we can determine the organization of molecules in aggregates comprising four or six molecules for **1*α*** and **1*β***, respectively. However, in the plane (010), we appreciate equivalent connections; in the *b* direction, the **1*β*** polymorph is richer in interactions involving the π aromatic systems.

The supramolecular organic frameworks built with the motifs discussed above generate in both cases a 2D-layer disposition in (102) and (101) for **1*α*** and **1*β***, respectively.

Connecting these layers and generating their final 3D supramolecular framework, we observed a C_{sp^2}–H···π interaction in the case of **1*α*** and a C_{sp^2}–H···Br in the case of the **1*β*** polymorph (motif VI, Table 1).

Supramolecular Organic Framework Topology (SOFT). Nowadays, the topological description of crystal structures is commonly used in crystal chemistry by using the net model, which focuses on the complete structure connectivity.[20] The construction of these nets can be done by taking into account the initial geometrical data as well as the chemically relevant interactions. Here, we use the lowercase three-letter code nomenclature for nets (related to prototypical structures or lattices) proposed by O'Keeffe and co-workers.[55]

The SOFT of **1*α*** and **1*β*** structures were studied as follows: (i) The 2S,2N-square BSM (motif I, common in **1*α*** and **1*β***) is the starting point in the construction of the node in each case (Table 1). (ii) The **1*β*** low symmetry generates three crystallographically independent molecules, which are related to the other three via motif I. Finally, $\pi\cdots\pi$ interactions (motifs III and IV in Table 1) complete the set of six molecules that form the topological node in **1*β*** SOF. The **1*α*** polymorph symmetry generates two crystallographically independent molecules connected via the 2S,2N-synthon. To find a comparable node to that of **1*β***, we took into account motifs I, III, and IV to build the topological node that relates a total of four molecules in this case. (iii) Once the nodes are defined, the interactions that join these nodes show in both SOFs that each node is connected through motif II and motif V, generating a 4-connected layer with a **sql** topology (Figure 5).[56] These 2D layers grow in (102) in the case of **1*α*** and (101) in the case of **1*β***. (iv) Finally, motif VI (which involves C–H···π interaction in polymorph **1*α*** and C–H···Br in polymorph **1*β***) joins the layers, leading to the generation of topologically different 3D supramolecular frameworks: a 6-connected **mab** underlying net (according to the RCSR

https://dx.doi.org/10.1021/jacs.0c08059
J. Am. Chem. Soc. 2020, 142, 17147−17155

symbols),[57] with point symbol $\{4^4.6^{10}.8\}$ in the case of **1α** and a 6-connected primitive cubic **pcu** net with point symbol $\{4^{12}.6^3\}$ in the case of **1β** (Figure 5).

Mechanochromic Phenomenon Explanation. As shown above, the SOFT analysis of both polymorphs is indicative of layered structures with a 4-connected **sql** net with point symbol $\{4^4.6^2\}$ (Figure 5), which connect to generate different 3D supramolecular networks through weak CH−π or CH−Br interactions.

Upon application of external force (shearing) on **1α**, the loosely bound layers could move along the direction of applied force with the expected rupture and reformation of the weak interlayer interactions. This process would lead to a permanent molecular migration, that is, irreversible deformation rendering the **1β** polymorph. This mechanical irreversibility is clearly appreciated with the different **pcu** topology generated for **1β** (Figure 5).

Theoretical Calculations. In an attempt to elucidate how the different supramolecular arrangement results in different optical properties, we performed TD-DFT calculations. Particularly, the wavelength and intensity for the lowest energy electronic transitions from the ground electronic state were calculated for all the different independent molecules and for the aggregates selected as topological nodes in the SOFT analysis. Note that the selected topological nodes (Figure 5) contain most of the close contacts in the crystals (motifs I−IV). For the different isolated molecules of **1**, very similar HOMO−LUMO (responsible for the $S_0 \rightarrow S_1$ electronic transition) energy gaps can be found (see Figures S13 and S14 in the Supporting Information). This behavior discards intramolecular geometrical factors as the cause of the color change experimentally observed. However, a comparison of the frontier molecular orbitals calculated for the aggregates extracted from both polymorphs show a significant destabilization of the HOMO level when comparing the representative aggregates of polymorph **1β** with respect to those of **1α**, while LUMO levels are only slightly affected (Figure 6). This behavior produces a HOMO−LUMO energy gap decrease and, thus, a lower energy difference between the ground and the first excited electronic state in the **1β** polymorph. This would explain the red shifting observed in the emission spectra of **1β** when compared to those of **1α**.

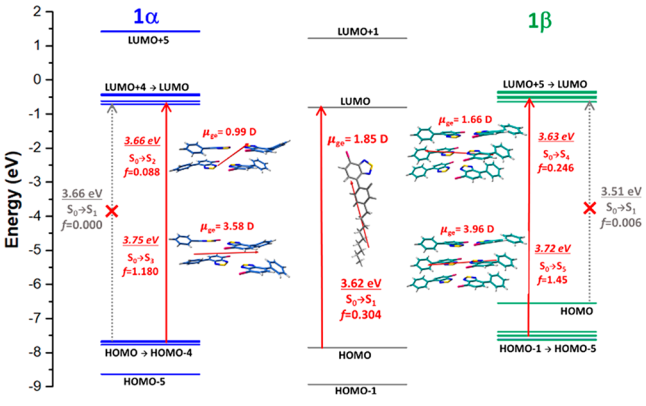

Figure 6. DFT-calculated (ωB97XD/6-31G**) frontier molecular orbital diagram for a single molecule **1** (gray) and for the supramolecular aggregates extracted from the X-ray structure analysis of **1α** (blue) and **1β** (green) polymorphs. The spatial orientation of the transition dipole moment (μ_{ge}) for the main allowed electronic transitions (red arrows) are also shown. The alkyl chains of the supramolecular aggregates have been omitted for clarity.

On the other hand, the lowest S_1 excited state of the aggregates is not optically coupled to the S_0 ground state, as shown by the negligible oscillator strength (f); see Figure 6. Consequently, the lowest energy band for the absorption spectrum involves transitions of higher excited states, concretely S_3 and S_4 for the **1α** polymorph and S_4 and S_5 for the **1β** polymorph (see Figures S13 and S14 in the Supporting Information). Interestingly, their transition dipole moments (μ_{ge}) are predicted to be oriented along the long axis of the molecules.

CONCLUSIONS

Two new BTD-based luminophore polymorphs (**1α** and **1β**) exhibiting different color emissions, which switch into each other in response to shear force and solvent vapors, are presented and their X-ray structures determined. With the aim of rationalizing the mechanochromic phase transformation, a supramolecular organic framework analysis (SOFA) has been performed and allowed us to identify their BSM and subsequent SSMs, which were selected in such a way that the studies are comparable. Hence, the importance of each type of motif manifests itself on the different levels of organization of the molecular crystals.

Supramolecular organic framework topology (SOFT) studies demonstrate that (i) both frameworks contain layers with identical **sql** topology but (ii) the pillaring among them is different, giving rise to **mab** and **pcu** topologies for **1α** and **1β**, respectively. These studies allow us to establish that (iii) the cause of the mechanochromic phase transformation between both polymorphs is the change of interactions among the layers under mechanical stress (**1α** → **1β**) and (iv) the reversible recovery (**1β** → **1α**) by chemical vapor is due to the restoration of the original supramolecular interaction of the pristine polymorph.

The interconversion between **1α** and **1β** polymorphs upon mechanical stress or solvent vapors was successfully followed by Raman spectroscopy, demonstrating similar conjugation lengths but different intermolecular interactions operating in both phases, in good agreement with the X-ray data. TD-DFT calculations on representative aggregates extracted from **1α** and **1β** crystals predict a lower energy difference between the ground and the first excited electronic states in the **1β** polymorph when compared to those of **1α**, thus explaining the different colors observed.

The result of this transversal study opens the door for establishing clear SOFT-property relationships. We hope our findings will inspire future research on the design of novel stimuli-responsive organic materials and on the elucidation of the underlying mechanism of their switchable properties through the analysis of their different supramolecular interactions.

ASSOCIATED CONTENT

Supporting Information

The Supporting Information is available free of charge at https://pubs.acs.org/doi/10.1021/jacs.0c08059.

Copy of ^{1}HNMR and ^{13}CNMR spectra of **1**, photophysical characterization, comparison of the experimental and simulated powder X-ray diffraction patterns and Raman spectroscopy of **1α** and **1β** polymorphs,

https://dx.doi.org/10.1021/jacs.0c08059
J. Am. Chem. Soc. 2020, 142, 17147−17155

differential scanning calorimetry and thermal study, and details on the theoretical study (PDF)

X-ray crystallographic data of **1α** polymorph (CIF)

X-ray crystallographic data of **1β** polymorph (CIF)

AUTHOR INFORMATION

Corresponding Authors

Berta Gomez-Lor − *Multifunctional and Supramolecular Materials Group, Materials Science Factory, Instituto de Ciencia de Materiales de Madrid-Consejo Superior de Investigaciones Cientificas (ICMM-CSIC), Madrid 28049, Spain;* orcid.org/0000-0002-2995-9624; Email: bgl@icmm.csic.es

Lina M. Aguirre-Díaz − *Multifunctional and Supramolecular Materials Group, Materials Science Factory, Instituto de Ciencia de Materiales de Madrid-Consejo Superior de Investigaciones Cientificas (ICMM-CSIC), Madrid 28049, Spain;* orcid.org/0000-0002-7510-1653; Email: Lina.Aguirre@csic.es

Authors

Marcelo Echeverri − *Multifunctional and Supramolecular Materials Group, Materials Science Factory, Instituto de Ciencia de Materiales de Madrid-Consejo Superior de Investigaciones Cientificas (ICMM-CSIC), Madrid 28049, Spain;* orcid.org/0000-0002-9290-4546

Constanza Ruiz − *Multifunctional and Supramolecular Materials Group, Materials Science Factory, Instituto de Ciencia de Materiales de Madrid-Consejo Superior de Investigaciones Cientificas (ICMM-CSIC), Madrid 28049, Spain*

Sergio Gamez-Valenzuela − *Department of Physical Chemistry, University of Malaga, Malaga 29071, Spain*

Irene Martín − *Multifunctional and Supramolecular Materials Group, Materials Science Factory, Instituto de Ciencia de Materiales de Madrid-Consejo Superior de Investigaciones Cientificas (ICMM-CSIC), Madrid 28049, Spain*

M. Carmen Ruiz Delgado − *Department of Physical Chemistry, University of Malaga, Malaga 29071, Spain;* orcid.org/0000-0001-8180-7153

Enrique Gutierrez-Puebla − *Multifunctional and Supramolecular Materials Group, Materials Science Factory, Instituto de Ciencia de Materiales de Madrid-Consejo Superior de Investigaciones Cientificas (ICMM-CSIC), Madrid 28049, Spain*

M. Angeles Monge − *Multifunctional and Supramolecular Materials Group, Materials Science Factory, Instituto de Ciencia de Materiales de Madrid-Consejo Superior de Investigaciones Cientificas (ICMM-CSIC), Madrid 28049, Spain;* orcid.org/0000-0003-2242-7593

Complete contact information is available at: https://pubs.acs.org/10.1021/jacs.0c08059

Notes

The authors declare no competing financial interest.

ACKNOWLEDGMENTS

Dedicated to Professor Catalina Ruiz-Perez (in memoriam). This work was financially supported by the MINECO (CTQ2016-78557-R, MAT2016-78465-R),MICINN (PID2019-104125RB-I00, PID2019-110305GB-I00) of Spain and Junta de Andalucia (UMA18-FEDERJA-080) project. S.G.V. thanks the MINECO for a FPU predoctoral fellowship (FPU 17/04908). The authors thankfully acknowledge the computer resources, technical expertise, and assistance provided by the SCBI (Supercomputing and Bioinformatics) Center of the University of Malaga.

REFERENCES

(1) Chi, Z.; Zhang, X.; Xu, B.; Zhou, X.; Ma, C.; Zhang, Y.; Liu, S.; Xu, J. Recent Advances in Organic Mechanofluorochromic Materials. *Chem. Soc. Rev.* **2012**, *41*, 3878−3896.

(2) Ma, Z.; Wang, Z.; Teng, M.; Xu, Z.; Jia, X. Mechanically Induced Multicolor Change of Luminescent Materials. *ChemPhysChem* **2015**, *16*, 1811−1828.

(3) Sagara, Y.; Yamane, S.; Mitani, M.; Weder, C.; Kato, T. Mechanoresponsive Luminescent Molecular Assemblies: An Emerging Class of Materials. *Adv. Mater.* **2016**, *28*, 1073−1095.

(4) Zhang, X.; Chi, Z.; Zhang, Y.; Liu, S.; Xu, J. Recent Advances in Mechanochromic Luminescent Metal Complexes. *J. Mater. Chem. C* **2013**, *1*, 3376−3390.

(5) Roy, B.; Reddy, M. C.; Hazra, P. Developing the Structure-Property Relationship to Design Solid State Multi-Stimuli Responsive Materials and Their Potential Applications in Different Fields. *Chem. Sci.* **2018**, *9*, 3592−3606.

(6) Wang, C.; Li, Z. Molecular Conformation and Packing: Their Critical Roles in the Emission Performance of Mechanochromic Fluorescence Materials. *Mater. Chem. Front.* **2017**, *1*, 2174−2194.

(7) Dong, Y.; Xu, B.; Zhang, J.; Tan, X.; Wang, L.; Chen, J.; Lv, H.; Wen, S.; Li, B.; Ye, L.; Zou, B.; Tian, W. Piezochromic Luminescence Based on the Molecular Aggregation of 9,10-Bis((E)-2-(Pyrid-2-Yl)Vinyl)Anthracene. *Angew. Chem., Int. Ed.* **2012**, *51*, 10782−10785.

(8) Harada, N.; Abe, Y.; Karasawa, S.; Koga, N. Polymorphic Equilibrium Responsive Thermal and Mechanical Stimuli in Light-Emitting Crystals of N -Methylaminonaphthyridine. *Org. Lett.* **2012**, *14*, 6282−6285.

(9) He, Z.; Zhang, L.; Mei, J.; Zhang, T.; Lam, J. W. Y.; Shuai, Z.; Dong, Y. Q.; Tang, B. Z. Polymorphism-Dependent and Switchable Emission of Butterfly-Like Bis(Diarylmethylene)Dihydroanthracenes. *Chem. Mater.* **2015**, *27*, 6601−6607.

(10) Seki, T.; Ito, H. Molecular-Level Understanding of Structural Changes of Organic Crystals Induced by Macroscopic Mechanical Stimulation. *Chem. - Eur. J.* **2016**, *22*, 4322−4329.

(11) Seki, T.; Sakurada, K.; Ito, H. Controlling Mechano- and Seeding-Triggered Single-Crystal-to-Single-Crystal Phase Transition: Molecular Domino with a Disconnection of Aurophilic Bonds. *Angew. Chem., Int. Ed.* **2013**, *52*, 12828−12832.

(12) Zhang, G.; Lu, J.; Sabat, M.; Fraser, C. L. Polymorphism and Reversible Mechanochromic Luminescence for Solid-State. *J. Am. Chem. Soc.* **2010**, *132*, 2160−2162.

(13) Yuan, M.-S.; Wang, D.-E.; Xue, P.; Wang, W.; Wang, J.-C.; Tu, Q.; Liu, Z.; Liu, Y.; Zhang, Y.; Wang, J. Fluorenone Organic Crystals: Two-Color Luminescence Switching and Reversible Phase Transformations between π-π Stacking-Directed Packing and Hydrogen Bond-Directed Packing. *Chem. Mater.* **2014**, *26*, 2467−2477.

(14) Jin, M.; Seki, T.; Ito, H. Mechano-Responsive Luminescence via Crystal-to-Crystal Phase Transitions between Chiral and Non-Chiral Space Groups. *J. Am. Chem. Soc.* **2017**, *139*, 7452−7455.

(15) Ge, C.; Liu, J.; Ye, X.; Han, Q.; Zhang, L.; Cui, S.; Guo, Q.; Liu, G.; Liu, Y.; Tao, X. Visualization of Single-Crystal-to-Single-Crystal Phase Transition of Luminescent Molecular Polymorphs. *J. Phys. Chem. C* **2018**, *122*, 15744−15752.

(16) Cardenas, J. C.; Aguirre-Diaz, L. M.; Galindo, J. F.; Alí-Torres, J.; Ochoa-Puentes, C.; Echeverri, M.; Gomez-Lor, B.; Monge, M. A.; Gutierrez-Puebla, E.; Sierra, C. A. Nature of Color Diversity in Phenylenevinylene-Based Polymorphs. *Cryst. Growth Des.* **2019**, *19*, 3913−3922.

(17) Varughese, S. Non-Covalent Routes to Tune the Optical Properties of Molecular Materials. *J. Mater. Chem. C* **2014**, *2*, 3499−3516.

(18) Yu, L. Polymorphism in Molecular Solids: An Extraordinary System of Red, Orange, and Yellow Crystals. *Acc. Chem. Res.* **2010**, *43*, 1257−1266.
(19) Jin, M.; Sumitani, T.; Sato, H.; Seki, T.; Ito, H. Mechanical-Stimulation-Triggered and Solvent-Vapor-Induced Reverse Single-Crystal-to-Single-Crystal Phase Transitions with Alterations of the Luminescence Color. *J. Am. Chem. Soc.* **2018**, *140*, 2875−2879.
(20) Blatov, V. A.; Proserpio, D. M. Topological Relations between Three-Periodic Nets. II. Binodal Nets. *Acta Crystallogr., Sect. A: Found. Crystallogr.* **2009**, *65*, 202−212.
(21) Xie, L. S.; Alexandrov, E. V.; Skorupskii, G.; Proserpio, D. M.; Dinca, M. Diverse π-π Stacking Motifs Modulate Electrical Conductivity in Tetrathiafulvalene-Based Metal-Organic Frameworks. *Chem. Sci.* **2019**, *10*, 8558−8565.
(22) Stock, N.; Biswas, S. Synthesis of Metal-Organic Frameworks (MOFs): Routes to Various MOF Topologies, Morphologies, and Composites. *Chem. Rev.* **2012**, *112*, 933−969.
(23) Reinares-Fisac, D.; Aguirre-Díaz, L. M.; Iglesias, M.; Snejko, N.; Gutierrez-Puebla, E.; Monge, M. A.; Gandara, F. A Mesoporous Indium Metal-Organic Framework: Remarkable Advances in Catalytic Activity for Strecker Reaction of Ketones. *J. Am. Chem. Soc.* **2016**, *138*, 9089−9092.
(24) Xu, W.; Pei, X.; Diercks, C. S.; Lyu, H.; Ji, Z.; Yaghi, O. M. A Metal-Organic Framework of Organic Vertices and Polyoxometalate Linkers as a Solid-State Electrolyte. *J. Am. Chem. Soc.* **2019**, *141*, 17522−17526.
(25) Lu, J.; Perez-Krap, C.; Suyetin, M.; Alsmail, N. H.; Yan, Y.; Yang, S.; Lewis, W.; Bichoutskaia, E.; Tang, C. C.; Blake, A. J.; Cao, R.; Schroder, M. A Robust Binary Supramolecular Organic Framework (SOF) with High CO2adsorption and Selectivity. *J. Am. Chem. Soc.* **2014**, *136*, 12828−12831.
(26) Oburn, S. M.; Sinnwell, M. A.; Ericson, D. P.; Reinheimer, E. W.; Proserpio, D. M.; Groeneman, R. H.; MacGillivray, L. Diversifying Molecular and Topological Space via a Supramolecular Solid-State Synthesis: A Purely Organic Mok Net Sustained by Hydrogen Bonds. *IUCrJ* **2019**, *6*, 1032−1039.
(27) Nguyen, H. L.; Hanikel, N.; Lyle, S. J.; Zhu, C.; Proserpio, D. M.; Yaghi, O. M. A Porous Covalent Organic Framework with Voided Square Grid Topology for Atmospheric Water Harvesting. *J. Am. Chem. Soc.* **2020**, *142*, 2218−2221.
(28) Baburin, I. A.; Blatov, V. A. Three-Dimensional Hydrogen-Bonded Frameworks in Organic Crystals: A Topological Study. *Acta Crystallogr., Sect. B: Struct. Sci.* **2007**, *63*, 791−802.
(29) Shishkin, O. V.; Zubatyuk, R. I.; Shishkina, S. V.; Dyakonenko, V. V.; Medviediev, V. V. Role of Supramolecular Synthons in the Formation of the Supramolecular Architecture of Molecular Crystals Revisited from an Energetic Viewpoint. *Phys. Chem. Chem. Phys.* **2014**, *16*, 6773−6786.
(30) Desiraju, G. R. Crystal Engineering: From Molecule to Crystal. *J. Am. Chem. Soc.* **2013**, *135*, 9952−9967.
(31) Saha, S.; Desiraju, G. R. Acid···Amide Supramolecular Synthon in Cocrystals: From Spectroscopic Detection to Property Engineering. *J. Am. Chem. Soc.* **2018**, *140*, 6361−6373.
(32) Ams, M. R.; Trapp, N.; Schwab, A.; Milic, J. V.; Diederich, F. Chalcogen Bonding "2S−2N Squares" versus Competing Interactions: Exploring the Recognition Properties of Sulfur. *Chem. - Eur. J.* **2019**, *25*, 323−333.
(33) Cozzolino, A. F.; Elder, P. J. W.; Vargas-Baca, I. A Survey of Tellurium-Centered Secondary-Bonding Supramolecular Synthons. *Coord. Chem. Rev.* **2011**, *255*, 1426−1438.
(34) Riwar, L. J.; Trapp, N.; Root, K.; Zenobi, R.; Diederich, F. Supramolecular Capsules: Strong versus Weak Chalcogen Bonding. *Angew. Chem., Int. Ed.* **2018**, *57*, 17259−17264.
(35) Tsuzuki, S.; Sato, N. Origin of Attraction in Chalgogen-Nitrogen Interaction of 1,2,5-Chalcogenadiazole Dimers. *J. Phys. Chem. B* **2013**, *117*, 6849−6855.
(36) This behavior is in contrast with that of its symmetrical analogue 4,7-di-(4-nonylphenyl)benzo[*c*][1,2,5]thiadiazole recently published by some of us. In that particular case the presence of two symmetrical flexible alkyl chains give rise to a lamellar arrangement with weak interaction planes (slip planes) and a thermochromic transformation occurs through a thermally induced sliding process: Echeverri, M.; Ruiz, C.; Gamez-Valenzuela, S.; Alonso-Navarro, M.; Gutierrez-Puebla, E.; Serrano, J. L.; Ruiz Delgado, M. C.; Gomez-Lor, B. Stimuli-Responsive Benzothiadiazole Derivative as a Dopant for Rewritable Polymer Blends. *ACS Appl. Mater. Interfaces* **2020**, *12*, 10929−10937.
(37) Ruiz, C.; Lopez Navarrete, J. T.; Ruiz Delgado, M. C.; Gomez-Lor, B. Triindole-Bridge-Triindole Dimers as Models for Two Dimensional Microporous Polymers. *Org. Lett.* **2015**, *17*, 2258−2261.
(38) Ruiz, C.; Arrechea-Marcos, I.; Benito-Hernandez, A.; Gutierrez-Puebla, E.; Monge, M. A.; Lopez Navarrete, J. T.; Ruiz Delgado, M. C.; Ortiz, R. P.; Gomez-Lor, B. Solution-Processed: N -Trialkylated Triindoles for Organic Field Effect Transistors. *J. Mater. Chem. C* **2018**, *6*, 50−56.
(39) Wang, Y.; Guo, H.; Ling, S.; Arrechea-Marcos, I.; Wang, Y.; Lopez Navarrete, J. T.; Ortiz, R. P.; Guo, X. Ladder-Type Heteroarenes: Up to 15 Rings with Five Imide Groups. *Angew. Chem., Int. Ed.* **2017**, *56*, 9924−9929.
(40) Martin, R. E.; Mader, T.; Diederich, F. Monodisperse Poly(Triacetylene) Rods: Synthesis of a 11.9 Nm Long Molecular Wire and Direct Determination of the Effective Conjugation Length by UV/Vis and Raman Spectroscopies. *Angew. Chem., Int. Ed.* **1999**, *38*, 817−821.
(41) Ferron, C. C.; Delgado, M. C. R.; Gidron, O.; Sharma, S.; Sheberla, D.; Sheynin, Y.; Bendikov, M.; Navarrete, J. T. L.; Hernandez, V. α-Oligofurans Show a Sizeable Extent of π-Conjugation as Probed by Raman Spectroscopy. *Chem. Commun.* **2012**, *48*, 6732−6734.
(42) Tsoi, W. C.; James, D. T.; Kim, J. S.; Nicholson, P. G.; Murphy, C. E.; Bradley, D. D. C.; Nelson, J.; Kim, J. S. The Nature of In-Plane Skeleton Raman Modes of P3HT and Their Correlation to the Degree of Molecular Order in P3HT:PCBM Blend Thin Films. *J. Am. Chem. Soc.* **2011**, *133*, 9834−9843.
(43) Tsoi, W. C.; James, D. T.; Domingo, E. B.; Kim, J. S.; Al-Hashimi, M.; Murphy, C. E.; Stingelin, N.; Heeney, M.; Kim, J. S. Effects of a Heavy Atom on Molecular Order and Morphology in Conjugated Polymer:Fullerene Photovoltaic Blend Thin Films and Devices. *ACS Nano* **2012**, *6*, 9646−9656.
(44) Kim, J.; Baeg, K. J.; Khim, D.; James, D. T.; Kim, J. S.; Lim, B.; Yun, J. M.; Jeong, H. G.; Amegadze, P. S. K.; Noh, Y. Y.; Kim, D. Y. Optimal Ambipolar Charge Transport of Thienylenevinylene-Based Polymer Semiconductors by Changes in Conformation for High-Performance Organic Thin Film Transistors and Inverters. *Chem. Mater.* **2013**, *25*, 1572−1583.
(45) Wood, S.; Kim, J. H.; Hwang, D. H.; Kim, J. S. Effects of Fluorination and Side Chain Branching on Molecular Conformation and Photovoltaic Performance of Donor-Acceptor Copolymers. *Chem. Mater.* **2015**, *27*, 4196−4204.
(46) Wood, S.; Kim, J. H.; Wade, J.; Park, J. B.; Hwang, D. H.; Kim, J. S. Systematic Control of Heteroatoms in Donor-Acceptor Copolymers and Its Effects on Molecular Conformation and Photovoltaic Performance. *J. Mater. Chem. C* **2016**, *4*, 7966−7978.
(47) Razzell-Hollis, J.; Fleischli, F.; Jahnke, A. A.; Stingelin, N.; Seferos, D. S.; Kim, J. S. Effects of Side-Chain Length and Shape on Polytellurophene Molecular Order and Blend Morphology. *J. Phys. Chem. C* **2017**, *121*, 2088−2098.
(48) Wang, Y.; Guo, H.; Harbuzaru, A.; Uddin, M. A.; Arrechea-Marcos, I.; Ling, S.; Yu, J.; Tang, Y.; Sun, H.; Lopez Navarrete, J. T.; Ortiz, R. P.; Woo, H. Y.; Guo, X. (Semi)Ladder-Type Bithiophene Imide-Based All-Acceptor Semiconductors: Synthesis, Structure-Property Correlations, and Unipolar n-Type Transistor Performance. *J. Am. Chem. Soc.* **2018**, *140*, 6095−6108.
(49) Brambilla, L.; Tommasini, M.; Botiz, I.; Rahimi, K.; Agumba, J. O.; Stingelin, N.; Zerbi, G. Regio-Regular Oligo and Poly(3-Hexyl Thiophene): Precise Structural Markers from the Vibrational Spectra of Oligomer Single Crystals. *Macromolecules* **2014**, *47*, 6730−6739.

(50) Milani, A.; Brambilla, L.; Del Zoppo, M.; Zerbi, G. Raman Dispersion and Intermolecular Interactions in Unsubstituted Thiophene Oligomers. *J. Phys. Chem. B* **2007**, *111*, 1271−1276.
(51) Sainbileg, B.; Lan, Y. B.; Wang, J. K.; Hayashi, M. Deciphering Anomalous Raman Features of Regioregular Poly(3-Hexylthiophene) in Ordered Aggregation Form. *J. Phys. Chem. C* **2018**, *122*, 4224−4231.
(52) Mosca, S.; Milani, A.; Pena-Alvarez, M.; Yamaguchi, S.; Hernandez, V.; Ruiz Delgado, M. C.; Castiglioni, C. Mechanochromic Luminescent Tetrathiazolylthiophenes: Evaluating the Role of Intermolecular Interactions through Pressure and Temperature-Dependent Raman Spectroscopy. *J. Phys. Chem. C* **2018**, *122*, 17537−17543.
(53) Milani, A.; Del Zoppo, M.; Tommasini, M.; Zerbi, G. The Effect of Intermolecular Dipole-Dipole Interaction on Raman Spectra of Polyconjugated Molecules: Density Functional Theory Simulations and Mathematical Models. *J. Phys. Chem. B* **2008**, *112*, 1619−1625.
(54) Bruno, I. J.; Cole, J. C.; Edgington, P. R.; Kessler, M.; Macrae, C. F.; McCabe, P.; Pearson, J.; Taylor, R. New Software for Searching the Cambridge Structural Database and Visualizing Crystal Structures. *Acta Crystallogr., Sect. B: Struct. Sci.* **2002**, *58*, 389−397.
(55) Delgado Friedrichs, O.; O'Keeffe, M.; Yaghi, O. M. Three-Periodic Nets and Tilings: Regular and Quasiregular Nets. *Acta Crystallogr., Sect. A: Found. Crystallogr.* **2003**, *59*, 22−27.
(56) Blatov, V. A.; Shevchenko, A. P.; Proserpio, D. M. Applied Topological Analysis of Crystal Structures with the Program Package Topospro. *Cryst. Growth Des.* **2014**, *14*, 3576−3586.
(57) O'Keeffe, M.; Peskov, M. A.; Ramsden, S. J.; Yaghi, O. M. The Reticular Chemistry Structure Resource (RCSR) Database of, and Symbols for, Crystal Nets. *Acc. Chem. Res.* **2008**, *41*, 1782−1789.

ACS APPLIED MATERIALS & INTERFACES

www.acsami.org Research Article

Stimuli-Responsive Benzothiadiazole Derivative as a Dopant for Rewritable Polymer Blends

Marcelo Echeverri, Constanza Ruiz, Sergio Gamez-Valenzuela, Matias Alonso-Navarro, Enrique Gutierrez-Puebla, Jose L. Serrano, M. Carmen Ruiz Delgado,* and Berta Gomez-Lor*

Cite This: ACS Appl. Mater. Interfaces 2020, 12, 10929−10937 Read Online

ACCESS | Metrics & More | Article Recommendations | Supporting Information

ABSTRACT: A new rod-shaped benzothiadiazole fluorophore, namely, 4,7-di-(4-nonylphenyl)benzo[*c*][1,2,5]thiadiazole, which strongly emits fluorescence both in solution and in solid state has been synthesized, and its photophysical properties were rationalized with the help of density functional theory calculations. This molecule crystallizes in two distinct light-emitting crystalline phases, which can be interconverted in response to pressure, temperature, and solvent vapors. Powder X-ray diffraction indicates that in both polymorph, molecules adopt a lamellar packing, the different interlayer spacing being the main difference between the two structures. Single-crystal analysis of one of the polymorphs allows us to identify weak interaction planes, which presumably facilitates the polymorphic transformation through mechanically or thermally induced sliding processes. The polymorphic transformation and the origin of the switchable fluorescence have been rationalized through a spectroscopic and theoretical study. This study suggests that the different colors observed are due to different intermolecular aromatic interactions owing to the displacement of the molecules with respect to the layer normal. Interestingly, blending this molecule with a biodegradable polymer such as poly(vinyl alcohol) gives rise to a thermally activated reversible switchable fluorescent system, which entitles this material as an attractive candidate for technological applications, such as thermal sensors, security inks, or rewritable paper.

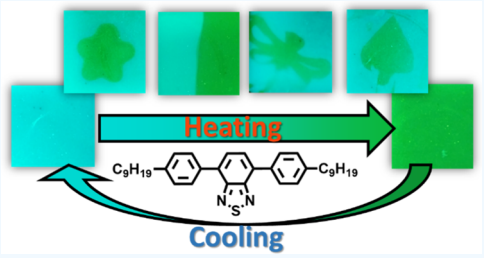

KEYWORDS: *mechanochromism, thermochromism, fluorescence, polymorphism, benzothiadiazole, phase transformation*

INTRODUCTION

Smart materials which switch their optical spectroscopic properties (i.e., color and fluorescence) upon physical external stimulation (i.e., pressure and temperature) arouse enormous interest and have found applications in fields such as sensing,[1,2] construction,[3,4] recording,[5,6] display technologies,[7,8] or rewritable paper.[9,10] Although highly efficient inorganic and metal-based chromogenic and fluorogenic materials[5,11−13] have been developed, the enormous structural diversity of organic chromophores and fluorophores gives these materials a privileged place in the area.[1−3,14,15] Particularly, the ready tunability of their optical properties together with their high compatibility with different flexible substrates makes these materials especially interesting for technological applications.

In the quest for efficient chromogenic compounds, benzothiadiazole (BTD) has emerged as an attractive moiety. This electron-deficient heterocycle presents high fluorescence quantum efficiencies both in solution and in solid state, properties that have been utilized for applications such as organic electronics[16,17] and bioimaging.[18,19] Recently, some BTD-based compounds that switch their emission color upon mechanical stress or thermal stimuli have been reported,[20−27] but in most of them, the origin of the color transformation is crystal to-amorphous transition. This fact prevents an in-depth study of the mechanism behind this process and limits the rational development of new chromophores with predesigned properties.

Herein, we present a new BTD derivative, namely, 4,7-di-(4-nonylphenyl)benzo[*c*][1,2,5]thiadiazole, which crystallize as a mixture of a blue-emitting (polymorph A) and green-emitting polymorph (polymorph B). Polymorph A can be readily converted to polymorph B in response to external stimuli (pressure and temperature). Vapor fuming provides the opposite transformation probably because of a solution recrystallization process to form the metastable phase. Interestingly, heating above the melting temperature of both polymorphs gives rise to a smectic mesophase (SmA) that upon cooling yields only polymorph B.

In this molecule, the BTD moiety is flanked by two phenyl groups substituted with long flexible chains, which make the assembly of these molecules into layers possible, as could be confirmed by single-crystal analysis of one of the two polymorphs. A combined spectroscopic and theoretical study has been performed in order to get an insight into the

Received: November 21, 2019
Accepted: February 11, 2020
Published: February 11, 2020

photophysical properties and polymorphic transformation of this material pointing to a supramolecular origin of the switchable fluorescence observed.

Interestingly, blending this molecule with a polymer such as poly(vinyl alcohol) (PVA) stabilizes the blue-emitting metastable phase, rendering a thermally activated fluorescent switchable system. The reversibility of this process is very promising for applications such as thermal sensors or rewritable paper.[10]

EXPERIMENTAL SECTION

Synthesis of 4,7-Bis(4-nonylphenyl)benzo[*c*][1,2,5]-thiadiazole. *Method 1.* A mixture of 4,7-dibromo[*c*][1,2,5]-thiadiazole (200 mg, 0.68 mmol), $Pd(PPh_3)_4$ (227 mg, 0.31 mmol), and 4-nonylphenyl boronic acid (337 mg, 1.36 mmol) in 0.5 mL of 2 M aqueous K_2CO_3 and 5 mL of tetrahydrofuran (THF) was thoroughly degassed. The solution was irradiated with an Anton Paar microwave irradiator (CEM) at 150 °C (80 W) for 180 min. The mixture was diluted with CH_2Cl_2, washed with water, and dried with $MgSO_4$; the solvent was then evaporated, and the residue was purified by chromatography with CH_2Cl_2/hexane (1:3) to give a yellow solid **1** (199 mg, 54%).

Method 2. A mixture of benzo[*c*]-1,2,3-thiadiazol-4,7-diyl-4,7-diboronic acid dipinacol ester (100 mg, 0.27 mmol), $Pd(dba)_2$ (16.9 mg, 0.03 mmol), P(*t*-Bu)$_3$ (6.3 mg, 0.03 mmol), KF (102.7 mg, 1.8 mmol), and 1-bromo-4-*n*-nonylbenzene (337 mg, 1.36 mmol) in 5 mL of THF was thoroughly degassed. The mixture was irradiated with an Anton Paar microwave irradiator (CEM) at 150 °C (80W) for 60 min. The mixture was diluted with CH_2Cl_2, washed with water, and dried with $MgSO_4$; the solvent was evaporated, and the residue was purified by chromatography with CH_2Cl_2/hexane (1:3) to give a yellow solid **1** (164 mg, 69%). ^{1}H NMR (300 MHz, $CDCl_3$): δ 7.90 (d, J = 8.2 Hz, 4H), 7.76 (s, 2H), 7.37 (d, J = 8.2 Hz, 4H), 2.87−2.53 (m, 4H), 1.88−1.54 (m, 4H), 1.31 (s, 28H), 0.90 (d, J = 6.9 Hz, 6H). ^{13}C NMR (50 MHz, $CDCl_3$): δ 154.4, 143.5, 135.0, 133.2, 129.3, 128.9, 128.1, 36.0, 32.1, 31.7, 29.8, 29.6, 22.9, 14.3. UV (CH_2Cl_2, 25 °C): λ_{max} (log ε) 275 (4.73), 391 (4.30). FAB MS m/z 540.84 (M^+); HRMS (FAB) calcd for $C_{36}H_{48}N_2S$, 540.3538; found, 540.3539.

Phase-Selective Crystal Growth. *Polymorph A.* A saturated solution of **1** in THF/H_2O (1:1) was placed in a 5 mL glass vial and tightly covered with a perforated Parafilm M film in order to allow slow evaporation of the solvents. Crystals were obtained in 2 days. The selectivity of the process was confirmed by powder X-ray diffraction of the bulk crystalline materials obtained (see Figure S1).

Polymorph B. A saturated solution of **1** in CH_2Cl_2/CH_3CN (1:1) was placed in a 5 mL glass vial and tightly covered with a perforated Parafilm M film in order to allow slow evaporation of the solvents. Crystals were obtained after 6 days. The selectivity of the process was confirmed by powder X-ray diffraction of the bulk crystalline materials obtained (see Figure S1).

Preparation of PVA Films Doped with 1 (1% wt). To a solution of 1.5 mg of **1** in 1 mL of THF, 1 mL of H_2O was added slowly, and the mixture was stirred for 30 min. Then, 150 mg of PVA powder (87−90% hydrolyzed, average mol wt 30,000−70,000, Sigma-Aldrich)[28] was added slowly, and the mixture was stirred for 2 h at 30 °C, subsequently filtered through a microporous filter (0.45 μm pore size), deposited onto a glass slide by dropcasting, and dried overnight at room temperature (RT). The resulting film was washed with dichloromethane and dried at RT.

Preparation of Polycarbonate Films Doped with 1 (1% wt). A solution of 150 mg of poly[bisphenol A carbonate-*co*-4,4′-(3,3,5-trimethylcyclohexylidene)diphenol carbonate] (Sigma-Aldrich) and 1.5 mg of **1** was stirred for 10 min and subsequently poured onto a leveled glass slide provided with a confinement ring. The film was dried by slow evaporation overnight at RT.

RESULTS AND DISCUSSION

Synthesis and Photophysical Properties. Compound **1** was obtained by palladium-catalyzed Suzuki cross-coupling reaction between 4,7-dibromo-2,1,3-benzo[*c*][1,2,5]thiadiazole and 2 equiv of 4-nonylphenylboronic acid under microwave heating conditions in 54% yield. Alternatively, this compound can be obtained by Suzuki coupling of 2,1,3-benzothiadiazole-4,7-bis(boronic acid pinacol ester) and 4-nonylphenylbromide (Scheme 1). Under these conditions, compound **1** is

Scheme 1. Synthesis of Compound 1

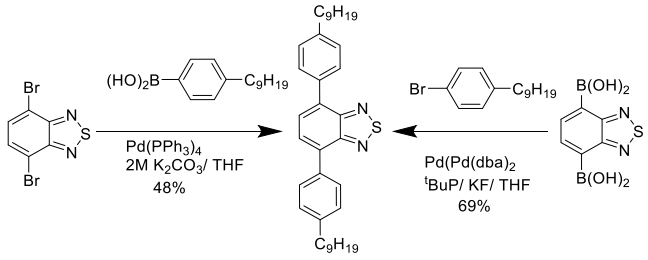

1

contaminated with a compound that was identified as 4-(4-nonylphenyl)-7-phenylbenzo[*c*][2,1,3]thiadiazole (Scheme S1). The formation of this byproduct can be rationalized by an aryl−aryl exchange between the Pd center and the phosphine ligands in the intermediate Pd(II) complex following the oxidative addition in the catalytic cycle.[15,29] A significant enhancement of the yield in the desired product (69%) could be achieved by changing the catalyst system to $Pd(dba)_2$/^{t}BuP, thus avoiding the only possible source of a phenyl moiety.

The photophysical properties of this molecule were studied by UV−vis and fluorescence spectroscopy (Figure 1) and rationalized with the help of density functional theory (DFT) calculations (Figures S3−S5). The UV−vis absorption spectrum of a 10^{-5} M solution of **1** in CH_2Cl_2 exhibits three predominant absorption bands localized at 274, 315, and 389 nm (Figure 1a). The fluorescence spectrum of a 10^{-5} M solution of **1** in CH_2Cl_2 is characterized by an emission band peaking at 510 nm with a quantum yield of 0.52 (Figure 1b). We have investigated the photophysical properties of **1** in different solvents, finding that while solvent polarity has a negligible influence in the UV−vis absorption spectrum of **1**, the fluorescence spectrum of **1** shows a moderate solvent dependence with emission bands shifting bathochromically as the solvent polarity is increased from hexane (481 nm) to methanol (522 nm). This behavior suggests a more polarized first excited S_1 state when compared to the S_0 ground state, highlighting the significant impact of the environment on the emission properties of these compounds.

We have performed DFT calculations in order to get a deeper understanding of the photophysical properties of molecule **1**. Figure 1c shows the simulated absorption spectrum of **1**. As we can see, the lowest energy band (observed at 389 nm) is attributed to a $S_0 \rightarrow S_1$ electronic transition (calculated at 354 nm) that arises mainly from a HOMO → LUMO excitation. This transition has a strong intramolecular charge-transfer (ICT) character as the highest occupied molecular orbital (HOMO) is delocalized over the whole conjugated backbone, while the lowest unoccupied molecular orbital (LUMO) is strongly localized on the central

https://dx.doi.org/10.1021/acsami.9b21209
ACS Appl. Mater. Interfaces 2020, 12, 10929−10937

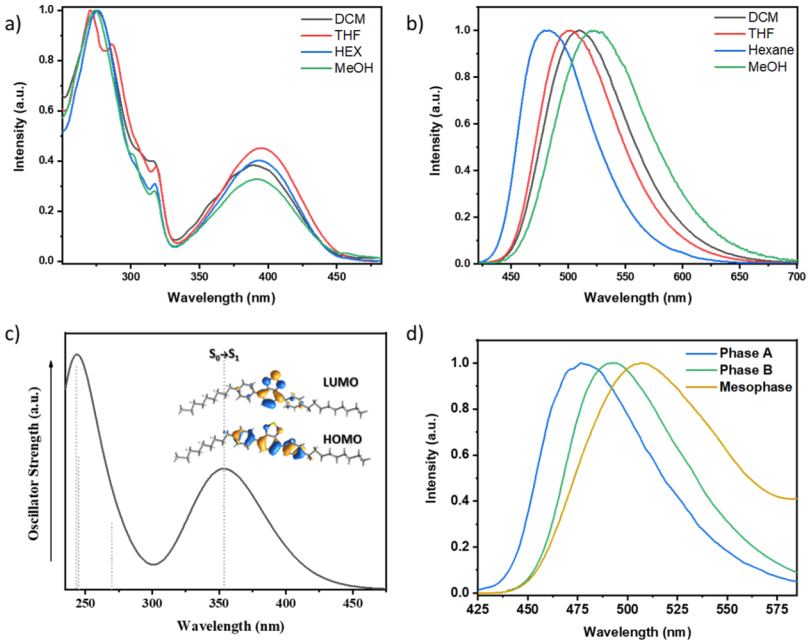

Figure 1. (a) UV−vis absorption spectrum of **1** in different solvents at a concentration of 10^{-5} M. (b) Fluorescence spectrum of **1** in different solvents at a concentration of 10^{-5} M. (c) Simulated absorption spectra for **1** together with the excitations (wavelength vs oscillator strength) shown as vertical bars, calculated at the ωB97XD/6-31G** level in dichloromethane solution. The HOMO and LUMO molecular orbital topologies are also shown. (d) Solid fluorescence spectra of both polymorphs of **1** (phase A and phase B) and of the mesophase (at 90 °C).

BTD unit (see Figure 1c). On the contrary, the bands observed at higher energies (274 and 315 nm) are described by electronic excitations between molecular orbitals either localized on specific segments or delocalized over the whole π-conjugated molecule, thus revealing a mixed π to π^* nature and ICT character (see Figures S3 and S4). Time-dependent DFT (TD-DFT) calculations of the first excited state (S_1) of molecule **1** in various solvents help us to explain the bathochromic shift of the emission spectra experimentally observed when increasing the solvent polarity. In fact, the predicted molecular dipole moment for the first excited S_1 state (μ_e) is about 3 times larger than that for the ground S_0 state (μ_g). Therefore, increasing the solvent polarity would result in a larger stabilization of the charge-separated resonance form in the S_1 state when compared to that in the S_0 state giving rise to lower energy transitions. Interestingly, upon $S_0 \rightarrow S_1$ excitation, the molecular geometries become more planar, presumably increasing the electronic delocalization in the excited state (see Tables S1 and S2).

Compound **1** is obtained as a polycrystalline solid in which it is possible to distinguish two types of crystals on the basis of their different morphology (clearly noticeable as observed under an optical microscope) and emission color when illuminated with a UV lamp. A comparison of the powder diffractograms of both polymorphs shows a similar packing arrangement characterized by major primary diffraction peaks at 3.82 and 3.21° for polymorphs A and B, respectively (Figure S1), together with a number of higher order lower intensity Bragg peaks, suggesting lamellar structures with interlayer distances of 23.4 and 27.4 Å. Interestingly, heating the mixture up to 70 °C gives rise exclusively to polymorph B, but this transformation is not reverted upon cooling. When the compound is further heated, it shows a liquid crystalline phase that extends in a broad temperature range (73.7−104.6 °C) and has been characterized as SmA on the basis of the typical fan-shaped textures observed by a polarizing optical microscope. Its X-ray diffractogram is indicative of a lamellar structure with a layer spacing of 32.9 Å (close to the molecule length in their most extended conformation 34.6 Å). The characterization of the mesophase [POM, X-ray diffractograms, and differential scanning calorimetry (DSC)] can be found in Figures S6 and S7. Cooling down from the SmA mesophase gives rise exclusively to the green-emitting polymorph B.

The compound in all three states, polymorphs A and B and SmA, strongly emits fluorescence when irradiated at 365 nm, showing a progressive red shift when transitioning from polymorph A ($\lambda_{max.}$ = 477 nm) to polymorph B ($\lambda_{max.}$ = 493 nm) and to SmA ($\lambda_{max.}$ = 507 nm). Quantum yields of Φ_F = 0.61 and Φ_F = 0.32 were obtained for polymorphs A and B, respectively, which suggest stronger intermolecular interactions in this last case and thus increased nonradiative decay processes. Similar lifetimes are observed for both polymorphs ($\tau_F \approx 7-11$ ns, see Figure S8).

Attempts to selectively grow the different crystalline phases were performed by slow evaporation of saturated solutions of **1** in different solvents and solvent mixtures. Fortunately, upon slow evaporation of a solution of **1** in THF/H_2O (1:1), the blue-emitting polymorph was exclusively obtained (Figure S1b), while evaporation of a CH_2Cl_2/CH_3CN (1:1) solution led to the green-emitting polymorph (Figure S1c).

Crystals of polymorph B of sufficient quality for single-crystal analysis could be selected, and the crystal structure is determined. In this polymorph, molecules crystallize in the monoclinic space group *P*21, with two independent molecules per unit cell, which differ mainly in the different torsion between the BTD unit and the phenyl linkers (in each molecule rotated in opposite directions by 40.56 and 29.15° and by 34.25 and 29.67°, respectively). Note that DFT calculations for an isolated molecule (at the B3LYP/6-31G** level of theory) predict a dihedral angle close to ±40° as the most stable structure according to the calculated dihedral potential energy hypersurface (Figure S5). The moderate

https://dx.doi.org/10.1021/acsami.9b21209
ACS Appl. Mater. Interfaces 2020, 12, 10929−10937

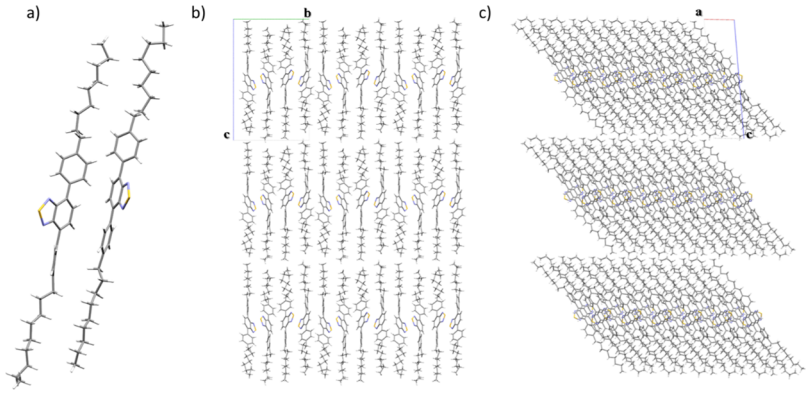

Figure 2. (a) View of the two independent molecules in the asymmetric unit in polymorph B, (b) crystal packing view along a, and (c) crystal packing view along (b).

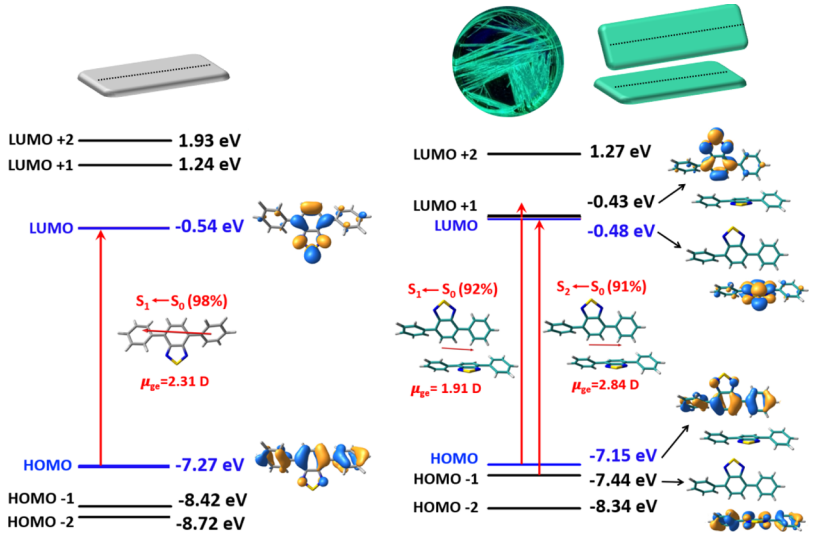

Figure 3. DFT-calculated (at the wB97XD/6-31G** level) frontier molecular orbital diagram for a single molecule **1** (left) and for a dimer when using the molecular coordinates obtained from the X-ray structure analysis of the two molecules integrating the unit cell of polymorph B. The spatial orientation of the transition dipole moment (μ_{ge}) and the CI contribution for the main electronic transitions are also shown. The alkyl chains of the monomer and the dimer have been omitted for clarity.

planarization observed by X-ray analysis is probably related to the packing effects.

The analysis of the crystal packing confirms the formation of a layered structure. As can be observed in Figure 2b,c, the flexible alkyl chains between neighboring layers are non-interdigitated, giving rise to weak interaction planes (slip-planes). Within the layers, neighboring molecules adopt a zigzag arrangement.

We have used TD-DFT calculations to shed light on the consequences that this particular supramolecular arrangement exerts on the optical properties of the crystal. Figure 3 compares the molecular orbital diagram for an isolated molecule and a dimer when using the molecular coordinates obtained from the X-ray structure analysis of polymorph B. When going from the isolated molecule to the dimer, the HOMO and LUMO levels become nearly degenerated with HOMO/HOMO − 1 being delocalized over the whole conjugated backbone of one single molecule and LUMO/LUMO + 1 localized on the acceptor unit of the same molecule. Therefore, the lowest energy absorption band which, as discussed above, is described by a $S_0 \rightarrow S_1$ transition associated with the HOMO → LUMO electronic excitation in the monomer, in the case of the dimer, corresponds to a mixture of $S_0 \rightarrow S_1$ and $S_0 \rightarrow S_2$ transitions, which are described by HOMO − 1 → LUMO and HOMO → LUMO + 1 electronic excitations. These calculations reveal that the ICT character of the lowest energy electronic transition is also preserved in this polymorph. Interestingly, the orientation of the transition dipole moment (μ_{ge}) takes place along the long axis of the molecule in both the single molecule (with a value of 2.31 D for the $S_0 \rightarrow S_1$ transition) and the dimer (with values of 1.91 and 2.84 D for $S_0 \rightarrow S_1$ and $S_0 \rightarrow S_2$ transitions, respectively).

Unfortunately, crystals of the blue polymorph A are too small and diffract poorly. Although a comparison of the powder diffractograms of both polymorphs shows a similar layered packing arrangement, the shorter interlayer distance observed for polymorph A can in principle be due to a higher tilt angle of the molecules with respect to the layer normal or to some degree of alkyl chains interdigitation in the layers. However, the infrared spectra of both polymorphs are identical in the region of CH stretching vibrations (3100−2700 cm^{-1}), thus suggesting that in this polymorph alkyl chains are again noninterdigitated (Figure S9) and pointing to a different

https://dx.doi.org/10.1021/acsami.9b21209
ACS Appl. Mater. Interfaces 2020, 12, 10929−10937

degree of tilting as the reason of the different diffractograms observed.

Organic single crystals offer an excellent opportunity to investigate the origin of the different light-emitting properties in bulk organic materials, as they provide accurate information on the relative arrangements of neighboring molecules and how molecules interact with each other as well as which are their conformational preferences, factors which will severely affect the macroscopic emission properties.[30−33] In this particular case, the lack of single-crystal data for one of the polymorphs does not allow us to determine how the molecules are interacting within the layers or give us information about the dihedral angle between the BTD and the attached phenyl rings; both factors are of great importance in determining the nature of the color changes. However, in an attempt to shed light on the origin of different colors observed and considering the high sensitivity of Raman spectroscopy not only to intramolecular changes but also to intermolecular interactions of π-conjugated molecules,[34−36] we have recorded the Raman spectra of both polymorphs using a laser excitation line of 785 nm (out-of-resonance conditions). As shown in Figure 4, we

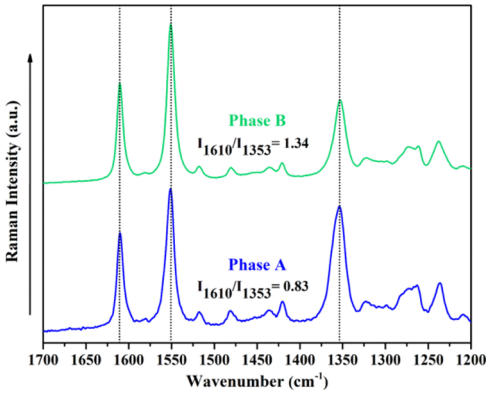

Figure 4. Comparison between Raman spectra of polymorphs A (blue line) and B (green line) at 785 nm excitation.

focused on the spectral region related with the most intense Raman bands (1200−1700 cm^{-1}) which are associated with skeletal C═C/C−C stretching vibrations of the conjugated backbone. Specifically, we observed three intense bands which are assigned to C═C/C−C stretching vibrations of the external phenyl rings (1610 cm^{-1}), the BTD unit (1353 cm^{-1}) and a collective vibration which involves the whole conjugated backbone (1551 cm^{-1}). The vibrational eigenvectors and the theoretical Raman spectrum (Figure S10) support this assignment and confirm the good validity of our discussion. Interestingly, the spectra of both polymorphs show identical shifts and differ only in the relative intensity ratios between the C−C stretching vibration of the outer phenyl rings (1610 cm^{-1}) and that localized in the BTD unit (1353 cm^{-1}), I_{1610}/I_{1353} bands.

In order to determine the intramolecular or supramolecular origin of these subtle differences, we have computed the Raman spectra for compound **1** as a function of torsional angle between the BTD unit and the phenyl ring. Our calculations predict a strong frequency shift of the main C−C stretching modes upon twisting the molecular core (i.e., the collective C−C vibration observed at 1551 cm^{-1} is predicted to shift 25 cm^{-1} when varying the dihedral torsional angle from 0 to 90°, see Figure S11). Therefore, the practically superimposable spectral profile of polymorphs A and B suggests similar dihedral torsional angles between the BTD unit and the phenyl rings in both cases. This means that the differences in the I_{1610}/I_{1353} bands have to be ascribed to different $\pi-\pi$ intermolecular arrangements that would result in different π-electron delocalizations when comparing the two polymorphs probably because of the sliding of the molecules along the long molecular axis, which would be favored by the presence of slip-planes in the crystals. Note that a recent study in unsubstituted oligothiophenes reveals that the interactions coming from an effective packing can induce pinning effects that diminish the delocalization of π electrons.[34]

Switching the Light-Emitting Properties. The similarity between the two structures, the easy transformation of polymorph A into B upon heating, and the presence of weak interaction planes induced us to evaluate in more detail the possible transformation between both polymorphs by subjecting them to different physical stimuli (temperature, mechanical stress, and solvent vapors).

Heating crystals of the two different polymorphs under a microscope equipped with a hot stage and illumination with a UV lamp (λ = 365 nm) allowed us to demonstrate that the thermal polymorphic transformation occurs even in single crystals. The single crystal-to-single crystal transformation of polymorph A into polymorph B (see Figure 5a) can be clearly

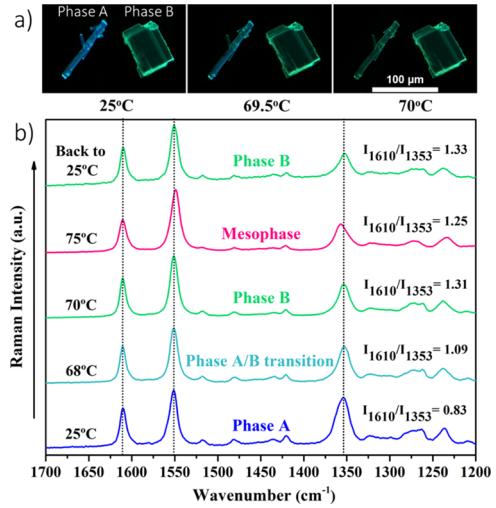

Figure 5. (a) Photomicrograph of the interconversion of both polymorphs (viewed under irradiation with a 365 nm lamp) upon thermal heating and (b) temperature-dependent Raman spectra from 25 to 75 °C and then cooling to RT collected by using a laser excitation line of 785 nm. The intensity ratios of the bands localized at 1610 and 1353 cm^{-1} are also shown.

visualized at 69.5 °C. Upon cooling, the blue emission is not regained. Note that color changes between single-crystalline polymorphs are challenging as it involves transformation of the supramolecular and/or intramolecular structure within the constrained environment of the crystal.[37−48]

Temperature-dependent Raman analysis allowed us to confirm the conversion from polymorph A to polymorph B and mesophase upon heating (Figure 5b). This dynamic interconversion can be analyzed in terms of the relative intensity ratio I_{1610}/I_{1353} between the C−C stretching vibration of the outer phenyl rings (1610 cm^{-1}) and the vibration mainly localized in the BTD unit (1353 cm^{-1}). As can be seen in

https://dx.doi.org/10.1021/acsami.9b21209
ACS Appl. Mater. Interfaces 2020, 12, 10929−10937

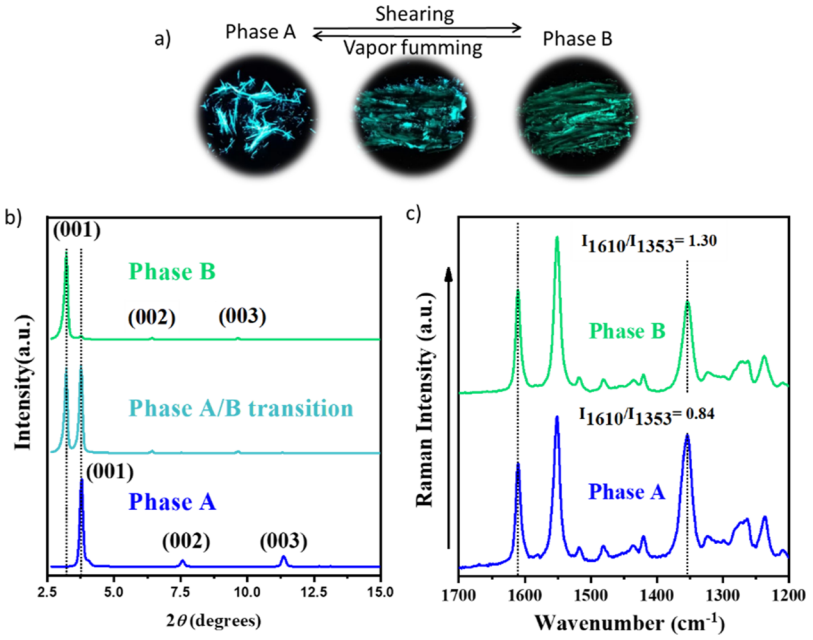

Figure 6. (a) Photograph of the interconversion of both polymorphs upon shearing (illuminated with a 365 nm lamp). (b) Interconversion process, followed by X-ray diffraction pattern changes (amplifications shown in Figure S12). (c) Raman spectra of polymorph A and after shearing (polymorph B).

Figure 5b, I_{1610}/I_{1353} increases from 0.83 in polymorph A at 25 °C to 1.31 in polymorph B at 70 °C, showing a value of 1.09 at 68 °C (which probably corresponds to a transition state as the I_{1610}/I_{1353} value is in between those obtained for polymorph A and polymorph B).

Interestingly, when increasing the temperature over 70 °C, new spectral changes are observed (i.e., broadening and upshifting of the band at 1610 cm^{-1} and upshifting of the band at 1353 cm^{-1}). These frequency shifts point to structural π-conjugational changes between the BTD unit and the external phenyl groups in the mesophase with respect to both A and B polymorphs. Note that changes in torsional dihedral angles of molecule **1** would result in C−C stretching mode frequency shifting, as discussed above (see Figure S11). Specifically, the upshift of the C−C stretching band of the BTD unit from 1353 cm^{-1} in polymorph B to 1357 cm^{-1} in the mesophases reveals more distorted conjugated backbones in this case, probably related to the higher fluidity of the liquid crystalline phase. Upon cooling the mesophase back to RT (see Figure 5), only polymorph B is obtained, thus confirming the observation previously made by microscopy and DSC (Figure S7).

In the same way, these two polymorphs can also be interconverted by mechanical stress or exposure to solvent vapors. Note that slip-planes have been identified as an attractive design principle in search of mechanochromic systems.[49] Thus, as monitored by powder X-ray diffraction and Raman spectroscopy, shearing polymorph A crystals on a substrate render exclusively polymorph B (Figure 6). Subsequent exposition of this sample to CH_2Cl_2 vapors produces again the metastable polymorph A, probably because of a partial dissolution−recrystallization process.

Hybrid Molecular-Polymeric Materials. Stimuli-responsive small-molecule dyes have aroused much interest as dopants of polymeric materials. Small amounts (<3%) are usually enough to confer these materials the desired optical switching behavior while maintaining the interesting mechanical properties of the polymeric matrix.[50−52] With this in mind, we have prepared films of PVA doped with 1% of compound **1**. Because of the biodegradable character and health safety of this polymer, PVA creates increasing interest in various industrial markets, such as food packaging, textiles, or pharmaceutical industry among others.

Blends were prepared by adding PVA powder to a suspension of **1** in 1:1 H_2O/THF mixture (see Figure S13). In this solvent mixture, **1** self-assembles into nanoparticles with a spherical shape and diameters ranging from 100 to 400 nm, as determined by dynamic light scattering and confocal microscopy (see Figure S15). Addition of the PVA powder does not significantly alter the nanoparticles that remain in suspension. Only a slight increase in the particle size distribution, probably because of some agglomeration between nanoparticles in this medium, is observed (see Figure 7).

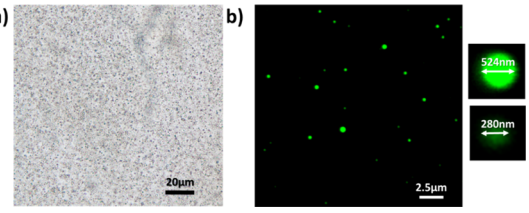

Figure 7. (a) Optical microphotographs of **1** nanoparticles with PVA in the medium and (b) confocal images of suspension of **1** nanoparticles in THF/H_2O and PVA.

Apparently, the polar protic contribution provided by the hydroxyl groups of the polymeric matrix maintains the solvophobic environment necessary to stabilize the nanoparticles formed. After dropcasting and drying the suspension, a thin film was obtained. Examination of this film under a polarized optical microscope (Figure 8) allows us to detect the formation of microscale crystallites embedded in the polymeric matrix, which shows cyan emission (Figure 8c) upon illumination with a UV lamp (365 nm). The presence of

https://dx.doi.org/10.1021/acsami.9b21209
ACS Appl. Mater. Interfaces 2020, 12, 10929−10937

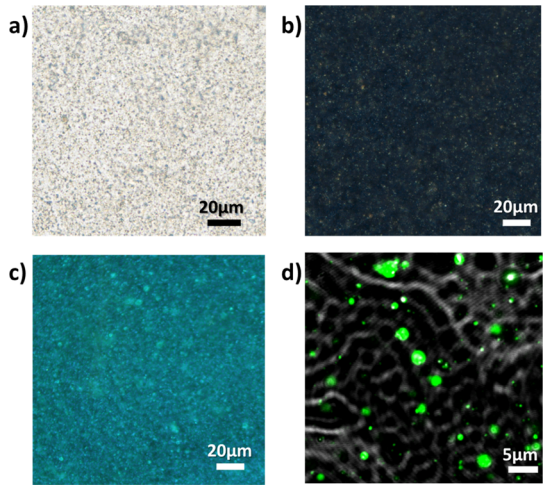

Figure 8. (a) Optical microphotographs of 1% of **1** in the PVA film under visible light. (b) Polarized optical microphotographs of a **1**:PVA film. (c) Optical microphotographs of a **1**:PVA film under UV light (365 nm) illumination. (d) Merged bright field with the corresponding fluorescence confocal images of a **1**:PVA film.

aggregates in the matrix could be confirmed by fluorescence confocal microscopy. As shown in Figure 8d, the overlay bright field with the corresponding fluorescence confocal images of a **1**:PVA film shows clearly the fluorophore as emitting punctual spots, dispersed in the matrix.

By heating the film, under a hot stage provided by a temperature controller, we can clearly observe a transformation of the emitting color to green at 75 °C (mesophase temperature). Interestingly, when cooling down this hybrid material, the blue emission is regained in contrast to that observed on thermal treatment of pristine **1**. This color transformation is maintained for at least 10 heating−cooling cycles. Apparently, the confinement in the polymeric matrix favors the growth of the metastable stable blue polymorph (phase A). Such a strategy has been previously successfully employed to select the preferred crystalline phases for pharmaceutical or electronic applications.[53−56]

Attempts to prepare the blends without the previous formation of the nanoparticles by mixing a solution of **1** in THF and a solution of PVA in H_2O led to the uneven crystallization of the dopant in the polymeric matrix, resulting in irreversible fluorochromic films. On the other hand, films prepared using other polymeric matrices (such as polycarbonate) present a much more homogeneous distribution of the chromophore, as could be determined by confocal fluorescence microscopy, but show no thermal response which highlights the importance of the confinement provided by the nanoparticles to accomplish the desired reversibility (see Figure S16).

The reversibility of this process renders this material a promising candidate as a rewriteable system. To demonstrate this possibility, a number of different motifs were "written" by approaching a heated aluminum stamp to these hybrid films. By heating the entire film above 75 °C and cooling down to RT, the drawing was completely erased and used again to write a new motif (Figure 9).

CONCLUSIONS

In conclusion, a new BTD-based luminophore has been synthesized, which crystallizes in two distinct polymorphs showing a layer-like organization and exhibits different light-emitting properties (blue and green emission) under UV illumination and can be readily interconverted by means of external stimuli. Single-crystal analysis of the green-emitting polymorph allows us to identify weak interaction planes, which are responsible for the switchable properties by facilitating mechanically or thermally induced sliding processes. Although the absence of single-crystal data of the blue-emitting polymorph does not allow us to unequivocally identify the origin of color change, Raman spectroscopy together with DFT calculations points to similar intramolecular twisted backbones but different $\pi-\pi$ intermolecular interactions when both polymorphs were compared. The result of this study points to a supramolecular origin of the color transformation because of the displacement of the molecules with respect to the layer normal. Interestingly, blends of this molecule with a biodegradable polymer such as PVA increase the reversibility of the thermally activated transformation, thus significantly expanding the potential applicability of this material in areas such a rewritable paper, intelligent inks, optical recording, or thermal sensing.

ASSOCIATED CONTENT

Supporting Information

The Supporting Information is available free of charge at https://pubs.acs.org/doi/10.1021/acsami.9b21209.

Crystallographic data of 1 (CIF)

Experimental details, copy of the ^{1}H NMR and ^{13}C NMR spectra of **1**, experimental and simulated powder

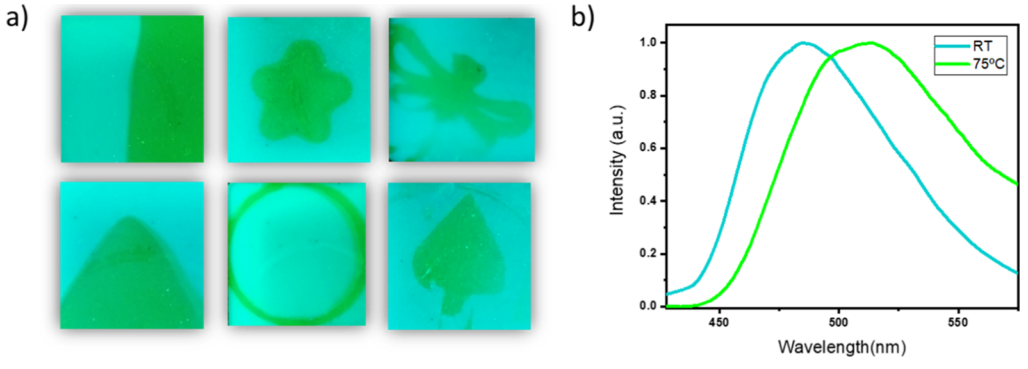

Figure 9. (a) Different motifs stamped on a sole **1**:PVA blend thin film following a written−erasing procedure. (b) Solid fluorescence spectrum of the PVA blend at RT and at 75 °C.

https://dx.doi.org/10.1021/acsami.9b21209
ACS Appl. Mater. Interfaces 2020, 12, 10929−10937

X-ray diffraction patterns of both polymorphs, liquid crystalline properties, DFT calculations, fluorescence lifetimes, IR spectroscopy, and details on the preparation of **1**:polymer hybrid materials (PDF)

AUTHOR INFORMATION

Corresponding Authors

M. Carmen Ruiz Delgado − *Department of Physical Chemistry, University of Malaga, 29071 Malaga, Spain;* orcid.org/0000-0001-8180-7153; Phone: (+34) 951953325; Email: carmenrd@uma.es

Berta Gomez-Lor − *Instituto de Ciencia de Materiales de Madrid, CSIC Cantoblanco, 28049 Madrid, Spain;* orcid.org/0000-0002-2995-9624; Phone: (+34) 91-3349031; Email: bgl@icmm.csic.es; Fax: (+34) 91-3720623

Authors

Marcelo Echeverri − *Instituto de Ciencia de Materiales de Madrid, CSIC Cantoblanco, 28049 Madrid, Spain;* orcid.org/0000-0002-9290-4546

Constanza Ruiz − *Instituto de Ciencia de Materiales de Madrid, CSIC Cantoblanco, 28049 Madrid, Spain*

Sergio Gamez-Valenzuela − *Department of Physical Chemistry, University of Malaga, 29071 Malaga, Spain*

Matias Alonso-Navarro − *Instituto de Ciencia de Materiales de Madrid, CSIC Cantoblanco, 28049 Madrid, Spain;* orcid.org/0000-0002-1618-4612

Enrique Gutierrez-Puebla − *Instituto de Ciencia de Materiales de Madrid, CSIC Cantoblanco, 28049 Madrid, Spain*

Jose L. Serrano − *Departamento de Quimica Organica, Instituto de Ciencia de Materiales de Aragon, Universidad de Zaragoza-CSIC, 50009 Zaragoza, Spain;* orcid.org/0000-0001-9866-6633

Complete contact information is available at: https://pubs.acs.org/10.1021/acsami.9b21209

Author Contributions

The manuscript was written through contributions of all authors. All authors have given approval to the final version of the manuscript.

Notes

The authors declare no competing financial interest.

ACKNOWLEDGMENTS

The work at the ICMM in Madrid was financially supported by the MINECO of Spain (CTQ2016-78557-R). The work at the University of Malaga was funded by the MINECO (CTQ2016-78557-R) and Junta de Andalucia (P09-FQM-4708 and UMA18-FEDERJA-080) projects. The authors thankfully acknowledge the computer resources, technical expertise, and assistance provided by the SCBI (Supercomputing and Bioinformatics) centre of the University of Malaga. S.G.V. thanks the MINECO for a FPU predoctoral fellowship (FPU 17/04908).

REFERENCES

(1) Mazza, M. M. A.; Raymo, F. M. Structural Designs for Ratiometric Temperature Sensing with Organic Fluorophores. *J. Mater. Chem. C* **2019**, *7*, 5333−5342.

(2) Wu, J.; Kwon, B.; Liu, W.; Anslyn, E. V.; Wang, P.; Kim, J. S. Chromogenic/Fluorogenic Ensemble Chemosensing Systems. *Chem. Rev.* **2015**, *115*, 7893−7943.

(3) Khandelwal, H.; Schenning, A. P. H. J.; Debije, M. G. Infrared Regulating Smart Window Based on Organic Materials. *Adv. Energy Mater.* **2017**, *7*, 1602209.

(4) Lampert, C. M. Chromogenic Smart Materials. *Mater. Today* **2004**, *7*, 28−35.

(5) Zhang, C.; Wang, B.; Li, W.; Huang, S.; Kong, L.; Li, Z.; Li, L. Conversion of Invisible Metal-Organic Frameworks to Luminescent Perovskite Nanocrystals for Confidential Information Encryption and Decryption. *Nat. Commun.* **2017**, *8*, 1138.

(6) Genovese, D.; Aliprandi, A.; Prasetyanto, E. A.; Mauro, M.; Hirtz, M.; Fuchs, H.; Fujita, Y.; Uji-I, H.; Lebedkin, S.; Kappes, M.; De Cola, L. Mechano-and Photochromism from Bulk to Nanoscale: Data Storage on Individual Self-Assembled Ribbons. *Adv. Funct. Mater.* **2016**, *26*, 5271−5278.

(7) Wang, X.; Li, W.; Li, W.; Gu, C.; Zheng, H.; Wang, Y.; Zhang, Y.-M.; Li, M.; Xiao-An Zhang, S. An RGB Color-Tunable Turn-on Electrofluorochromic Device and its Potential for Information Encryption. *Chem. Commun.* **2017**, *53*, 11209−11212.

(8) Ogasawara, K.; Nakamura, K.; Kobayashi, N. Thermally Controlled Dual-Mode Display Media with Red-Green-Blue Coloration and Fluorescence Via Energy Transfer between Emission Materials and Leuco Dyes. *J. Mater. Chem. C* **2016**, *4*, 4805−4813.

(9) Chen, L.; Weng, M.; Huang, F.; Zhang, W. Long-Lasting and Easy-to-Use Rewritable Paper Fabricated by Printing Technology. *ACS Appl. Mater. Interfaces* **2018**, *10*, 40149−40155.

(10) Khazi, M. I.; Jeong, W.; Kim, J.-M. Functional Materials and Systems for Rewritable Paper. *Adv. Mater.* **2018**, *30*, 1705310.

(11) Grzelczak, M.; Liz-Marzan, L. M.; Klajn, R. Stimuli-Responsive Self-Assembly of Nanoparticles. *Chem. Soc. Rev.* **2019**, *48*, 1342−1361.

(12) Chen, L.-J.; Yang, H.-B. Construction of Stimuli-Responsive Functional Materials via Hierarchical Self-Assembly Involving Coordination Interactions. *Acc. Chem. Res.* **2018**, *51*, 2699−2710.

(13) McConnell, A. J.; Haynes, C. J. E.; Grommet, A. B.; Aitchison, C. M.; Guilleme, J.; Mikutis, S.; Nitschke, J. R. Orthogonal Stimuli Trigger Self-Assembly and Phase Transfer of $FeII_4L_4$ Cages and Cargoes. *J. Am. Chem. Soc.* **2018**, *140*, 16952−16956.

(14) Sagara, Y.; Yamane, S.; Mitani, M.; Weder, C.; Kato, T. Mechanoresponsive Luminescent Molecular Assemblies: an Emerging Class of Materials. *Adv. Mater.* **2016**, *28*, 1073−1095.

(15) Kong, K. C.; Cheng, C. H. Facile Aryl-Aryl Exchange between the Palladium Center and Phosphine Ligands in Palladium(II) Complexes. *J. Am. Chem. Soc.* **1991**, *113*, 6313−6315.

(16) Findlay, N. J.; Breig, B.; Forbes, C.; Inigo, A. R.; Kanibolotsky, A. L.; Skabara, P. J. High Brightness Solution-Processed OLEDs Employing Linear, Small Molecule Emitters. *J. Mater. Chem. C* **2016**, *4*, 3774−3780.

(17) Wang, Y.; Michinobu, T. Benzothiadiazole and its [Small π]-Extended, Heteroannulated Derivatives: Useful Acceptor Building Blocks for High-Performance Donor-Acceptor Polymers in Organic Electronics. *J. Mater. Chem. C* **2016**, *4*, 6200−6214.

(18) Liou, S.-Y.; Ke, C.-S.; Chen, J.-H.; Luo, Y.-W.; Kuo, S.-Y.; Chen, Y.-H.; Fang, C.-C.; Wu, C.-Y.; Chiang, C.-M.; Chan, Y.-H. Tuning the Emission of Semiconducting Polymer Dots from Green to Near-Infrared by Alternating Donor Monomers and Their Applications for in Vivo Biological Imaging. *ACS Macro Lett.* **2016**, *5*, 154−157.

(19) Neto, B. A. D.; Carvalho, P. H. P. R.; Correa, J. R. Benzothiadiazole Derivatives as Fluorescence Imaging Probes: Beyond Classical Scaffolds. *Acc. Chem. Res.* **2015**, *48*, 1560−1569.

(20) Dou, C.; Chen, D.; Iqbal, J.; Yuan, Y.; Zhang, H.; Wang, Y. Multistimuli-Responsive Benzothiadiazole-Cored Phenylene Vinylene Derivative with Nanoassembly Properties. *Langmuir* **2011**, *27*, 6323−6329.

(21) Gautam, P.; Maragani, R.; Mobin, S. M.; Misra, R. Reversible Mechanochromism in Dipyridylamine-Substituted Unsymmetrical Benzothiadiazoles. *RSC Adv.* **2014**, *4*, 52526−52529.

(22) Ito, S.; Yamada, T.; Taguchi, T.; Yamaguchi, Y.; Asami, M. N-Boc-Indolylbenzothiadiazole Derivatives: Efficient Full-Color Solid-

State Fluorescence and Self-Recovering Mechanochromic Luminescence. *Chem.—Asian J.* **2016**, *11*, 1963−1970.
(23) Naeem, K. C.; Neenu, K.; Nair, V. C. Effect of Differential Self-Assembly on Mechanochromic Luminescence of Fluorene-Benzothiadiazole-Based Fluorophores. *ACS Omega* **2017**, *2*, 9118−9126.
(24) Shimogawa, H.; Yoshikawa, O.; Aramaki, Y.; Murata, M.; Wakamiya, A.; Murata, Y. 4,7-Bis[3-(dimesitylboryl)thien-2-yl]-benzothiadiazole: Solvato-, Thermo-, and Mechanochromism Based on the Reversible Formation of an Intramolecular B−N Bond. *Chem.—Eur. J.* **2017**, *23*, 3784−3791.
(25) Echeverri, M.; Martín, I.; Concellon, A.; Ruiz, C.; Anselmo, M. S.; Gutierrez-Puebla, E.; Serrano, J. L.; Gomez-Lor, B. Fluorescent and Electroactive Monoalkyl BTD-Based Liquid Crystals with Tunable Self-Assembling and Electronic Properties. *ACS Omega* **2018**, *3*, 11857−11864.
(26) Jadhav, T.; Dhokale, B.; Patil, Y.; Mobin, S. M.; Misra, R. Multi-Stimuli Responsive Donor−Acceptor Tetraphenylethylene Substituted Benzothiadiazoles. *J. Phys. Chem. C* **2016**, *120*, 24030−24040.
(27) Aguiar, L. d. O.; Regis, E.; Tuzimoto, P.; Girotto, E.; Bechtold, I. H.; Gallardo, H.; Vieira, A. A. Investigation of Thermal and Luminescent Properties in 4,7-Diphenylethynyl-2,1,3-benzothiadiazole Systems. *Liq. Cryst.* **2018**, *45*, 49−58.
(28) The molecular weight as well as degree of hydrolysis of the PVA matrix do not affect significantly the thermochromic behavior of the doped films but strongly affect their processability.
(29) O'Keefe, D. F.; Dannock, M. C.; Marcuccio, S. M. Palladium Catalysed Coupling of Halobenzenes with Arylboronic Acids: Role of the Triphenylphosphine Ligand. *Tetrahedron Lett.* **1992**, *33*, 6679−6680.
(30) Cardenas, J. C.; Aguirre-Díaz, L. M.; Galindo, J. F.; Alí-Torres, J.; Ochoa-Puentes, C.; Echeverri, M.; Gomez-Lor, B.; Monge, M. A.; Gutierrez-Puebla, E.; Sierra, C. A. Nature of Color Diversity in Phenylenevinylene-Based Polymorphs. *Cryst. Growth Des.* **2019**, *19*, 3913−3922.
(31) Varughese, S. Non-covalent Routes to Tune the Optical Properties of Molecular Materials. *J. Mater. Chem. C* **2014**, *2*, 3499−3516.
(32) Yu, L. Polymorphism in Molecular Solids: An Extraordinary System of Red, Orange, and Yellow Crystals. *Acc. Chem. Res.* **2010**, *43*, 1257−1266.
(33) Liu, H.; Cheng, X.; Bian, Z.; Ye, K.; Zhang, H. Four Organic Crystals Displaying Distinctively Different Emission Colors Based on an ESIPT-active Organic Molecule. *Chin. Chem. Lett.* **2018**, *29*, 1537−1540.
(34) Milani, A.; Brambilla, L.; Del Zoppo, M.; Zerbi, G. Raman Dispersion and Intermolecular Interactions in Unsubstituted Thiophene Oligomers. *J. Phys. Chem. B* **2007**, *111*, 1271−1276.
(35) Mosca, S.; Milani, A.; Pena-Alvarez, M.; Yamaguchi, S.; Hernandez, V.; Ruiz Delgado, M. C.; Castiglioni, C. Mechanochromic Luminescent Tetrathiazolylthiophenes: Evaluating the Role of Intermolecular Interactions through Pressure and Temperature-Dependent Raman Spectroscopy. *J. Phys. Chem. C* **2018**, *122*, 17537−17543.
(36) Milani, A.; Del Zoppo, M.; Tommasini, M.; Zerbi, G. The Effect of Intermolecular Dipole−Dipole Interaction on Raman Spectra of Polyconjugated Molecules: Density Functional Theory Simulations and Mathematical Models. *J. Phys. Chem. B* **2008**, *112*, 1619−1625.
(37) Dong, Y.; Xu, B.; Zhang, J.; Tan, X.; Wang, L.; Chen, J.; Lv, H.; Wen, S.; Li, B.; Ye, L.; Zou, B.; Tian, W. Piezochromic Luminescence Based on the Molecular Aggregation of 9,10-Bis((E)-2-(pyrid-2-yl)vinyl)anthracene. *Angew. Chem., Int. Ed.* **2012**, *51*, 10782−10785.
(38) Harada, N.; Abe, Y.; Karasawa, S.; Koga, N. Polymorphic Equilibrium Responsive Thermal and Mechanical Stimuli in Light-emitting Crystals of N-Methylaminonaphthyridine. *Org. Lett.* **2012**, *14*, 6282−6285.
(39) He, Z.; Zhang, L.; Mei, J.; Zhang, T.; Lam, J. W. Y.; Shuai, Z.; Dong, Y. Q.; Tang, B. Z. Polymorphism-Dependent and Switchable Emission of Butterfly-Like Bis(diarylmethylene)dihydroanthracenes. *Chem. Mater.* **2015**, *27*, 6601−6607.
(40) Seki, T.; Ito, H. Molecular-Level Understanding of Structural Changes of Organic Crystals Induced by Macroscopic Mechanical Stimulation. *Chem. - Eur. J.* **2016**, *22*, 4322−4329.
(41) Zhang, G.; Lu, J.; Sabat, M.; Fraser, C. L. Polymorphism and Reversible Mechanochromic Luminescence for Solid-State Difluoroboron Avobenzone. *J. Am. Chem. Soc.* **2010**, *132*, 2160−2162.
(42) Yuan, M.-S.; Wang, D.-E.; Xue, P.; Wang, W.; Wang, J.-C.; Tu, Q.; Liu, Z.; Liu, Y.; Zhang, Y.; Wang, J. Fluorenone Organic Crystals: Two-Color Luminescence Switching and Reversible Phase Transformations between $\pi-\pi$ Stacking-Directed Packing and Hydrogen Bond-Directed Packing. *Chem. Mater.* **2014**, *26*, 2467−2477.
(43) Wang, C.; Li, Z. Molecular Conformation and Packing: their Critical Roles in the Emission Performance of Mechanochromic Fluorescence Materials. *Mater. Chem. Front.* **2017**, *1*, 2174−2194.
(44) Jin, M.; Sumitani, T.; Sato, H.; Seki, T.; Ito, H. Mechanical-Stimulation-Triggered and Solvent-Vapor-Induced Reverse Single-Crystal-to-Single-Crystal Phase Transitions with Alterations of the Luminescence Color. *J. Am. Chem. Soc.* **2018**, *140*, 2875−2879.
(45) Seki, T.; Sakurada, K.; Ito, H. Controlling Mechano- and Seeding-Triggered Single-Crystal-to-Single-Crystal Phase Transition: Molecular Domino with a Disconnection of Aurophilic Bonds. *Angew. Chem., Int. Ed.* **2013**, *52*, 12828−12832.
(46) Jin, M.; Seki, T.; Ito, H. Mechano-Responsive Luminescence via Crystal-to-Crystal Phase Transitions between Chiral and Non-Chiral Space Groups. *J. Am. Chem. Soc.* **2017**, *139*, 7452−7455.
(47) Ge, C.; Liu, J.; Ye, X.; Han, Q.; Zhang, L.; Cui, S.; Guo, Q.; Liu, G.; Liu, Y.; Tao, X. Visualization of Single-Crystal-to-Single-Crystal Phase Transition of Luminescent Molecular Polymorphs. *J. Phys. Chem. C* **2018**, *122*, 15744−15752.
(48) Liu, B.; Di, Q.; Liu, W.; Wang, C.; Wang, Y.; Zhang, H. Red-Emissive Organic Crystals of a Single-Benzene Molecule: Elastically Bendable and Flexible Optical Waveguide. *J. Phys. Chem. Lett.* **2019**, *10*, 1437−1442.
(49) Krishna, G. R.; Devarapalli, R.; Prusty, R.; Liu, T.; Fraser, C. L.; Ramamurty, U.; Reddy, C. M. Structure-Mechanical Property Correlations in Mechanochromic Luminescent Crystals of Boron Difluoride Dibenzoylmethane Derivatives. *IUCrJ* **2015**, *2*, 611−619.
(50) Ciardelli, F.; Ruggeri, G.; Pucci, A. Dye-Containing Polymers: Methods for Preparation of Mechanochromic Materials. *Chem. Soc. Rev.* **2013**, *42*, 857−870.
(51) Seeboth, A.; Lotzsch, D.; Ruhmann, R.; Muehling, O. Thermochromic Polymers—Function by Design. *Chem. Rev.* **2014**, *114*, 3037−3068.
(52) Calvino, C.; Guha, A.; Weder, C.; Schrettl, S. Self-Calibrating Mechanochromic Fluorescent Polymers Based on Encapsulated Excimer-Forming Dyes. *Adv. Mater.* **2018**, *30*, 1704603.
(53) Eral, H. B.; O'Mahony, M.; Shaw, R.; Trout, B. L.; Myerson, A. S.; Doyle, P. S. Composite Hydrogels Laden with Crystalline Active Pharmaceutical Ingredients of Controlled Size and Loading. *Chem. Mater.* **2014**, *26*, 6213−6220.
(54) Diao, Y.; Helgeson, M. E.; Siam, Z. A.; Doyle, P. S.; Myerson, A. S.; Hatton, T. A.; Trout, B. L. Nucleation under Soft Confinement: Role of Polymer−Solute Interactions. *Cryst. Growth Des.* **2012**, *12*, 508−517.
(55) Diao, Y.; Helgeson, M. E.; Myerson, A. S.; Hatton, T. A.; Doyle, P. S.; Trout, B. L. Controlled Nucleation from Solution Using Polymer Microgels. *J. Am. Chem. Soc.* **2011**, *133*, 3756−3759.
(56) Ha, J.-M.; Wolf, J. H.; Hillmyer, M. A.; Ward, M. D. Polymorph Selectivity under Nanoscopic Confinement. *J. Am. Chem. Soc.* **2004**, *126*, 3382−3383.

CHEMISTRY OF MATERIALS
Cite This: Chem. Mater. 2019, 31, 6971−6978
Article
pubs.acs.org/cm

Effect of the Linkage Position on the Conjugation Length of Truxene-Based Porous Polymers: Implications for Their Sensing Performance of Nitroaromatics

Marcelo Echeverri,[†] Sergio Gamez-Valenzuela,[‡] Rafael C. Gonzalez-Cano,[‡] Jordy Guadalupe,[†,§] Sandra Cortijo-Campos,[†] Juan Teodomiro Lopez Navarrete,[‡] Marta Iglesias,*[,†] M. Carmen Ruiz Delgado,*[,‡] and Berta Gomez-Lor*[,†]

[†]Instituto de Ciencia de Materiales de Madrid, CSIC, C/Sor Juana Ines de la Cruz 3, Cantoblanco, Madrid 28049, Spain
[‡]Department of Physical Chemistry, University of Malaga, Campus de Teatinos s/n, 29071 Malaga, Spain

Supporting Information

ABSTRACT: Four highly porous truxene-based organic polymers have been synthesized via C−C cross coupling methodologies (under Yamamoto and Suzuki−Miyaura conditions) starting from two different brominated hexamethyltruxene isomers (2,7,12- and 3,8,13-tribromohexamethyltruxene). We have found that the linkage position in these polymers has a strong influence not only on the porosity but also on the absorption and light emitting properties of the final materials. We have performed a joint theoretical and experimental investigation to shed light on the role of the positional isomeric effect of the monomers on the degree of π-conjugation of the final materials. Our study indicates that the 2,7,12 linkage significantly enhances the electronic communication between the covalently linked building units, thus strongly influencing the conjugation length and the position of the energy levels of the final materials. The result of this work provides us with a new design tool to fine-tune the electronic properties of conjugated porous polymers with important implications for their potential applications, as demonstrated by their sensing performance for the detection of nitroaromatic compounds.

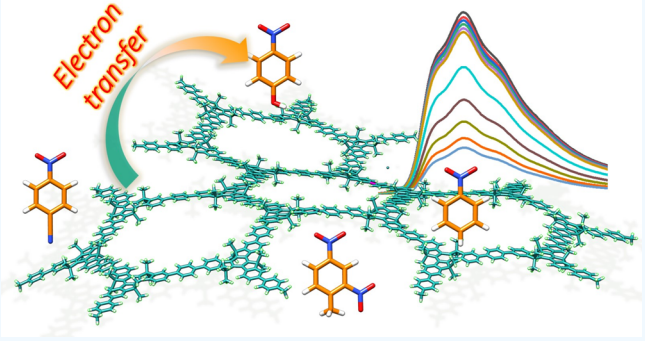

INTRODUCTION

In recent years, considerable attention has been paid to the design and synthesis of porous organic materials, built up from organic building units covalently linked. These materials have found utilities in fields such as adsorption, separation, or catalysis by virtue of their high thermal and chemical stability and permanent surface area.[1,2] On the other hand, the combination of the porous character of these polymers with the inherent functionality of the organic building blocks has enormously broadened their potential applications. Representative examples are porous π-conjugated polymers[3,4] that have emerged as promising candidates for organic electronics,[5] photocatalysis,[6] sensing,[7−13] or energy applications[14] by taking advantage of the light emitting or semiconducting properties of the constituent monomers and of the extended three-dimensional conjugation of the resultant polymers. Multiple synthetic protocols ranging from metal-mediated couplings (Suzuki−Miyaura, Yamamoto, Sonogashira, Heck, etc.) to acid- or base-catalyzed polycondensation reactions or trimerizations have been used for the generation of conjugated porous polymers,[3] allowing for great control of the nature of the linker groups and of the effective conjugation length of the resultant polymers. However, while many efforts have been provided to modulate the electronic properties of these polymers through the convenient choice of the bridging connectors,[15,16] the effect of the linker position on such properties has been very scarcely investigated.[17−19]

Among the plethora of π-conjugated molecules with light emitting or semiconducting properties that have been used as monomers in the construction of conjugated porous polymers, we and others have recently become interested in heptacyclic truxene, which can be considered as a 1,3,5-triphenylbenzene planarized through three bridging methylenes.[20,21] These methylene groups give rise to three additional fused five-membered rings (Scheme 1), thus enhancing the delocalization of the π-system, which confers upon this molecule interesting photoactive properties and excellent electron donating capabilities.[22] Curiously, in contrast to the structurally related 1,3,5-triphenylbenzene, truxene has been very scarcely explored as a building block in the construction of porous organic polymers.

Special Issue: Jean-Luc Bredas Festschrift

Received: April 11, 2019
Revised: July 1, 2019
Published: July 2, 2019

DOI: 10.1021/acs.chemmater.9b01432
Chem. Mater. 2019, 31, 6971−6978

Scheme 1. Synthesis of Tx2-CMP, Tx3-CMP, PhTx2-CMP, and PhTx3-CMP Based on Heptacyclic Truxene (black)

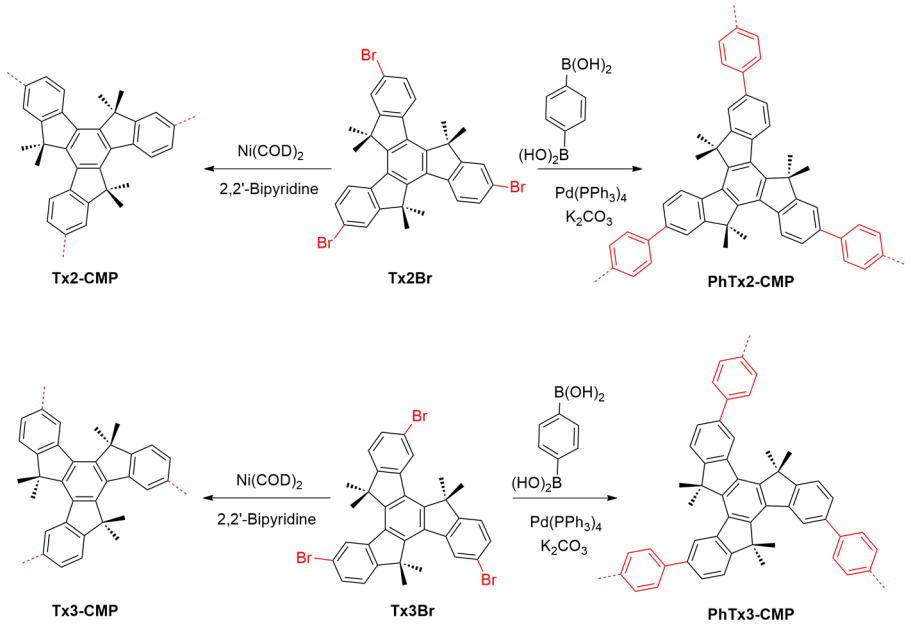

Herein, we report the synthesis of four truxene-based large-surface area porous organic polymers by starting from two different tribromohexamethyltruxene isomers [2,7,12- and 3,8,13-tribromohexamethyltruxene, named **Tx2Br** and **Tx3Br**, respectively (Scheme 1)]. The preorganization of the bromofunctional groups will direct the growth of the polymers in different directions via different C−C cross coupling methodologies (under Yamamoto and Suzuki−Miyaura conditions). Figure 1 shows the idealized structure of the expected polymers. We have found that the optoelectronic properties of both homocoupled polymers [**Tx2-CMP** and **Tx3-CMP** (see Scheme 1)] and those with truxene units connected through phenylene spacers [**PhTx2-CMP** and **PhTx3-CMP** (see Scheme 1)] are greatly affected by the position of the linkers. The effect of linkage position on the electronic properties of these polymers has been rationalized through a combined Raman spectroscopy and density functional theory (DFT) study.

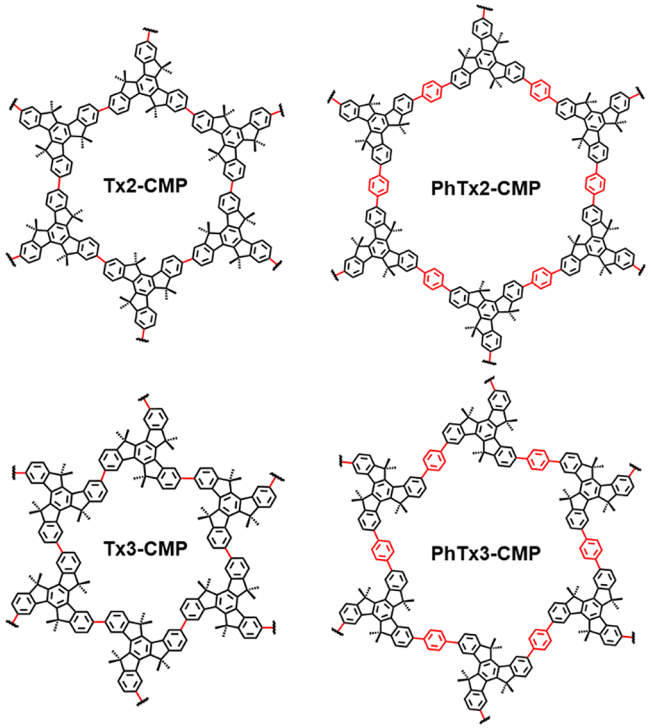

Figure 1. Idealized structures of **Tx2-CMP**, **Tx3-CMP**, **PhTx2-CMP**, and **PhTx3-CMP**.

The results of this work open the door to the control of the degree of π-conjugation and therefore the optoelectronic properties of these materials via engineering substituent position effects, with important implications for their potential applications, as highlighted by the different sensing behavior of these polymers toward nitroaromatic compounds.

RESULTS AND DISCUSSION

Synthesis and Characterization. The synthesis of the monomers 2,7,12-tribromohexamethyltruxene (**Tx2Br**)[23] and 3,8,13-tribromohexamethyltruxene (**Tx3Br**) was performed in just two steps starting from commercially available 6- and 5-bromoindanone. Thus, cyclotrimerization of 6- and 5-bromoindanone mediated by *p*-toluenesulfonic and propionic acid cyclotrimerization rendered 2,7,12-tribromotruxene[24] and 3,8,13-tribromotruxene,[25] respectively. Subsequent treatment of truxenes with KO^{t}Bu and alkylation with MeI yielded **Tx2Br**[23] and **Tx3Br** in excellent yields.

Homocoupled polymers (**Tx2-CMP** and **Tx3-CMP**) were obtained by bis(cyclooctadiene)nickel(0) [Ni(COD)$_2$]-catalyzed self-condensation of the differently substituted monomers under Yamamoto conditions. On the other hand, palladium-catalyzed Suzuki−Miyaura cross coupling between the tribromohexamethyltruxenes and benzene 1,4-diboronic acid under microwave heating conditions[26] rendered polymers **PhTx2-CMP**[27] and **PhTx3-CMP**, in which the building units are separated by phenylene linkers (see Scheme 1). After filtration and thorough washing with H_2O, aqueous diluted acids, and different organic solvents, the four polymers where obtained in good yields as whitish amorphous solids.

DOI: 10.1021/acs.chemmater.9b01432
Chem. Mater. 2019, 31, 6971−6978

The chemical composition and connectivity of the polymeric solids were investigated by Fourier transform infrared (FT-IR), elemental analysis, and solid-state ^{13}C cross-polarization magic angle spinning (CP-MAS) nuclear magnetic resonance (NMR).

In the FT-IR spectra of the four polymers (Figure S1), it is possible to observe a number of bands around 1606 and 2927 cm^{-1} that could be assigned to aromatic C=C and C−H bonds, respectively, and are attributed to the vibrations of the truxene skeleton and the phenylene linker. The absorption peaks for the C−H bending of the aromatic ring are observed around 816 cm^{-1}. Elemental analyses of the truxene-based polymers are presented in the Supporting Information (Table S1) showing values for C and H slightly lower than the calculated values. This can be attributed to some residual occluded solvent in the pores or incomplete combustion of the polymers, which is common in porous polymers.[28]

The solid ^{13}C CP-MAS NMR spectra of the four polymers exhibit a peak at 23 ppm in the aliphatic region and another peak at 47 ppm, which are ascribed to the methyl and methylene carbons of the truxene, respectively. In the aromatic region, all of the spectra show a group of signals between 120 and 135 ppm, assigned to the aromatic C carbons of the truxene and of the phenylene linkers in the case of **PhTx2-CMP** and **PhTx3-CMP**, and three signals between 140 and 155 ppm attributed to the quaternary aromatic carbons of the truxene units, which are slightly downfield shifted in the polymers with the truxene connected through the 2, 7, and 12 positions when compared to those connected through the 3, 8, and 13 positions (Figure S2).

All polymers showed high thermal stability with a decomposition pattern in two steps (Figure S3), the first one attributed to the loss of the methyl groups and a second one at higher temperature due to generalized polymer degradation. Curiously, polymers **Tx2-CMP** and **Tx3-CMP** with directly connected truxene units are significantly more stable than those connected through phenylene moieties **PhTx2-CMP** and **PhTx3-CMP**.

The accessible surface areas and pore size distributions were determined by Brunauer−Emmett−Teller (BET) analysis at 77 K under nitrogen (Table 1 and Figures S4 and S5). The N_2 adsorption analyses yield surface areas (calculated in the relative pressure range from 0.01 to 0.1) of 1167 and 520 $m^2\ g^{-1}$ for homocoupled polymers **Tx2** and **Tx3-CMP**, respectively, and 700 and 588 $m^2\ g^{-1}$ for phenylene-connected polymers **PhTx2-CMP** and **PhTx3-CMP**, respectively. The adsorption isotherms exhibit high rates of uptake at low relative pressures with a continuous increase and a broad hysteresis upon desorption[29] (note that the hysteresis down to low pressures indicates a trapping effect). Apparently, linking the truxene building units through the 2, 7, and 12 positions gives rise to larger surface areas, which can be rationalized if we observe the idealized porous structure of the polymers (see Scheme 1) as the 2,7,12-substitution of the C_3 symmetrical building units would give rise to more regular round-shaped porous. This trend is also observed when we compare the average pore volumes of the four polymers because higher values are observed in 2,7,12-linked polymers versus the 3,8,13-linked analogues (0.94 and 0.47 $cm^3\ g^{-1}$ for **Tx2-CMP** and **Tx3-CMP**, respectively, and 0.38 and 0.46 $cm^3\ g^{-1}$ for **PhTx2-CMP** and **PhTx3-CMP**, respectively).

Table 1. Porous Properties of Truxene-Based Porous Polymers under Study

	SA_{BET}[a] ($m^2\ g^{-1}$)	pore volume ($cm^3\ g^{-1}$)[b]	pore size (nm)[c]
Tx2-CMP	1167.4	0.94	3.23
Tx3-CMP	520.1	0.38	2.92
PhTx2-CMP	700.7	0.47	2.65
PhTx3-CMP	588.3	0.46	3.10

[a]BET surface area calculated from the nitrogen adsorption isotherm. [b]At a P/P_0 ratio of 0.99. [c]Average pore size calculated by N-DFT methods.

The morphology of the polymers is characterized in all cases by the formation of agglomerates of small particles showing a globular shape (see Figure S6), as could be determined by scanning electron microscopy (SEM). This is a common morphology displayed by porous polymers. On the other hand, the X-ray diffractograms of the polymers present the broad halo characteristic of disordered structures confirming their amorphous character (see Figure S7).

Electronic Properties. As we can observe in Figure 2, via comparison of the ultraviolet (UV) absorption and fluorescence spectroscopy of the four polymers in CH_2Cl_2 suspensions, the linkage position has also a strong influence on the optoelectronic properties of these truxene-based polymers. The spectra show a broad structure, with largely red-shifted tails, especially for **Tx2-CMP** and **PhTx2-CMP** polymers, which can be ascribed to their large polydispersity. Interestingly, when the truxene units are connected through the 2, 7, and 12 positions, both absorption and fluorescence spectra are significantly red-shifted when compared with those of the polymers connected through the 3, 8, and 13 positions. The insertion of phenylene spacers between the truxene units has only a weak influence on the optoelectronic properties of these truxene-based polymers, resulting in absorption and emission maxima very similar to those found in the homocoupled polymers in polymers connected through the 3, 8, and 13 positions while moderate blue-shifted bands are found in aryl-spaced polymers linked through the 2, 7, and 12 positions. On the other hand, solid-state ultraviolet−visible diffuse reflectance (UV-DRS) experiments performed to estimate the HOMO−LUMO gap of the four polymers show that band gap energies are slightly larger for polymers **Tx3-CMP** and **PhTx3-CMP** (3.42 and 3.53 eV, respectively) than for **Tx2-CMP** and **PhTx2-CMP** (3.10 and 3.33 eV, respectively) as estimated using the Kubelka−Munk function (Figure S9).

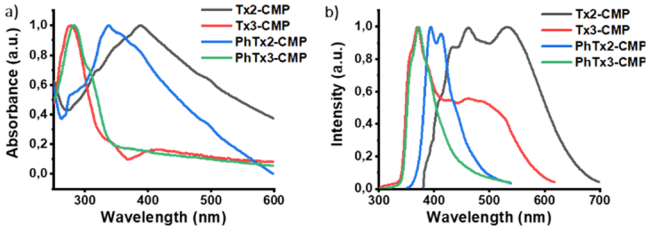

Figure 2. (a) Normalized experimental UV absorption and (b) emission spectra of **Tx2-CMP**, **Tx3-CMP**, **PhTx2-CMP**, and **PhTx3-CMP** porous polymers.

Curiously, the fluorescence spectra of homopolymers **Tx3-CMP** and **Tx2-CMP** show a broad structureless band in addition to the main band that can be ascribed to some degree of aggregation of the truxene units, which suggest that the presence of flexible aryl spacers in **PhTx2-CMP** and **PhTx3-CMP** prevents chromophore aggregation. Note that truxene derivatives have a strong tendency to self-assemble both in solution

DOI: 10.1021/acs.chemmater.9b01432
Chem. Mater. 2019, 31, 6971−6978

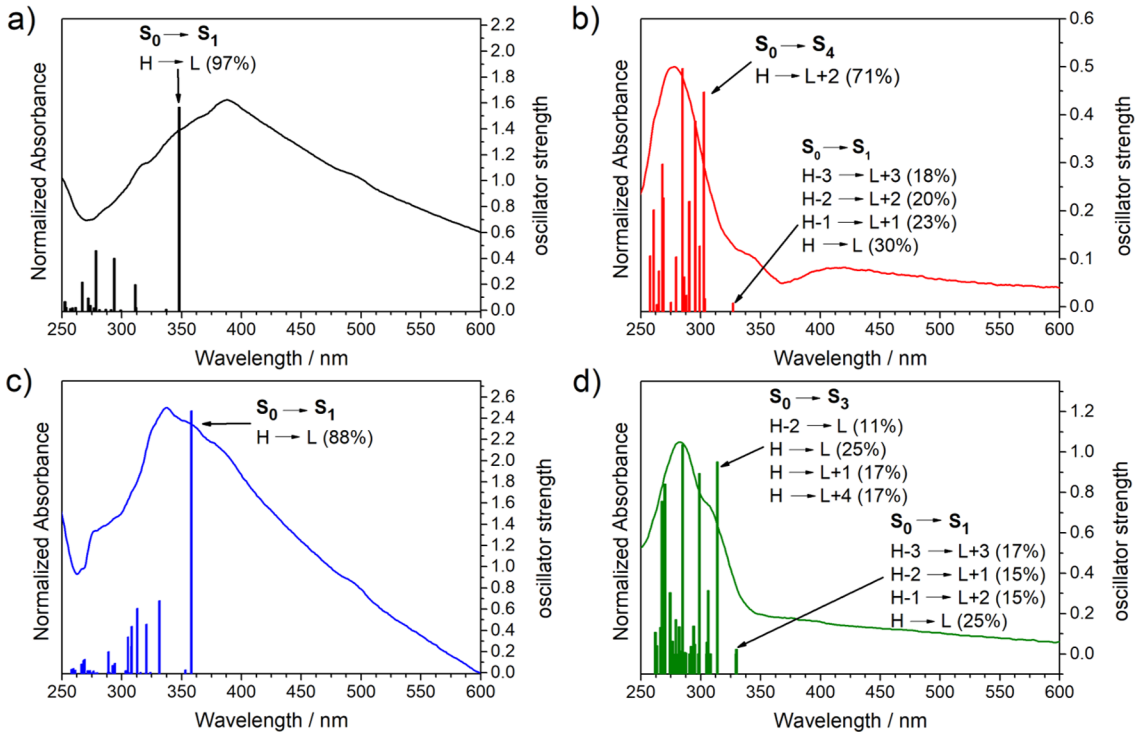

Figure 3. Comparison between the experimental UV absorption spectra of (a) **Tx2-CMP**, (b) **Tx3-CMP**, (c) **PhTx2-CMP**, and (d) **PhTx3-CMP** porous polymers and the vertical excited-state transitions (solid bars) calculated at the TD-DFT//B3LYP/6-31G** level for their respective dimeric models. The compositions of the frontier molecular orbitals involved in the main transitions are also shown.

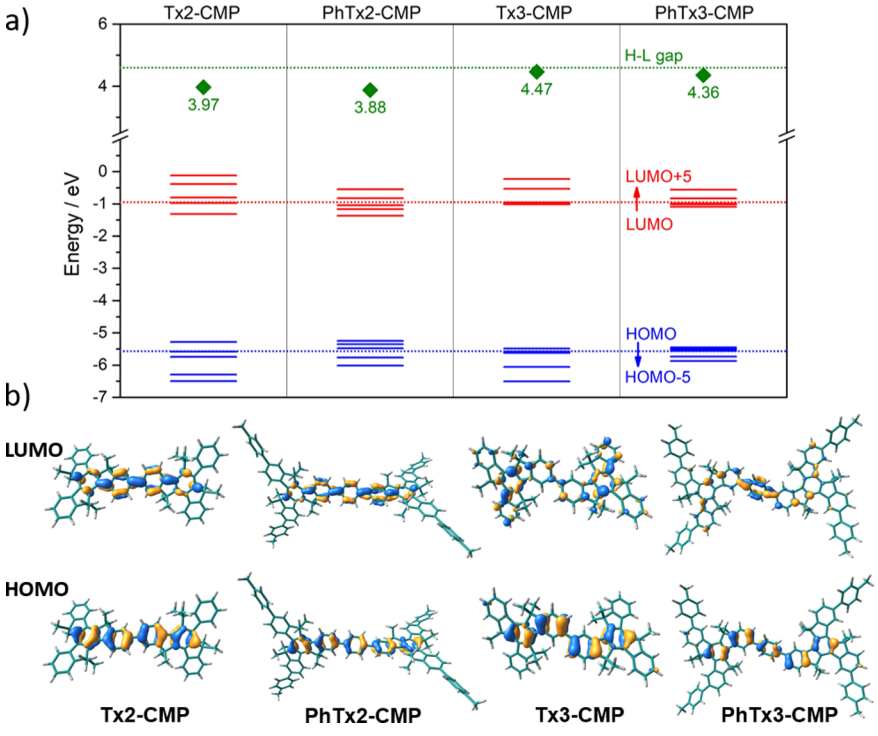

Figure 4. (a) DFT-calculated molecular orbital energies (B3LYP/6-31G** level) for the dimeric models of the truxene-based polymers, in comparison with those calculated for the hexamethyl truxene Tx system (dotted lines). (b) Topologies of the HOMO and LUMO orbitals.

and in the condensed phase, which usually has a strong influence on their optical properties.[30−32]

DFT Calculations. To understand the origin of the differences exerted by the linkage position, we have performed a theoretical study of four dimeric models in which two truxene units are linked with or without a phenylene spacer through the two different positions under study (see the Supporting Information). TD-DFT calculations help us to shed light on how this factor influences the effective conjugation length of the polymers by analyzing the electronic nature of the main

DOI: 10.1021/acs.chemmater.9b01432
Chem. Mater. 2019, 31, 6971−6978

absorption bands. As shown in Figure 3, the TD-DFT vertical excitation energies reproduce very well the experimental red-shifting observed when comparing the absorption spectra of polymers connected through the 2, 7, and 12 positions with those linked through the 3, 8, and 13 positions. Note that the most intense absorption band for the 2,7,12-dimers corresponds to an $S_0 \rightarrow S_1$ transition that is assigned to a HOMO−LUMO one-electron promotion, while that in the 3,8,13-dimers is assigned to a combination of one-electron excitations between ground state S_0 and different excited states of higher energies (the intensity of the $S_0 \rightarrow S_1$ transition is very low). These results are in good accordance with (i) the decrease in the HOMO−LUMO gap when the linkage position between adjacent truxene units is varied from the 3,8,13 to the 2,7,12 connections [4.47 eV in the **Tx3** dimer and 3.97 eV in the **Tx2** dimer (see Figure 4a)] and (ii) the near degeneracy adopted for HOMO, HOMO−1, and HOMO−2 orbitals and LUMO, LUMO+1, and LUMO+2 orbitals in dimers connected through the 3, 8, and 13 positions. The reduction of the HOMO−LUMO gap can be ascribed to the better extension of the π-conjugation observed in the HOMO and LUMO orbitals of the **Tx2-CMP** model when compared to that of **Tx3-CMP**. As one can see in Figure 5b, the

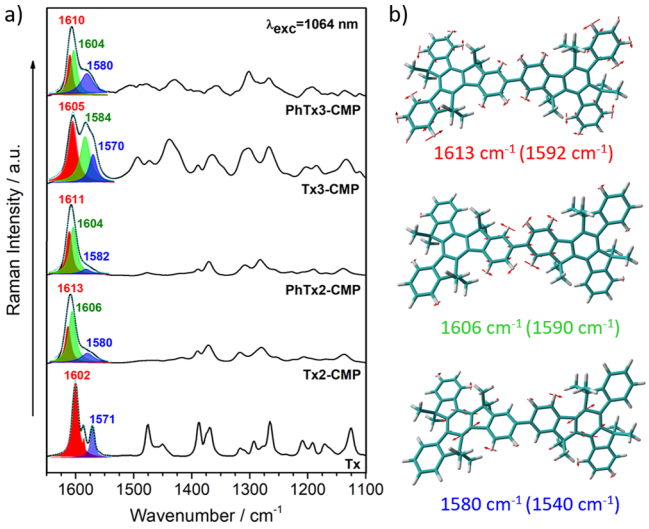

Figure 5. (a) FT-Raman spectra for the truxene-based porous polymers and for the hexamethyl truxene **Tx** monomer system, in the solid state. Deconvolution of the 1570−1610 cm^{-1} Raman band into three distinct peaks based on Lorentzian fitting is shown. (b) B3LYP/6-31G** vibrational eigenvectors associated with the most outstanding C═C/C−C Raman features of **Tx2-CMP**. The experimental and theoretical (in parentheses) wavenumbers are also shown.

HOMO and LUMO orbitals of the **Tx2-CMP** model spread over the six central rings, which includes the adjacent *para*-connected fluorene units of each truxene unit. In contrast, the connection of truxene units at the *meta* positions (3,8,13 connections) does not allow for direct conjugation, and the pathway of alternating single and double bonds extends only through the two directly connected central phenyl rings. The small electronic delocalization found in the **Tx3-CMP** model is in consonance with the fact that its HOMO and LUMO energy levels are very similar to those found for the hexamethyl truxene monomer (see Figure 4a). A similar reduction in the HOMO−LUMO gap is found by comparing the phenyl-substituted systems with different linkage positions [i.e., HOMO−LUMO gap values decrease from 4.36 to 3.88 eV going from **PhTx3-CMP** to **PhTx2-CMP** models, respectively (see Figure 4a)]. These results follow the same trends as the values experimentally observed when varying the linkage position from *meta* (3,8,13) to *para* (2,7,12) connections and reflect an increase in the conjugation length along the truxene backbones.

On the other hand, the insertion of a phenylene spacer between the truxene units affects only slightly the position of the TD-DFT-calculated vertical electronic transitions and the HOMO−LUMO gap when compared to those of the homocoupled dimeric systems (see Figure 3). This suggests that the insertion of phenylene bridges barely affects the π-electron delocalization between the truxene units; this might be related to their moderately distorted configuration [note that the dihedral angles calculated between the truxene and phenyl bridges are ∼38° (see the Supporting Information)].

Vibrational Properties. Raman spectroscopy is a fast, high-resolution, and nondestructive characterization tool that has been widely used to explore the electronic properties of π-conjugated materials. This suitability resides on the selective enhancement of the C═C/C−C stretching vibrations related with the one-dimensional path of π-electrons due to the strong electron−phonon coupling of the π-conjugated systems.[33,34] In this sense, Raman spectroscopy can provide relevant information about the electronic coupling between covalently connected conjugated moieties and the effective π-conjugation length in polymers.[35−37]

Figure 5 compares the FT-Raman spectra of the four porous polymers and the hexamethyl truxene **Tx** monomer. Interestingly, the Raman bands collected in the 1500−1600 cm^{-1} region, which are related with the C═C/C−C stretching modes, are selectively enhanced in the spectra. When compared to that of the **Tx** monomer, a band broadening of the strongest Raman band is observed in the polymers due to the higher conformational flexibility. In addition, an increase in the intensity of the CC stretching modes with respect to the rest of the bands recorded below 1500 cm^{-1} is found in the polymers, which reflects better electronic communication when compared to that of the monomers (see the Supporting Information); this is especially relevant in the case of **PhTx2-CMP** and **Tx2-CMP** as a result of the better electronic communication between the covalently linked moieties through the 2,7,12 connections than through the 3,8,13 connections.

It was possible to deconvolute the 1570−1610 cm^{-1} Raman band for the four porous polymers into distinct peaks by fitting with a Lorentzian function. With the help of the DFT calculations, the three different peak contributions are assigned to the same CC stretching mode (i.e., mode 8a of benzene[38]) but located in different rings. The band at the highest frequencies (related to the experimental signal at ∼1610 cm^{-1}, colored red) involves the external benzene rings. The band at intermediate frequencies (experimentally observed at ∼1605 cm^{-1}, colored green) corresponds to the covalently linked external benzene rings. The band observed at lower frequencies is localized in the internal benzene ring of each truxene unit (experimentally observed at ∼1580 cm^{-1}, colored blue). With these considerations, the experimental I_{1610}/I_{1580} intensity ratio can serve as a measure to estimate the effectiveness of the conjugation along the structures. As this ratio increases, the conjugation becomes more efficient.[16,39] If we compare all of the polymers, we can observe that **Tx2-CMP** and **PhTx2-CMP** give the highest intensity ratio while the lower ratio is obtained for **Tx3-CMP**. This indicates that polymers in which truxene units are covalently linked in *para* positions are much better

DOI: 10.1021/acs.chemmater.9b01432
Chem. Mater. 2019, 31, 6971−6978

conjugated than their *meta*-substituted isomers, in good accordance with the conclusions previously obtained in the electronic analysis.

Sensing of Nitroaromatics. One of the most appealing applications of π-conjugated porous polymers is the detection of analytes of interest.[7−13] Inspired by the pioneering work by Swager on their linear π-conjugated counterparts,[40] electron rich light-emitting porous conjugated polymers have aroused much interest as sensors of electron deficient compounds (such as nitroaromatics). The persistent porosity that characterizes these polymers facilitates the confinement and the close contact of the analyte with the photofunctional organic unit, thus resulting in an enhanced optical response.[7−13]

We have evaluated the potential use of the truxene-based polymers for the detection of electron deficient nitroaromatics (analytes of relevance for sectors that go from security to human health)[41] to determine the implication of the different linkage position on their sensing performance. With this goal in mind, the variation of the fluorescence spectra of polymers **PhTx2-CMP** and **PhTx3-CMP** suspended in CH_2Cl_2 were recorded in the presence of a constant concentration (100 μM) of *p*-nitrobenzonitrile (**NBN**), dinitrotoluene (**DNT**), *p*-nitrobenzene (**NB**), and *p*-nitrophenol (**NP**). Experiments were performed on **PhTx2-CMP** and **PhTx3-CMP**, as the aggregation observed in the fluorescence spectra of suspended homopolymers **Tx2-CMP** and **Tx3-CMP** may complicate the interpretation of the results. Changes in the spectra of **PhTx3-CMP** are much more important than those observed for polymer **PhTx2-CMP**. In this case, only **NP** showed a significant quenching efficiency (Figure 6a).

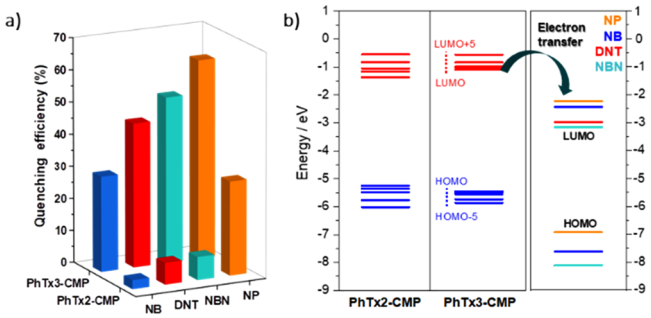

Figure 6. (a) Quenching efficiencies of **PhTx2-CMP** and **PhTx3-CMP** with **NB**, **DNT**, **NBN**, and **NP** at 100 μM. (b) DFT-calculated molecular orbital energies (B3LYP/6-31G** level) for the dimeric models of the truxene-based polymers **PhTx2-CMP** and **PhTx3-CMP**, in comparison with the orbital energies of the analytes.

Note that fluorescence quenching of electron rich π-conjugated porous polymers by electron deficient analytes is often achieved through a photoinduced electron transfer (PET) mechanism, in which electron deficient species act as electron acceptors for photoexcited electrons of the polymers (see Figure 6b). Therefore, the larger the difference between the fluorophore and the guest LUMO levels, the most favorable the electron transfer process will be.[42] With these considerations in mind, the superior quenching response to the nitroaromatic analytes exhibited by **TxPh3-CMP** can be understood in terms of LUMO energy levels; i.e., the higher LUMO of the polymer **TxPh3-CMP** in comparison to that of **TxPh2-CMP** would result in a more exergonic electron transfer to the LUMO of the analytes.

Titration of the polymer suspensions with increasing amounts (0−350 μM) of the different nitroaromatics and analysis of the quenching data using the Stern−Volmer equation $I_o/I = 1 + K_{SV}[Q]$ [which provides a quantitative relationship between the changes in fluorescence intensity (I_o/I) and the concentration of added nitroaromatic compounds ([Q])] confirmed these initial observations (See Figure 7). Stern−Volmer binding constants

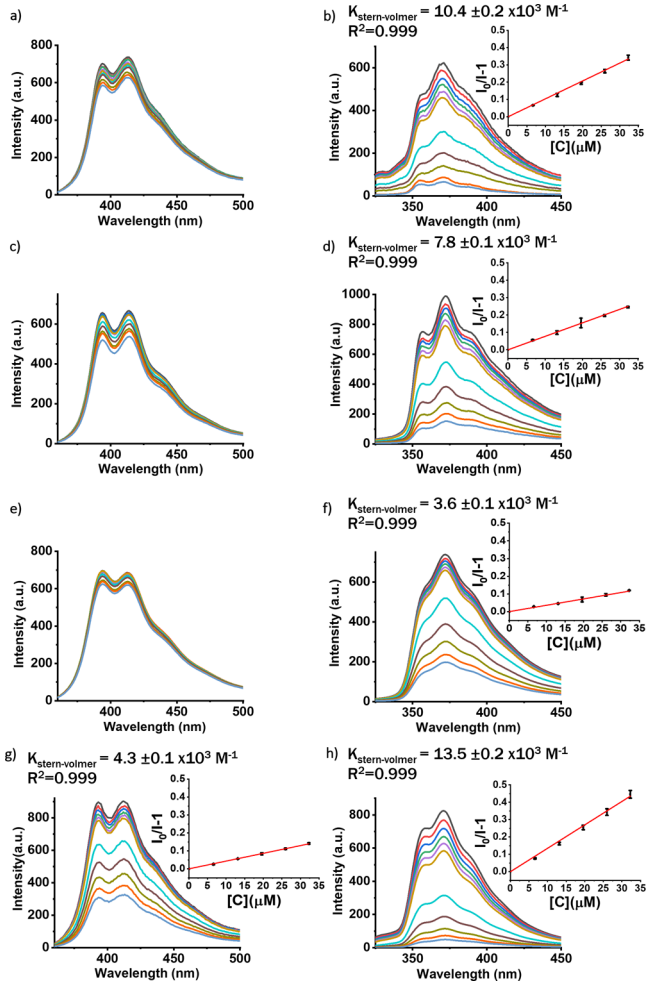

Figure 7. Fluorescence spectral changes of **PhTx2-CMP** (left) and **PhTx3-CMP** (right) upon addition of increasing amounts (0−350 μM) of (a and b) **NBN**, (c and d) **DNT**, (e and f) **NB**, and (g and h) **NP**. The insets show the corresponding Stern−Volmer plots with standard deviations.

for **PhTx3-CMP** toward **NP**, **NBN**, **DNT**, and **NB** were 13.5×10^3, 10.4×10^3, 7.8×10^3, and 3.6×10^3 M^{-1}, respectively, while the K_{SV} for **PhTx2-CMP** toward **NP** was 4.3×10^3 M^{-1}.

The detection limits (LODs) calculated using the equation LOD = $3\sigma/\rho$ (σ is the standard deviation of blank measurements of the polymer suspension, and ρ is the slope of the calibration curve of relative fluorescent intensity vs sample concentration) were in all cases in the micromolar range (see Table 2)

As one can observe, the calculated constant values for the different analytes follow the order **NP** > **NBN** > **DNT** > **NB** for **PhTx3-CMP**. The trend observed when going from **NBN** to **NB** can be rationalized again on the basis of a PET mechanism (Figure 6b). The lower the LUMO level of the analyte, the greater the difference between the fluorophore and the guest and therefore the more favored the electron transfer. However, the

DOI: 10.1021/acs.chemmater.9b01432
Chem. Mater. 2019, 31, 6971−6978

Table 2. Stern−Volmer Constants and Detection Limits of PhTx2-CMP and PhTx3-CMP for *p*-Nitrobenzonitrile (NBN), Dinitrotoluene (DNT), *p*-Nitrobenzene (NB), and *p*-Nitrophenol (NP)

analyte	polymer	K_{SV} ($\times 10^3$ M^{-1})	COD[a]	LOD[b] (μM)
NP	**PhTx2-CMP**	4.3 ± 0.1	0.999	5.3
	PhTx3-CMP	13.5 ± 0.2	0.999	2.8
NBN	**PhTx3-CMP**	10.4 ± 0.2	0.999	3.4
DNT	**PhTx3-CMP**	7.8 ± 0.1	0.999	4.1
NB	**PhTx3-CMP**	3.6 ± 0.1	0.999	8.2

[a]Coefficient of determination (R^2). [b]Limit of detection.

higher sensitivity to the less electron deficient **NP** indicates that a PET mechanism is not the only governing factor responsible for fluorescence quenching in this case. In fact, comparison of the absorption spectra of the different analytes with the fluorescence spectra of the two polymers shows some spectral overlap for **NP** (Figure S12). This suggests that for this particular analyte, some contribution of an energy transfer mechanism[42] might occur, thus explaining the higher efficiency observed for **NP** and its less pronounced sensitivity to the linking position of the fluorophore.

The sensitivities of the fluorescence spectra of these polymers to potential impurities coming from the synthetic protocols were evaluated by recording the variation of the fluorescence spectra of polymers **PhTx2-CMP** and **PhTx3-CMP** suspended in CH_2Cl_2, in the presence of a constant concentration (100 μM) of the different potential contaminants (DMF, THF, H_2O, HCl, HNO_3, etc.). We have observed no change in the fluorescence intensity; furthermore, we have found that these contaminants do not interfere with the sensing behavior as demonstrated by measuring the quenching efficiency of **NBN** in the presence or absence of these potential contaminants. In addition, we have also studied the variation of fluorescence in the presence of benzene and nitromethane finding no response, which indicates that it is necessary to have both an aromatic ring and a nitro group to guarantee the sensing behavior.

CONCLUSIONS

In summary, we have synthesized four stable truxene-based porous organic polymers (SA_{BET} = 520−1167 m^2 g^{-1}) by covalently linking the truxene monomers through the 2, 7, and 12 or 3, 8, and 13 positions, with or without a phenylene spacer. Both experimental (UV−vis absorption, fluorescence, and Raman spectroscopy) and theoretical results point to the fact that connecting the truxene monomers through the 2, 7, and 12 positions results in better electronic communication between the covalently linked building units, thus strongly influencing the extension on the conjugation, reducing the HOMO−LUMO gap and influencing the energy levels of the final materials. Interestingly, the strong influence that the positional connectivity exerts on the LUMO level of these polymers explains the different sensing behavior of these polymers toward nitroaromatic compounds. The results of this work highlight the importance of the linkage position as a new design tool for tuning the electronic properties of electroactive porous polymers for emerging real-life applications.

ASSOCIATED CONTENT

Supporting Information

The Supporting Information is available free of charge on the ACS Publications website at DOI: 10.1021/acs.chemmater.9b01432.

Methods, synthesis and characterization of the monomers and polymers, characterization of polymers, sensing of nitroaromatic compounds, and DFT calculations (PDF)

AUTHOR INFORMATION

Corresponding Authors

*E-mail: marta.iglesias@icmm.csic.es.
*E-mail: bgl@icmm.csic.es.
*E-mail: carmenrd@uma.es.

ORCID

Marcelo Echeverri: 0000-0002-9290-4546
Marta Iglesias: 0000-0001-7373-4927
M. Carmen Ruiz Delgado: 0000-0001-8180-7153
Berta Gomez-Lor: 0000-0002-2995-9624

Present Address

§J.G.: Instituto de Ciencia y Tecnologia de Polimeros, CSIC, C/ Juan de la Cierva 3, Madrid 28006, Spain.

Funding

MINECO of Spain (MAT2017-82288-C2-2-P and CTQ2016-78557-R), MINECO of Spain (CTQ2015-66897), and Junta de Andalucia (P09-FQM-4708).

Notes

The authors declare no competing financial interest.

ACKNOWLEDGMENTS

The work at the University of Malaga was funded by the MINECO (CTQ2015-66897) and Junta de Andaluc1a (P09-FQM-4708) projects. The authors thankfully acknowledge the computer resources, technical expertise, and assistance provided by the SCBI (Supercomputing and Bioinformatics) center of the University of Malaga. S.G.-V. thanks the MINECO for a FPU predoctoral fellowship (FPU 17/04908). The work at the CSIC was funded by the MINECO of Spain (MAT2017-82288-C2-2-P and CTQ2016-78557-R).

REFERENCES

(1) Jiang, J.-X.; Cooper, A. I. Microporous Organic Polymers: Design, Synthesis, and Function. In *Functional Metal-Organic Frameworks: Gas Storage, Separation and Catalysis*; Schroder, M., Ed.; Springer: Berlin, 2010; pp 1−33.
(2) Das, S.; Heasman, P.; Ben, T.; Qiu, S. Porous Organic Materials: Strategic Design and Structure−Function Correlation. *Chem. Rev.* **2017**, *117*, 1515−1563.
(3) Xu, Y.; Jin, S.; Xu, H.; Nagai, A.; Jiang, D. Conjugated microporous polymers: design, synthesis and application. *Chem. Soc. Rev.* **2013**, *42*, 8012−8031.
(4) Cooper, A. I. Conjugated Microporous Polymers. *Adv. Mater.* **2009**, *21*, 1291−1295.
(5) Bildirir, H.; Gregoriou, V.; Avgeropoulos, A.; Scherf, U.; Chochos, C. Porous Organic Polymers as Emerging New Materials for Organic Photovoltaic Applications: Current Status and Future Challenges. *Mater. Horiz.* **2017**, *4*, 546.
(6) Wong, Y. L.; Tobin, J. M.; Xu, Z.; Vilela, F. Conjugated porous polymers for photocatalytic applications. *J. Mater. Chem. A* **2016**, *4*, 18677−18686.
(7) Liu, X.; Xu, Y.; Jiang, D. Conjugated Microporous Polymers as Molecular Sensing Devices: Microporous Architecture Enables Rapid

Response and Enhances Sensitivity in Fluorescence-On and Fluorescence-Off Sensing. *J. Am. Chem. Soc.* **2012**, *134*, 8738−8741.
(8) Namgung, H.; Lee, J. J.; Gwon, Y. J.; Lee, T. S. Synthesis of tetraphenylethylene-based conjugated microporous polymers for detection of nitroaromatic explosive compounds. *RSC Adv.* **2018**, *8*, 34291−34296.
(9) Mothika, V. S.; Raupke, A.; Brinkmann, K. O.; Riedl, T.; Brunklaus, G.; Scherf, U. Nanometer-Thick Conjugated Microporous Polymer Films for Selective and Sensitive Vapor-Phase TNT Detection. *ACS Applied Nano Materials* **2018**, *1*, 6483−6492.
(10) Geng, T.-M.; Li, D.-K.; Zhu, Z.-M.; Zhang, W.-Y.; Ye, S.-N.; Zhu, H.; Wang, Z.-Q. Fluorescent conjugated microporous polymer based on perylene tetraanhydride bisimide for sensing o-nitrophenol. *Anal. Chim. Acta* **2018**, *1011*, 77−85.
(11) Zhang, Q.; Yu, S.; Wang, Q.; Xiao, Q.; Yue, Y.; Ren, S. Fluorene-Based Conjugated Microporous Polymers: Preparation and Chemical Sensing Application. *Macromol. Rapid Commun.* **2017**, *38*, 1700445.
(12) Geng, T.-M.; Li, D.-K.; Zhu, Z.-M.; Guan, Y.-B.; Wang, Y. The synthesis and fluorescence detection properties of benzoquinone-based conjugated microporous/mesoporous polymers. *Microporous Mesoporous Mater.* **2016**, *231*, 92−99.
(13) Novotney, J. L.; Dichtel, W. R. Conjugated Porous Polymers For TNT Vapor Detection. *ACS Macro Lett.* **2013**, *2*, 423−426.
(14) Vilela, F.; Zhang, K.; Antonietti, M. Conjugated porous polymers for energy applications. *Energy Environ. Sci.* **2012**, *5*, 7819−7832.
(15) Jiang, J.-X.; Trewin, A.; Adams, D. J.; Cooper, A. I. Band gap engineering in fluorescent conjugated microporous polymers. *Chem. Sci.* **2011**, *2*, 1777−1781.
(16) Ruiz, C.; Lopez Navarrete, J. T.; Ruiz Delgado, M. C.; Gomez-Lor, B. Triindole-Bridge-Triindole Dimers as Models for Two Dimensional Microporous Polymers. *Org. Lett.* **2015**, *17*, 2258−2261.
(17) Rao, K. V.; Mohapatra, S.; Kulkarni, C.; Maji, T. K.; George, S. J. Extended phenylene based microporous organic polymers with selective carbon dioxide adsorption. *J. Mater. Chem.* **2011**, *21*, 12958−12963.
(18) Xu, Y.; Jiang, D. Structural insights into the functional origin of conjugated microporous polymers: geometry-management of porosity and electronic properties. *Chem. Commun.* **2014**, *50*, 2781−2783.
(19) Yang, C.; Ma, B. C.; Zhang, L.; Lin, S.; Ghasimi, S.; Landfester, K.; Zhang, K. A. I.; Wang, X. Molecular Engineering of Conjugated Polybenzothiadiazoles for Enhanced Hydrogen Production by Photosynthesis. *Angew. Chem.* **2016**, *128*, 9348−9352.
(20) Battula, V. R.; Singh, H.; Kumar, S.; Bala, I.; Pal, S. K.; Kailasam, K. Natural Sunlight Driven Oxidative Homocoupling of Amines by a Truxene-Based Conjugated Microporous Polymer. *ACS Catal.* **2018**, *8*, 6751−6759.
(21) Guadalupe, J.; Ray, A. M.; Maya, E. M.; Gomez-Lor, B.; Iglesias, M. Truxene-based porous polymers: from synthesis to catalytic activity. *Polym. Chem.* **2018**, *9*, 4585−4595.
(22) Goubard, F.; Dumur, F. Truxene: a promising scaffold for future materials. *RSC Adv.* **2015**, *5*, 3521−3551.
(23) Kim, Y.; Das, S.; Bhattacharya, S.; Hong, S.; Kim, M. G.; Yoon, M.; Natarajan, S.; Kim, K. Metal-Ion Metathesis in Metal−Organic Frameworks: A Synthetic Route to New Metal−Organic Frameworks. *Chem. - Eur. J.* **2012**, *18*, 16642−16648.
(24) Amick, A. W.; Scott, L. T. Trisannulated Benzene Derivatives by Acid Catalyzed Aldol Cyclotrimerizations of Cyclic Ketones. Methodology Development and Mechanistic Insight. *J. Org. Chem.* **2007**, *72*, 3412−3418.
(25) Gomez-Lor, B.; Frutos, O. d.; Ceballos, P. A.; Granier, T.; Echavarren, A. M. Synthesis of New C3h and C3v Truxene Derivatives. *Eur. J. Org. Chem.* **2001**, *2001*, 2107−2114.
(26) Merino, E.; Verde-Sesto, E.; Maya, E. M.; Corma, A.; Iglesias, M.; Sanchez, F. Mono-functionalization of porous aromatic frameworks to use as compatible heterogeneous catalysts in one-pot cascade reactions. *Appl. Catal., A* **2014**, *469*, 206−212.
(27) While this work was in progress, the synthesis and photocatalytic properties of this polymer were reported. See ref 21.
(28) Jiang, J.-X.; Su, F.; Trewin, A.; Wood, C. D.; Campbell, N. L.; Niu, H.; Dickinson, C.; Ganin, A. Y.; Rosseinsky, M. J.; Khimyak, Y. Z.; Cooper, A. I. Conjugated Microporous Poly(aryleneethynylene) Networks. *Angew. Chem., Int. Ed.* **2007**, *46*, 8574−8578.
(29) Makhseed, S.; Samuel, J. Microporous organic polymers incorporating dicarboximide units for H2 storage and remarkable CO2 capture. *J. Mater. Chem. A* **2013**, *1*, 13004−13010.
(30) Gomez-Esteban, S.; Pezella, M.; Domingo, A.; Hennrich, G.; Gomez-Lor, B. Solvent-Dependent Truxene-Based Nanostructures. *Chem. - Eur. J.* **2013**, *19*, 16080−16086.
(31) Galisteo-Lopez, J. F.; Gomez-Esteban, S.; Gomez-Lor, B.; Lopez, C. Tunable emission in dye-doped truxene-based organogels through RET. *J. Mater. Chem. C* **2015**, *3*, 5764−5768.
(32) Shi, K.; Wang, J.-Y.; Pei, J. π-Conjugated Aromatics Based on Truxene: Synthesis, Self-Assembly, and Applications. *Chem. Rec.* **2015**, *15*, 52−72.
(33) Castiglioni, C.; Lopez Navarrete, J. T.; Zerbi, G.; Gussoni, M. A simple interpretation of the vibrational spectra of undoped, doped and photoexcited polyacetylene: Amplitude mode theory in the GF formalism. *Solid State Commun.* **1988**, *65*, 625−630.
(34) Hernandez, V.; Castiglioni, C.; Del Zoppo, M.; Zerbi, G. Confinement potential and \ensuremath{\pi}-electron delocalization in polyconjugated organic materials. *Phys. Rev. B: Condens. Matter Mater. Phys.* **1994**, *50*, 9815−9823.
(35) Ferron, C. C.; Delgado, M. C. R.; Gidron, O.; Sharma, S.; Sheberla, D.; Sheynin, Y.; Bendikov, M.; Navarrete, J. T. L.; Hernandez, V. α-Oligofurans show a sizeable extent of π-conjugation as probed by Raman spectroscopy. *Chem. Commun.* **2012**, *48*, 6732−6734.
(36) Ferron, C. C.; Sheynin, Y.; Li, M.; Patra, A.; Bendikov, M.; Lopez Navarrete, J. T.; Hernandez, V.; Ruiz Delgado, M. C. Raman Spectroscopic Characterization of Polyselenophenes and Poly(3,4-ethylenenedioxyselenophene)s. *Isr. J. Chem.* **2014**, *54*, 759−766.
(37) Wang, Y.; Guo, H.; Harbuzaru, A.; Uddin, M. A.; Arrechea-Marcos, I.; Ling, S.; Yu, J.; Tang, Y.; Sun, H.; Lopez Navarrete, J. T.; Ortiz, R. P.; Woo, H. Y.; Guo, X. (Semi)ladder-Type Bithiophene Imide-Based All-Acceptor Semiconductors: Synthesis, Structure−Property Correlations, and Unipolar n-Type Transistor Performance. *J. Am. Chem. Soc.* **2018**, *140*, 6095−6108.
(38) Wilson, E. B.; Decius, J. C.; Cross, P. C. *Molecular vibrations: The theory of infrared and Raman vibrational spectra*; McGraw-Hill: New York, 1955.
(39) Ruiz, C.; Pandey, U. K.; Termine, R.; García-Frutos, E. M.; Lopez-Espejo, G.; Ortiz, R. P.; Huang, W.; Marks, T. J.; Facchetti, A.; Ruiz Delgado, M. C.; Golemme, A.; Gomez-Lor, B. Mobility versus Alignment of a Semiconducting π-Extended Discotic Liquid-Crystalline Triindole. *ACS Appl. Mater. Interfaces* **2016**, *8*, 26964−26971.
(40) Yang, J.-S.; Swager, T. M. Fluorescent Porous Polymer Films as TNT Chemosensors: Electronic and Structural Effects. *J. Am. Chem. Soc.* **1998**, *120*, 11864−11873.
(41) Toal, S. J.; Trogler, W. C. Polymer sensors for nitroaromatic explosives detection. *J. Mater. Chem.* **2006**, *16*, 2871−2883.
(42) Sun, X.; Wang, Y.; Lei, Y. Fluorescence based explosive detection: from mechanisms to sensory materials. *Chem. Soc. Rev.* **2015**, *44*, 8019−8061.

DOI: 10.1021/acs.chemmater.9b01432
Chem. Mater. 2019, 31, 6971−6978

Journal of Materials Chemistry C

ROYAL SOCIETY OF CHEMISTRY

PAPER

View Article Online
View Journal | View Issue

Cite this: J. Mater. Chem. C, 2020, 8, 15416

In silico design of 2D polymers containing truxene-based platforms: insights into their structural and electronic properties†

Sergio Gámez-Valenzuela,[a] Marcelo Echeverri,[b] Berta Gómez-Lor,[b]* José I. Martínez[b]* and M. Carmen Ruiz Delgado[a]*

In the present work, we investigate two-dimensional (2D) conjugated polymers based on C_3-symmetric truxene-based cores at the density functional theory (DFT) level. In total, 27 different 2D polymers have been exhaustively studied with the aim to explore the impact of the following effects on the electronic and charge-transport properties: (i) the nature of the conjugated platform, going from electron-rich truxene (**Tx**) and triindole (**Tr**) units to electron-deficient truxenone (**To**) cores, (ii) the spacing of the cores with different bridges, *i.e.*, phenylene (**Ph**) or ethynylene (**A**) units, (iii) the linker position (2,7,12-substitution in the $\mathbf{T_2}$ polymers and 3,8,13-substitution in $\mathbf{T_3}$ polymers), and (iv) the increased number of π-bridges connecting the cores, from three linkers in $\mathbf{T_2}$ and $\mathbf{T_3}$ to six linkers in $\mathbf{T_{2,3}}$. To this end, we have carried out a large battery of DFT calculations on fragments extracted from the 2D polymers (dimers and trimers) as well as on the corresponding periodic 2D structures (infinite monolayers and self-assembled monolayers) using periodic boundary conditions. Our results show that simultaneous manipulation of the pore surface size and band-gap engineering together with charge-transport parameters can be achieved in these truxene-based 2D polymers by fine-tuning their structural features. The contributions of this study to the overall understanding of the structure–electronic property relationships of these semiconducting polymers and its correlation with available experimental work are highlighted. Our results provide interesting guidelines to design novel 2D materials with applications ranging from sensing to photocatalysis or electronics.

Received 2nd July 2020,
Accepted 10th September 2020

DOI: 10.1039/d0tc03139a

rsc.li/materials-c

Introduction

After three decades of enormous research effort, the field of organic semiconductors is currently a mature workbench that has already reached the market.[1–3] Advances in this area have been closely related to the continuous improvement in the ability of organic semiconductors to transport charge carriers (holes or electrons), which is quantified by their charge carrier mobility μ. While the highest mobilities are usually observed in crystalline or liquid crystalline materials, in the pursuit of an optimal balance between mobility and processability, semiconducting polymers are the preferred candidates.[4] These materials are usually constituted by conjugated one-dimensional (1D) chains and offer continuous electronic delocalization along the chain axis, and favor the efficient one-dimensional migration of charge carriers. However, hopping of charge carriers between chains is significantly hindered, thus resulting in slow down.

Expanding the π-conjugation has emerged as an efficient strategy to address the aforementioned drawback; this expansion permits the achievement of equally efficient electron delocalization in two dimension (2D) or three dimension (3D). This possibility has focused increasing attention on 2D organic polymers as semiconducting materials with enhanced transport dimensionality.[5]

2D covalent organic frameworks (COFs) are porous crystalline solids obtained by the polymerization of organic building blocks functionalized with reactive groups that predetermine their growth along two or more directions through dynamic covalent chemistry.[6,7] This design strategy gives rise to well-defined, high-surface-area materials whose final properties, topologies and porosities can be conveniently tuned by the choice of monomers and linking groups and by the position of the reactive groups, which determines the growth direction.

[a] Department of Physical Chemistry, University of Malaga, Campus de Teatinos s/n, 29071, Malaga, Spain. E-mail: carmenrd@uma.es
[b] Instituto de Ciencia de Materiales de Madrid, CSIC. C/Sor Juana Inés de la Cruz 3, Cantoblanco, Madrid 28049, Spain. E-mail: bgl@icmm.csic.es, joseignacio.martinez@icmm.csic.es

† Electronic supplementary information (ESI) available: Theoretical methods and computational details; chemical structures of the molecular fragments studied theoretically and Study of 2D conjugated polymer networks. See DOI: 10.1039/d0tc03139a

Achieving crystalline order in COFs relies on the reversibility of the chemical reactions used to connect the constituting molecular units *via* an error-correction mechanism.[8] Among the small number of chemical reactions that are sufficiently dynamic to enable the synthesis of COFs, Schiff base (imine) formation is the only chemical transformation that gives rise to π-conjugated structures.[9] However, imine linkages are far from ideal to induce efficient π-delocalization between connected units owing to their high polarization.[10,11] In order to facilitate exciton migration and carrier transportation across these frameworks, efforts are being focused on the search for linkages that promote π-electron delocalization. Interestingly, the choice of planar π-conjugated monomers has allowed the synthesis of 2D conjugated microporous polymers (CMPs), even in irreversible coupling conditions, by performing the coupling reactions on the surface[12–14] or in confined liquid–liquid interfaces.[10,15,16] This strategy has demonstrated crystalline sheet-like organic frameworks with building units directly linked or connected through bridges and are prone to efficient electronic delocalization (diyne, phenyl, alkyne, *etc.*).[17]

Our group has long been involved in the development of high-mobility self-assembling molecular materials based on different heptacyclic truxene-related platforms. Truxene can be considered as a 1,3,5-triphenylbenzene planarized through three bridging methylene groups, giving rise to a π-conjugated heptacyclic system with three additional fused 5-member rings. Varying the nature of the bridging groups (*i.e.*, changing methylene units to amino or ketone units) allows us to obtain molecules that share the truxene-like geometry but show completely different redox and semiconducting behaviors. Thus, while triindole[18,19] and truxene[20] are p-type semiconductors, truxenone[21] behaves as a high-mobility n-type semiconductor.

Because of their flat trigonal topology, these molecules have recently aroused interest as building units in the construction of functional COFs and CMPs. In fact, recently, microporous polymers based on these semiconducting monomers have been reported, with photocatalytic properties,[22–24] sensing ability,[25,26] thermoelectric,[27] supercapacitor behavior[28] or field effect behavior.[16] Optimizing materials for these applications requires the fine-tuning of different parameters, such as energy levels, π-conjugation or exciton/charge transport. In this sense, theoretical calculations are found to be very useful to predict or rationalize the relationships between chemical structural modifications and the properties of the resulting materials. DFT calculations on the electronic structures of different 2D conjugated polymers have been previously reported, with an emphasis on the role played by the network topology,[29–31] lattice symmetry[32] or structural differences between 1D and 2D,[33–35] among other structural factors.[36–39] However, while isolated truxene-based molecules have been amply theoretically explored, a systematic study of their 2D conjugated polymers has not yet been reported.[40–42]

In this work, we performed an exhaustive investigation of truxene-based 2D conjugated polymers with the aim to explore their chemical structure–electronic property relationships to guide the design of novel optimized 2D materials. To this end, we combined an oligomer approach with periodic boundary conditions (PBC) calculations for the 2D lattices. Our selection of truxene-based 2D polymers for this work is shown in Fig. 1. A total of 27 different 2D polymers were investigated with the ultimate goal of exploring how their electronic and charge-transport properties can be tuned by engineering the organic building blocks (*i.e.*, by changing the nature of the core from **Tx** to **Tr** or **To** or by using different π-bridges, from phenylene to alkyne) and the connecting mode (*i.e.*, by changing the linkage position from $\mathbf{T_2}$ to $\mathbf{T_3}$ or by increasing the number of π-bridges from three units in $\mathbf{T_2}$ and $\mathbf{T_3}$ to six units in $\mathbf{T_{2,3}}$). Among the selected 2D polymers, four truxene-based (*i.e.*, $\mathbf{Tx_2}$, $\mathbf{Tx_3}$, $\mathbf{Ph\text{-}Tx_2}$ and $\mathbf{Ph\text{-}Tx_3}$)[25] and one triindole-based ($\mathbf{Ph\text{-}Tr_2}$) polymer have been successfully reported[16] and showed promising applications in sensing and electronics, respectively. We anticipate that this class of truxene-based 2D conjugated networks are potential versatile semiconducting materials for optoelectronic applications.

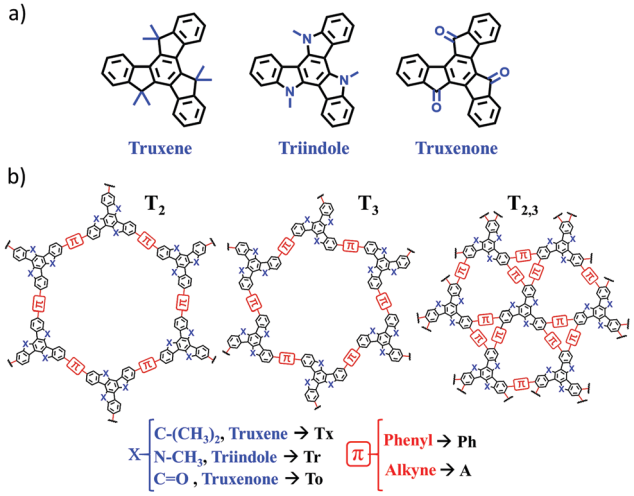

Fig. 1 General chemical structures of the conjugated cores (a) and 2D polymers (b) examined in this study with the notation used throughout the text. Note that $\mathbf{T_2}$ and $\mathbf{T_3}$ polymers refer to tri-substituted materials with different linkage positions (2,7,12 in $\mathbf{T_2}$ and 3,8,13 in $\mathbf{T_3}$), while $\mathbf{T_{2,3}}$ corresponds to hexa-substituted materials in the 2,3,7,8,12 and 13 positions.

It is worth noting that most of the first-principles theoretical frameworks adopted here have been very recently used to rationalize similar compounds, such as the first example of a solid-state fluorescent 2D-COF bonded *via* imine linkage[37] or highly-efficient metal-free COF catalysts towards the oxygen reduction reaction and hydrogen evolution processes.[43] Taking advantage of this not-yet-fully-harvested theoretical workbench, this exhaustive and systematic study provides a powerful protocol for prefiltering of novel candidate materials towards different potential application fields according to the targeted functionality.

Results and discussion

The structural and electronic properties of 2D conjugated polymers containing truxene-based platforms were theoretically investigated

using a canonical bottom-up approach. First, molecular equivalent fragments extracted from the 2D polymeric structures were investigated in order to evaluate the impact produced by the nature of the core as well as the influence of the nature, number and linkage positions of the bridging connectors on the electronic communication between the conjugated C_3-symmetric platforms. To this end, we focused on the relationships between the HOMO–LUMO gaps, topologies and structural reorganization energies for hole and electron transport and the chemical structures of these 2D materials. Second, these molecular fragments were then sequentially assembled to form larger subsystems, and truxene-based 2D lattices were generated. The structural features (pore size, geometry of the monolayer, interlayer stacking) and electronic band structures of these 2D COFs were investigated in detail. This study allowed us to explore the pore surface size and band-gap engineering of these promising 2D materials and their potential as charge-transport materials, with important implications for their application in fields ranging from electronics to photocatalysis or sensing.

1. Molecular fragments

We first focused on performing DFT calculations for the molecular fragments of the 2D polymers under study (Fig. S1 and S2, ESI†). Note that it has been recently demonstrated that calculations of fragments of molecules provide important information about the molecular and electronic structures of 2D conjugated networks.[44–50]

1.1 Structural features. Fig. 2a displays the optimized ground-state structures for the molecular constituents of the $\mathbf{T_2}$ polymers. As we can observe, systematic similar torsions ($\sim 36^\circ$) are found when the cores are linked through a phenylene-bridged unit or when they are directly connected, while coplanar structures are found in alkyne-linked fragments.

Interestingly, the nature of the C_3-symmetric conjugated platforms plays a key role in their internal disorder: (i) in the truxene (**Tx**) cores, each methyl group is oriented out of the plane of the conjugated platform and therefore does not sterically hinder the planarity of the overall system, (ii) the trivalent nature of the nitrogen atoms of the triindole (**Tr**) core results in a moderate distortion of the platform due to the steric hindrance caused by the only existing methyl groups and the outermost benzene rings, and (iii) the truxenone (**To**) cores are totally coplanar as a consequence of the favorable intramolecular interactions between the C═O groups and adjacent hydrogen atoms of the outermost benzene rings (with C═O···H distances of 2.12 Å). The change of the linkage position from *para* (2,7,12) connections in $\mathbf{T_2}$ to *meta* (3,8,13) connections in $\mathbf{T_3}$ yields very similar geometrical distortions (Fig. S4, ESI†). Importantly, an increase of the number of peripheral linkers from three to six units in $\mathbf{T_{2,3}}$ results in more extended and coplanar skeletons when the cores are directly linked due to the formation of fully fused benzene rings between the platforms or when alkyne groups are connecting the cores (see Fig. 2b). However, in the hexaphenyl-substituted **Ph-T$_{2,3}$** polymers, three-dimensional cyclic cavities are created between the three external phenylene units connecting the cores that are significantly distorted by ~ 50–67° (see **Ph-Tr$_{2,3}$** taken as a model in Fig. 2b).

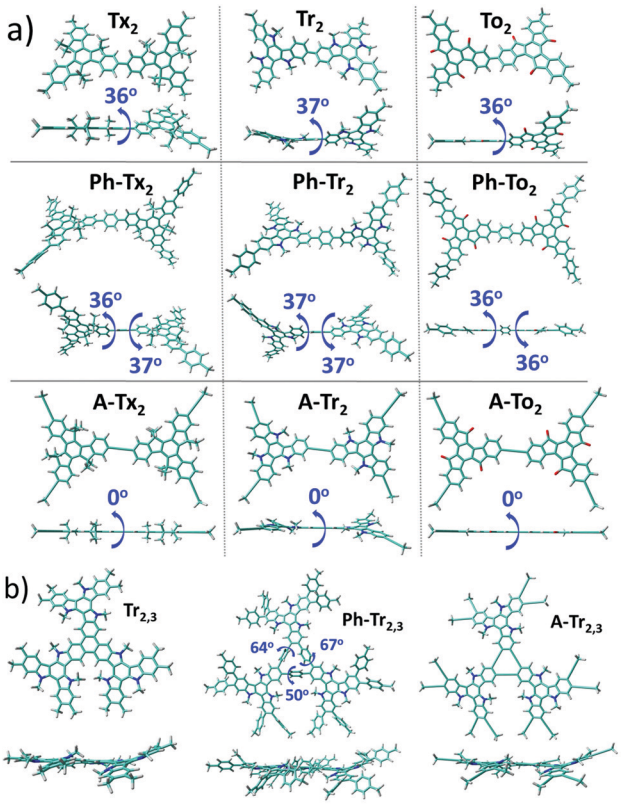

Fig. 2 Top and lateral views of the DFT-optimized structures (PBE0/6-31G** level) for the (a) $\mathbf{T_2}$ dimeric models (see Fig. S3a (ESI†) for the $\mathbf{T_3}$ systems) and (b) $\mathbf{Tr_{2,3}}$ trimeric models chosen as representatives for the series of the hexa-substituted $\mathbf{T_{2,3}}$ systems under study (see Fig. S3b (ESI†) for the rest of the $\mathbf{T_{2,3}}$ systems). The dihedral angles between the conjugated cores and the π-bridges (in absolute values) are also shown.

1.2 Electronic features. Fig. 3a shows the frontier molecular orbital energies for the $\mathbf{T_2}$ and $\mathbf{T_3}$ fragment models. For the sake of comparison, the influences of the nature of the core, the π-bridges and the different linkage positions were analyzed separately: (i) both the HOMO and LUMO levels are destabilized (stabilized) on going from the **Tx** to the **Tr** or **To** systems; this effect is more pronounced in the case of the HOMO (LUMO), in accordance with the electron-donating and electron-withdrawing character of the **Tr** and **To** units, respectively. This results in a HOMO–LUMO gap decrease in the following order: **Tx** > **Tr** > **To**, which can be rationalized in terms of the extension of the π-conjugation (Fig. 3b). As evidenced by the frontier molecular orbitals of the directly connected systems, the HOMOs and LUMOs of the **Tx**-based systems spread over the central rings along the CC backbone; however, significant contributions from the nitrogen atoms were also found in the HOMOs of the **Tr**-based systems, while the LUMOs of the **To**-based systems also spread over more internal ketone groups (see Fig. 3b). Note that similar observations have been previously reported for the isolated trigonal building units.[40–42] (ii) Considering the effects of the π-bridge,

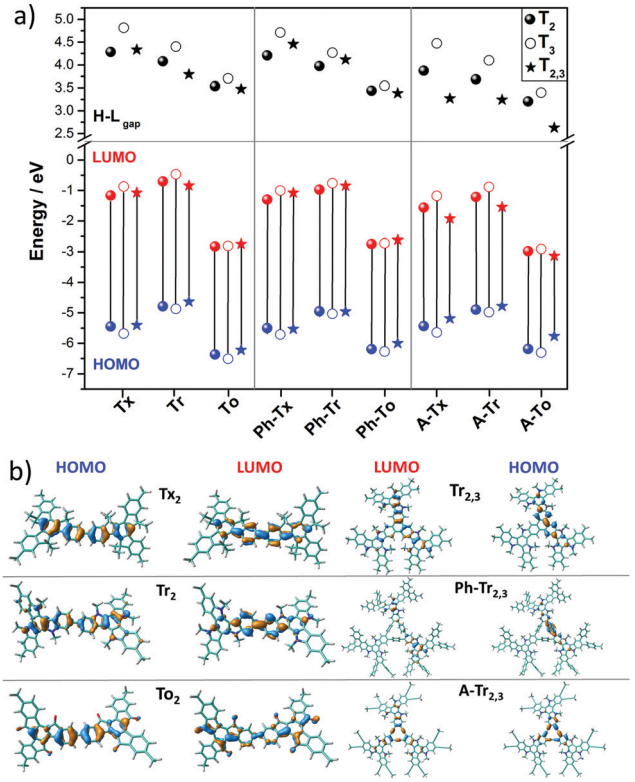

Fig. 3 (a) DFT-calculated (PBE0/6-31G** level) HOMO–LUMO gaps (a) and frontier molecular orbital energies (b) for the $\mathbf{T_2}$ (solid circles), $\mathbf{T_3}$ (open circles) and $\mathbf{T_{2,3}}$ (solid triangle) models. (b) HOMO and LUMO topologies of the directly connected $\mathbf{T_2}$ dimeric models and $\mathbf{Tr_{2,3}}$ trimeric models chosen as representatives (see Fig. S6 (ESI†) for the remaining compounds).

the insertion of a phenylene spacer between the cores exerts a slight impact on the HOMO and LUMO energy levels when compared to the directly connected systems, suggesting a minor influence on the π-electron delocalization between platforms. This is in consonance with the similar distortions found for both the directly connected and phenylene-bridged systems. Conversely, the presence of ethylene linkers produces a significant decrease of the HOMO–LUMO gap, which is associated with moderate stabilization of the LUMO, whereas the HOMO level is slightly affected. Note that the HOMO and LUMO wavefunctions of the alkyne-substituted systems show strong participation of the bridge in the overall π-conjugation, whereas the contribution of the spacer in their phenylene-linked analogues is less pronounced (see the ESI†). This indicates more efficient electronic π-conjugation in the alkyne-substituted systems, in agreement with the electron-accepting nature and the cylindrical symmetry of the alkyne group. (iii) A moderate increase of the HOMO–LUMO gaps was observed when varying the linkage position from $\mathbf{T_2}$ to $\mathbf{T_3}$ due to the similar LUMO destabilization and HOMO stabilization. This is in line with our previously reported study on **Tx**-based porous polymers,[25] where we demonstrated that polymers with truxene cores covalently linked in *para* positions are better conjugated than their *meta*-substituted isomers. A comparison of the molecular orbitals for the $\mathbf{T_2}$ and $\mathbf{T_3}$ models (Fig. S6, ESI†) shows that the connecting conjugated units at the *meta* positions allow for shorter pathways of alternating single and double bonds, thus providing a less efficient conjugation pathway than the units at the *para* positions. (iv) Finally, increasing the number of connecting groups has a mixed influence on the energy of the frontier energy levels. Thus, while the HOMO/LUMO energies are barely affected when comparing the directly connected $\mathbf{T_2}$ and $\mathbf{T_{2,3}}$ systems, which show similar HOMO and LUMO wave functions and delocalization over the same number of adjacent rings (for example, compare the HOMO and LUMO orbitals for $\mathbf{Tr_2}$ and $\mathbf{Tr_{2,3}}$ taken as models in Fig. 3b), the presence of six connecting phenylene units results in moderately larger HOMO–LUMO gaps. This can be ascribed to the distorted configuration of the phenyl groups (~60°, as shown in Fig. 2b). In contrast, increasing the number of alkyne bridges from three to six results in lower HOMO–LUMO gaps, indicating better conjugation between the cores, as supported by the more extended electronic delocalization in the HOMO and LUMO orbitals (*i.e.*, see the orbitals for **A-Tr**$_{2,3}$ in Fig. 3b).

The nucleus-independent chemical shift (NICS) values for the $\mathbf{T_2}$ and $\mathbf{T_3}$ fragment models were calculated at the geometrical centers of all the phenyl rings (NICS(0)) and at 1 Å above (NICS(1)); see Fig. S8 and S9 (ESI†). The NICS methodology is a widely employed indicator of chemical aromaticity;[51,52] the more negative the NICS value, the more aromatic the system. On the basis of the calculated data, the aromaticity of these systems is significantly affected by the nature of the core but is barely influenced by the linker units or linkage position. When compared to the reference **Tx**-based derivatives: (i) the presence of electron-rich **Tr** platforms results in more negative NICS values (around 2 ppm), suggesting that the platforms become more aromatic. (ii) The insertion of **To** cores leads to less negative NICS values, and this effect is more important in the innermost benzene rings (with NICS(0) values of around −1.2 ppm in the **To**-based systems compared to values of around −6.8 ppm for the **Tx**-based systems); this can be explained in terms of the electron-withdrawing character of the ketone groups, which decreases the aromaticity of the structure in consonance with better electronic delocalization, as previously pointed out by their lowest HOMO–LUMO gap values in the series.

The intramolecular reorganization energy is one of the key molecular parameters governing charge transport,[53] and it reveals the geometrical adjustments necessary to accommodate a positive or a negative charge. The smaller the value of λ, the larger the expected charge mobility. With this in mind, we analyzed the effects of the electronic nature of the conjugated platforms on the intramolecular reorganization energies associated with hole (λ_h) and electron (λ_e) transfer. Fig. 4 shows the computed λ values for the $\mathbf{T_2}$ and $\mathbf{T_3}$ dimeric models. The calculated λ_h [λ_e] values are in the range of 71–217 [102–369] meV. Note that these values are on the same order of those previously obtained for 2D COF fragments based on pyrene (with λ_h = 134 meV and λ_e = 192 meV) or porphyrin (with λ_h = 54 meV and λ_e = 170 meV) cores for which high charge-carrier mobility values were predicted.[49] Among the series, the **Tr**-based and

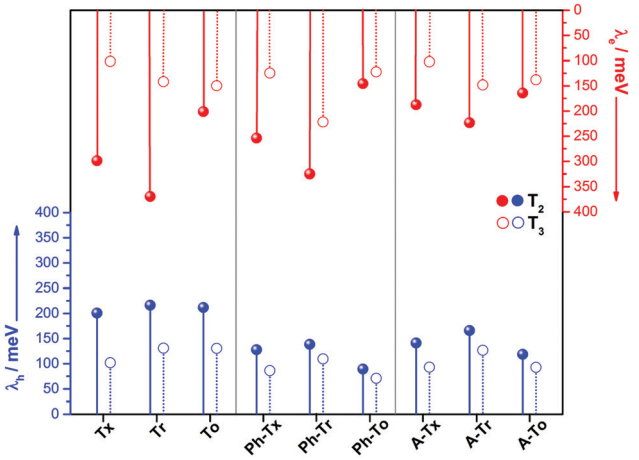

Fig. 4 DFT-calculated (PBE0/6-31G** level) hole (red) and electron (blue) reorganization energies for the $\mathbf{T_2}$ (solid circles) and $\mathbf{T_3}$ (open circles) dimeric models.

To-based systems exhibit the largest and lowest λ values, respectively; this can be attributed to the large distortion found in **Tr** platforms due to the steric hindrance between the *N*-methyl groups and the outermost benzene rings, whereas the **To** cores exhibit totally coplanar skeletons, allowing for better geometrical relaxation upon charging. The insertion of π-bridges results in smaller λ values, especially for alkyne groups. For instance, linking the cores with phenyl [alkyne] groups results in λ_h and λ_e decreases of 123 [56] and 93 [37] meV, respectively, for the $\mathbf{To_2}$ derivatives; this behavior can be related to the previously observed enhancement of the π-electron delocalization between the heptacyclic platforms and to the overall relaxation of the structure upon core elongation. Finally, the structural reorganization needed to accommodate both positive and negative charges decreases by an average of 30% and 40%, respectively, when the linkage position changes from $\mathbf{T_2}$ to $\mathbf{T_3}$; this effect is more pronounced when the cores are directly linked.

2. 2D conjugated polymer networks

We next investigated the electronic structures of single-layer truxene-based 2D polymers built by sequentially assembling the previously studied molecular fragments. For all the materials under study, honeycomb-Kagome-like hexagonal lattices were observed, where within the primitive unit cell, the connection between the conjugated platforms exhibits an arrangement of a kagome sublattice while the centers of the cores form a honeycomb sublattice.[54]

2.1 Structural characterization of single-layer 2D COFs. The analysis of the optimized geometries of the $\mathbf{T_2}$, $\mathbf{T_3}$ and $\mathbf{T_{2,3}}$ COFs revealed that pore surface engineering of these materials can be achieved by suitable structural design (see Fig. 5 and 6). Whereas the $\mathbf{T_2}$ and $\mathbf{T_3}$ COFs lead to hexagonal mesopores (accessible pore diameters up to 26 Å), the $\mathbf{T_{2,3}}$ COFs bear two different kinds of micropores: hexagonal (accessible pore diameter of ~6–11 Å) and triangular (accessible pore diameter of ~4–6 Å). Interestingly, the size of the hexagonal mesopores can also be modulated by the insertion of π-bridges between the cores (*i.e.*, increases of 8 and 4 Å, respectively, were found in $\mathbf{T_2}$ and $\mathbf{T_3}$ when comparing the phenylene- or alkyne-based COFs with their directly linked homologues) or by changing the linkage position (*i.e.*, the pore size decreases by ~5 Å when going from *para*-connected $\mathbf{T_2}$ to *meta*-connected $\mathbf{T_3}$). The wide range of pore sizes and pore geometries should bring novel functionalities to these materials, such as multi-selectivity, that can be exploited in versatile applications such as adsorption and separation science. It is interesting to remark that surface pore engineering is currently attracting paramount interest.[55–57]

In accordance with the optimized molecular fragments, the optimized periodic single layers predict that the **Tx**- and **To**-based COF structures are planar, while the **Tr**-homologues have a moderately distorted configuration as a consequence of the steric repulsions between the *N*-methyl groups and the hydrogen atoms of the adjacent phenyl groups. This structural feature plays a role in the electronic total charge distribution of these 2D materials. Fig. 5 and 6 depict colour total electronic density maps (increasing charge density from the light green to the red/purple regions) associated with the cutting-planes of the 3D total charge isodensity, which becomes slightly inhomogeneous in specific regions of some of the compounds due to out-of-plane distortions of the structures. The distorted configuration of the **Tr**-based COF monolayer will have a strong implication for the preferential interlayered bulk stacking, as discussed below.

2.2 Electronic structures of the single-layer 2D COFs. We next examined the electronic band structures of the 2D polymers under study. One interesting finding that can be extracted from the band structures is that these systems can be classified as semiconducting 2D materials with band-gaps in the range of 1.17–3.13 eV (Fig. 7); therefore, they are very interesting for photovoltaic applications according to the Shockley–Queisser limit.[58] In good analogy with the HOMO–LUMO gap trends calculated for the fragment models, the following observations can be pointed out: (i) a decrease of the band-gap occurs when going from the **Tx** and **Tr** cores to the **To** core (*i.e.*, from 2.37, 2.22 and 1.77 eV going from $\mathbf{Tx_2}$ and $\mathbf{Tr_2}$ to $\mathbf{To_2}$). (ii) A moderate bandgap increase was found when changing the linkage

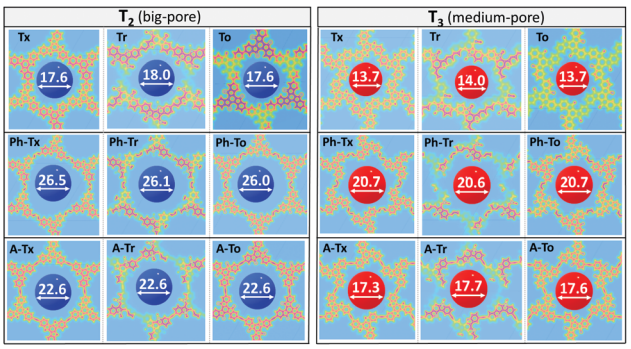

Fig. 5 DFT-PBE-calculated surface charge density colour maps in the *xy*-plane (at the *z*-position) for all the $\mathbf{T_2}$ and $\mathbf{T_3}$ 2D COFs under study. Accessible pore diameter (Å) values are also shown.

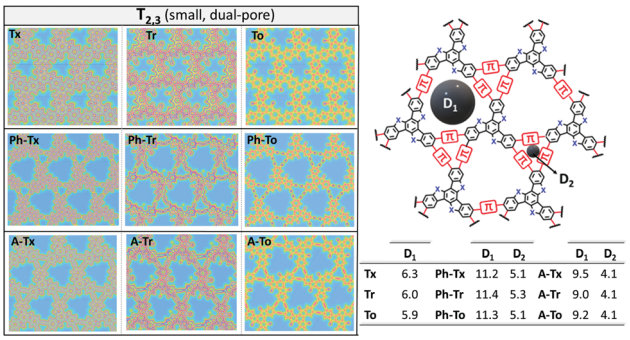

	D_1		D_1	D_2		D_1	D_2
Tx	6.3	Ph-Tx	11.2	5.1	A-Tx	9.5	4.1
Tr	6.0	Ph-Tr	11.4	5.3	A-Tr	9.0	4.1
To	5.9	Ph-To	11.3	5.1	A-To	9.2	4.1

Fig. 6 DFT-PBE-calculated surface charge density colour maps in the *xy*-plane (at the *z*-position) for the $\mathbf{T_{2,3}}$ 2D COFs under study. Accessible pore diameter (Å) values for the hexagonal (D1) and trigonal (D2) pores are also shown.

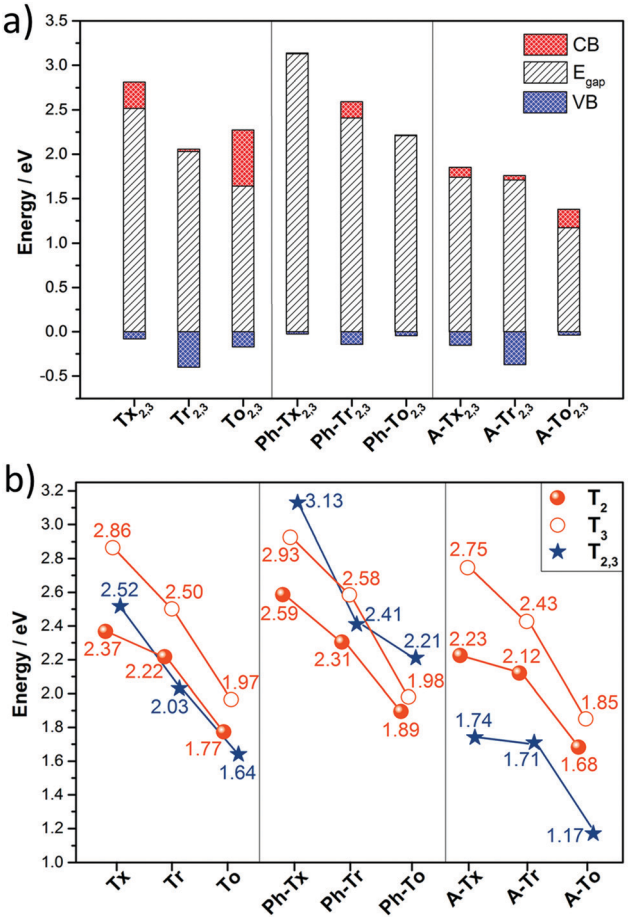

Fig. 7 (a) Calculated band-gaps and bandwidths for the conduction bands (CBs) and valence bands (VBs) of all the hexa-substituted truxene-based 2D COFs. (b) Comparison of the calculated band-gaps for all the 2D polymers under study. The zero energy is taken to correspond to the valence band maximum.

position from the *para* to the *meta* connection, suggesting more effective conjugation pathways in the $\mathbf{T_2}$ COFs compared to the $\mathbf{T_3}$ COFs. (iii) The insertion of phenylene spacers slightly alter the bandgaps in $\mathbf{T_2}$ and $\mathbf{T_3}$ polymers but results in larger band-gaps in the $\mathbf{T_{2,3}}$ polymers (*i.e.*, from 2.50 [2.03] to 2.58 [2.41] eV on going from $\mathbf{Tr_2}$ [$\mathbf{Tr_{2,3}}$] to $\mathbf{Ph\text{-}Tr_2}$ [$\mathbf{Ph\text{-}Tr_{2,3}}$], respectively), which can be ascribed to the more twisted structures of the latter, thus decreasing the electronic conjugation between the core. (iv) A significant decrease of the bandgap was found in the alkyne-connected 2D polymers, with the lowest value found for $\mathbf{A\text{-}To_{2,3}}$ (1.17 eV); that is, the flat truxenone platforms hexa-substituted with alkyne spacers facilitate the extension of the electronic conjugation and enable better electronic communication between the cores.

The DFT-PBE0 band structures of the $\mathbf{T_2}$ and $\mathbf{T_{2,3}}$ COFs are displayed in Fig. 8. The three-armed platforms in the $\mathbf{T_2}$ COFs lead to the formation of highly symmetric kagome-like lattices,[32] which results in a totally flat top of the valence band (VB) and bottom of the conduction band (CB); this affords fully localized charge carriers and infinitive carrier effective masses, which translates into vanishing charge carrier mobilities (Fig. 8a). Only a very slight gain of the valence band dispersion is observed when the cores are directly connected through *meta* connections in $\mathbf{T_3}$ (Fig. S10, ESI†). The insertion of phenylene or alkyne π-bridges between the cores retained the totally flat character of the bands around the Fermi level in both the $\mathbf{T_2}$ and $\mathbf{T_3}$ COFs (Fig. S10 and S11, ESI†). These predicted flat bands contrast with the high mobility values experimentally obtained for $\mathbf{Ph\text{-}Tr_2}$ COFs, one of the benchmark hole transport 2D conjugated polymers reported to date.[16] In this case, the high mobility values probably reflect the favorable electronic coupling between the cores of the adjacent layers, which may increase the bandwidths along the vertical direction. To reinforce this hypothesis, we analyzed the preferential interlayer stacking of different selected 2D COFs (see the Discussion in Section 2.3).

On the other hand, the electronic structures of COFs based on six-armed cores result in more dispersive bands (Fig. 7a and 8b). In this context, it is worth noting that the more dispersive the valence band [conduction band] at the VB maximum [BC minimum], the larger the expected hole [electron] charge carrier mobility. Interestingly, a large variation of the bandwidths was found in the $\mathbf{T_{2,3}}$ COFs (*i.e.*, in the range of 26–400 meV and 6–633 meV for the CB and VB, respectively). Particularly large CB [VB] bandwidths and low effective masses for holes [electrons] were found for the $\mathbf{Tr_{2,3}}$ [$\mathbf{A\text{-}To_{2,3}}$] polymers; therefore, these systems are promising hole and electron charge-transport 2D materials, respectively. On the other hand, large bandwidths for both CB and VB (and low hole and electron effective masses) were obtained for $\mathbf{To_{2,3}}$, $\mathbf{A\text{-}Tx_{2,3}}$ and $\mathbf{A\text{-}Tr_{2,3}}$; therefore, they are attractive ambipolar charge carrier materials (see Fig. 8b for the directly connected $\mathbf{T_{2,3}}$ COFs and Fig. S12 (ESI†) for the alkyne-substituted $\mathbf{A\text{-}T_{2,3}}$ COFs).

At this point, it is interesting to remark that all the compounds analyzed in this study mainly exhibit π-type semiconducting character, with the Fermi energy almost pinning the valence band in some cases. The 3D isosurfaces of the orbital electronic densities corresponding to the valence and conduction bands of the different extended 2D COF systems studied here provide

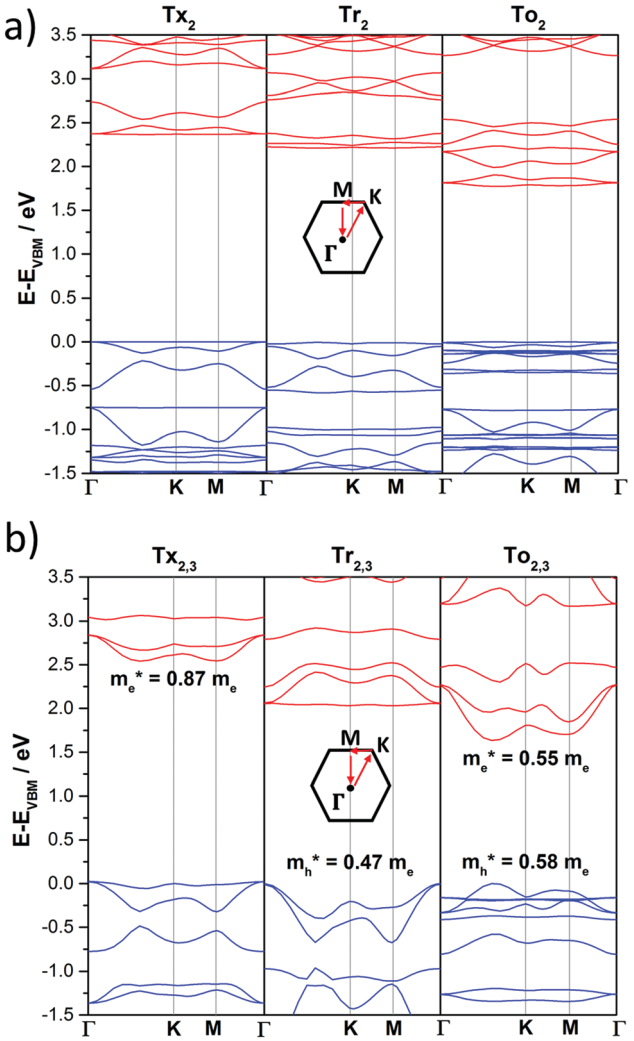

Fig. 8 DFT-PBE-calculated electronic band structures of directly core-connected 2D polymers: **Tx$_2$**, **Tr$_2$** and **To$_2$** (a) and **Tx$_{2,3}$**, **Tr$_{2,3}$** and **To$_{2,3}$** (b). The valence and conduction bands are marked in blue and red, respectively. The zero energy is taken to correspond to the valence band maximum, E_{VBM}, while the *x*-axis labels denote a path through the 3D space of the *k*-vectors. Points of high symmetry in the Brillouin zone are labeled as *Γ* (0,0,0), *M* (0,1/2,0) and *K* (1/3,2/3,0), all in reciprocal space coordinates. For the electronic band structures of the remaining 2D polymers under study, see Fig. S10–S13 (ESI†).

valuable information about the spatial localization and delocalization degrees of these states, the homogeneity in the spatial distribution of the states, and the preferential carrier transport paths across the compounds (Fig. S13–S16, ESI†). For instance, the engineered **A-Tr$_{2,3}$** system, which is predicted to have narrower band-gaps and pronounced electronic *k*-dispersions, exhibits similar morphologies for the valence and conduction bands, with a more delocalized spatial distribution of the valence band (Fig. S16, ESI†).

The time-dependent DFT-based UV-Vis absorption spectra of the **T$_2$** and **T$_3$** 2D polymers were also calculated (Fig. S17, ESI†). A good correlation can be found with the experimental results previously reported for truxene-based (**Tx$_2$**, **Tx$_3$**, **Ph-Tx$_2$** and **Ph-Tx$_3$**)[25] polymers. Please note that UV-Vis absorption (photoexcitation) spectra are of fundamental importance for applications ranging from sensing to photocatalysis and photovoltaics. We have found that in these systems, it is possible to modulate the absorption spectral response from the UV region to the near infrared region through suitable chemical modification, such as from 325 nm in **Tx$_3$** to 726 nm in **A-To$_2$** (a more detailed explanation can be found in the ESI†). These differences are also of fundamental interest for their sensing behavior, as we recently demonstrated for some of these truxene-related-materials.[25] The character of the symmetry of these valence and conduction orbital states (see Fig. S13–S16, ESI†) will be crucial to yield the permitted optical transitions captured by the computed photoabsorption spectra (see Fig. S17, ESI†) because the main contribution to the primary electronic excitation in these compounds comes from excitation of an electron from the valence band towards the conduction band (see the ESI†).

2.3 Preferential interlayer stacking of 2D COFs. In order to check the preferential interlayered bulk-stacking fashion adopted by the different 2D layers, we computed the infinite crystal-bulk configurations for the alkyne-based **T$_2$** and **T$_3$** COFs (which showed more pronounced band dispersion in the 2D layers) in both AA and AB stacking modes. The results of these calculations are reflected in Fig. 9. Other intermediate configurations between AA and AB stacking were analyzed, yielding unfavourable results in all cases compared with the canonical AA and AB stacking modes. It is interesting to note that on average, and as expected, the cohesive energy (E_c) increases with decreasing inter-layer distance (with *L* values ranging between 2.21 and 4.38 Å). We obtained a wide range of cohesive energies for the different systems, going from systems for which subtle emerging inter-layer chemistry turns into significant *via* potential π–π stacking or some other type of interlayer

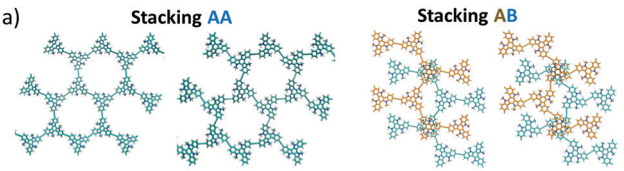

b)

2D polymer	Pore	Stacking	L (Å)	E_c (kcal/mol)
A-Tx$_2$	big	AA	3.86	+87.75
		AB	3.22	-34.20
A-Tr$_2$	big	AA	3.79	-35.67
		AB	2.21	-58.80
A-To$_2$	big	AA	4.12	-46.42
		AB	4.25	-24.12
A-Tx$_3$	medium	AA	3.94	+341.08
		AB	3.23	-36.83
A-Tr$_3$	medium	AA	3.79	-36.00
		AB	2.49	-67.01
A-To$_3$	medium	AA	4.20	-33.24
		AB	4.38	-28.07

Fig. 9 (a) Pictorial top views of the two different stacking AA and AB configurations. (b) Computed data of the fully optimized inter-layer stacking distance (in Å) and inter-layer cohesive energy (in kcal mol^{-1}), defined as the difference between the total energy crystal-bulk (with one layer per unit cell) and the isolated single-layer, for the **A-T$_2$** and **A-T$_3$** compounds.

electronic hybridization, such as the case of the **A-Tr** compounds (cohesive energies in the range of -65 kcal mol^{-1}), and other systems with only electrostatic and vdW interlayer cohesion, such as the **A-To** compounds (around -25 kcal mol^{-1}). On the other hand, AA stacking of the **A-Tx** systems leads to unstable configurations due to physical steric impediment towards stacking, which is reflected in their high positive cohesive energies due to the numerical instabilities when the lattice-parameter relaxation algorithm is applied. However, it is worth noting that AB stacking is the preferential stacking configuration for the **A-Tr** and **A-Tx** systems, while the **A-To** compounds prefer to stack in AA fashion. Interestingly, these results are in good accordance with the available X-ray data reported for triindole[18,59,60] (truxenone)[21] cores in self-assembling systems, where a preferential staggered (eclipsed) stacking conformation of the cores is adopted for which large electronic couplings are obtained. This favourable electronic coupling between the cores of the adjacent layers may increase the bandwidth along the vertical direction and probably explains the high carrier mobility of the experimentally obtained **Ph-Tr$_2$**[16] despite the flat bands predicted for the **T$_2$** and **T$_3$** single-layer COFs.

Interestingly, this variety of possible scenarios predicted by our theoretical protocol leads to high versatility in selecting candidates for different applications: going from easy-to-delaminate systems, allowing the transfer of a 2D single layer to more interesting inert technological substrates, up to highly robust stacked crystals with potential use in optoelectronic applications or for interpore gas-sensing purposes.

Conclusions

In summary, we have performed a comprehensive and exhaustive investigation at the DFT level of the structural and electronic features of 27 different 2D conjugated polymer networks based on C_3-symmetric platforms (*i.e.*, truxene, triindole and truxenone). The conjugated cores are connected directly or through alkyne or phenylene spacers, whose number and linkage position (from *para* to *meta*) have also been explored. Semiconductors band-gap values in the range between 1.17 and 3.13 eV are predicted.

Our results show that wide tuning of the structural properties (*i.e.*, geometry or pore size) and electronic properties (*i.e.* HOMO–LUMO levels, band-gap or band dispersion) can be achieved in these truxene-based 2D polymers by suitable selection of the trigonal building blocks and the nature and position of the connecting moieties. In the same line, a strong modulation of the absorption spectral response from the UV region to the near infrared region is found through suitable chemical modification. Please note that the above parameters will determine properties such as the selectivity/sensitivity of sensing polymers towards analytes of interest and will dictate their photocatalytic activity.

On the other hand, large bandwidths and low effective masses (and thus, high carrier mobilities) are predicted for 2D polymers with six-armed triindole and truxenone cores, connected directly (**Tr$_{2,3}$** and **To$_{2,3}$**) or through alkyne bridges (**A-Tr$_{2,3}$** and **A-To$_{2,3}$**). Preferential interlayered stacking is also expected to result in favorable electronic couplings between the cores and may increase the bandwidths along the vertical direction, thus positively affecting the charge-carrier mobilities. This probably explains the high mobility experimentally determined for **Ph-Tr$_2$**[16] in spite of the fact that flat bands are predicted for polymers with three-armed cores (**T$_2$** and **T$_3$**). In fact, the calculations suggest preferred AB stacking between layers for the related triindole-based polymers, which would lead to a staggered arrangement of neighbouring cores. This organization has been previously demonstrated to result in pronounced electronic coupling and high hole mobilities in triindole self-assembling systems.[18,59,60] The synthesis of selected candidates (particularly those with monomers connected *via* six ethynyl linkers) is now actively ongoing in our laboratories in an attempt to obtain high mobility semiconductors and validate our theoretical results.

Overall, our findings shed light on the structure–property relationships of 2D truxene-based conjugated polymers and provide interesting guidelines to design novel 2D materials with applications ranging from sensing to photocatalysis or electronics. Additionally, this computational first-principles-based strategy emerges as a powerful tool to achieve *in silico* pre-filtering of future similar 2D materials, which, by adequate and careful selection of building blocks, will permit the prediction, within the limits of the level of theory employed, of emerging optoelectronic features as a lighthouse to experimentalists according to the desired targeted functionality.

Conflicts of interest

There are no conflicts to declare.

Acknowledgements

This work was financially supported by the MINECO (CTQ2016-78557-R) and MICINN (PID2019-104125RB-I00) of Spain. JIM acknowledges financial support from Spanish MINECO (MAT2017-85089-C2-1-R, RYC-2015-17730), Comunidad de Madrid *via* Programa de Investigación Tecnologías 2018 (FOTOART-CM S2018/NMT-4367), and the innovation program under grant agreements 785219 and 881603 (GrapheneCore2 and GrapheneCore3-Graphene-based disruptive technologies, respectively). The work at the University of Málaga was funded by the MICINN (PID2019-110305GB-I00) and by the Junta de Andalucıa (P09-FQM-4708, UMA18-FEDERJA-080). S. G.-V. thanks the MINECO for a FPU predoctoral fellowship (FPU17/04908). Computer resources, technical expertise and assistance provided by the SCBI (Supercomputing and Bioinformatics) centre of the University of Málaga are gratefully acknowledged.

Notes and references

1 P. Samorí and V. Palermo, *Flexible Carbon-based Electronics*, Wiley-VCH, Weinheim, 2018.

2 H. Klauk, *Organic electronics: materials, manufacturing, and applications*, Wiley-VCH, Weinheim, 2006.
3 H. Klauk, *Organic electronics II: more materials and applications*, Wiley-VCH, Weinheim, 2012.
4 S. Fratini, M. Nikolka, A. Salleo, G. Schweicher and H. Sirringhaus, *Nat. Mater.*, 2020, **19**, 491–502.
5 D. F. Perepichka and F. Rosei, *Science*, 2009, **323**, 216–217.
6 M. S. Lohse and T. Bein, *Adv. Funct. Mater.*, 2018, **28**, 1705553.
7 H. V. Babu, M. G. M. Bai and M. Rajeswara Rao, *ACS Appl. Mater. Interfaces*, 2019, **11**, 11029–11060.
8 Y. Li, W. Chen, G. Xing, D. Jiang and L. Chen, *Chem. Soc. Rev.*, 2020, **49**, 2852–2868.
9 J. L. Segura, M. J. Mancheño and F. Zamora, *Chem. Soc. Rev.*, 2016, **45**, 5635–5671.
10 D. Zhou, X. Tan, H. Wu, L. Tian and M. Li, *Angew. Chem., Int. Ed.*, 2019, **58**, 1376–1381.
11 M. R. Rao, Y. Fang, S. De Feyter and D. F. Perepichka, *J. Am. Chem. Soc.*, 2017, **139**, 2421–2427.
12 W. Liu, X. Luo, Y. Bao, Y. P. Liu, G. H. Ning, I. Abdelwahab, L. Li, C. T. Nai, Z. G. Hu, D. Zhao, B. Liu, S. Y. Quek and K. P. Loh, *Nat. Chem.*, 2017, **9**, 563–570.
13 L. Cardenas, R. Gutzler, J. Lipton-Duffin, C. Fu, J. L. Brusso, L. E. Dinca, M. Vondráček, Y. Fagot-Revurat, D. Malterre, F. Rosei and D. F. Perepichka, *Chem. Sci.*, 2013, **4**, 3263–3268.
14 D. Cui, D. F. Perepichka, J. M. MacLeod and F. Rosei, *Chem. Soc. Rev.*, 2020, **49**, 2020–2038.
15 S. Wu, M. Li, H. Phan, D. Wang, T. S. Herng, J. Ding, Z. Lu and J. Wu, *Angew. Chem., Int. Ed.*, 2018, **57**, 8007–8011.
16 C. Li, Y. Wang, Y. Zou, X. Zhang, H. Dong and W. Hu, *Angew. Chem., Int. Ed.*, 2020, **59**, 9403–9407.
17 C. Ruiz, J. T. López Navarrete, M. C. Ruiz Delgado and B. Gómez-Lor, *Org. Lett.*, 2015, **17**, 2258–2261.
18 C. Ruiz, U. K. Pandey, R. Termine, E. M. García-Frutos, G. López-Espejo, R. P. Ortiz, W. Huang, T. J. Marks, A. Facchetti, M. C. Ruiz Delgado, A. Golemme and B. Gómez-Lor, *ACS Appl. Mater. Interfaces*, 2016, **8**, 26964–26971.
19 A. Benito-Hernández, U. K. Pandey, E. Cavero, R. Termine, E. M. García-Frutos, J. L. Serrano, A. Golemme and B. Gómez-Lor, *Chem. Mater.*, 2013, **25**, 117–121.
20 K. Q. Zhao, C. Chen, H. Monobe, P. Hu, B. Q. Wang and Y. Shimizu, *Chem. Commun.*, 2011, **47**, 6290–6292.
21 S. Gómez-Esteban, A. Benito-Hernandez, R. Termine, G. Hennrich, J. T. L. Navarrete, M. C. Ruiz Delgado, A. Golemme and B. Gómez-Lor, *Chem. – Eur. J.*, 2018, **24**, 3576–3583.
22 J. Guadalupe, A. M. Ray, E. M. Maya, B. Gómez-Lor and M. Iglesias, *Polym. Chem.*, 2018, **9**, 4585–4595.
23 V. R. Battula, H. Singh, S. Kumar, I. Bala, S. K. Pal and K. Kailasam, *ACS Catal.*, 2018, **8**, 6751–6759.
24 A. Valverde-González, C. G. López Calixto, M. Barawi, M. Gomez-Mendoza, V. A. De La Peña O'Shea, M. Liras, B. Gómez-Lor and M. Iglesias, *ACS Appl. Energy Mater.*, 2020, **3**, 4411–4420.
25 M. Echeverri, S. Gámez-Valenzuela, R. C. González-Cano, J. Guadalupe, S. Cortijo-Campos, J. T. López Navarrete, M. Iglesias, M. C. Ruiz Delgado and B. Gómez-Lor, *Chem. Mater.*, 2019, **31**, 6971–6978.
26 X. Liu, Y. Xu and D. Jiang, *J. Am. Chem. Soc.*, 2012, **134**, 8738–8741.
27 A. E. Sadak, E. Karakuş, Y. M. Chumakov, N. A. Dogan and C. T. Yavuz, *ACS Appl. Energy Mater.*, 2020, **3**, 4983–4994.
28 X. C. Li, Y. Zhang, C. Y. Wang, Y. Wan, W. Y. Lai, H. Pang and W. Huang, *Chem. Sci.*, 2017, **8**, 2959–2965.
29 A. V. Kuklin, G. V. Baryshnikov, B. F. Minaev, N. Ignatova and H. Ågren, *J. Phys. Chem. C*, 2018, **122**, 22216–22222.
30 Y. Jing and T. Heine, *J. Am. Chem. Soc.*, 2019, **141**, 743–747.
31 M. A. Springer, T. J. Liu, A. Kuc and T. Heine, *Chem. Soc. Rev.*, 2020, **49**, 2007–2019.
32 S. Thomas, H. Li, C. Zhong, M. Matsumoto, W. R. Dichtel and J. L. Bredas, *Chem. Mater.*, 2019, **31**, 3051–3065.
33 R. Gutzler and D. F. Perepichka, *J. Am. Chem. Soc.*, 2013, **135**, 16585–16594.
34 J. Wen, D. Luo, L. Cheng, K. Zhao and H. Ma, *Macromolecules*, 2016, **49**, 1305–1312.
35 R. Gutzler and Phys Chem, *Chem. Phys.*, 2016, **18**, 29029–29100.
36 D. J. Rizzo, Q. Dai, C. Bronner, G. Veber, B. J. Smith, M. Matsumoto, S. Thomas, G. D. Nguyen, P. R. Forrester, W. Zhao, J. H. Jørgensen, W. R. Dichtel, F. R. Fischer, H. Li, J. L. Bredas and M. F. Crommie, *Nano Lett.*, 2020, **20**, 963–970.
37 P. Albacete, J. I. Martínez, X. Li, A. López-Moreno, S. Mena-Hernando, A. E. Platero-Prats, C. Montoro, K. P. Loh, E. M. Pérez and F. Zamora, *J. Am. Chem. Soc.*, 2018, **140**, 12922–12929.
38 P. Zhu and V. Meunier, *J. Chem. Phys.*, 2012, **137**, 244703.
39 S. Thomas, H. Li, R. R. Dasari, A. M. Evans, I. Castano, T. G. Allen, O. G. Reid, G. Rumbles, W. R. Dichtel, N. C. Gianneschi, S. R. Marder, V. Coropceanu and J. L. Brédas, *Mater. Horiz.*, 2019, **6**, 1868–1876.
40 M. Reig, G. Bagdziunas, A. Ramanavicius, J. Puigdollers and D. Velasco, *Phys. Chem. Chem. Phys.*, 2018, **20**, 17889–17898.
41 A. Tripathi and C. Prabhakar, *J. Phys. Org. Chem.*, 2019, **32**, e3944.
42 A. Benito-Hernández, M. T. El-Sayed, J. T. López Navarrete, M. C. Ruiz Delgado and B. Gómez-Lor, *Org. Chem. Front.*, 2018, **5**, 1748–1755.
43 S. Royuela, E. Martínez-Periñán, M. P. Arrieta, J. I. Martínez, M. M. Ramos, F. Zamora, E. Lorenzo and J. L. Segura, *Chem. Commun.*, 2020, **56**, 1267–1270.
44 L. Li, Z. Cai, Q. Wu, W. Y. Lo, N. Zhang, L. X. Chen and L. Yu, *J. Am. Chem. Soc.*, 2016, **138**, 7681–7686.
45 G. V. Baryshnikov, B. F. Minaev, N. N. Karaush and V. A. Minaeva, *RSC Adv.*, 2014, **4**, 25843–25851.
46 L. Li, W. Y. Lo, Z. Cai, N. Zhang and L. Yu, *Macromolecules*, 2016, **49**, 6903–6909.
47 J. Wen, D. Luo, L. Cheng, K. Zhao and H. Ma, *Macromolecules*, 2016, **49**, 1305–1312.
48 R. Gutzler and D. F. Perepichka, *J. Am. Chem. Soc.*, 2013, **135**, 16585–16594.
49 S. Thomas, H. Li, R. R. Dasari, A. M. Evans, I. Castano, T. G. Allen, O. G. Reid, G. Rumbles, W. R. Dichtel, N. C. Gianneschi,

S. R. Marder, V. Coropceanu and J. L. Brédas, *Mater. Horiz.*, 2019, **6**, 1868–1876.

50 S. Jhulki, A. M. Evans, X. L. Hao, M. W. Cooper, C. H. Feriante, J. Leisen, H. Li, D. Lam, M. C. Hersam, S. Barlow, J. L. Brédas, W. R. Dichtel and S. R. Marder, *J. Am. Chem. Soc.*, 2020, **142**, 783–791.

51 P. V. R. Schleyer, C. Maerker, A. Dransfeld, H. Jiao and N. J. R. Van Eikema Hommes, *J. Am. Chem. Soc.*, 1996, **118**, 6317–6318.

52 T. K. Zywietz, H. Jiao, P. V. R. Schleyer and A. De Meijere, *J. Org. Chem.*, 1998, **63**, 3417–3422.

53 V. Coropceanu, J. Cornil, D. A. da Silva Filho, Y. Olivier, R. Silbey and J. L. Brédas, *Chem. Rev.*, 2007, **107**, 926–952.

54 C. Barreteau, F. Ducastelle and T. Mallah, *J. Phys.: Condens. Matter*, 2017, **29**, 465302.

55 R. R. Liang, S. Q. Xu, L. Zhang, A. Ru-Han, P. Chen, F. Z. Cui, Q. Y. Qi, J. Sun and X. Zhao, *Nat. Commun.*, 2019, **10**, 4609.

56 T. Y. Zhou, S. Q. Xu, Q. Wen, Z. F. Pang and X. Zhao, *J. Am. Chem. Soc.*, 2014, **136**, 15885–15888.

57 A. Nagai, Z. Guo, X. Feng, S. Jin, X. Chen, X. Ding and D. Jiang, *Nat. Commun.*, 2011, **2**, 536.

58 W. Shockley and H. J. Queisser, *J. Appl. Phys.*, 1961, **32**, 510–519.

59 E. M. García-Frutos, E. Gutierrez-Puebla, M. A. Monge, R. Ramírez, P. de Andrés, A. de Andrés, R. Ramírez and B. Gómez-Lor, *Org. Electron.*, 2009, **10**, 643–652.

60 E. M. García-Frutos, G. Hennrich, E. Gutierrez, A. Monge and B. Gómez-Lor, *J. Org. Chem.*, 2010, **75**, 1070–1076.

6. EXPERIMENTAL SECTION

The experimental sections are directly taken from the documents “supporting information” of each publications. They will appear in the same order as the publications.

Supporting Information

Fluorescent and Electroactive Monoalkyl BTD-based Liquid Crystals with Tunable Self-assembling and Electronic Properties.

Marcelo Echeverri,[1] Irene Martín,[1] Alberto Concellón,[2] Constanza Ruiz,[1] María San Anselmo,[2] Enrique Gutiérrez-Puebla,[1] José L. Serrano,[2] Berta Gómez-Lor*[1]

[1]Material Sciences Factory, Instituto de Ciencia de Materiales de Madrid, Cantoblanco, 20849-Madrid (Spain), Fax: (+34)913720623, E-mail: bgl@icmm.csic.es

[2]Departamento de Química Orgánica, Instituto de Nanociencia de Aragón, Universidad de Zaragoza-CSIC, 50009- Zaragoza (Spain)

Supporting Information

1. Copy of the ^{1}H NMR and ^{13}C NMR spectra of compounds 2-7

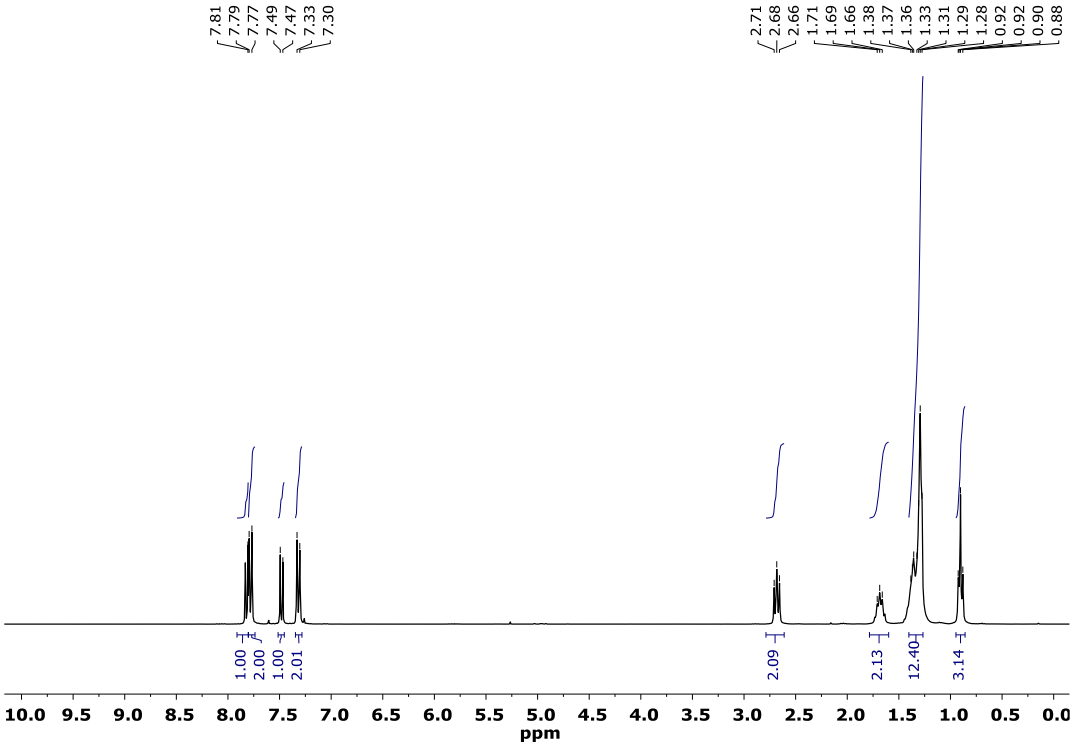

Figure S1. Copy of ^{1}H NMR spectrum (300 MHz, $CDCl_3$) of compound 2

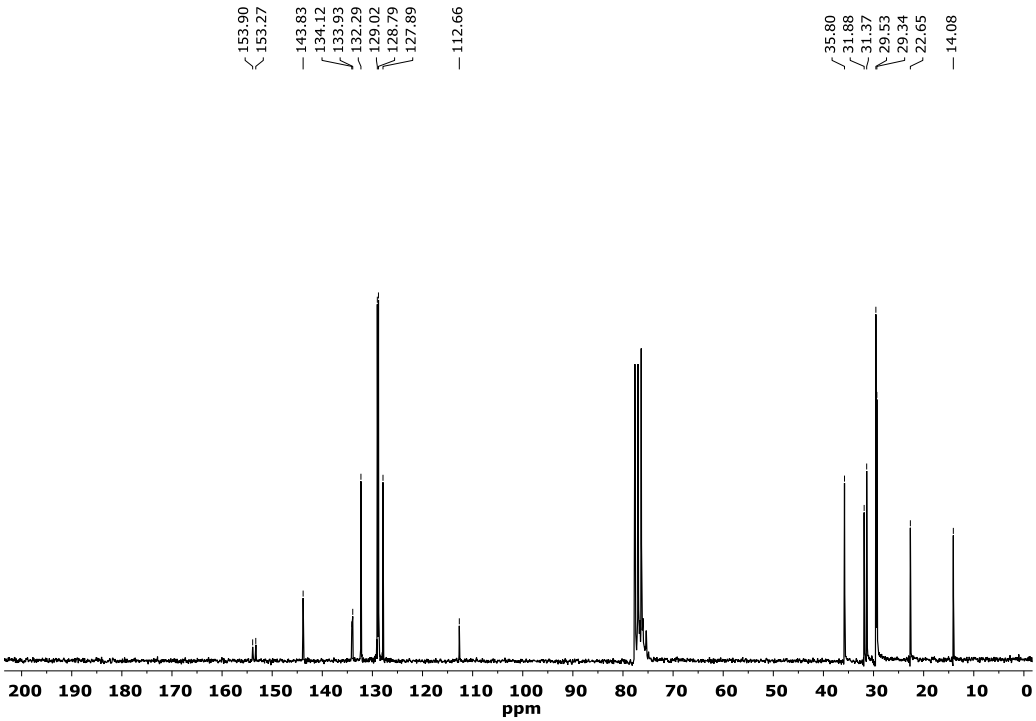

Figure S2. Copy of ^{13}C NMR spectrum (50 MHz, $CDCl_3$) of compound 2

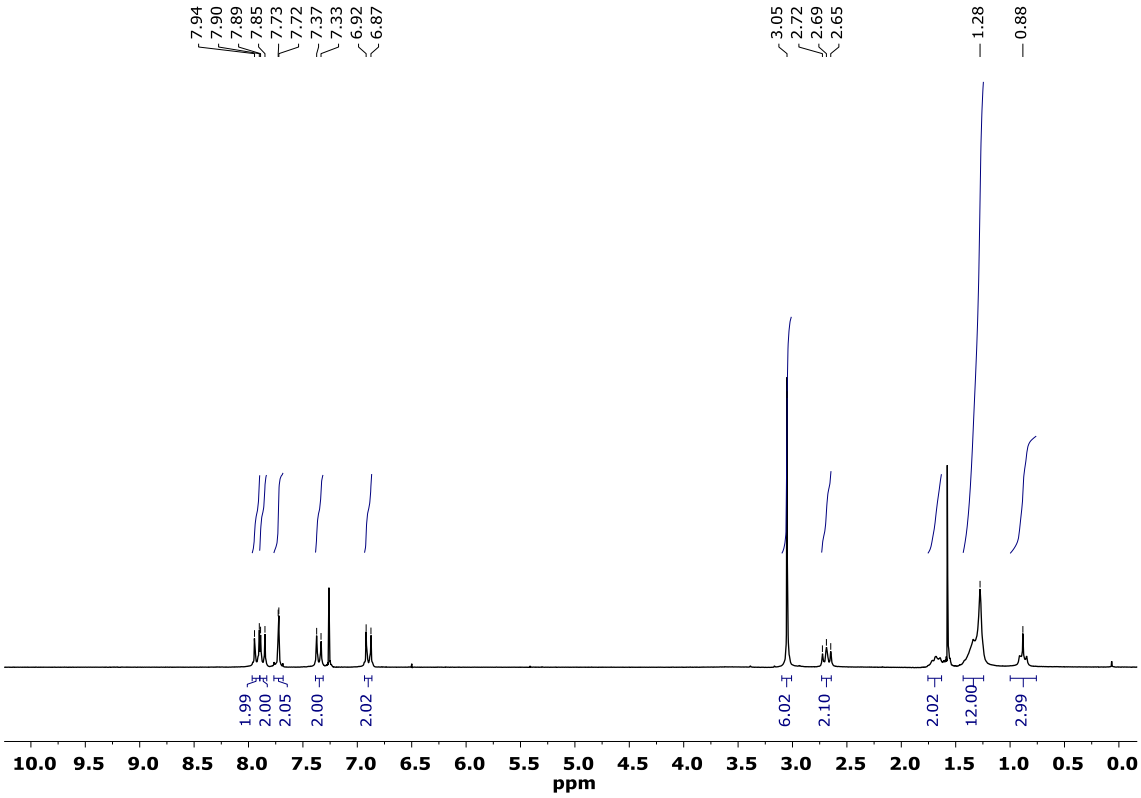

Figure S3. Copy of ^{1}H NMR spectrum (300 MHz, $CDCl_3$) of compound 3

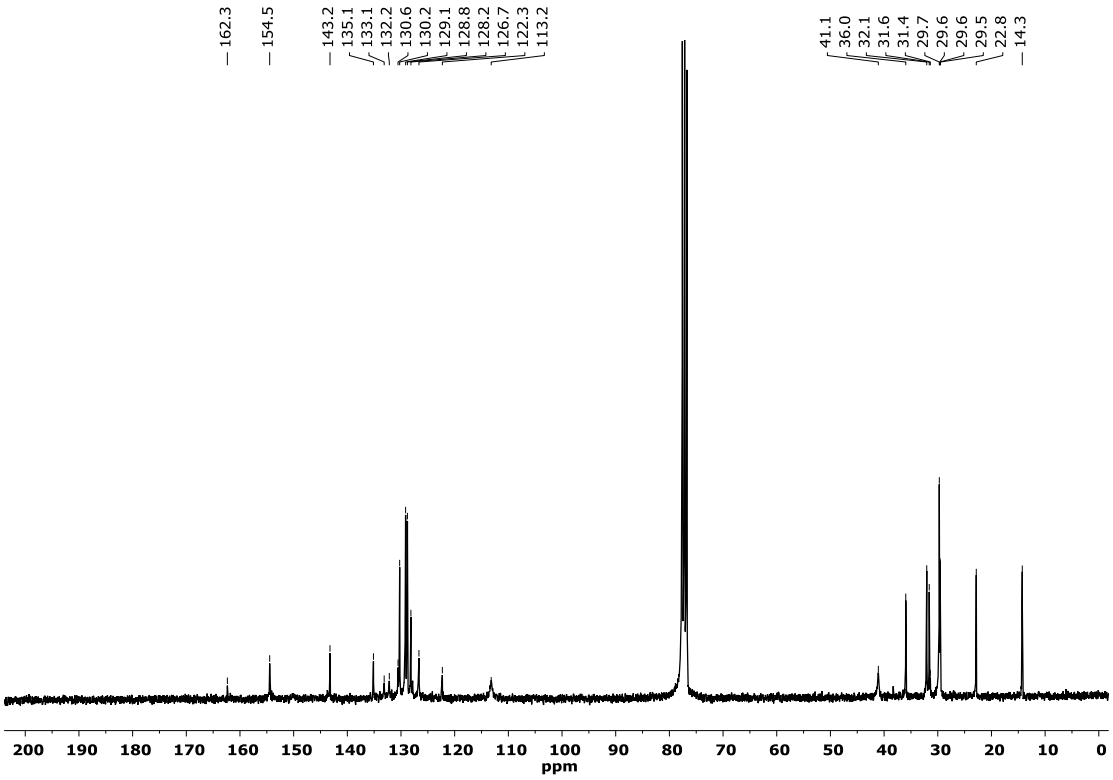

Figure S4. Copy of ^{13}C NMR spectrum (50 MHz, $CDCl_3$) of compound 3

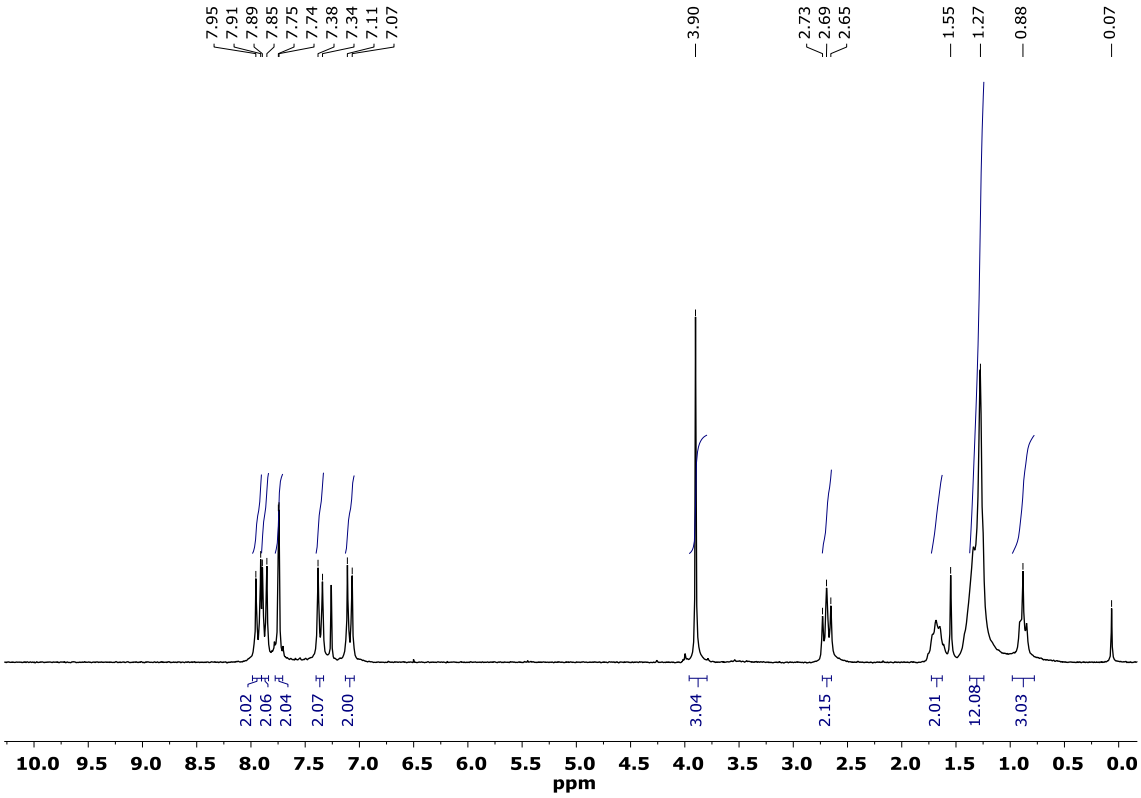

Figure S5. Copy of ^{1}H NMR spectrum (300 MHz, $CDCl_3$) of compound 4

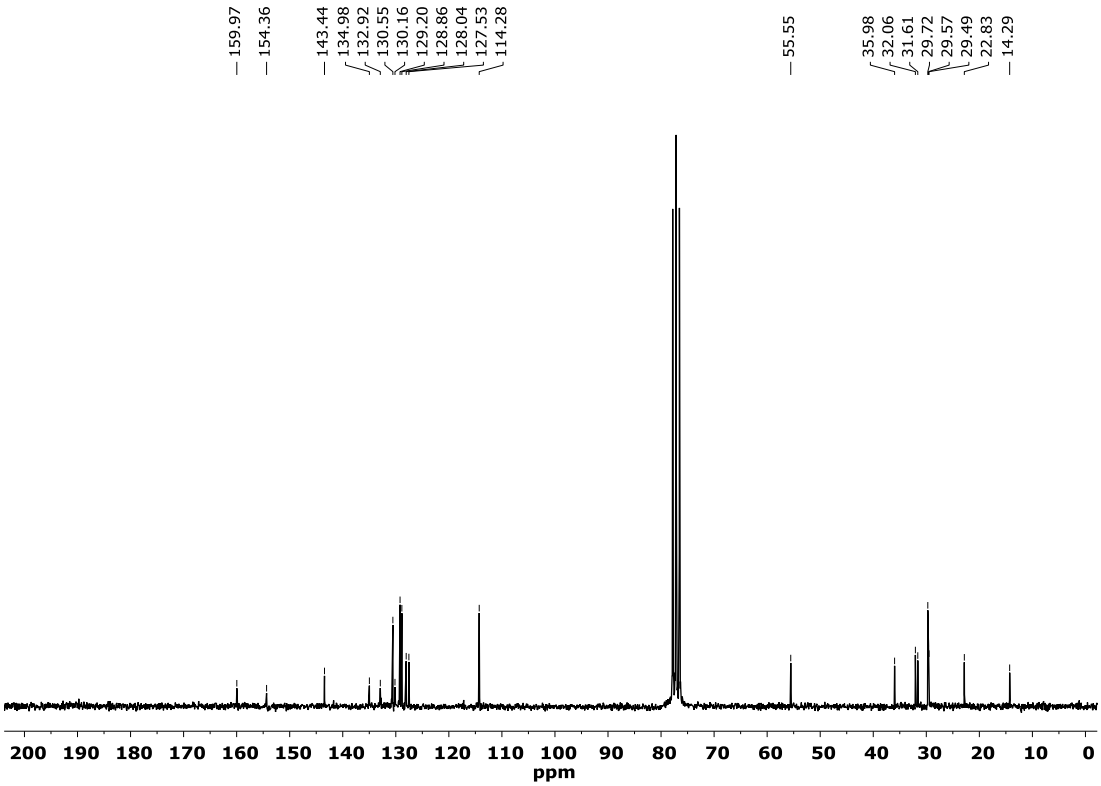

Figure S6. Copy of ^{13}C NMR spectrum (50 MHz, $CDCl_3$) of compound 4

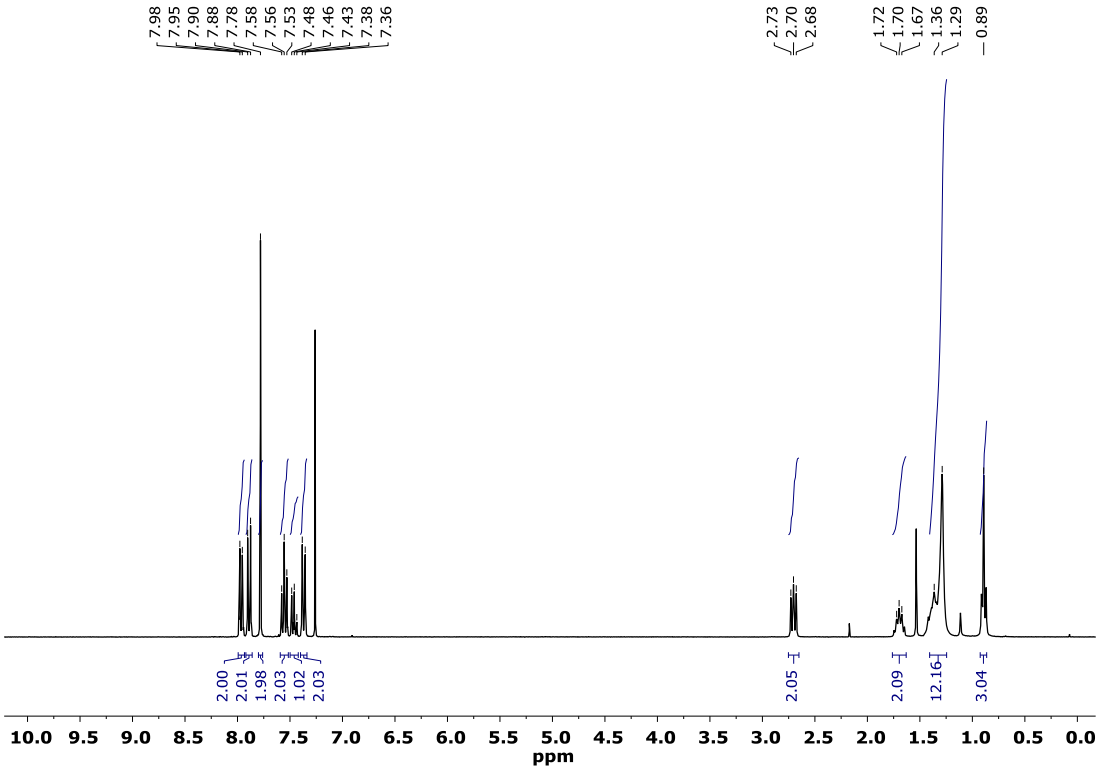

Figure S7. Copy of ^{1}H NMR spectrum (300 MHz, $CDCl_3$) of compound 5

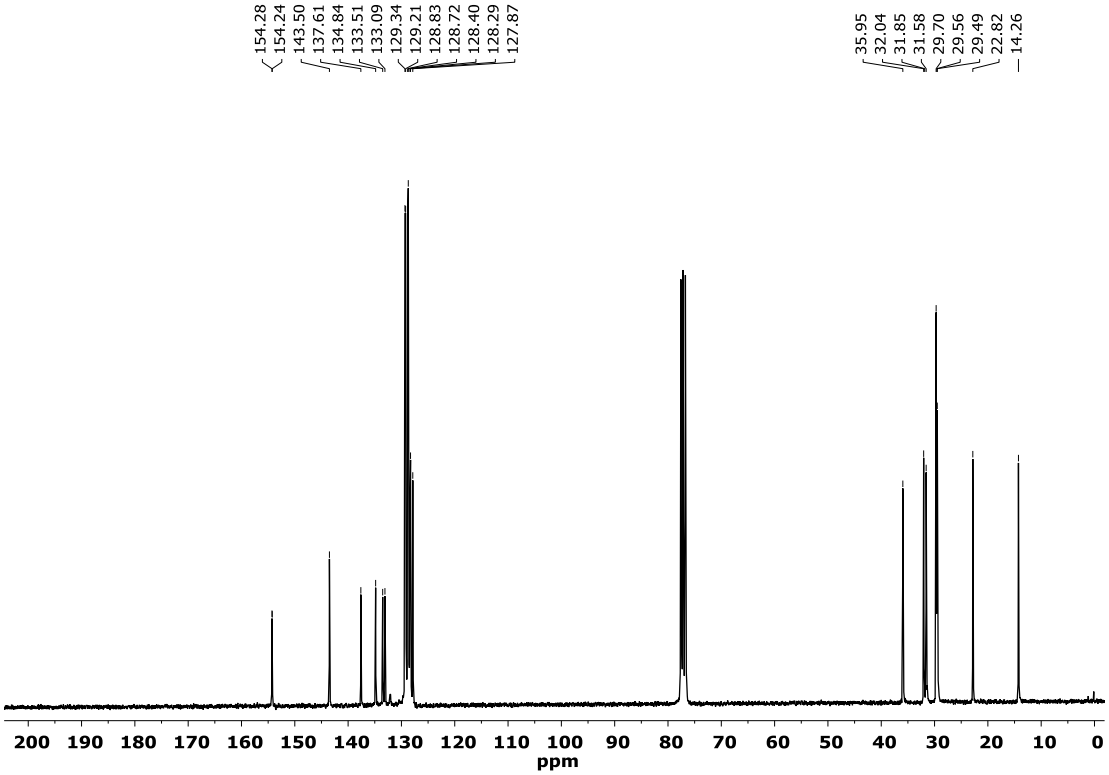

Figure S8. Copy of ^{13}C NMR spectrum (50 MHz, $CDCl_3$) of compound 5

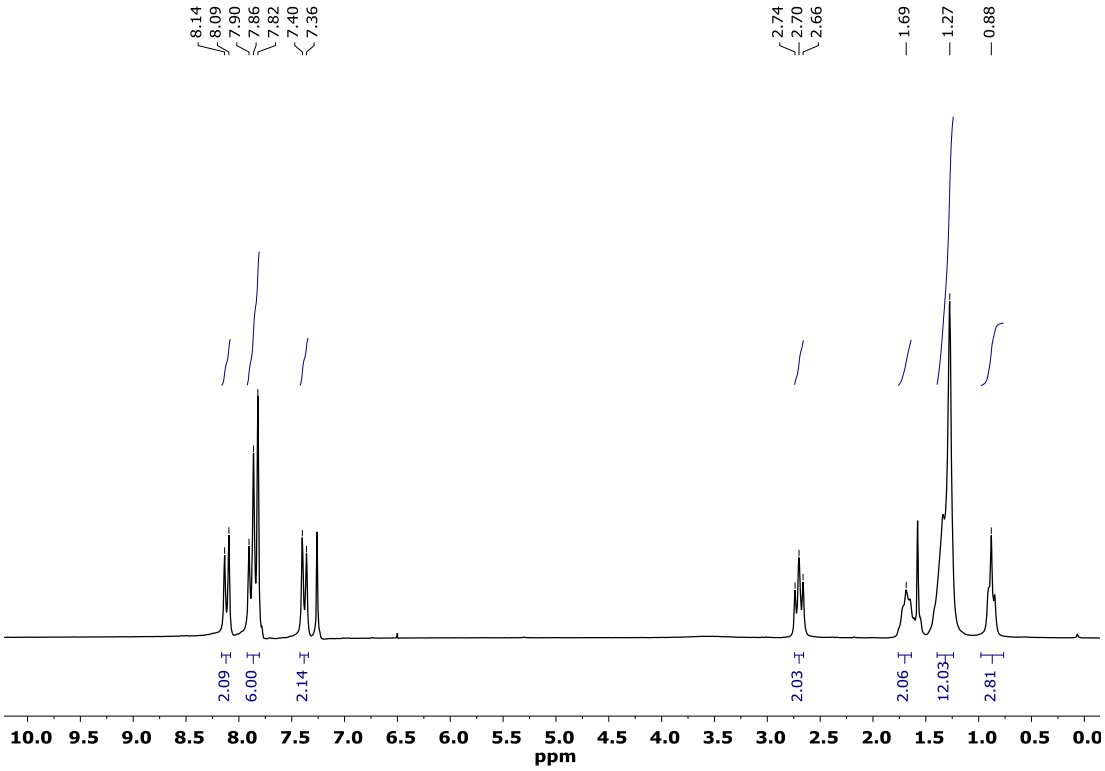

Figure S9. Copy of ^{1}H NMR spectrum (300 MHz, $CDCl_3$) of compound 6

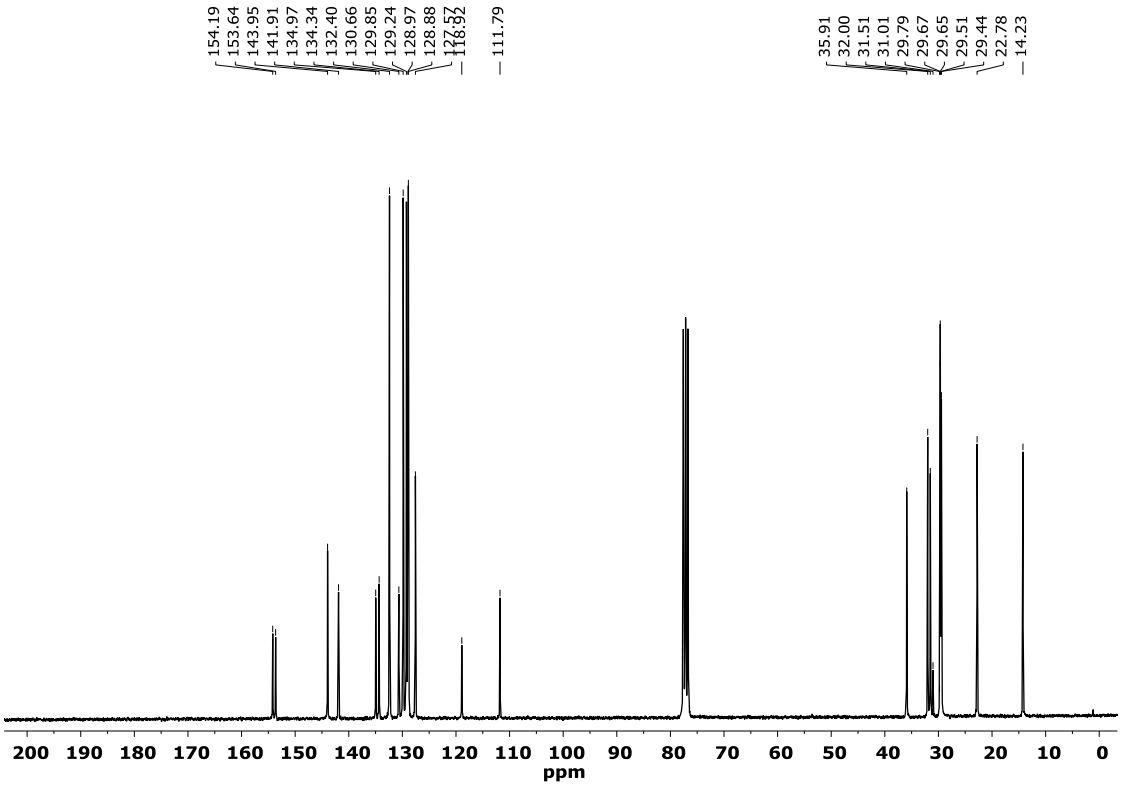

Figure S10. Copy of ^{13}C NMR spectrum (50 MHz, $CDCl_3$) of compound 6

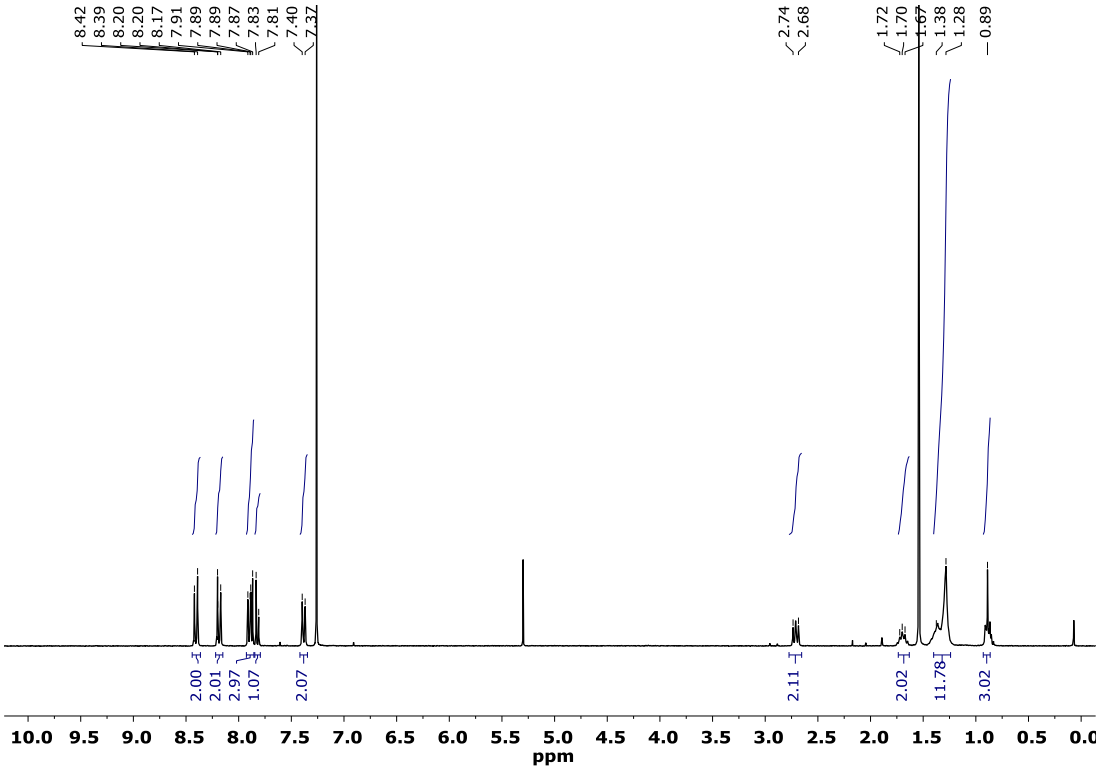

Figure S11. Copy of ^{1}H NMR spectrum (300 MHz, $CDCl_3$) of compound 7

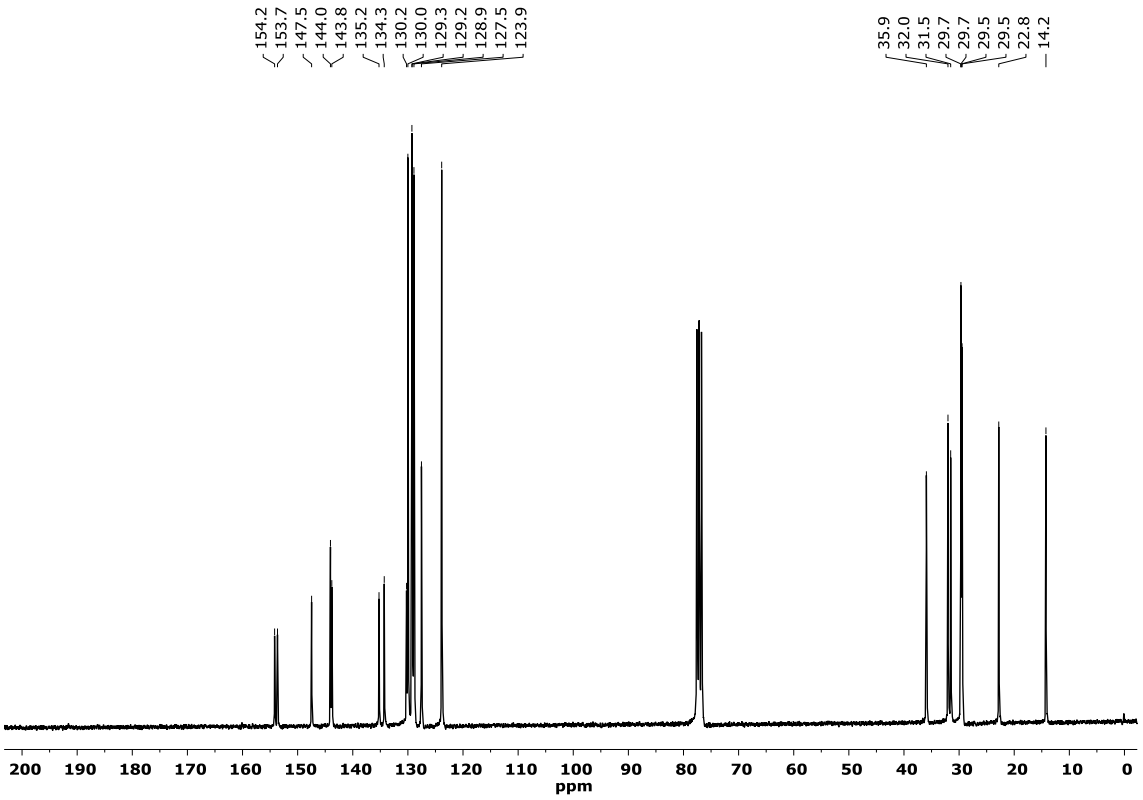

Figure S12. Copy of ^{13}C NMR spectrum (50 MHz, $CDCl_3$) of compound 7

2. Mesomorphic properties of compounds 3-6

Phase transitions of compounds 3-6

Compound	Phase transitions[b]	
	1st and 2nd Heating	1st Cooling
3	Cr 102 (31.2) I N+Cr 32 (-9.8) Cr 100 (28.5) I	I 88 (0.5) N 22 (2.9) N+Cr
4	Cr 101 (37.6) N 114 (0.4) I N+Cr 70 (-10.5) Cr 101 (37.2) N 114 (0.5) I	I 112 (0.5) N 48 (20.4) N+Cr
5	Cr 63 (32.6) I Cr 62 (31.2) I	I 26 (24.3) Cr
6	Cr_1 70 (7.2) Cr_2 94 (19.9) SmA 117 (0.6) I Cr_1 69 (4.9) Cr_2 92 (19.5) SmA 117 (0.7) I	I 114 (1.3) SmA 52 (27.7) Cr_1
7	Cr 106 (42.3) I Cr 106 (42.6) I	I 74 (0.5) N 32 (28.5) Cr

[a] Temperature at which 2% mass lost is detected in the thermogravimetric curve.
[b] DSC data from the first heating and cooling scans are on the first line, and data from the second heating are in the second line. Temperatures are read at the maximum of the corresponding peaks, and enthalpies (kJ/mol) are in brackets. Cr: crystal, N: nematic mesophase, SmA: smectic A mesophase, I: isotropic liquid.

Table S1. Phase transitions of **3-7**.

Differential Scanning Calorimetry traces of compounds 3-6

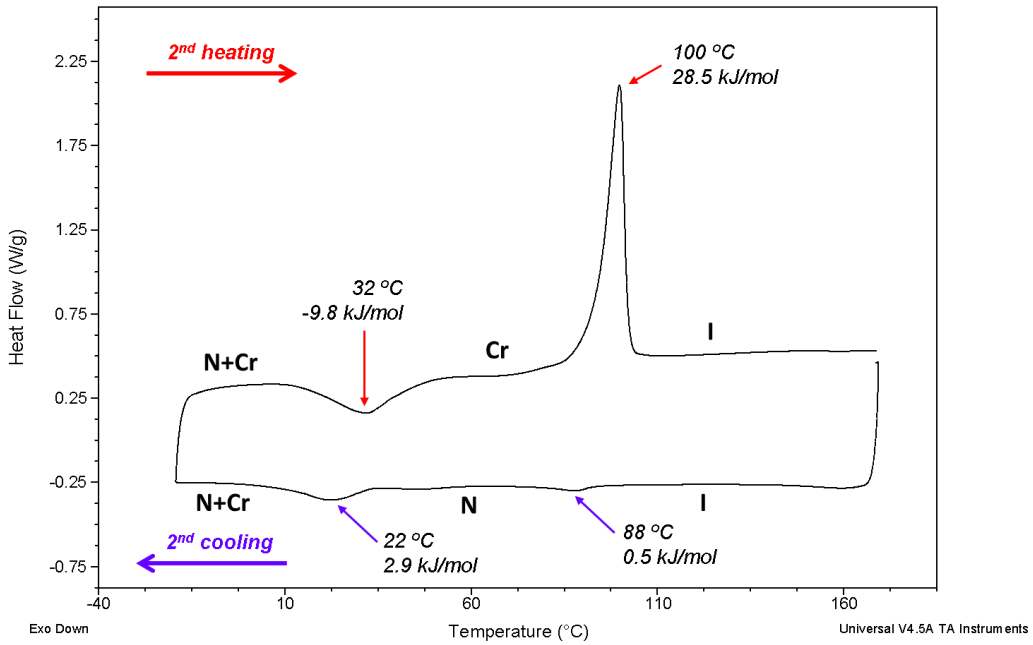

Figure S13. DSC traces of **3** corresponding to the second scan (10 $^{o}Cmin^{-1,}$ Exo down). Cr: crystal, N: nematic mesophase, I: isotropic liquid.

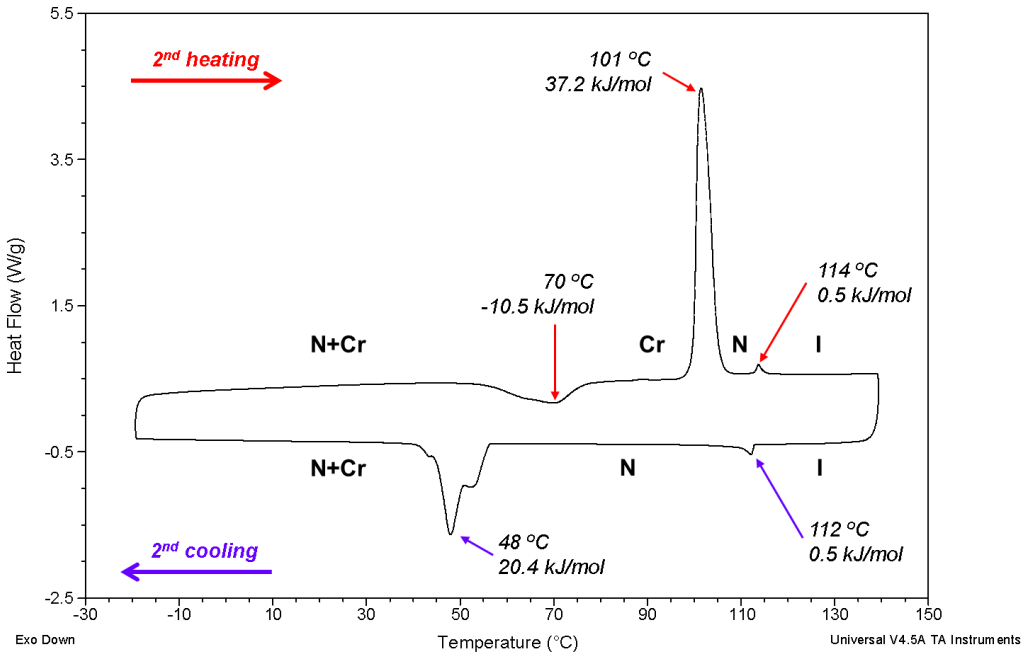

Figure S14. DSC traces of **4** corresponding to the second scan (10 ^{o}Cmin$^{-1,}$ Exo down). Cr: crystal, N: nematic mesophase, I: isotropic liquid.

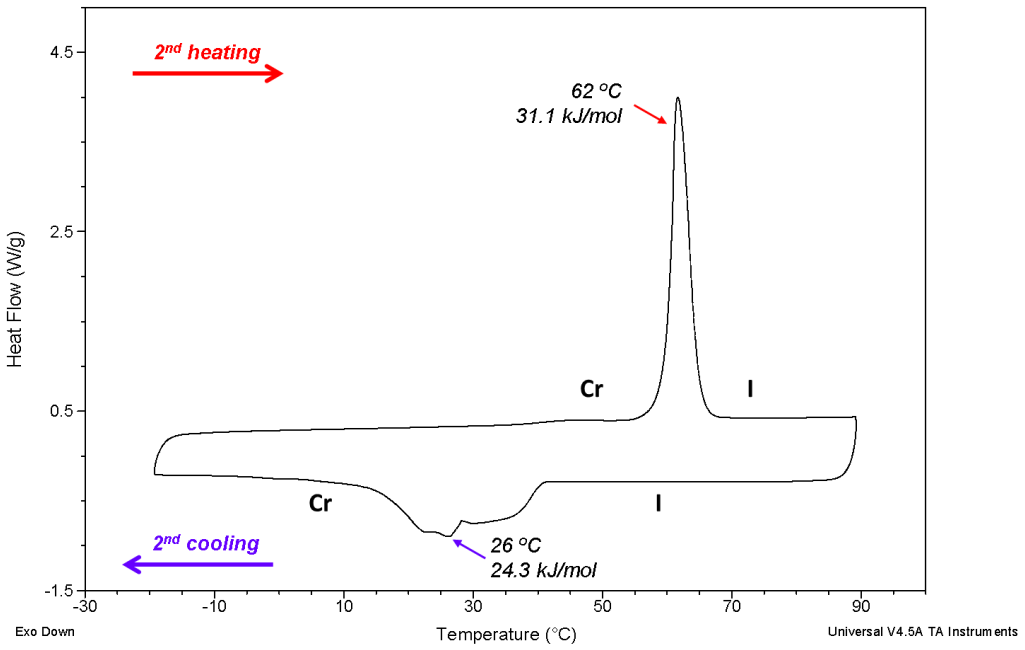

Figure S15. DSC traces of **5** corresponding to the second scan (10 ^{o}Cmin$^{-1,}$ Exo down). Cr: crystal, I: isotropic liquid.

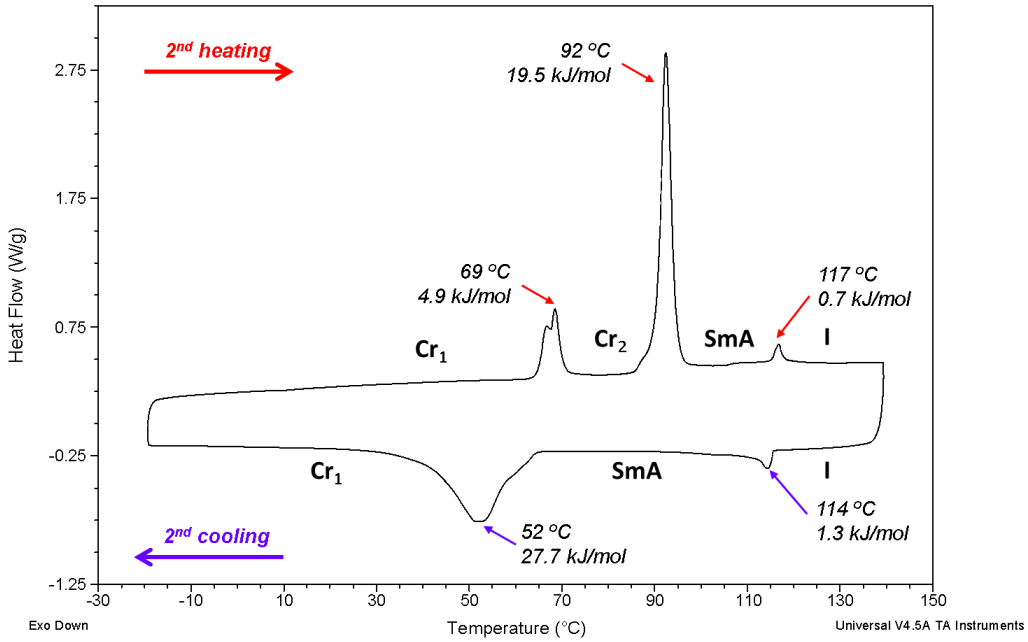

Figure S16. DSC traces of **6** corresponding to the second scan (10 °Cmin$^{-1,}$ Exo down). Cr: crystal, SmA: smectic A mesophase, I: isotropic liquid.

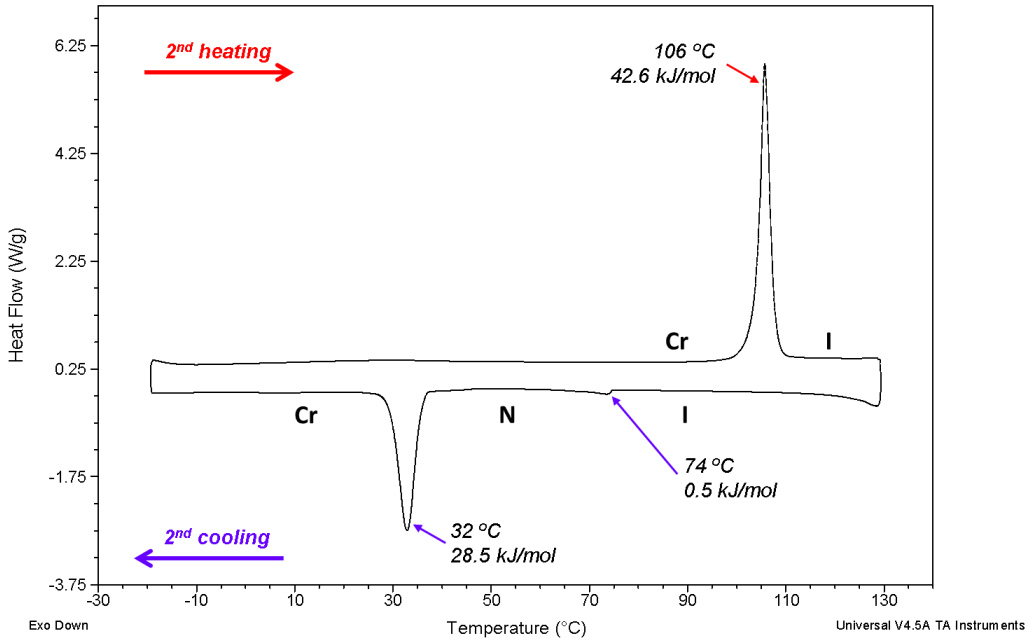

Figure S17. DSC traces of **7** corresponding to the second scan (10 °Cmin$^{-1,}$ Exo down). Cr: crystal, N: nematic mesophase, I: isotropic liquid.

POM microphotographs of 3-6 in the mesophases

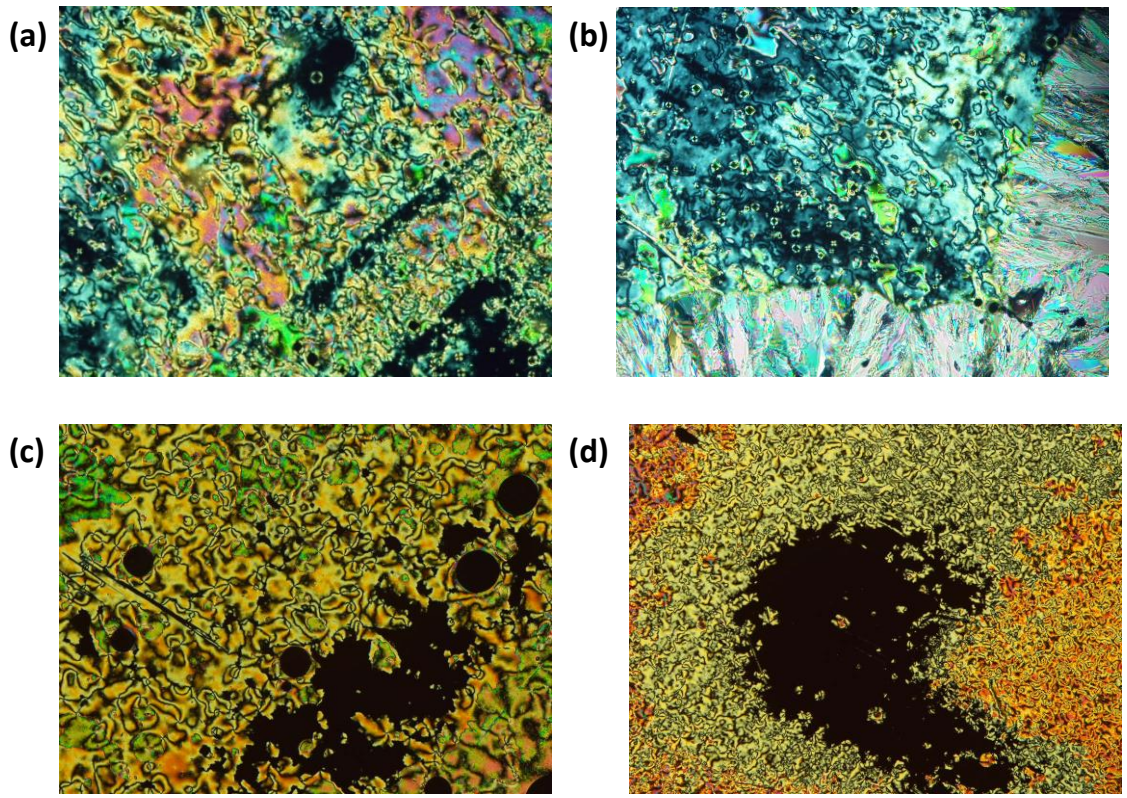

Figure S18. (a) Micrograph of the textures observed by POM for **4** at 90ºC (cooling, x20), (b) **4** at 50ºC (cooling, x20), (c) **6** at 110ºC (cooling, x50) and (d) **6** at 90ºC (cooling, x20).

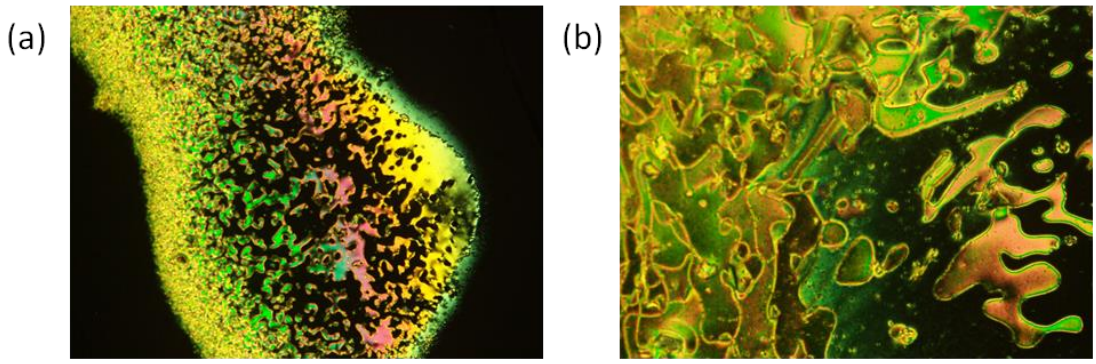

Figure S19. (a) Micrograph of the textures observed by POM for **3** at 75ºC (cooling, x20) and (b) **3** at 50ºC (cooling, x20).

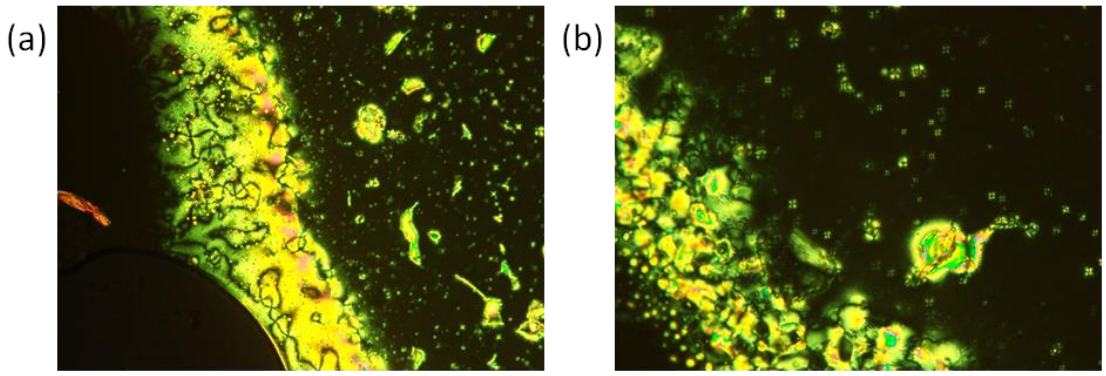

Figure S20. (a) Micrograph of the textures observed by POM for **7** at 70°C (cooling, x20) and (b) **7** at 75°C (cooling, x20).

X-Ray diffraction

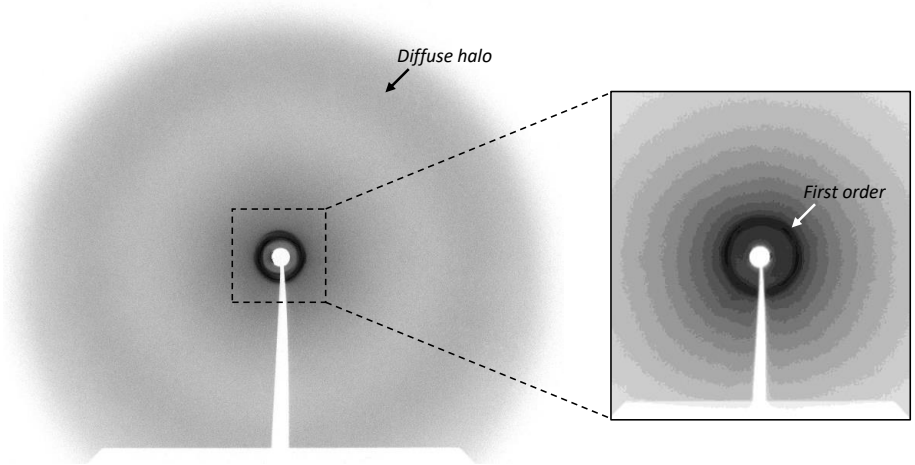

Figure S21. XRD pattern of **6** at 105°C in the SmA mesophase.

3. Linear spectroscopy: UV-Visible and fluorescence studies of compounds 3-7

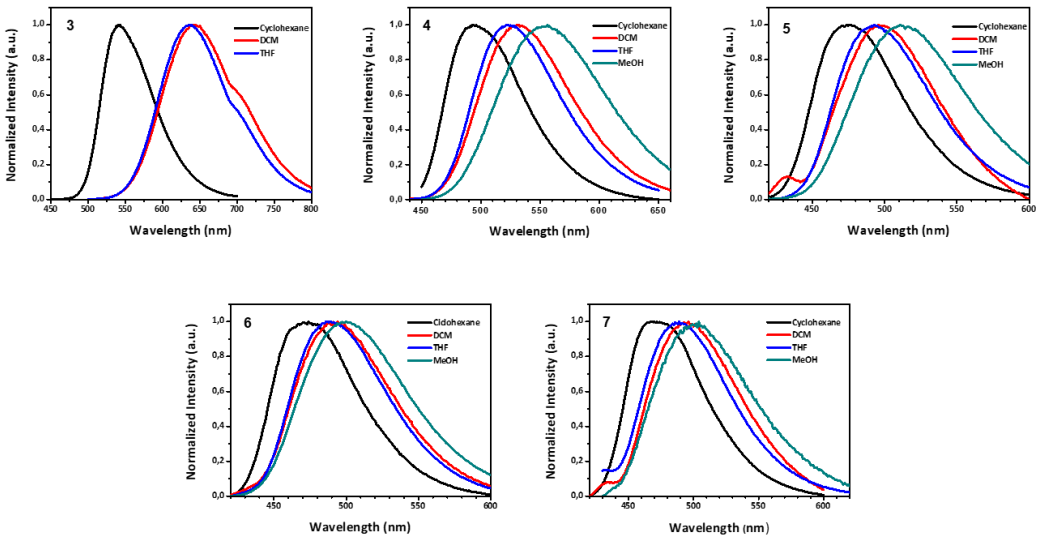

Figure S22. Normalized fluorescence spectra of compounds **3-7** in different solvents.

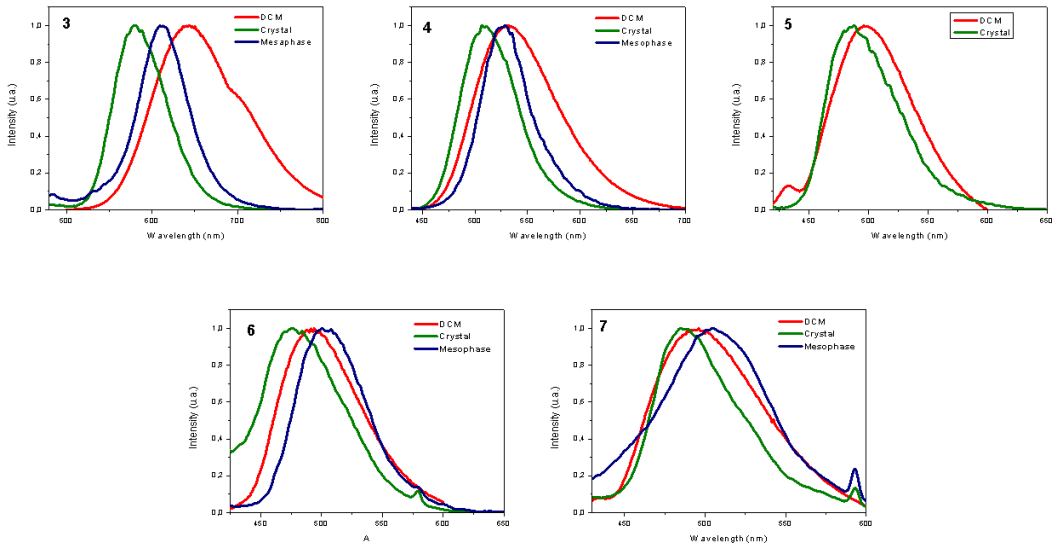

Figure S23. Comparison of the fluorescence spectra of compounds **3-7** in CH_2Cl_2, c = 5 x 10^{-6} M solution, solid state and in the mesophase.

Supporting Information

Untangling the Mechanochromic Properties of Benzothiadiazole-based Luminescent Polymorphs through Supramolecular Organic Framework Topology

Marcelo Echeverri†, Constanza Ruiz†, Sergio Gámez-Valenzuela‡, Irene Martín†, M. Carmen Ruiz Delgado‡ Enrique Gutiérrez-Puebla†, M. Ángeles Monge†, Lina M. Aguirre-Díaz†*, Berta Gómez-Lor†*

† Multifunctional and Supramolecular Materials group, Materials Science Factory, Instituto de Ciencia de Materiales de Madrid-Consejo Superior de Investigaciones Científicas (ICMM-CSIC), Sor Juana Inés de la Cruz 3, Cantoblanco 28049, Madrid, Spain. ‡ Department of Physical Chemistry, University of Málaga, Campus de Teatinos s/n, 29071, Málaga, Spain.

Table of Contents

1. Experimental Procedure

1.1. General

All reagents and solvents employed were commercially available and used as received without further purification. NMR spectra were recorded in a Bruker 200 equipment using $CDCl_3$ as solvent. Powder X-ray diffraction (PXRD) patterns were measured with a Bruker D8 diffractometer, with step size = 0.02° and exposure time = 0.5 s/step. UV-Visible studies were carried out on a PerkinElmer Lambda XLS+ spectrometer. Fluorescence spectra were recorded on an Aminco SLM 8000 spectrophotometer. PXRD measurements were used to check the purity of the obtained microcrystalline products by a comparison of the experimental results with the simulated patterns obtained from single-crystal X-ray diffraction data. The FT-Raman spectra (1064 nm) of both **1α** and **1β** polymorphs were recorded with an FT-Raman accessory kit (RamII)) linked to a Bruker Vertex70 spectrometer. A continuous-wave Nd-YAG laser working at λ=1064 nm was employed for excitation. A germanium detector operating at liquid nitrogen temperature was used. Raman scattering radiation was collected in a back-scattering configuration with a standard spectral resolution of 4 cm^{-1}. The power of the laser beam was kept at a level lower than 100 mW in all cases. Around 3000–4000 scans were averaged for each spectrum to optimize the signal-to-noise ratio.

1.2 Synthesis and characterization of 4-bromo-7-(4-nonylphenyl)benzo[*c*][1,2,5]thiadiazole (1).

A mixture of 4,7-dibromo[c][1,2,5]thiadizole (200 mg, 0,68mmol), $Pd(PPh_3)_4$ (227 mg, 0.31 mmol), 4-nonylphenyl boronic acid (168 mg, 0,68 mmol) in 0.5 mL of 2M aqueous K_2CO_3 and 5 mL of THF was degassed. The solution was irradiated with Anton Paar microwave irradiator (CEM) at 150°C (80W) for 180 min. The mixture was diluted with CH_2Cl_2, washed with water, and dried ($MgSO_4$); the solvent was then evaporated and the residue was purified by chromatography with CH_2Cl_2 /hexane (1:3) to give a yellow solid 1 (191mg, 68%). 1H NMR (200 MHz, $CDCl_3$)δ 7.80 (dd, J = 11.3, 7.9 Hz, 3H), 7.48 (d, J = 7.6 Hz, 1H), 7.32 (d, J = 8.1 Hz, 2H), 2.71-2.66 (m, 2H), 1.69-1.66 (m, 2H), 1.37-1.28 (m, 12H), 0.92-0.88 (m, 3H). 13C NMR (50 MHz, $CDCl_3$) δ 153.9, 153.3, 143.8, 134.1, 133.9, 132.3, 129.0, 128.8, 127.9, 112.7, 35.8, 31.9, 31.4, 29.5, 29.3, 22.7, 14.1. FAB MS m/z 417.41 (M+); HRMS (FAB) calcd. for $C_{21}H_{25}N_2SBr$: 416.0922, found: 416.0923.

1.3 Copy of ^{1}H-NMR and ^{13}C-NMR spectra of 1

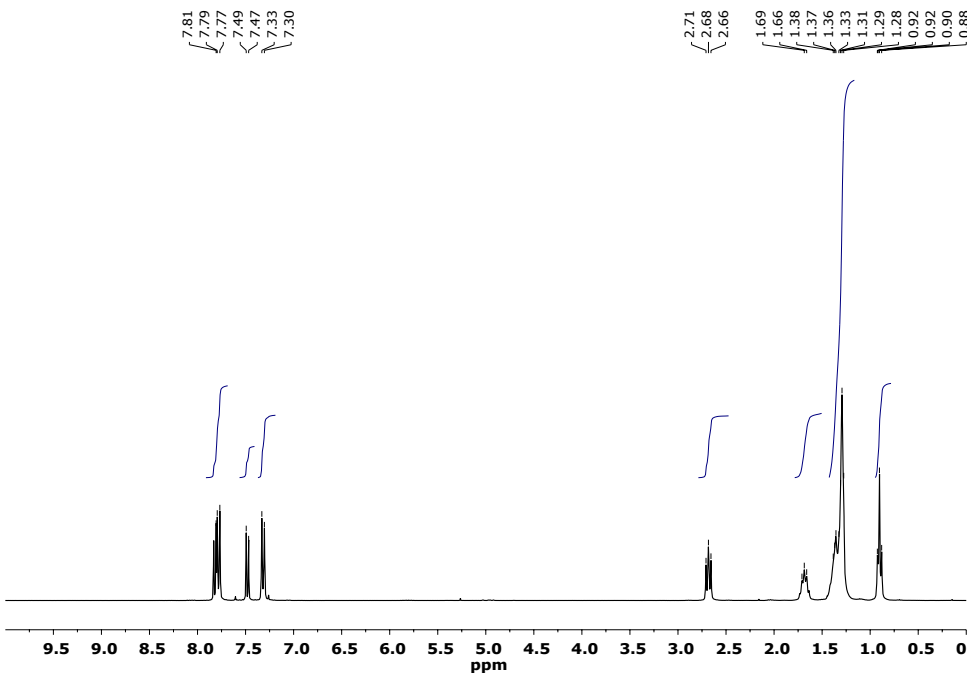

Figure S1. 1H-NMR experimental spectra for the 4-bromo-7-(4 nonylphenyl)benzo[c][1,2,5]thiadiazole compound.

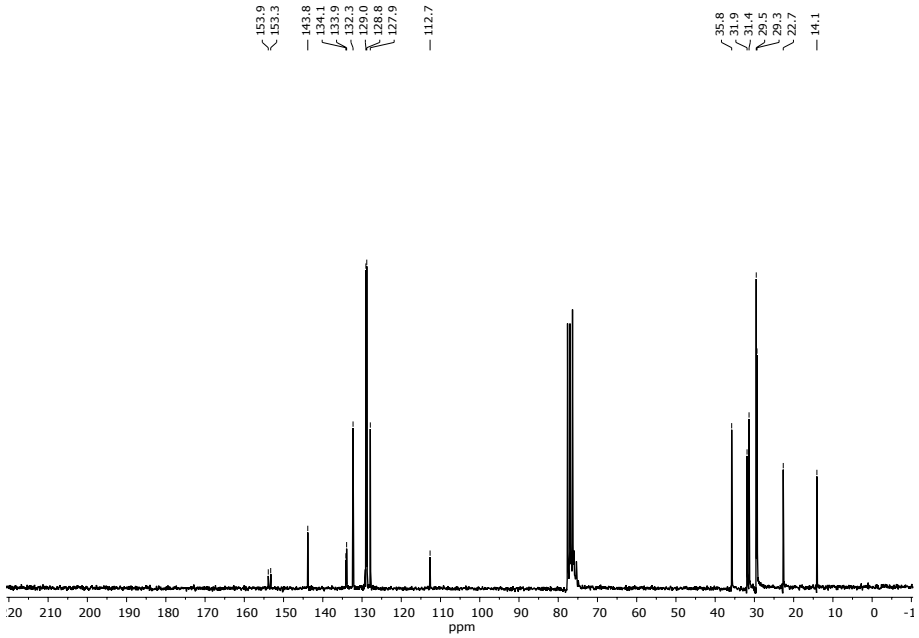

Figure S2. ^{13}CNMR experimental spectra for the 4-bromo-7-(4 nonylphenyl)benzo[c][1,2,5]thiadiazole compound.

2. Photophysical characterization

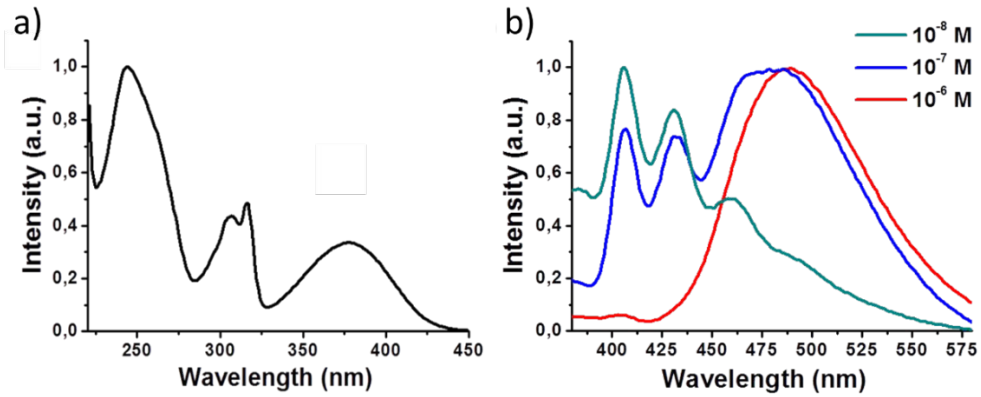

Figure S3. UV-vis absorption spectrum of 1 in a 10^{-5} M CH_2Cl_2 solution (a) and variation of the fluorescence spectrum of 1 in CH_2Cl_2 solution upon increasing the concentration (b).

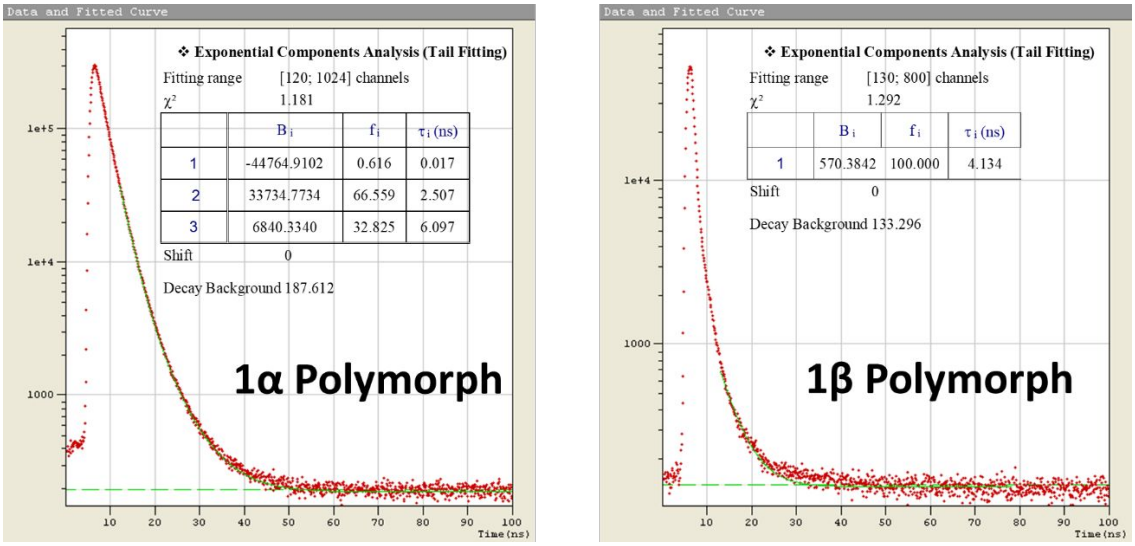

Figure S4. Fluorescence decays of polymorphs α and β with an excitation wavelength of 370 nm. Decays show biexponential and monoexponential character for α and β.

3. Single crystal X-ray structure determination

Table S1 summarizes the main crystal and refinement data for **1α** and **1β** polymorphs. Crystals were selected under a polarizing optical microscope and glued on a glass fiber for a single-crystal X-ray diffraction experiment. Single-crystal X-ray data were obtained in a Bruker four circle kappa-diffractometer equipped with a Cu INCOATED microsource, operated at 30 W power (45kV, 0.60mA) to generate Cu Kα radiation (λ = 1.54178 Å), and a Bruker VANTEC 500 area detector (microgap technology). Single crystal X-Ray diffraction data were collected exploring over a hemisphere of the reciprocal space in a combination of φ and ω scans to reach a resolution of 0.86 Å, using a Bruker APEX2[1] software suite (each exposure of 40 s covered 1º in ω. Unit cell dimensions were determined for least-squares fit of reflections with I > 20 σ. A semi-empirical absorption and scale correction based on equivalent reflection was carried out using SADABS.[2] The space group determination was carried out using XPREP.[3] The structures were solved by direct methods. The final cycles of refinement were carried out by full-matrix least-squares analyses with anisotropic thermal parameters of all non-hydrogen atoms. The hydrogen atoms were fixed at their calculated positions using distances and angle constraints. All calculations were performed using SMART[4] and APEX2[1] software for data collection, SAINT[2] for data reduction, SHELXTL[3] and OLEX2[5] to resolve and refine the structure respectively. CCDC 1536460 and CCDC 1536461 contain the supplementary crystallographic data for **1α** and **1β** polymorphs respectively.

Table S1. Main crystallographic and refinement data for the different isolated crystals of **1α** and **1β** polymorphs.

Compound	**1α**	**1β**
Formula	$C_{21}H_{25}BrN_2S$	$C_{21}H_{25}BrN_2S$
Molecular Weight /gmol^{-1}	417.40	417.39
Temperature/K	223(2)	223(2)
Wavelength/Å	1.54178	1.54178
Crystal System	Monoclinic	Triclinic
Space Group	$P2_1/c$	*P-1*
a/Å	16.0916(6)	13.7998(5)
b/Å	7.4220(4)	13.8498(6)
c/Å	33.1407(12)	16.5347(6)
α/°	90	81.092(2)
β/°	99.948(2)	86.1640(10)
γ/°	90	70.111(2)
V/Å3	4259.9(8)	2935.5(2)
Z	8	6
Dx/ g.cm-3	1.445	1.417
μ/mm-1	3.851	3.888
F(000)	1728	1296
GOF F2	0.995	1.022
Final R indexes [I>2σ(I)]	R1: 0.0700 wR2: 0.1815	R1: 0.0466 wR2: 0.1500
R indices (all data)	R1: 0.1320 wR2: 0.2370	R1: 0.0679 wR2: 0.2120

4. PXRD for mechanochromic and vapochromism in 1α and 1β polymorphs

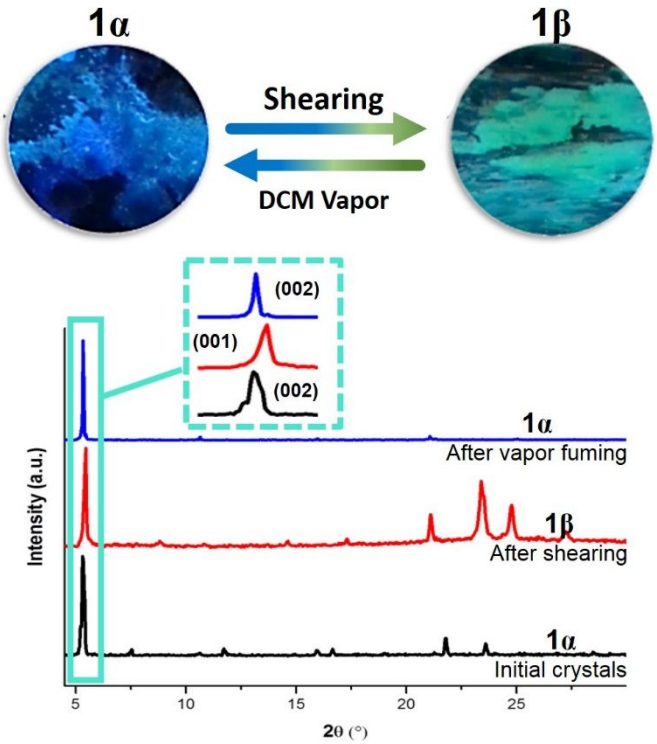

Figure S5. Above: Photograph of the reversible interconversion of both polymorphs under different conditions (viewed upon irradiation with a 365 nm lamp). Below: Interconversion process followed by PXRD showing the pattern changes from samples of **1α** and **1β** polymorphs.

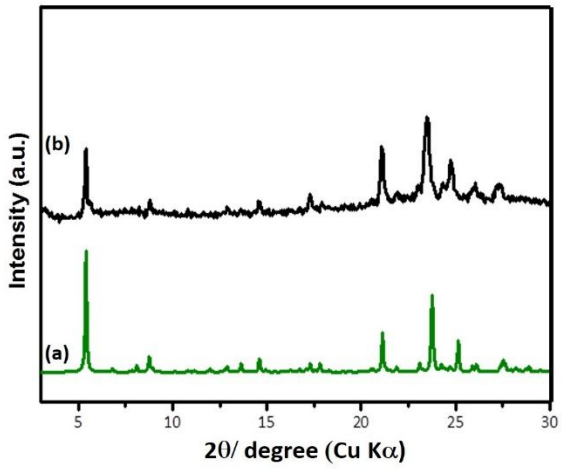

Figure S6. PXRD patterns (a) Simulated pattern of **1β** obtained using the single crystal data (b) Experimental pattern of the sample obtained after sheared **1α** with a spatula on a substrate.

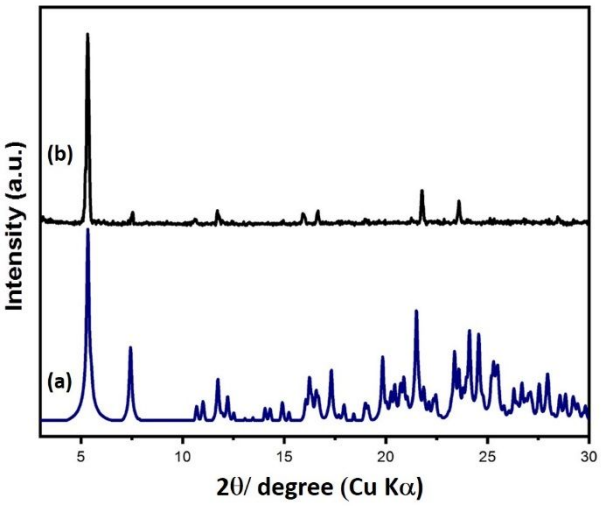

Figure S7. PXRD patterns (a) Simulated pattern of **1α** obtained using the single crystal data (b) Experimental pattern of a film of **1β** after exposure to CH_2Cl_2 vapors.

4. Differential Scanning Calorimetry and Thermal study

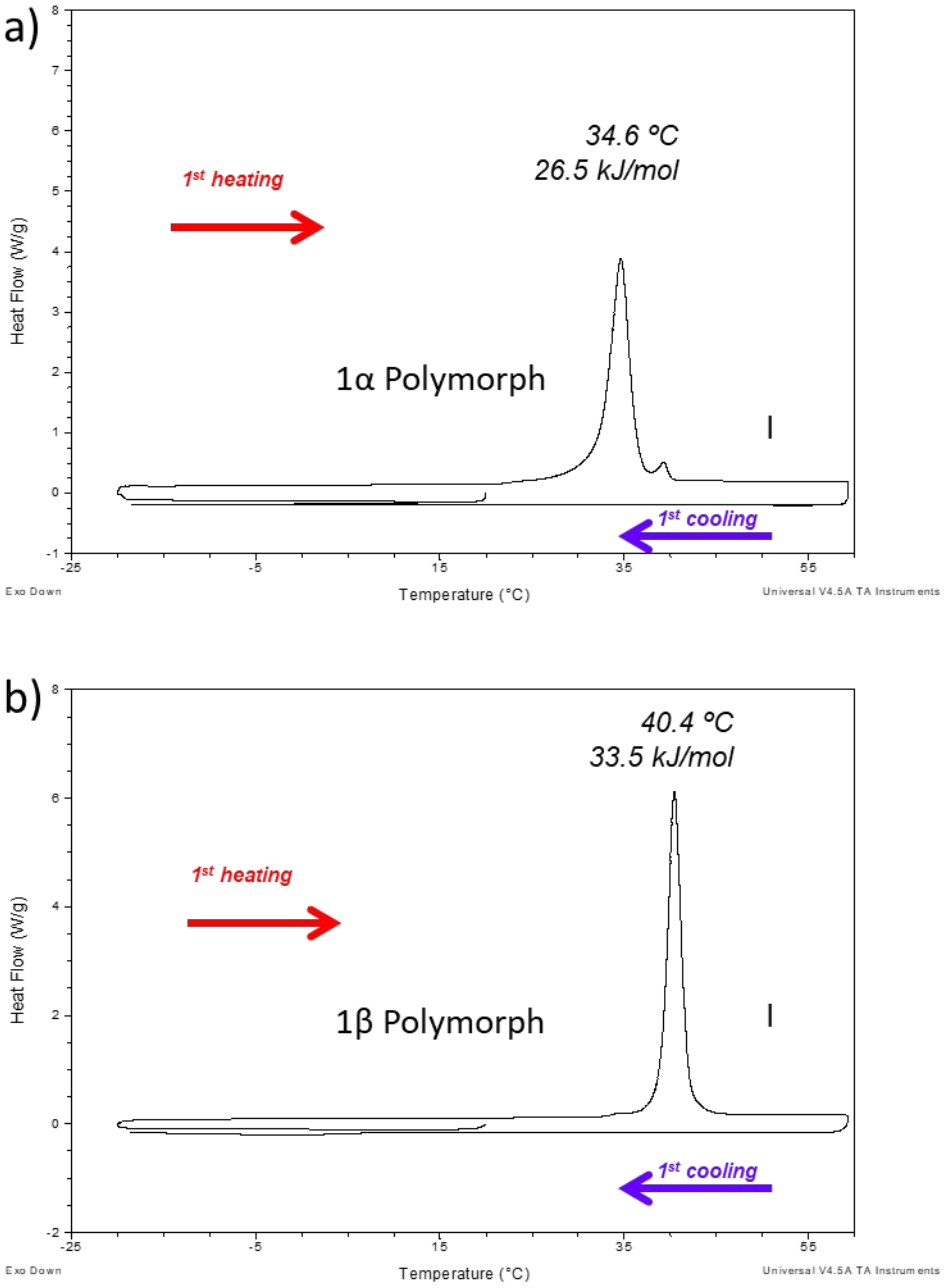

Figure S8. DSC traces of **1α** (a) and **1β** (b) corresponding to first scan (10 $^{o}Cmin^{-1,}$ Exo down). I: isotropic liquid.

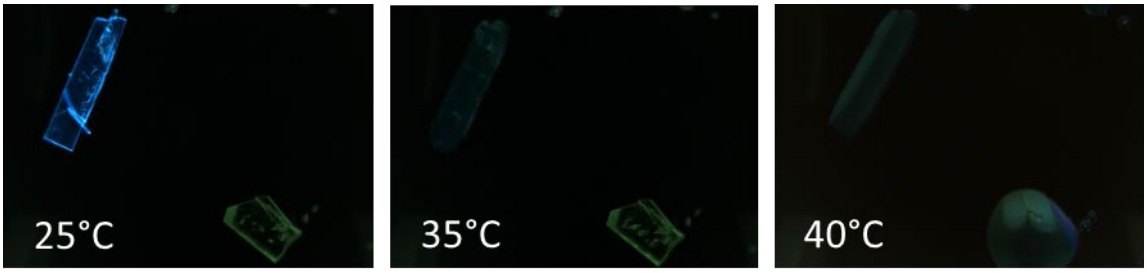

Figure S9. Photomicrograph of both polymorphs (viewed under irradiation with a 365 nm lamp) upon thermal heating.

5. Computational details and DFT calculations

4.1. Computational details

The calculations were performed at the Density Functional Theory (DFT) level using the GAUSSIAN16 program.[7] The B3LYP[8-9]and ωB97XD[10] functional and a 6-31G** basis set[11-12] were considered. The molecular geometry of monomer 1 was fully optimized in solution by using the SCRF (self-consistent-reaction-field) theory using the PCM (Polarized Continuum Model) approach.[13] No imaginary frequencies were observed, which ensures the finding of the global minimum energy. The simulated Raman spectrum was calculated from a previously optimized monomer system at the B3LYP/6-31G** level.

In solid state, the molecular structures for a tetramer (**1α** polymorph) and a hexamer (**1β** polymorph) were directly extracted from the crystal data, and the experimentally obtained structure was maintained for the rest of calculations. The vertical electronic excitation energies were computed by using the time-dependent DFT (TD-DFT) approach[14-15] at the ωB97XD/6-31G** level on the resulted molecular geometries. Absorption spectra were simulated through convolution of the vertical transition energies and oscillator strengths with Gaussian functions (half width at half-maximum of 0.33 eV). Vibrational eigenvector and molecular orbitals were plotted using the Chemcraft 1.8 molecular modelling software.[16]

4.2. DFT Calculations

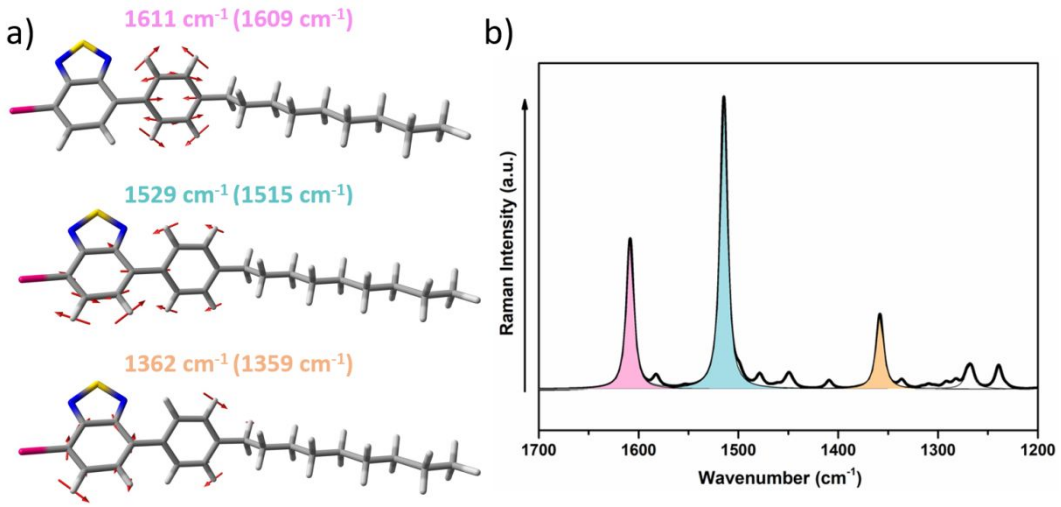

Figure S10. Theoretical Raman spectrum and vibrational eigenvectors associated with the most outstanding C=C/C-C Raman features for the previously optimized structure of 1 at B3LYP/6-31G** level. The experimental and theoretical (in parentheses) wavenumbers are also shown.

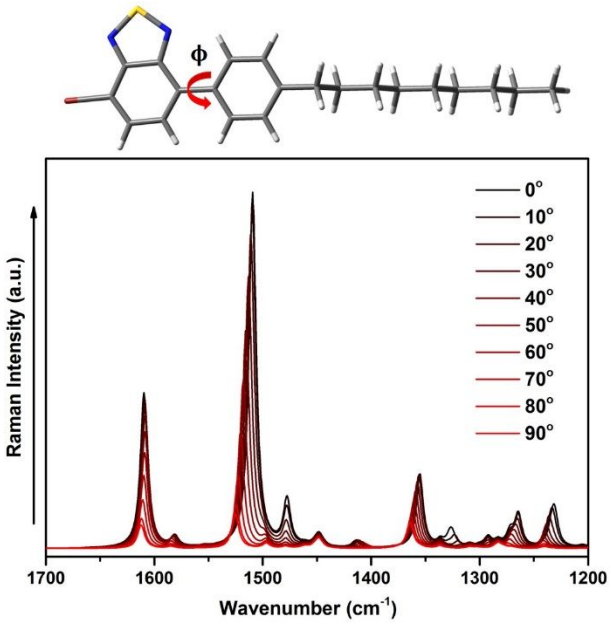

Figure S11. Frequency shifting of the main Raman bands upon twisting increment between the BTD and phenyl rings of 1 at B3LYP/6-31G** level.

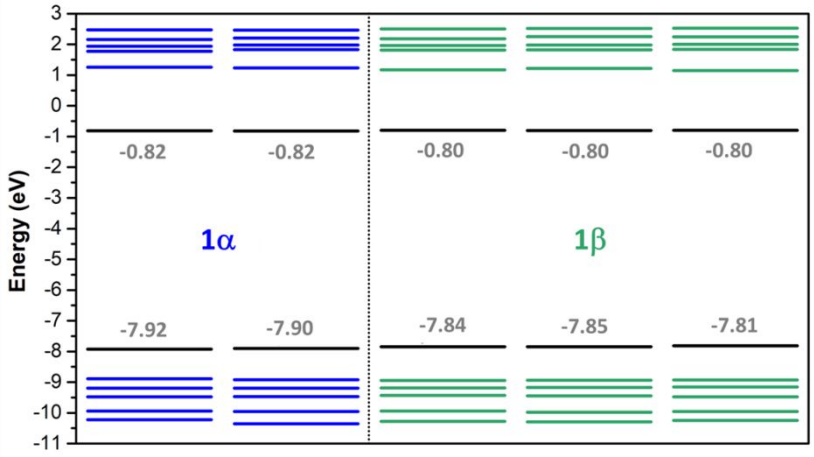

Figure S12. DFT-calculated molecular orbital energies (B3LYP/6-31G** level) for the isolated molecules extracted from polymorphs**1α** and **1β** respectively.

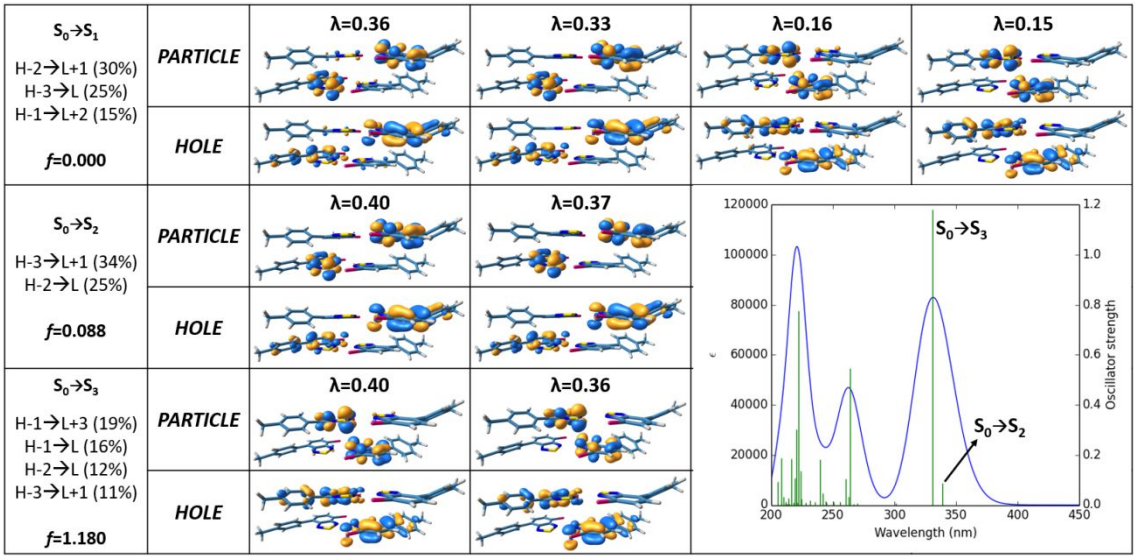

Figure S13. Simulated absorption spectra and main excitations (shown as vertical bars) for the tetrameric aggregate extracted from the X-ray structure analysis of **1α** polymorph. Hole- and electron natural transition orbitals (NTO) for the excited states responsible to the lowest energy band are also shown. The computations were done at the TD-DFT level, by using ωB97XD functional and 6-31G** basis set.

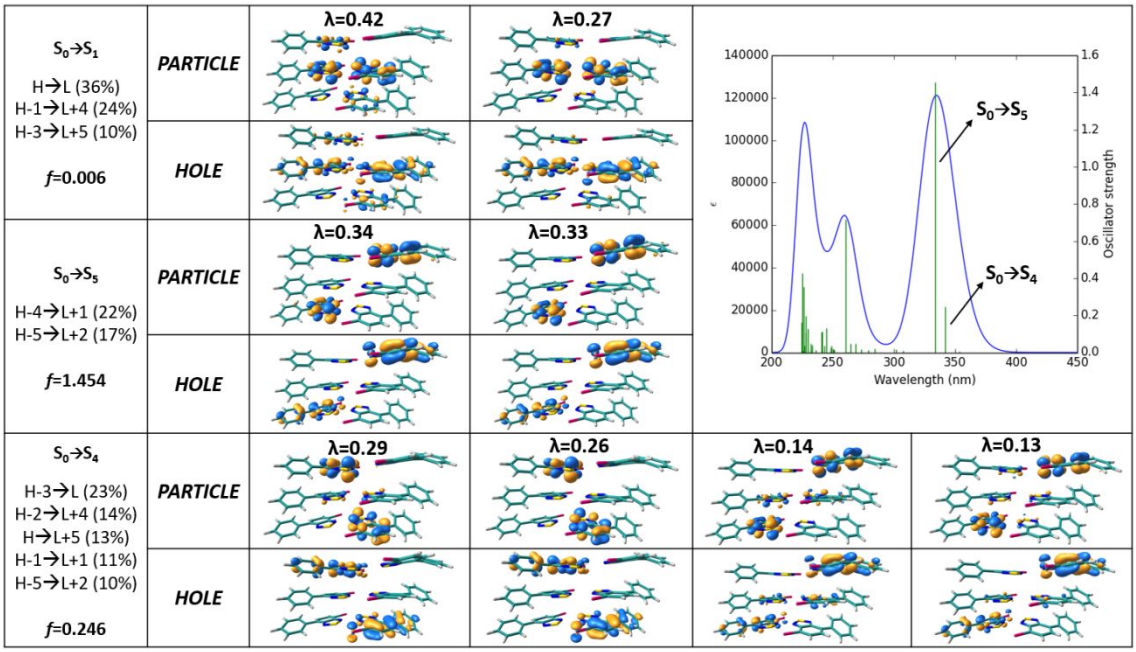

Figure S14. Simulated absorption spectra and main excitations (shown as vertical bars) for the hexameric aggregate extracted from the X-ray structure analysis of **1β** polymorph. Hole- and electron natural transition orbitals (NTO) for the excited states responsible to the lowest energy band are also shown. The computations were done at the TD-DFT level, by using ωB97XD functional and 6-31G** basis set.

6. Additional Supramolecular data

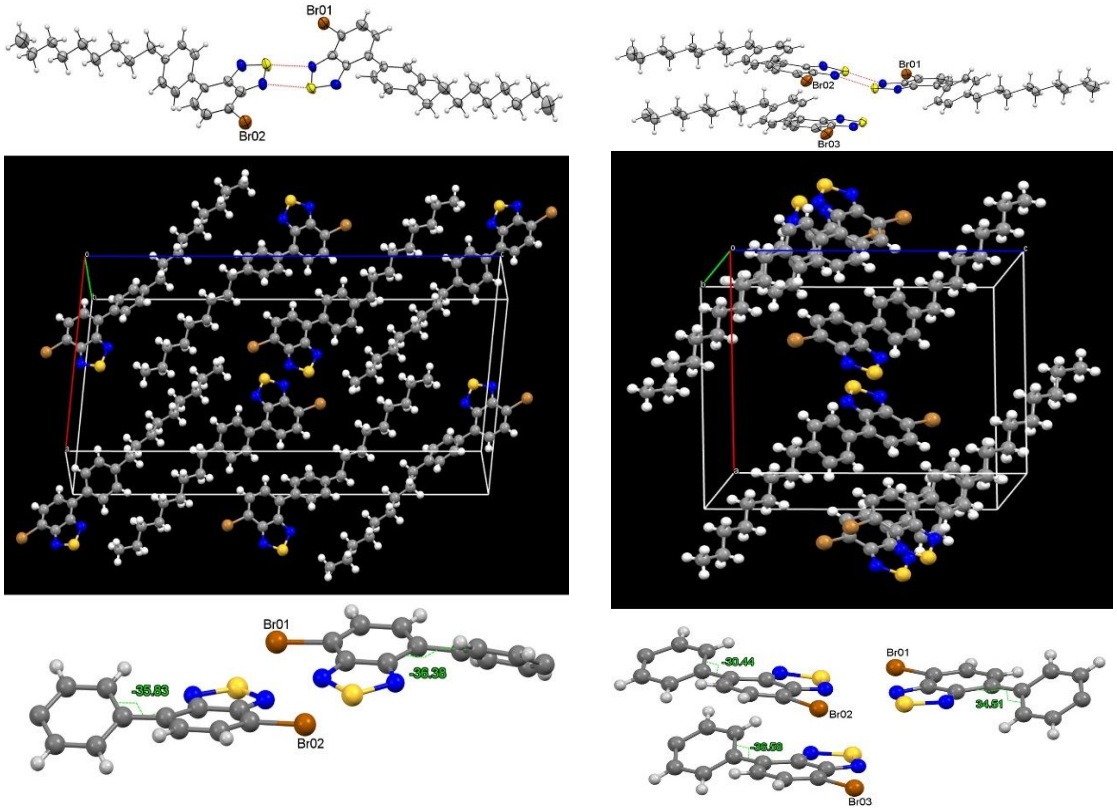

Figure S15. From top to bottom: Asymmetric unit, packing and torsion angles (dihedral angles between the BTD moieties and the phenyl rings) for both polymorphs. (Drawings and angle measurements performed with Mercury Crystallographic program[6]).

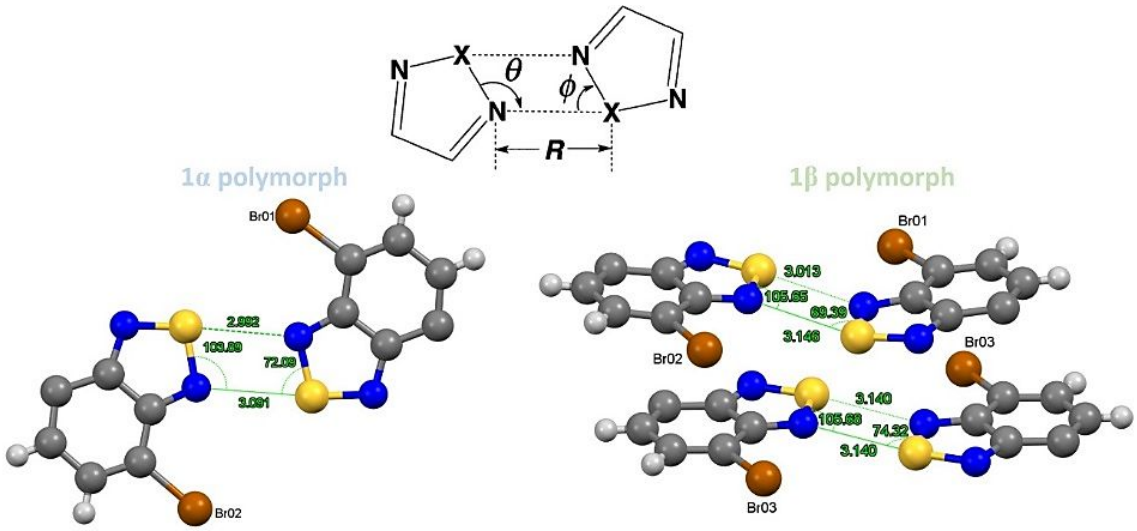

Figure S16. 2S,2N square motif I (BSM) showing the defined distances and angles for **1α** and **1β** polymorphs**.**

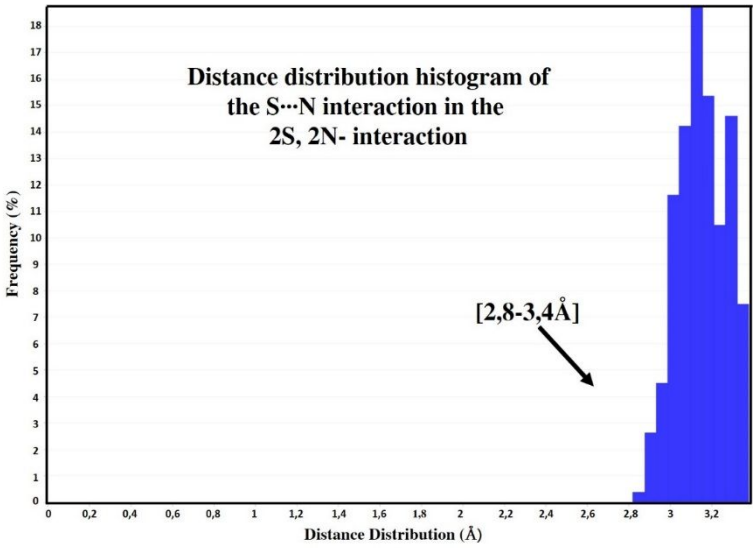

Figure S17. Histogram showing the S•••N distance distribution. Data obtained in 2019 using the ConQuest program of the CCDC database.

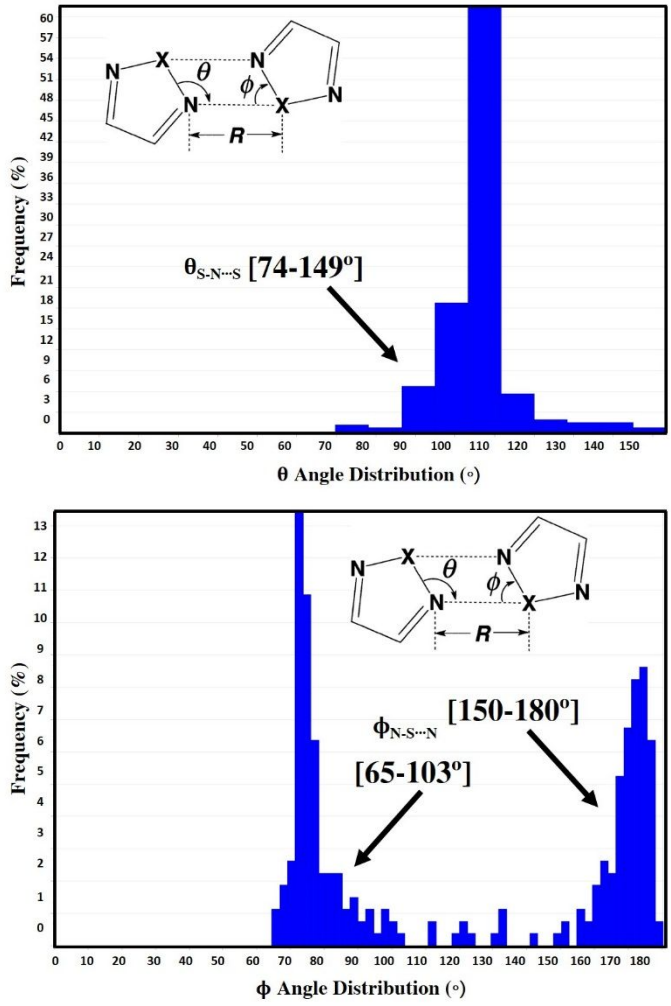

Figure S18. Histogram showing the S-N•••N (above) and the N-S•••N (down) angle distribution. Data obtained in 2019 using the ConQuest program of the CCDC database.

7. References

1. APEX2; Bruker-AXS: Madison, WI, 2006.
2. Siemens SAINT Data Collection and Procedure Software for the SMART System, Siemens Analytical X-ray Instruments, Inc., Madison, WI, 1995.
3. Siemens SHELXTL, Version 5.0, Siemens Analytical X-ray Instruments Inc., Madison, WI, 1995.
4. Software for the SMART System V5. 0.4 and SHELXTL V 5.1, Bruker-Siemens Analytical X-ray Instrument Inc., Madison, WI, 1998.
5. Dolomanov, O. V.; Bourhis, L. J.; Gildea, R. J.; Howard, J. A. K.; Puschmann, H. *J. Appl. Crystallogr.* **2009**, *42*, 339-341.
6. C. F. Macrae, I. Sovago, S. J. Cottrell, P. T. A. Galek, P. McCabe, E. Pidcock, M. Platings, G. P. Shields, J. S. Stevens, M. Towler and P. A. Wood, *J. Appl. Cryst.,* **2020**, 53, 226-235
7. M. J. Frisch, G. W. T., H. B. Schlegel, G. E. Scuseria, M. A. Robb, J. R. Cheeseman, G. Scalmani, V. Barone, G. A. Petersson, H. Nakatsuji, X. Li, M. Caricato, A. V. Marenich, J. Bloino, B. G. Janesko, R. Gomperts, B. Mennucci, H. P. Hratchian, J. V. Ortiz, A. F. Izmaylov, J. L. Sonnenberg, D. Williams-Young, F. Ding, F. Lipparini, F. Egidi, J. Goings, B. Peng, A. Petrone, T. Henderson, D. Ranasinghe, V. G. Zakrzewski, J. Gao, N. Rega, G. Zheng, W. Liang, M. Hada, M. Ehara, K. Toyota, R. Fukuda, J. Hasegawa, M. Ishida, T. Nakajima, Y. Honda, O. Kitao, H. Nakai, T. Vreven, K. Throssell, J. A. Montgomery, Jr., J. E. Peralta, F. Ogliaro, M. J. Bearpark, J. J. Heyd, E. N. Brothers, K. N. Kudin, V. N. Staroverov, T. A. Keith, R. Kobayashi, J. Normand, K. Raghavachari, A. P. Rendell, J. C. Burant, S. S. Iyengar, J. Tomasi, M. Cossi, J. M. Millam, M. Klene, C. Adamo, R. Cammi, J. W. Ochterski, R. L. Martin, K. Morokuma, O. Farkas, J. B. Foresman, and D. J. Fox. , Gaussian 16, Revision B.01. *Gaussian, Inc., Wallingford CT,* **2016**.
8. Lee, C.; Yang, W.; Parr, R. G., Development of the Colle-Salvetti correlation-energy formula into a functional of the electron density. *Phys. Rev. B* **1988,** *37* (2), 785-789.
9. Becke, A. D., Density-functional thermochemistry. III. The role of exact exchange. *J. Chem. Phys* **1993,** *98* (7), 5648-5652.
10. Chai, J.-D.; Head-Gordon, M., Long-range corrected hybrid density functionals with damped atom–atom dispersion corrections. *Physical Chemistry Chemical Physics* **2008,** *10* (44), 6615-6620.
11. Hehre, W. J.; Ditchfield, R.; Pople, J. A., Self—Consistent Molecular Orbital Methods. XII. Further Extensions of Gaussian—Type Basis Sets for Use in Molecular Orbital Studies of Organic Molecules. *J. Chem. Phys* **1972,** *56* (5), 2257-2261.
12. Francl, M. M.; Pietro, W. J.; Hehre, W. J.; Binkley, J. S.; Gordon, M. S.; DeFrees, D. J.; Pople, J. A., Self-consistent molecular orbital methods. XXIII. A polarization-type basis set for second-row elements. *J. Chem. Phys* **1982,** *77* (7), 3654-3665.
13. Tomasi, J.; Persico, M., Molecular Interactions in Solution: An Overview of Methods Based on Continuous Distributions of the Solvent. *Chemical Reviews* **1994,** *94* (7), 2027-2094.
14. Runge, E.; Gross, E. K. U., Density-Functional Theory for Time-Dependent Systems. *Phys. Rev. Lett.* **1984,** *52* (12), 997-1000.
15. Heinze, H. H.; Görling, A.; Rösch, N., An efficient method for calculating molecular excitation energies by time-dependent density-functional theory. *J. Chem. Phys* **2000,** *113* (6), 2088-2099.
16. **https://www.chemcraftprog.com**, Chemcraft - graphical software for visualization of quantum chemistry computations.

Supporting Information for

A Stimuli-responsive Benzothiadiazole Derivative as a Dopant for Rewritable Polymer Blends

Marcelo Echeverri[1], Constanza Ruiz[1], Sergio Gámez-Valenzuela,[2] Matias Alonso-Navarro[1], Enrique Gutierrez-Puebla[1], José L. Serrano[3], *M. Carmen Ruiz Delgado,[*2] Berta Gómez-Lor*[*1]*

1 Instituto de Ciencia de Materiales de Madrid, CSIC Cantoblanco, 28049 Madrid (Spain).

2 Department of Physical Chemistry, University of Málaga, 29071 Málaga, Spain.

3 Departamento de Química Orgánica, Instituto de Ciencia de Materiales de Aragón, Universidad de Zaragoza-CSIC, 50009- Zaragoza (Spain)

E-mails: carmenrd@uma.es, bgl@icmm.csic.es

List of contents: **Page**

S1. Experimental details

Raman spectra: Raman spectra of both A and B polymorphs were recorded by using the 1x1 camera of a Bruker Senterra dispersive Raman microscope equipped with a CCD camera operating at -50oC, a confocal microscope with a x40 objective, a neon lamp and a Nd:YAG laser with excitation at λ = 785 nm. This set up has a spectral resolution of 3–5 cm^{-1}. The power of the laser beam was kept at a level of 10 mW in all cases. The final spectrum is calculated as the average between 25 spectra of 10 seconds each to optimize the signal-to-noise ratio. The temperature of the sample was controlled by a Linkam temperature stage (BCS196) and changed in the temperature range from 25^{o}C to 80^{o}C.

FT-IR spectra: FT-IR spectra were recorded with a Golden Gate Single Reflection Diamond ATR System (Graseby Specac) fitted into a Bruker Vertex 70 FT-IR spectrometer. The infrared spectra were collected with a standard spectral resolution of 4 cm^{-1}. The final spectrum is calculated as the average between 5 spectra of 64 scans each with the aim to obtain a high signal to noise ratio.

Linear Spectroscopy: UV-Visible studies were carried out on a PerkinElmer Lambda XLS+ spectrometer. Fluorescence spectra were recorded on an Aminco SLM 8000 spectrophotometer.

Fluorescence quantum yield: The absolute quantum yield was registered in an Edinburgh Instruments FLS920 fluorometer, equipped with an integrating sphere, using a 450W Xe lamp as excitation source and the supplied blanking plug as blank sample.

Confocal microscopy: Confocal microphotographs were registered in a Confocal multispectral Leica TCS SP5 system with Laser lines: 405 and 488 nm.

Viscosities: Viscosities were measured in a DSA 5000M coupled with LOVIS 2000 ME module from Anton Paar.

Refraction index: Refraction index calculation were measured in a Krüss AR 3D - Abbe refractometernD with a Sodium wavelength 589 nm

Dynamic Light Scattering: Dynamic Light Scattering measurements were performed in a VASCO 2 NP size analyzer Cordouan Technologies.

X-ray structure determinations: Crystal of **1** showing well defined faces were mounted Bruker four circle kappa-diffractometer equipped with a Cu INCOATED microsource, operated at 30 W power (45 kV, 0.60 mA) to generate CuKα radiation (λ = 1.54178 Å), and a Bruker VANTEC 500 area detector (microgap technology). Diffraction data were collected exploring over a hemisphere of the reciprocal space in a combination of φ and ω scans to reach a resolution of 0.86 Å, using a Bruker APEXII software suite (APEX2; Bruker-AXS: Madison, WI, 2006). The structures were solved by the Multan and Fourier methods. Most of the calculations were carried out with APEXII software for data collection and reduction, and OLEX2[1] for structure solution and refinements.

Crystal data for **1** (Phase B): $C_{72}H_{96}N_4S2$, M= 1081.64 crystal dimensions: 0.35 x 0.04 x 0.04 mm3, monoclinic, P 1 21 1 space group, unit cell dimensions: a = 7.0246(4), b = 17.2258(11)), c = 27.700(2) Å, β = 95.667(4) °, V = 3335.5 Å3, T= 250 K, Z = 2, ρ_{calcd} = 1.077 g/cm3. The structure was refined anisotropically R_1(F) = 0.1124 for observed data (I>2σ(I)), final R values (all data) R_1 (F) = 0.1806, wR_2 (F) = 0.3842 for all data.

The experimental data were collected at 250K. The 9-Cs chains are very affected by thermal vibrations due to the lack of intermolecular interactions among them and their contributions to the diffraction experiments were very poor, especially at medium-high angles. So, these C9 chains were modelled and their geometric parameters were restricted

with soft restraints (DFIX and DANG); the high thermal vibration of some of the chain atoms were consider isotropic. Because of these, the A and B alerts, which appears in the checkcif report concerning these atoms can be explain.

Several trials to dismiss this issue lowering the data collection temperature result several disordered chain models very difficult to model without any substantial improvement in compare to the 250K structure.

S2. Synthesis scheme

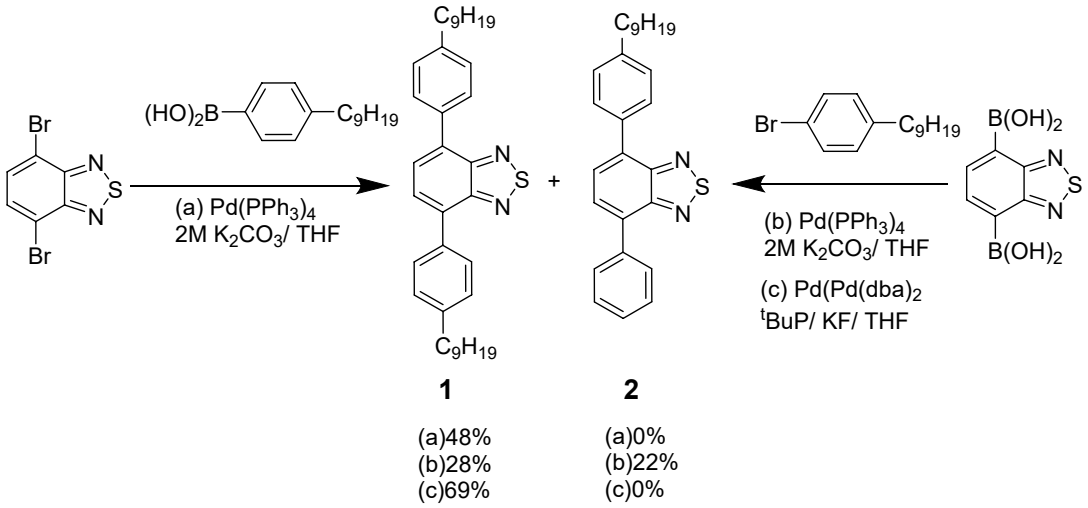

Scheme S1: Synthesis of compound **1** and **2**.

S3. Experimental and simulated powder X-ray diffraction patterns of 1

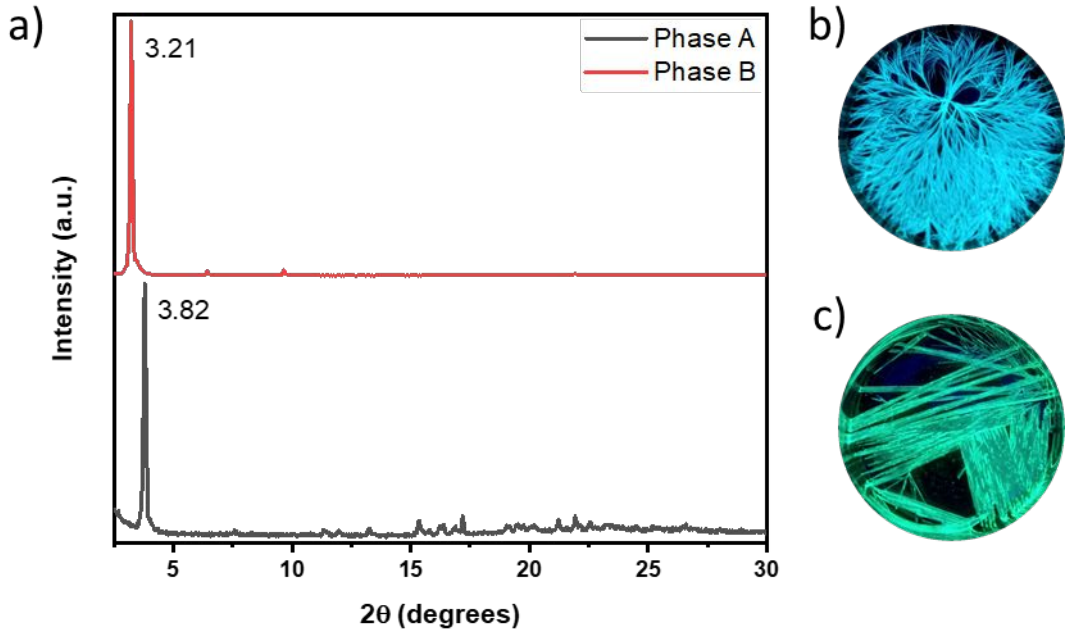

Figure S1. a) Comparison of powder X-ray diffraction pattern of Phase A and Phase B. b) Phase A crystals under 365 nm excitation. c) Phase B crystals under 365 nm excitation

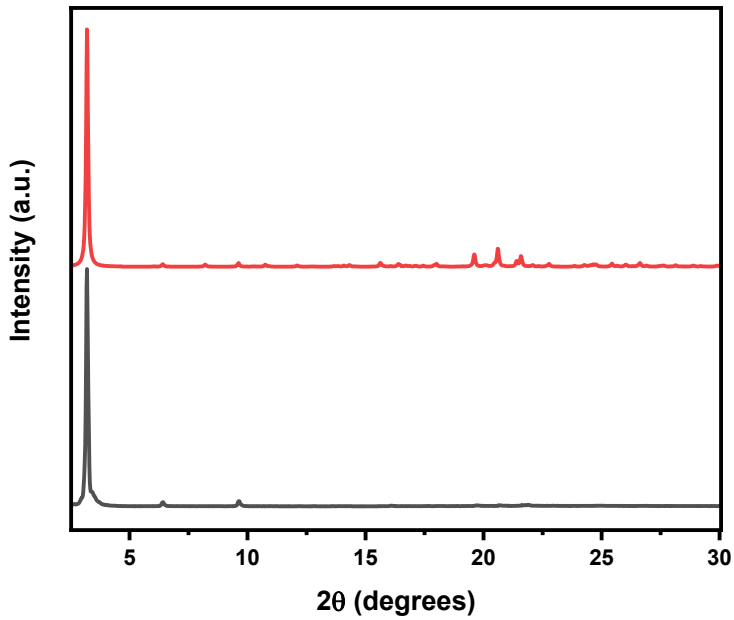

Figure S2. Comparison of the simulated powder X-ray diffraction pattern of Phase B obtained using the single crystal data with the experimental powder diffractogram.

S4. DFT-calculations

Computational Details. All the calculations were carried out at the framework of the Density Functional Theory (DFT) level using the B3LYP[2-3] and ωB97XD[4] functionals and a 6-31G** basis set[5-6], as implemented in the GAUSSIAN16 program[7]. Depending on the environment, the two following approaches were considered:

- In solid state, the molecular structures for the monomer and dimer of polymorph B were directly extracted from the crystal data, and the experimentally obtained structure was maintained for the rest of calculations.

- In solution, the molecular geometry of monomer **1** was fully optimized where all geometrical parameters were allowed to vary independently. No imaginary frequencies were observed, which ensures the finding of the global minimum energy. Solvent effects were considered in all calculations by using the SCRF (self-consistent-reaction-field) theory using the PCM (Polarized Continuum Model) approach to model the interaction between the molecules and the solvent (*n*-hexane, tetrahydrofuran, dichloromethane or methanol). The PCM model[8] developed by Tomasi considers the solvent as a continuous medium with a dielectric constant, ε, and represents the solute by means of a cavity built with a number of interlaced spheres.

In both cases, vertical electronic excitation energies were computed by using the time-dependent DFT (TD-DFT) approach[9-10] on the resulted molecular geometries. The thirty-five lowest-energy electronic excited states were computed for all cases. Absorption spectra were simulated through convolution of the vertical transition energies and oscillator strengths with Gaussian functions (half width at half-maximum of 0.33 eV).

Furthermore, the first excited state of monomer and dimer species was fully studied by using TD-DFT approach on the previously obtained ground state molecular geometries.

The simulated Raman Spectrum was calculated from a previously optimized monomer specie at the B3LYP/6-31G** level. We used an adjustment of the theoretical force fields where the frequencies were scaled down by a factor of 0.965 to disentangle experimental misassignments, as recommended by Scott and Random[11]. The theoretical spectrum was obtained by convolution the scaled frequencies with Gaussian functions (4 cm^{-1} widths at the half-height).

Vibrational eigenvector and molecular orbitals were plotted using the Chemcraft 1.8 molecular modelling software.[12]

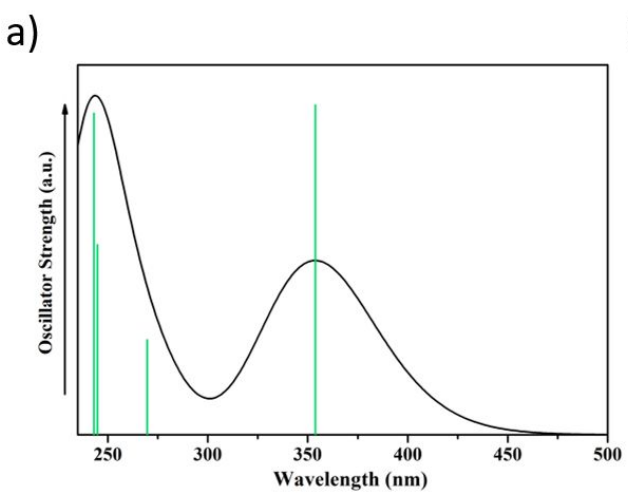

Electronic transitions	Description	$E_{max}(\lambda_{max})$	*f*
1	H→L (95%)	3.51 eV (354 nm)	0.523
2	H-4→L (79%)	4.60 eV (270 nm)	0.222
3	H-3→L (39%) H→L+1 (28%)	5.07 eV (245 nm)	0.344
4	H→L+1 (41%) H-3→L (21%) H-5→L (13%)	5.10 eV (243 nm)	0.513

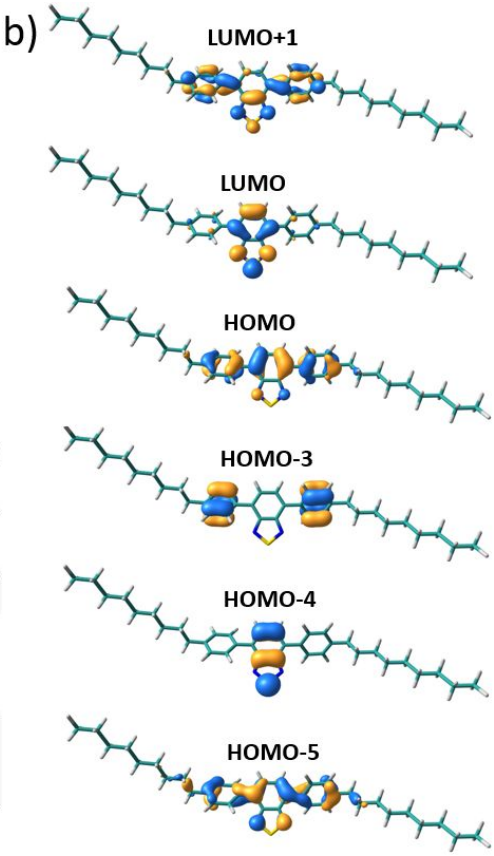

Figure S3. A) DFT-calculated vertical excited state transitions (green solid bars) at the ωB97XD/6-31G** level for an optimized single molecule **1** in dichloromethane solution. B) The frontier molecular orbitals topologies involved in the main electronic transitions are also shown.

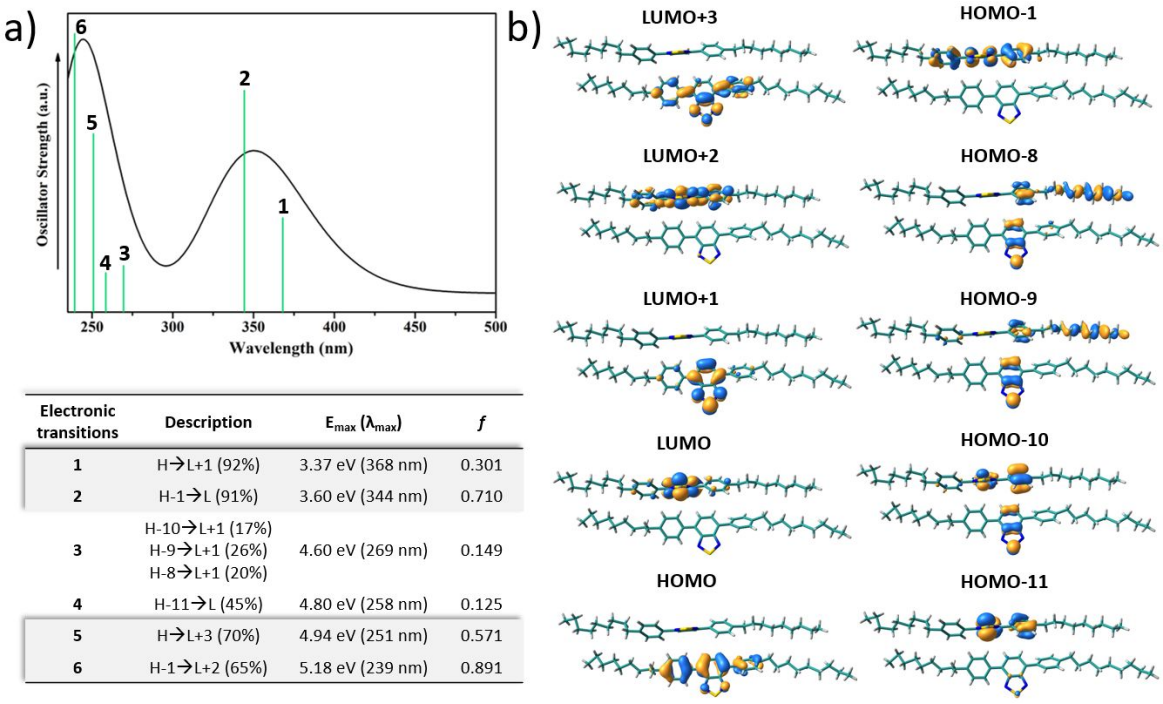

Electronic transitions	Description	E_{max} (λ_{max})	*f*
1	H→L+1 (92%)	3.37 eV (368 nm)	0.301
2	H-1→L (91%)	3.60 eV (344 nm)	0.710
3	H-10→L+1 (17%) H-9→L+1 (26%) H-8→L+1 (20%)	4.60 eV (269 nm)	0.149
4	H-11→L (45%)	4.80 eV (258 nm)	0.125
5	H→L+3 (70%)	4.94 eV (251 nm)	0.571
6	H-1→L+2 (65%)	5.18 eV (239 nm)	0.891

Figure S4. a) DFT-calculated vertical excited state transitions (green solid bars) at the ωB97XD/6-31G** level in dichloromethane for a dimer by using the experimental molecular coordinates obtained from X-ray analysis. B) The frontier molecular orbitals topologies involved in the main electronic transitions are also shown.

Table S1. DFT-calculated molecular dipole moment for the ground (μ_g) and first excited states (μ_e) for a fully optimized isolated molecule **1** in different solvents at the B3LYP/6-31G** (top) and ωB97XD/6-31G** (bottom) level of theory.

Molecular Dipole Moments → B3LYP/6-31G**		
Medium (ε)	**μ_g (D)**	**μ_e (D)**
Vacuum	1.6	5.4
N-Hexane (1.88)	1.8	6.1
Tetrahydrofuran (7.43)	2.1	7.1
Dichloromethane (8.93)	2.1	7.2
Methanol (32.61)	2.2	7.5

Molecular Dipole Moments → ωB97XD/6-31G**		
Medium (ε)	**μ_g (D)**	**μ_e (D)**
Vacuum	1.5	4.8
N-Hexane (1.88)	1.7	5.4
Tetrahydrofuran (7.43)	2.0	6.3
Dichloromethane (8.93)	2.1	6.4
Methanol (32.61)	2.2	6.7

Table S2. DFT-calculated average inter-ring dihedral angles between the two phenyl groups and the BTD unit for an optimized isolated molecule **1** in the ground state (S_0) and first excited state (S_1), respectively, in different solvents at the B3LYP/6-31G** (top) and ωB97XD/6-31G** (bottom) level.

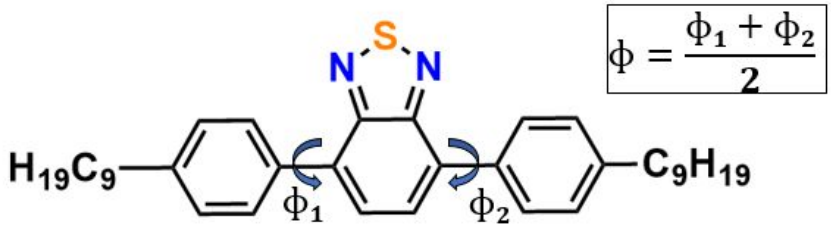

Dihedral Angles ϕ (°) → B3LYP/6-31G**		
Medium (Ɛ)	**Ground State**	**First Excited State**
Vacuum	36	19
N-Hexane (1.88)	36	19
Tetrahydrofuran (7.43)	37	20
Dichloromethane (8.93)	38	20
Methanol (32.61)	38	20

Dihedral Angles ϕ (°) → ωB97XD/6-31G**		
Medium (Ɛ)	**Ground State**	**First Excited State**
Vacuum	40	21
N-Hexane (1.88)	41	22
Tetrahydrofuran (7.43)	41	20
Dichloromethane (8.93)	41	20
Methanol (32.61)	42	20

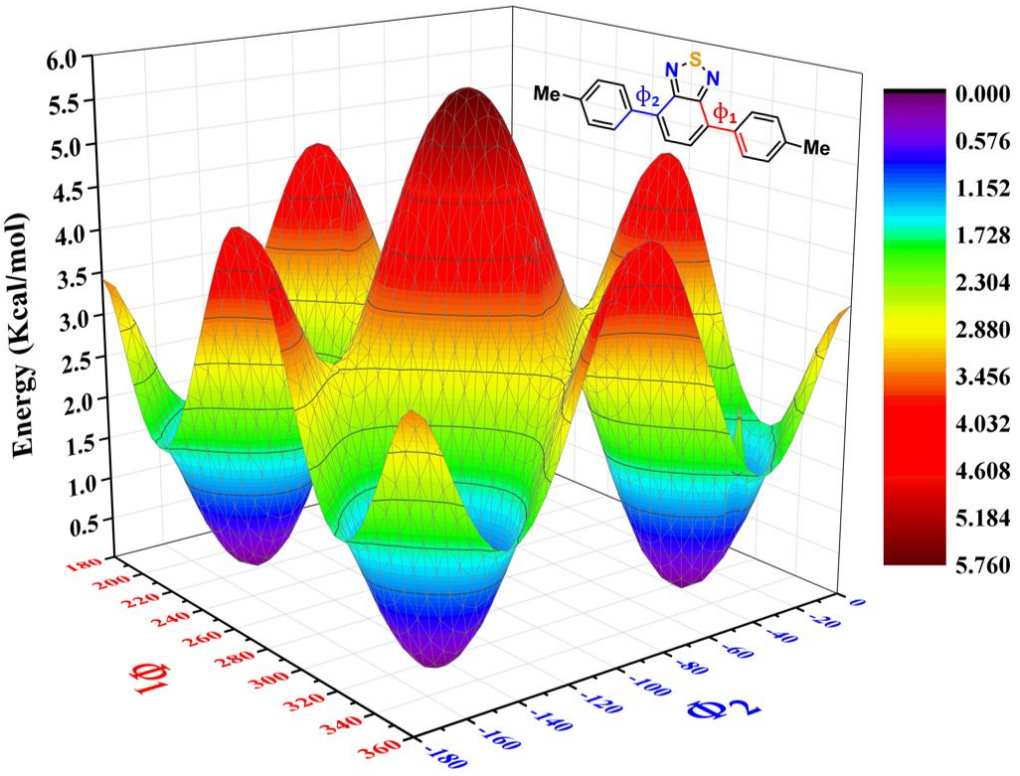

Figure S5. Dihedral potential energy hypersurface E=E(ϕ_1,ϕ_2) calculated for an isolated molecule **1** at the B3LYP/6-31G**. In order to reduce the computational cost, the alkyl chains were replaced by methyl groups.

S5. Liquid crystalline properties

Mesomorphic Properties

The optical textures of the mesophases were studied with an Olympus polarising microscope BX51 equipped with a Linkam hot-stage and Linkam TMS 91 central processor. The transition temperatures and enthalpies were measured by differential scanning calorimetry with a TA Instruments Q20 instrument operated at a scanning rate of 10°C min^{-1} on both heating and cooling. The apparatus was calibrated with indium (156.6°C; 28.71 Jg^{-1}) as the standard. TGA was carried out in a TGA-Q5000 apparatus at a heating rate of 10º/min under nitrogen up to 600ºC and under air from 600° to 750°C. The XRD patterns at the mesophases were obtained with a pinhole camera (Anton-Paar) operating with a point-focused Ni-filtered Cu-Kα beam. The sample was held in Lindemann glass capillary (1 mm diameter) and heated, when necessary, with a variable-temperature oven. The capillary axis is perpendicular to the X-ray beam and the pattern is collected on flat photographic film perpendicular to the X-ray beam. Spacing was obtained via Bragg's law.

Thermal Properties

The thermal properties of this compound was investigated by thermogravimetric analysis (TGA), polarized optical microscopy (POM), differential scanning calorimetry (DSC) and X-ray diffraction (XRD). The transition temperatures and enthalpy values are summarized in **Table S3**.

Table S3. Thermal properties and structural parameters

$T_{2\%}$ [a] (ºC)	Phase transitions[b]	T_{XRD} [c] (ºC)	d_{obs} (Å)	*h k l*	Structural parameters
225	Cr 73.7 (17.7) SmA 104.6 (4.6) I	95	32.9	1 0 0	d = 32.9 Å
			16.5	2 0 0	S = 27.3 Å^2
			4.5 (br)		

[a] Temperature at which 2% mass lost is detected in the thermogravimetric curve.

[b] DSC data of the second heating process at a rate of 10ºC/min. Temperatures (ºC) are read at the maximum of the corresponding peaks and enthalpies (kJ/mol) are in brackets. Cr: crystal, SmA: smectic A mesophase, I: isotropic liquid.

[c] Temperature of the XRD study.

Upon heating compound **1** showed a crystal-crystal transitions at 69.5ºC, followed by a crystal-to mesophase transition at 74.6ºC. Upon cooling from the isotropic state, a fan-shaped texture was observed (Figure S6**),** and homeotropic domains could be obtained on applying mechanical stress to the samples, suggesting an orthogonal character of the mesophases.

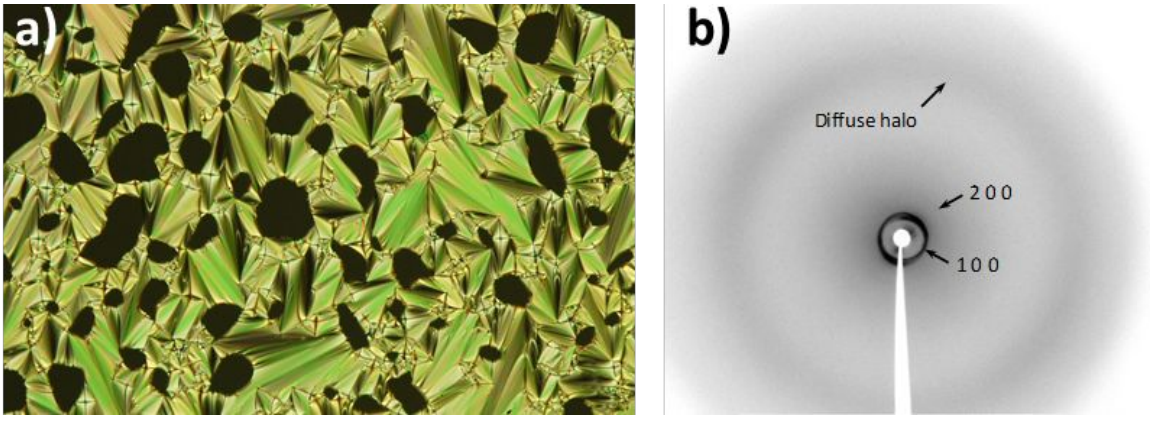

Figure S6. a) POM microphotographs for **1** (taken at 90 ºC in the cooling process), and (b) XRD patterns of: **1** (taken at 95 ºC).

The XRD patterns of the mesophase contain in the low-angle region two sharp maxima which can be assigned to the first and second order reflections from a lamellar structure. In the high-angle region a broad, diffuse halo is detected 4.5 Å and this corresponds to the short-range correlations between the conformationally disordered alkyl chains. This kind of XRD diffractogram is characteristic of a smectic mesophase without positional order within the layer. Given the ortohogonal character of these mesophases, this supports the assignation of the mesophase of **1** as smectic A. The layer spacing (*d*) of the SmA mesophase estimated by applying Bragg's law is 32.9 Å, similar to the molecule length in their most extended conformation (34.6Å for **1**). This suggests that the mesophase adopts a monolayer structure.

Additional support for this structural model can be obtained by simple cross-section calculations. The density (ρ) of a smectic mesophase is related to the molecular mass (M) and the layer spacing (d) by the formula:

$$\rho = (M \times Z \times 10^{24})/(d \times S \times N_A)$$

where Z is the number of molecules per layer, S is the molecule cross-section, and N_A is Avogadro's number. Assuming ρ = 1 g·cm^{-3} (reasonable value for liquid crystals) and a monolayer structure of the mesophase (Z= 1), it is deduced a cross-section of around 30 Å^2 per hydrocarbon chain (**Table S3**). Considering that 20 Å^2 would be the cross-section expected for a fully-extended hydrocarbon chain, a S≈30 Å^2 value can be explained by the conformational disorder of the hydrocarbon chains and by the interpenetration between the chains of molecules in neighbouring layers.

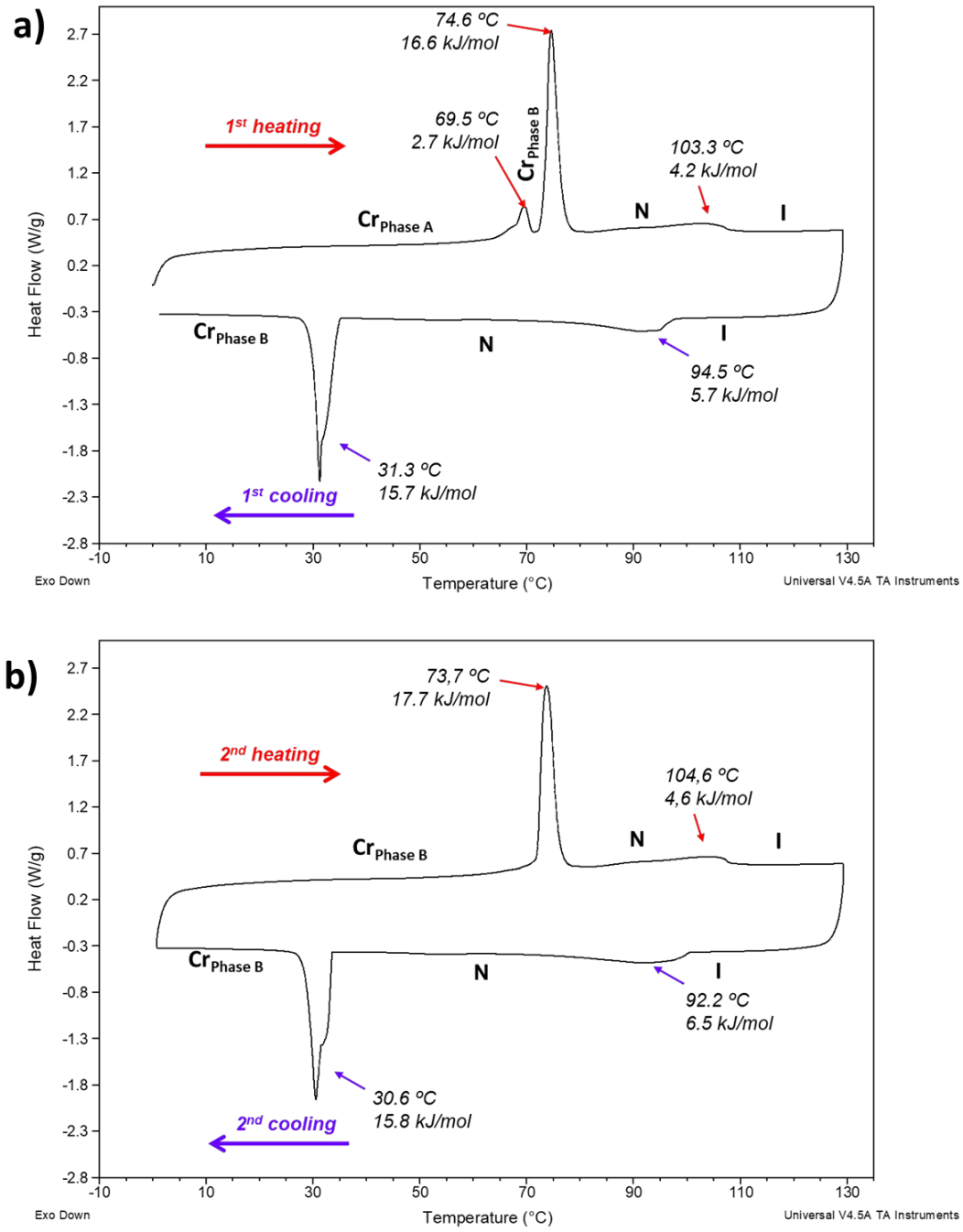

Figure S7. DSC traces of **1** corresponding to: a) first scan (10 ^{o}Cmin$^{-1,}$ Exo down). Cr: crystal, N: nematic mesophase, I: isotropic liquid. b) second scan (10 ^{o}Cmin$^{-1,}$ Exo down).

S6. Fluorescence lifetimes

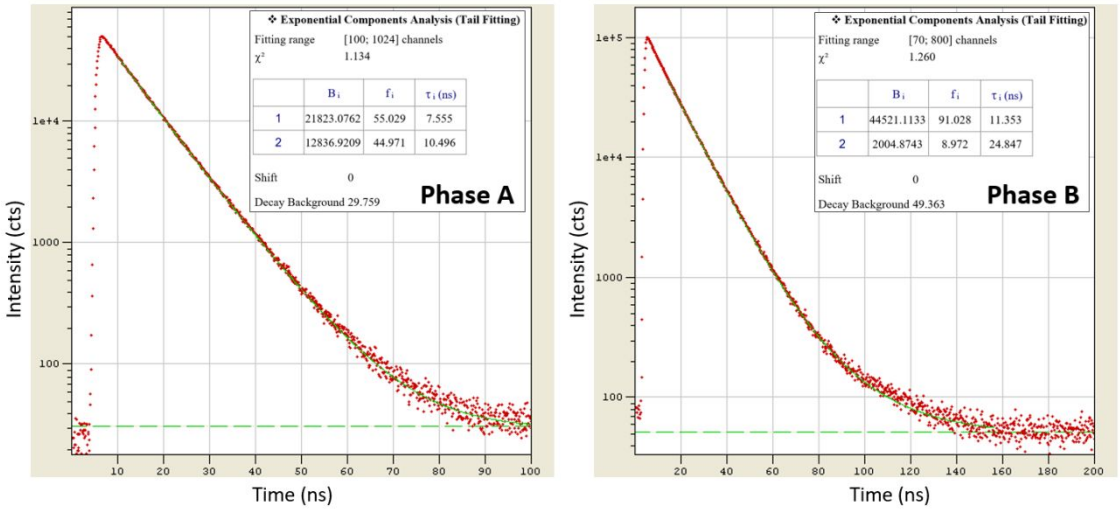

Figure S8. Fluorescence decays of polymorphs A and B with an excitation wavelength of 370 nm. Decays show biexponential character.

S7. Experimental and Theoretical IR Spectra

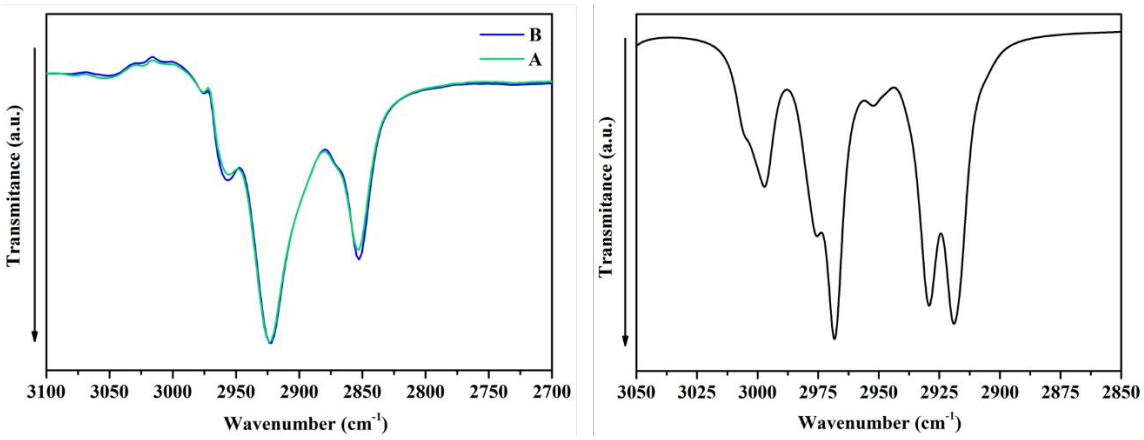

Figure S9. Experimental infrared spectra of polymorph A and B showing the spectral region of CH stretching vibrations (left). The theoretical infrared spectrum of molecule **1** calculated at the B3LYP/6-31G** level (right).

S8. Theoretical Raman Spectra

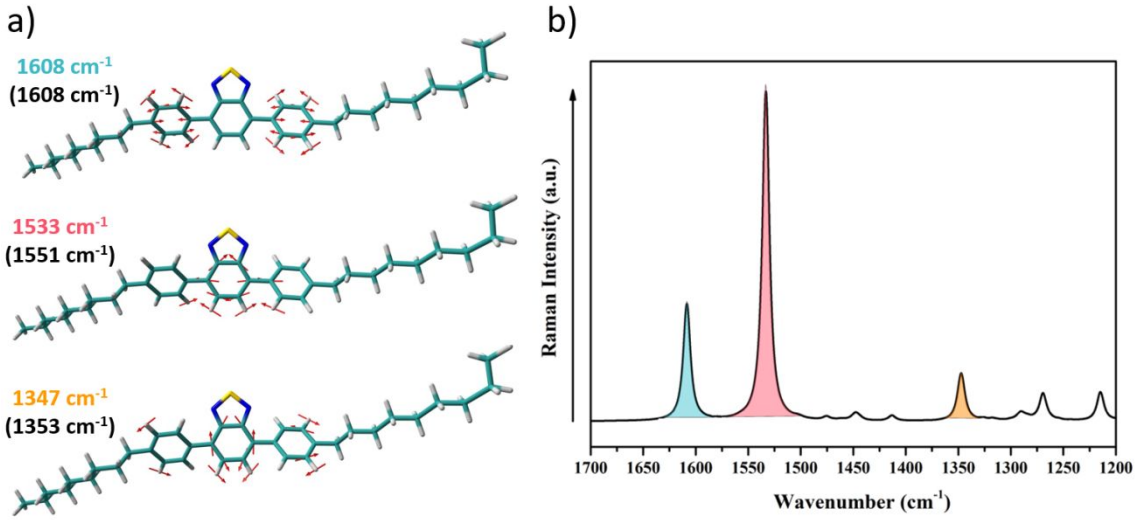

Figure S10. (a) B3LYP/6-31G** vibrational eigenvectors associated with the most outstanding C=C/C-C Raman features of molecule **1**. The theoretical and experimental (in parentheses) wavenumbers are also shown. (b) DFT-calculated Raman spectrum of molecule **1** at the B3LYP/6-31G** level.

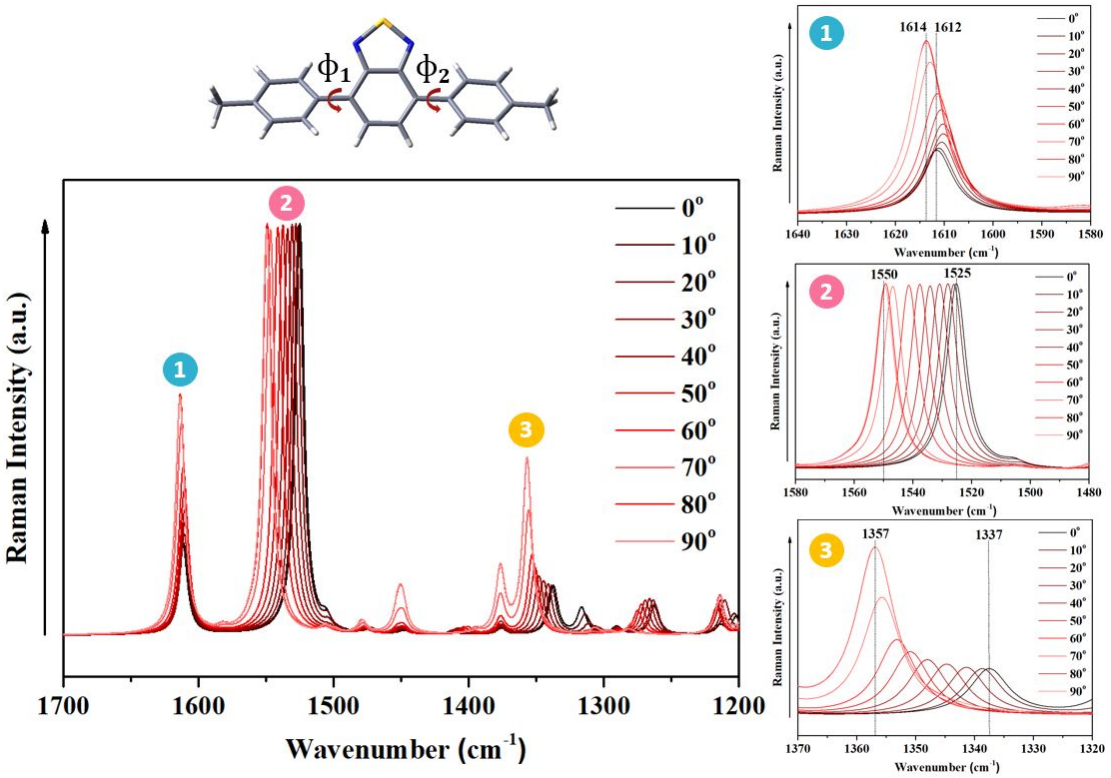

Figure S11. DFT-calculated Raman spectrum of molecule **1** at the B3LYP/6-31G** level as a function of the dihedral angle between the BTD unit and the external phenyl rings. Note that Φ_1 and Φ_2 has been kept fixed ($\Phi_1 = \Phi_2$). In order to reduce the computational cost, the alkyl chains were replaced by methyl groups.

S9. Amplification of X-ray diffractograms showing the shearing induced phase transformation

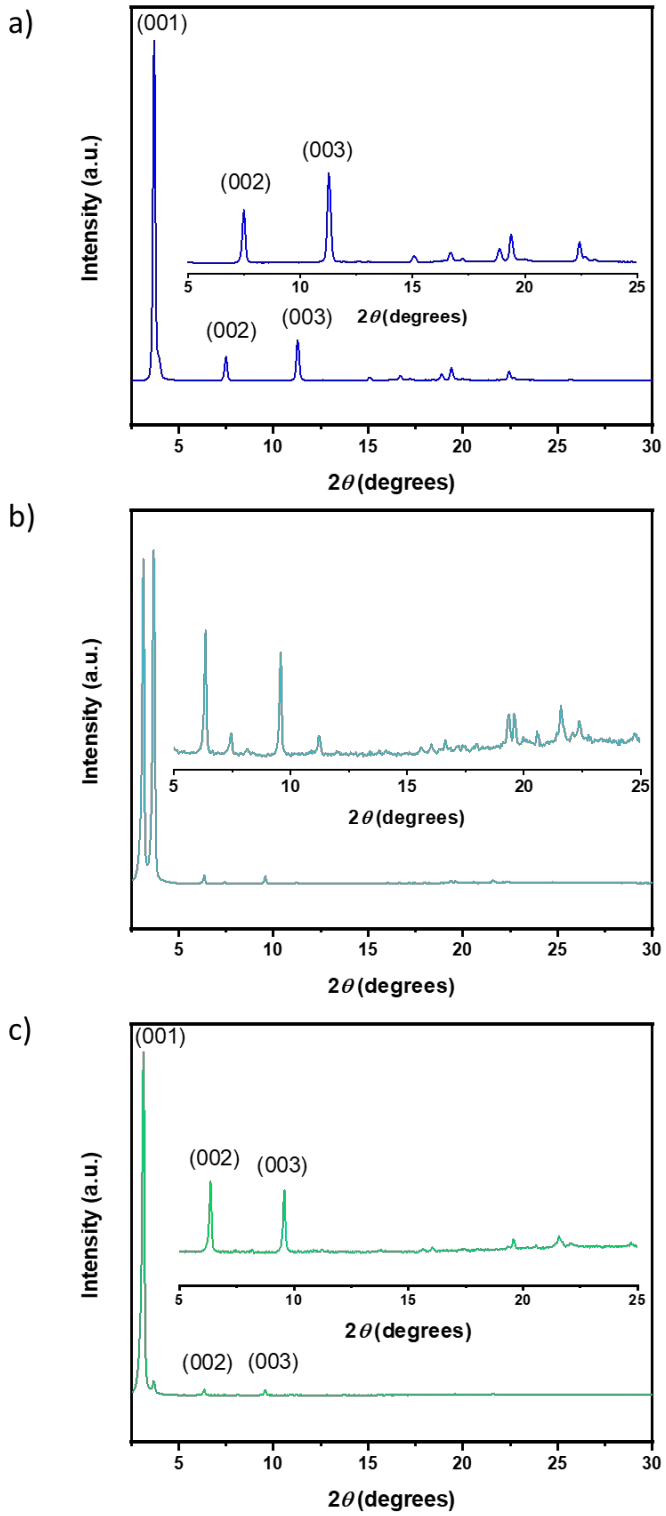

Figure S12. Powder X-ray diffraction pattern of Phase A (a), shearing (b) and Phase B obtained by shearing (c).

S10. Details on the preparation of 1:polymer hybrid materials

S10.1. Schematic Representation of doped polymeric films

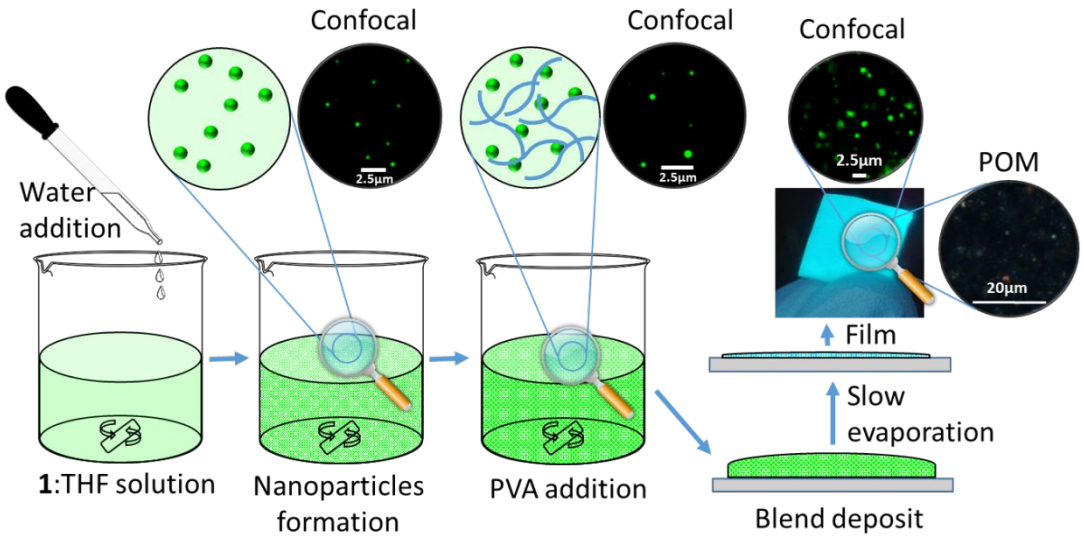

Figure S13. Schematic representation of the preparation **1**:polyvinylalcohol films.

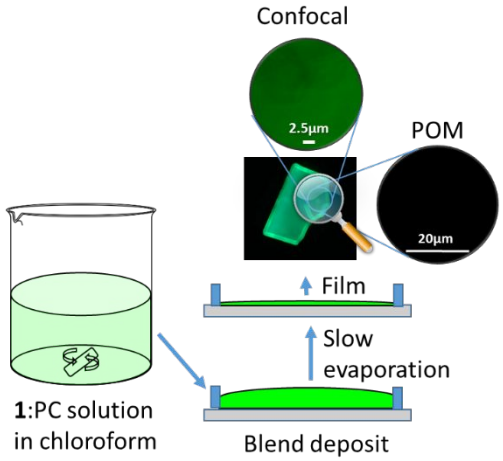

Figure S14. Schematic representation of the preparation **1**:polycarbonate films.

S10.2. Dynamic Light Scattering nanoparticles sizes

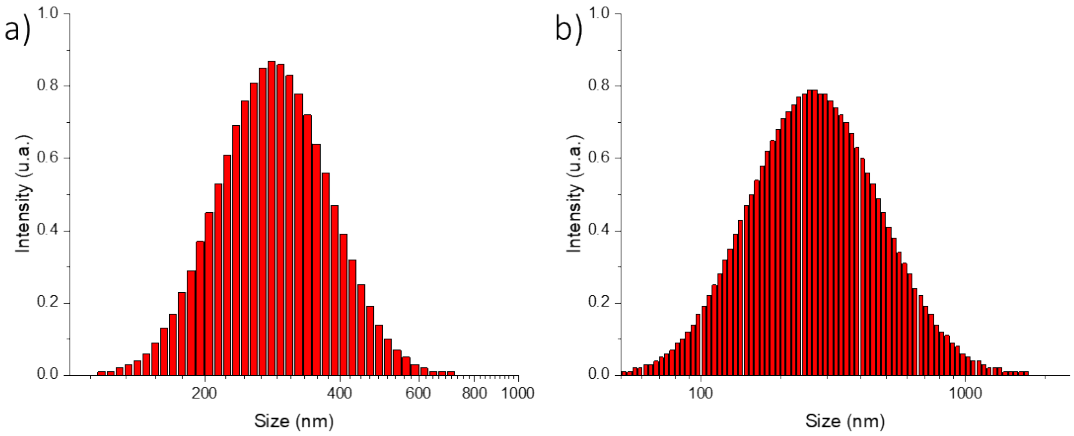

Figure S15. Size dispersion by Intensity calculate by Dynamic Light Scattering (DLS) for a) THF/H_2O micelles of **1**; b) THF/H_2O micelles of 1 in presence of PVA.

S10.3. Confocal microscopy study

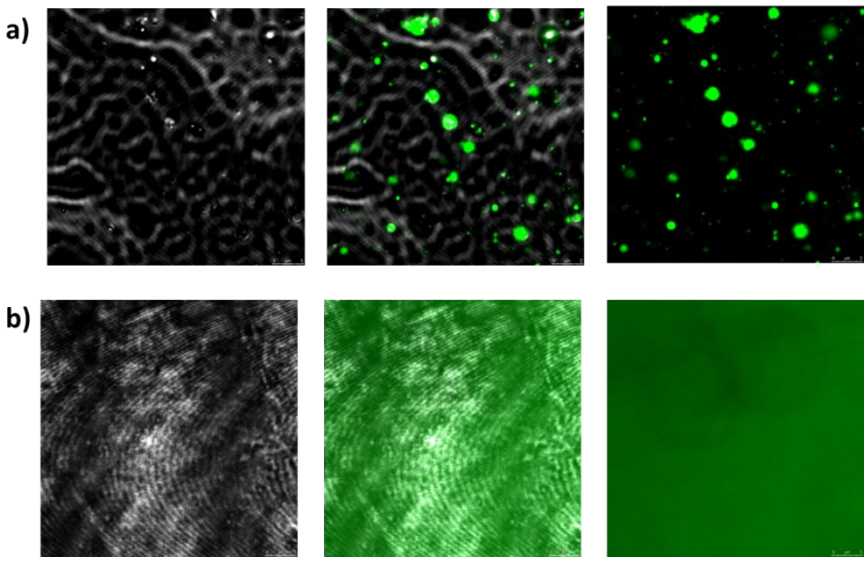

Figure S16. Bright field, fluorescence and the merged confocal images of a **1:**PVA film (a) and a **1**:polycarbonate film (b).

S11. Copy of the ^{1}H NMR and ^{13}C NMR spectra of compound 1

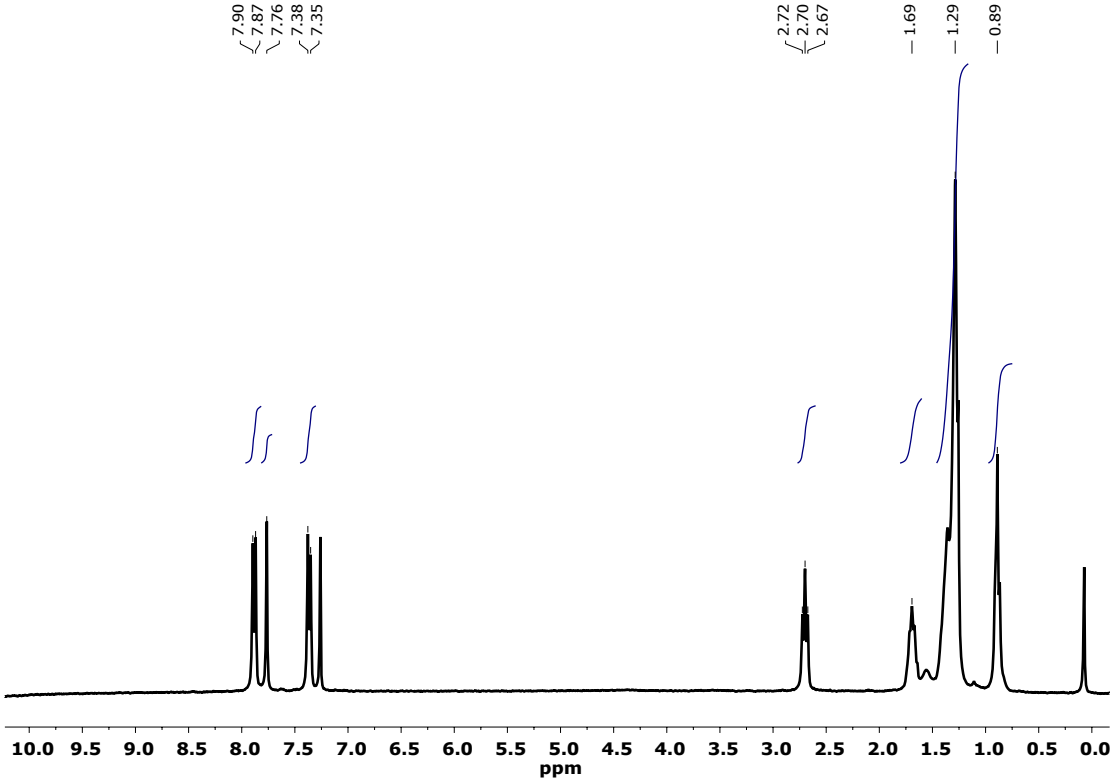

Figure S17. Copy of ^{1}H NMR spectrum (300 MHz, $CDCl_3$) of compound **1**.

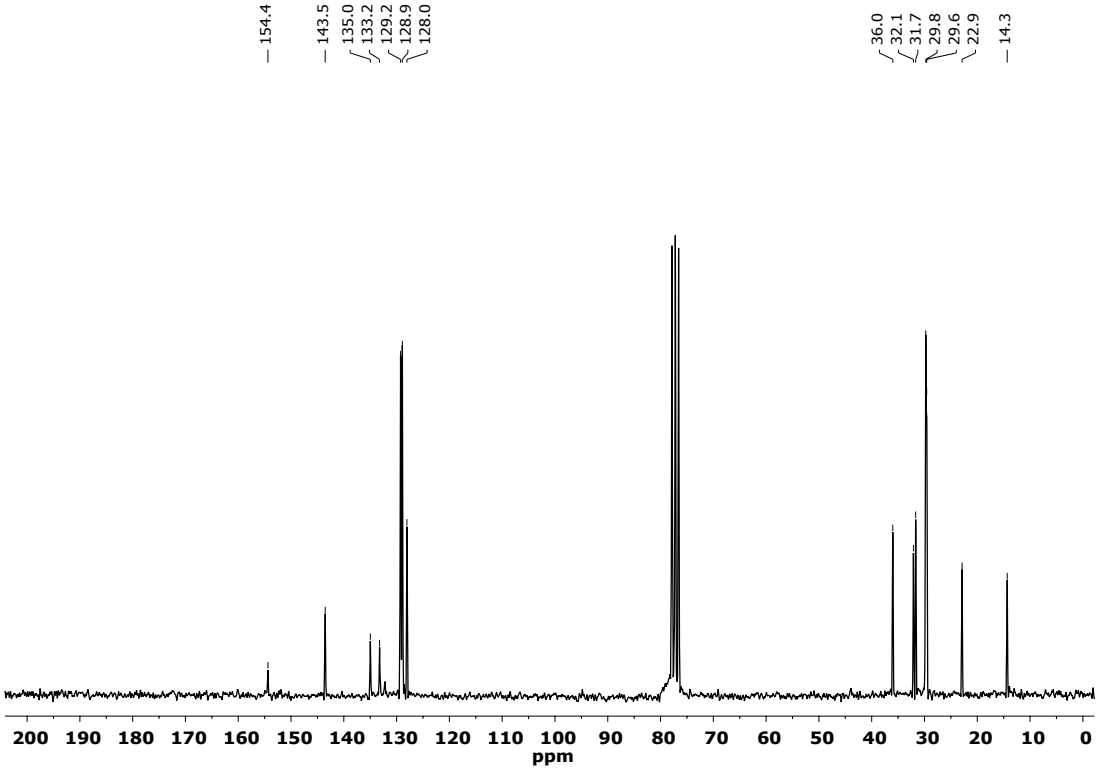

Figure S18. Copy of ^{13}C NMR spectrum (50 MHz, $CDCl_3$) of compound **1**.

S12. References

1. Dolomanov, O. V.; Bourhis, L. J.; Gildea, R. J.; Howard, J. A. K.; Puschmann, H., OLEX2: a complete structure solution, refinement and analysis program. *J. Appl. Crystallogr.* **2009,** *42* (2), 339-341.

2. Lee, C.; Yang, W.; Parr, R. G., Development of the Colle-Salvetti correlation-energy formula into a functional of the electron density. *Phys. Rev. B* **1988,** *37* (2), 785-789.

3. Becke, A. D., Density-functional thermochemistry. III. The role of exact exchange. *J. Chem. Phys* **1993,** *98* (7), 5648-5652.

4. Chai, J.-D.; Head-Gordon, M., Long-range corrected hybrid density functionals with damped atom–atom dispersion corrections. *PCCP* **2008,** *10* (44), 6615-6620.

5. Hehre, W. J.; Ditchfield, R.; Pople, J. A., Self—Consistent Molecular Orbital Methods. XII. Further Extensions of Gaussian—Type Basis Sets for Use in Molecular Orbital Studies of Organic Molecules. *J. Chem. Phys* **1972,** *56* (5), 2257-2261.

6. Francl, M. M.; Pietro, W. J.; Hehre, W. J.; Binkley, J. S.; Gordon, M. S.; DeFrees, D. J.; Pople, J. A., Self-consistent molecular orbital methods. XXIII. A polarization-type basis set for second-row elements. *J. Chem. Phys* **1982,** *77* (7), 3654-3665.

7. M. J. Frisch, G. W. T., H. B. Schlegel, G. E. Scuseria, M. A. Robb, J. R. Cheeseman, G. Scalmani, V. Barone, G. A. Petersson, H. Nakatsuji, X. Li, M. Caricato, A. V. Marenich, J. Bloino, B. G. Janesko, R. Gomperts, B. Mennucci, H. P. Hratchian, J. V. Ortiz, A. F. Izmaylov, J. L. Sonnenberg, D. Williams-Young, F. Ding, F. Lipparini, F. Egidi, J. Goings, B. Peng, A. Petrone, T. Henderson, D. Ranasinghe, V. G. Zakrzewski, J. Gao, N. Rega, G. Zheng, W. Liang, M. Hada, M. Ehara, K. Toyota, R. Fukuda, J. Hasegawa, M. Ishida, T. Nakajima, Y. Honda, O. Kitao, H. Nakai, T. Vreven, K. Throssell, J. A. Montgomery, Jr., J. E. Peralta, F. Ogliaro, M. J. Bearpark, J. J. Heyd, E. N. Brothers, K. N. Kudin, V. N. Staroverov, T. A. Keith, R. Kobayashi, J. Normand, K. Raghavachari, A. P. Rendell, J. C. Burant, S. S. Iyengar, J. Tomasi, M. Cossi, J. M. Millam, M. Klene, C. Adamo, R. Cammi, J. W. Ochterski, R. L. Martin, K. Morokuma, O. Farkas, J.

B. Foresman, and D. J. Fox. , Gaussian 16, Revision B.01. *Gaussian, Inc., Wallingford CT,* **2016**.

8. Tomasi, J.; Persico, M., Molecular Interactions in Solution: An Overview of Methods Based on Continuous Distributions of the Solvent. *Chem. Rev.* **1994,** *94* (7), 2027-2094.

9. Runge, E.; Gross, E. K. U., Density-Functional Theory for Time-Dependent Systems. *Phys. Rev. Lett.* **1984,** *52* (12), 997-1000.

10. Heinze, H. H.; Görling, A.; Rösch, N., An efficient method for calculating molecular excitation energies by time-dependent density-functional theory. *J. Chem. Phys* **2000,** *113* (6), 2088-2099.

11. Scott, A. P.; Radom, L., Harmonic Vibrational Frequencies: An Evaluation of Hartree−Fock, Møller−Plesset, Quadratic Configuration Interaction, Density Functional Theory, and Semiempirical Scale Factors. *J. Phys. Chem.* **1996,** *100* (41), 16502-16513.

12. https://www.chemcraftprog.com, Chemcraft - graphical software for visualization of quantum chemistry computations.

Supporting Information

Effect of the Linkage Position on the Conjugation Length of Truxene-Based Porous Polymers: Implications on Their Sensing Performance of Nitroaromatics

Marcelo Echeverri,[a] Sergio Gámez-Valenzuela,[b] Rafael C. González-Cano,[b] Jordy Guadalupe,[a] Sandra Cortijo-Campos,[a] Juan Teodomiro López Navarrete,[b] Marta Iglesias,[a]* M. Carmen Ruiz Delgado[b]* and Berta Gómez-Lor[a]*

[a]Instituto de Ciencia de Materiales de Madrid, CSIC. C/ Sor Juana Inés de la Cruz 3, Cantoblanco, Madrid 28049, Spain.
[b] Department of Physical Chemistry, University of Malaga, Campus de Teatinos s/n, 29071, Malaga, Spain

*Corresponding author: marta.iglesias@icmm.csic.es; carmenrd@uma.es; bgl@icmm.csic.es;

S1. Methods

FT-IR: Fourier Transform Infrared Spectra (FT-IR) were recorded on a Perkin-Elmer RX-1 instrument with 1.0 ± 0.1 cm^{-1} resolution.

TGA: Thermogravimetric analyses (TGA) were obtained on a TA TGA Q-500 analyzer under air atmosphere, using approximately 5 mg of sample under a flow of nitrogen of 60 mL/min and a flow of air of 40 mL/min. The samples were heated at 10°C/min from room temperature to 850°C. The decomposition temperature (Td_{onset}) was determined from the intersection of the two tangents at the start of degradation and at the temperature of maximum rate of weight loss.

NMR; ^{1}H-NMR spectra were recorded on an Bruker 200 spectrometer operating at 200 MHz.

MAS-NMR: ^{13}C solid-state MAS-NMR measurement was recorded with a Bruker AV400 WB spectrometer (Larmor frequencies of 400 and 100 MHz, using 4 mm MAS probes spinning at 10 kHz rate).

Elemental analysis: Elemental analysis (%C, %N and %H) were determined in a Carlo-Erba EA 1108 analyzer.

SEM: Scanning electron microscopy (SEM) micrographs were obtained with a FE-SEM FEI Nova NANOSEM 230 microscope operating at 0.5 kV. The samples were prepared directly by dispersing the powder onto a double-sided adhesive surface.

BET: The specific surface areas and porosity analysis were performed using N_2 adsorption isotherms (Micromeritics, ASAP 2020 Micropore Dry Analyzer) using BET method for surface area calculation.

Powder X-ray diffractograms: X-ray powder diffractograms were recorded in a Bruker D8 diffractometer with a Sol-X energy dispersive detector, working at 40 kV and 30 mA and employing CuKα (λ = 1.5418 Å) filtered radiation. The diffractograms were registered with a step size of 0.02º and exposure time of 0.5 s per step and a 2θ range of 2.5-30º.

UV-Visible spectra: UV-Visible studies were carried out on a PrekinElmer Lambda XLS+ spectrometer. Fluorescence spectra were recorded on an Aminco SLM 8000 spectrophotometer. UV–Vis Diffuse reflectance spectra were carried out on a Shimadzu UV-2401 PC UV-Visible Spectrometer.

Raman spectra: The FT-Raman spectra (1064 nm) were recorded with an FT-Raman accessory kit (RamII)) linked to a Bruker Vertex70 spectrometer. A continuous-wave Nd-YAG laser working at λ=1064 nm was employed for excitation. A germanium detector operating at

liquid nitrogen temperature was used. Raman scattering radiation was collected in a back-scattering configuration with a standard spectral resolution of 4 cm-1. The power of the laser beam was kept at a level lower than 100 mW in all cases. Around 3000–4000 scans were averaged for each spectrum to optimize the signal-to-noise ratio.

S2. Synthesis of monomers Tx2Br and Tx3Br

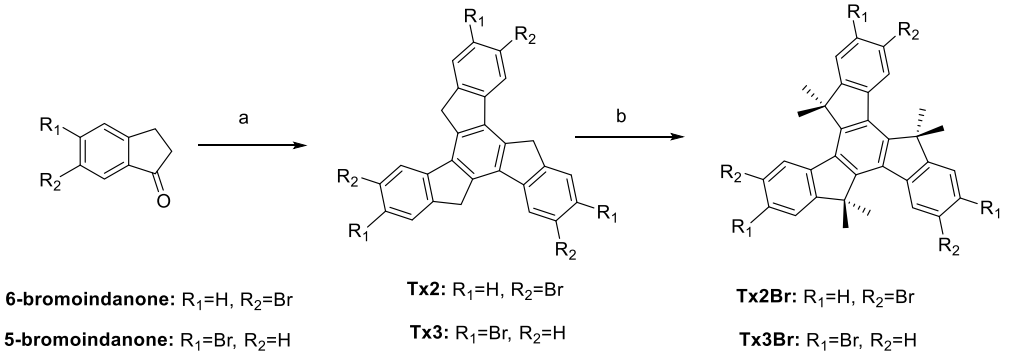

6-bromoindanone: R_1=H, R_2=Br

5-bromoindanone: R_1=Br, R_2=H

Tx2: R_1=H, R_2=Br

Tx3: R_1=Br, R_2=H

Tx2Br: R_1=H, R_2=Br

Tx3Br: R_1=Br, R_2=H

a) p-toluenesulfonic acid,propionic acid,1-4dichlorobenzene
b) tBuOK,MeI, DMSO

2,7,12-tribromo-10,15-dihydro-5*H*-diindeno[1,2-*a*;1',2'-*c*]fluorene (Tx2) [1]

A mixture of 5-bromo-1-indanone (1.7g, 8.10 mmol), p-toluene sulfonic acid (5.4g, 28.3 mmol) and propionic acid (2.1mL, 28 mmol) in 1,4-dichlorobenzene (7 mL) was stirred at 105ºC for 16 hours. At the resulting yellow suspension was added methanol (10mL) and was neutraliced with NaOH solution (5M). The light yellow solid obtained was washed with H_2O, methanol, dichloromethane and acetone. The compound was obtained with 58% yield.

^{1}H-NMR (500 MHz, $C_2D_2Cl_4$-*d*) δ (ppm) 7.86 (s, 3H), 7.79 (d, *J*=8.1 Hz, 3H), 7.66 (d, *J*=8.2 Hz,3H), 4.27 (s, 6H).

3,8,13-tribromo-10,15-dihydro-5*H*-diindeno[1,2-*a*;1',2'-*c*]fluorene (Tx3) [2]

A mixture of 6-bromo-1-indanone (1.7g, 8.10 mmol), p-toluene sulfonic acid (5.4g, 28.3 mmol) and propionic acid (2.1mL, 28 mmol) in 1,4-dichlorobenzene (7 mL) was stirred at 105ºC for 16 hours. At the resulting yellow suspension was added methanol (10mL) and was neutraliced with NaOH solution (5M). The light yellow solid obtained was washed with H_2O, methanol, dichloromethane and acetone. The compound was obtained with 72% yield.

^{1}H-NMR (500 MHz, $C_2D_2Cl_4$-*d*) δ (ppm) 8.08 (s, 3H), 7.60 (d, *J*=8.0 Hz, 3H), 7.55 (d, *J*=8.0 Hz,3H), 4.29 (s, 6H).

2,7,12-tribromo-5,5,10,10,15,15-hexamethyl-10,15-dihydro-5H-diindeno[1,2-*a*:1',2'-*c*]fluorene (TxBr2) [3]

To a stirred suspension of 2,7,12-tribromo-10,15-dihydro-5*H*-diindeno[1,2-*a*;1',2'-*c*]fluorene (1g, 1.73 mmol) in DMSO (12 mL) was added ^{t}BuOK (1.2 g, 10.73 mmol). The resulting red solution was cooled to 0ºC and then, MeI (1.47 g, 10.36 mmol) was added dropwise. The mixture was allowed to warm to room temperature and stirred 30 minutes. Then, a second addition of ^{t}BuOK (0.592 g) and MeI (0,655 mL) was performed and the resulting mixture was stirred at room temperature for 16 hours. Finally 1.77 g of ^{t}BuOK and 0.592 mL of MeI were added and the reaction was stirred for 2 hours. Then the mixture was poured into ice and extracted with dichloromethane. After removing the solvent, the solid obtained was purified by column chromatography on silica gel, using a mixture of hexane and dichloromethane (5:1). The compound was obtained with 73% yield.

^{1}H-NMR (200 MHz, $CDCl_3$-*d*) δ (ppm) 8.12 (d, *J*=8.5 Hz, 3H), 7.67 (s, 3H), 7.56 (d, *J*=8.5 Hz, 3H), 1.85 (s, 18H).

3,8,13-tribromo-5,5,10,10,15,15-hexamethyl-10,15-dihydro-5H-diindeno[1,2-*a*:1',2'-*c*]fluorene (TxBr3)

To a stirred suspension of 3,8,13-tribromo-10,15-dihydro-5*H*-diindeno[1,2-*a*;1',2'-*c*]fluorene (1g, 1.73 mmol) in DMSO (12 mL) was added ^{t}BuOK (1.2 g, 10.73 mmol). The resulting red solution was cooled to 0ºC and then, MeI (1.47 g, 10.36 mmol) was added dropwise. The mixture was allowed to warm to room temperature and stirred 30 minutes. Then, a second addition of ^{t}BuOK (0.592 g) and MeI (0,655 mL) was performed and the resulting mixture was stirred at room temperature for 16 hours. Finally 1.77 g of ^{t}BuOK and 0.592 mL of MeI were added and the reaction was stirred for 2 hours. Then the mixture was poured into ice and extracted with dichloromethane. After removing the solvent, the solid obtained was purified by column chromatography on silica gel, using a mixture of hexane and dichloromethane (5:1). The compound was obtained with 80% yield.

^{1}H-NMR (200 MHz, $CDCl_3$-*d*) δ (ppm) 8.38(s, 3H), 7.53 (d, *J*=8.1 Hz, 3H), 7.41 (d, *J*=8.1 Hz,3H), 1.85 (s, 18H); ^{13}C-NMR (50 MHz, $CDCl_3$-*d*) δ156.04, 149.25, 138.44, 129.87, 128.49, 124.00, 120.18, 46.74, 23.84; MALDI-TOF MS m/z 664.0 (M+); HRMS (MALDI-TOF) Calc. $C_{33}H_{27}Br_3$: 663.9646, Found: 663.9622.

S3. Synthesis of polymers Tx2-CMP, PhTx2-CMP and Tx3-CMP and PhTx3-CMP.

Synthesis of Tx2-CMP and Tx3-CMP

General procedure: Inside a dry box, **TxBr2** or **TxBr3**(100 mg, 0.150 mmol), 2,2´-bipyridyl (132 mg, 0.750 mmol), $Ni(cod)_2$ (206 mg, 0.750 mmol), 1,5-cyclooctadiene (110 μL) and 15.5 mL of dry DMF were place in a pyrex tube and the mixture stirred at 80°C for 4 days. Then, the reaction was cooled at room temperature and concentrated HCl was added. The mixture was filtered and the residue s washed with $CHCl_3$ and THF. The resulting solid was washed at 100°C for 2 hours with a mixture of 100 mL of water, 2 mL of HCl and 2 mL of HNO_3. The light brown solid obtained was washed with H_2O, ethanol and diethyl ether and then dried was dried under vacuum at 120°C for 4 hours. Yield: **Tx2-CMP**: 75%; **Tx3-CMP:** 82%.

Synthesis of PhTx2-CMP and PhTx3-CMP

General procedure: **TxBr2** or **TxBr3** (100 mg, 0.150 mmol), 1,4-phenylenediboronic acid (39 mg, 0.24 mmol), triphenylphosphine (60 mg,0.23 mmol), sodium bicarbonate (56 mg) and palladium acetate (6.7 mg, 0.03 mmol) were suspended in a mixture of DMF (2 mL) and water (0.5 mL) and degassed by bubbling N_2. Microwave heating was performed in a computer-controlled CEM Discover or ANTON PAAR microwave with temperature and pressure control. The initial heating was performed at a power input of 75 W. After the pressure reached around 12 bar, the heating was stopped and allowed to cool at 60ºC. Then the heating was continued until a reaction temperature of around 145ºC was reached. The reaction was performed at this temperature and a pressure of around 5–7 bar for 10 minutes. After cooling to room temperature, the mixture was filtered and the crude product was washed with DMF and water and then with conc. HCl (1 mL), conc. HNO_3 (1 mL). Finally, the product was washed with water, THF and diethyl ether. After drying in vacuum at 100ºC for 12 h a yellowish powder was obtained. Yield: **PhTx2-CMP:** 80%; **PhTx3-CMP:** 78%.

S4. Characterization of polymers Tx2-CMP, PhTx2-CMP, Tx3-CMP and PhTx3-CMP

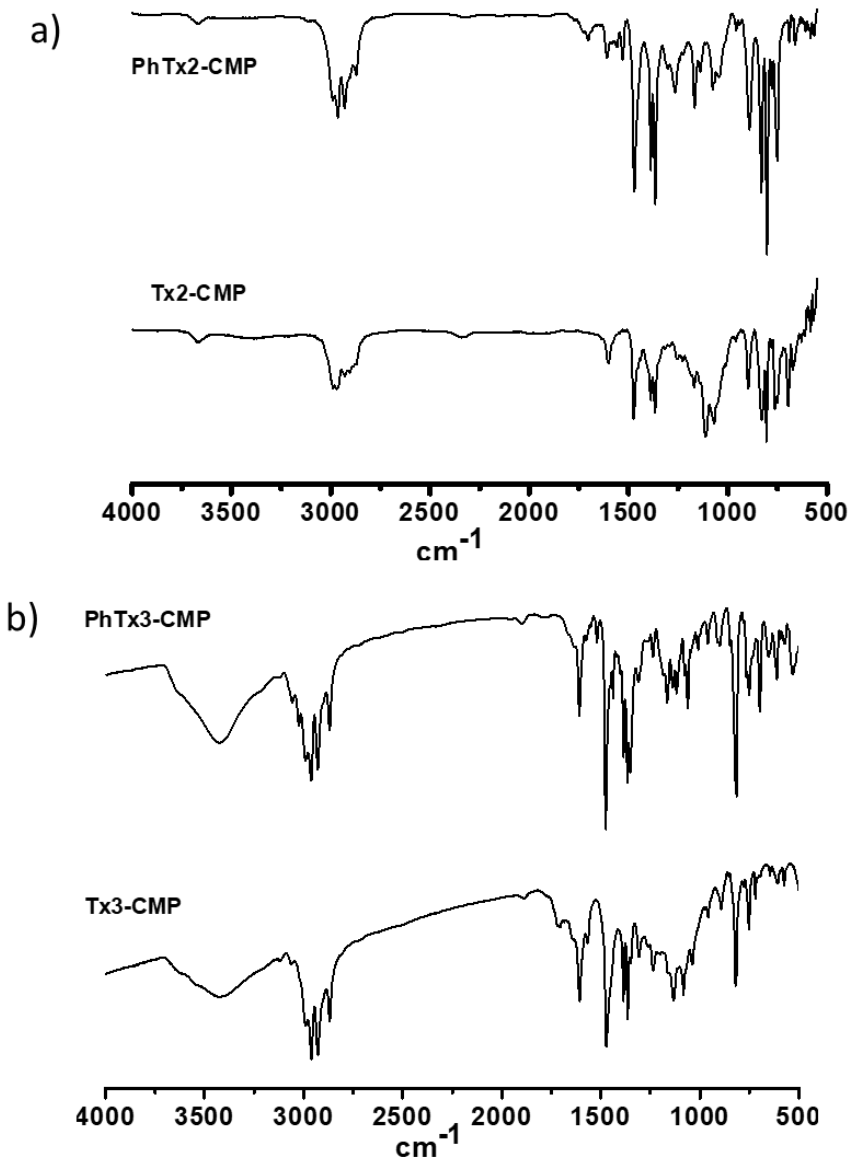

Figure S1. FT-IR of (a) homocoupled Truxene-based polymers **Tx2-CMP** and **Tx3-CMP** and of (b) phenylene spaced polymers **PhTx2-CMP** and **PhTx3-CMP**.

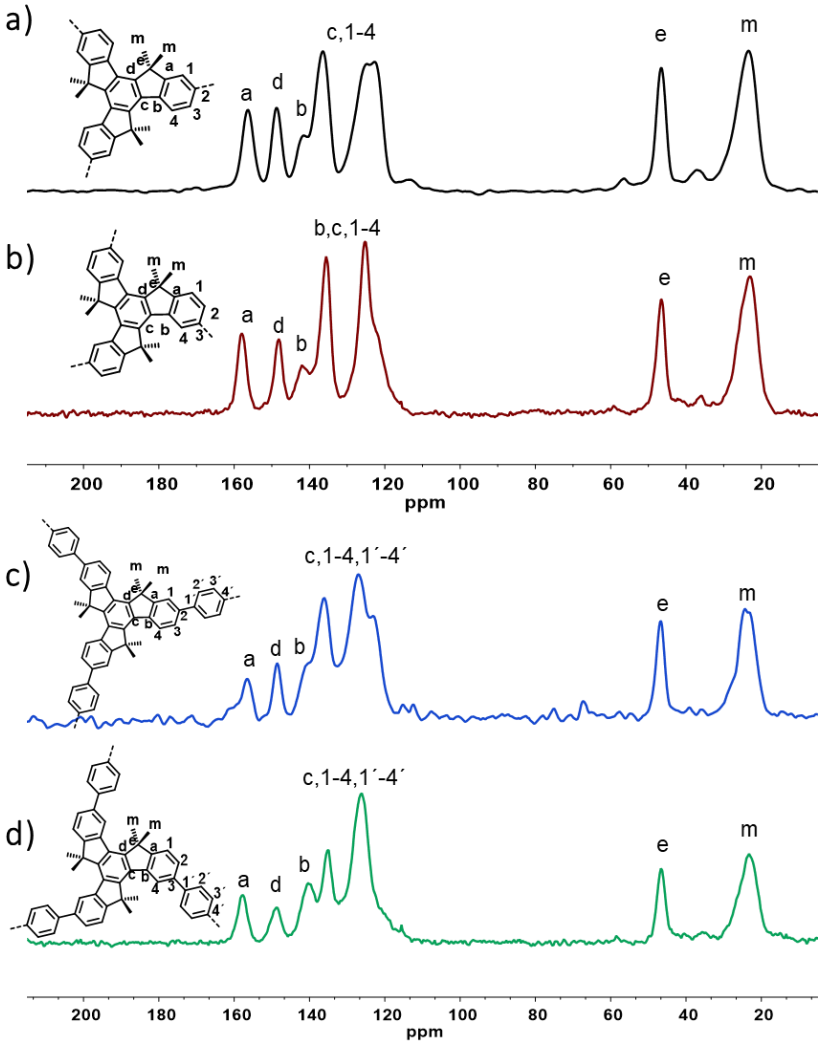

Figure S2.[13]C CP-MAS NMR spectra of Tx2-CMP, Tx3-CMP, PhTx2-CMP and PhTx3-CMP porous polymers.

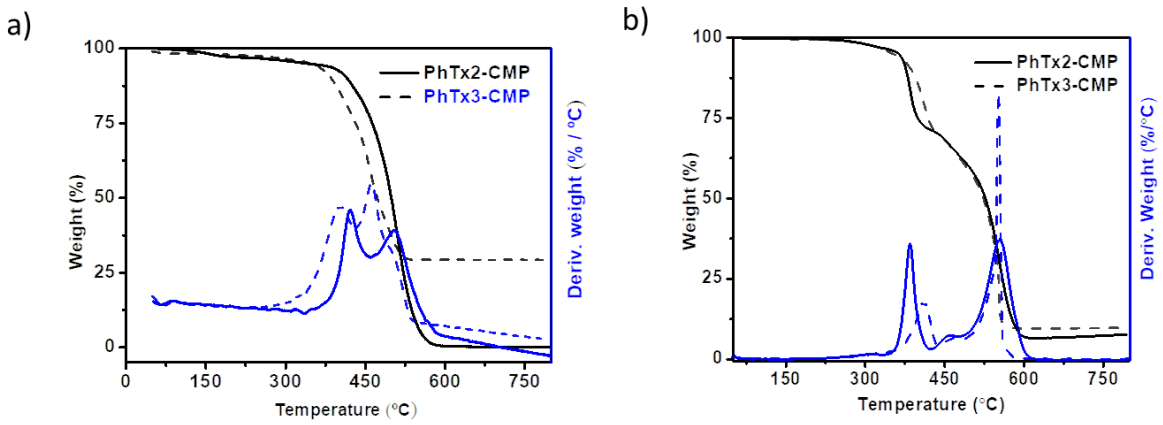

Figure S3. (a) Thermogravimetric analyses (TGA) of **Tx2-CMP**, **Tx3-CMP**. (b) Thermogravimetric analyses (TGA) of **PhTx2-CMP** and **PhTx3-CMP.**

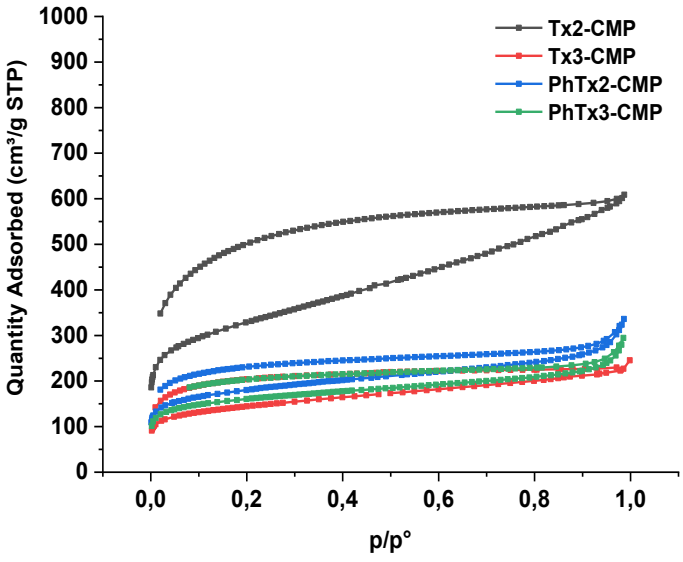

Figure S4. Nitrogen adsorption and desorption isotherms of **Tx2-CMP**, **Tx3-CMP**, **PhTx2-CMP** and **PhTx3-CMP** porous polymers.

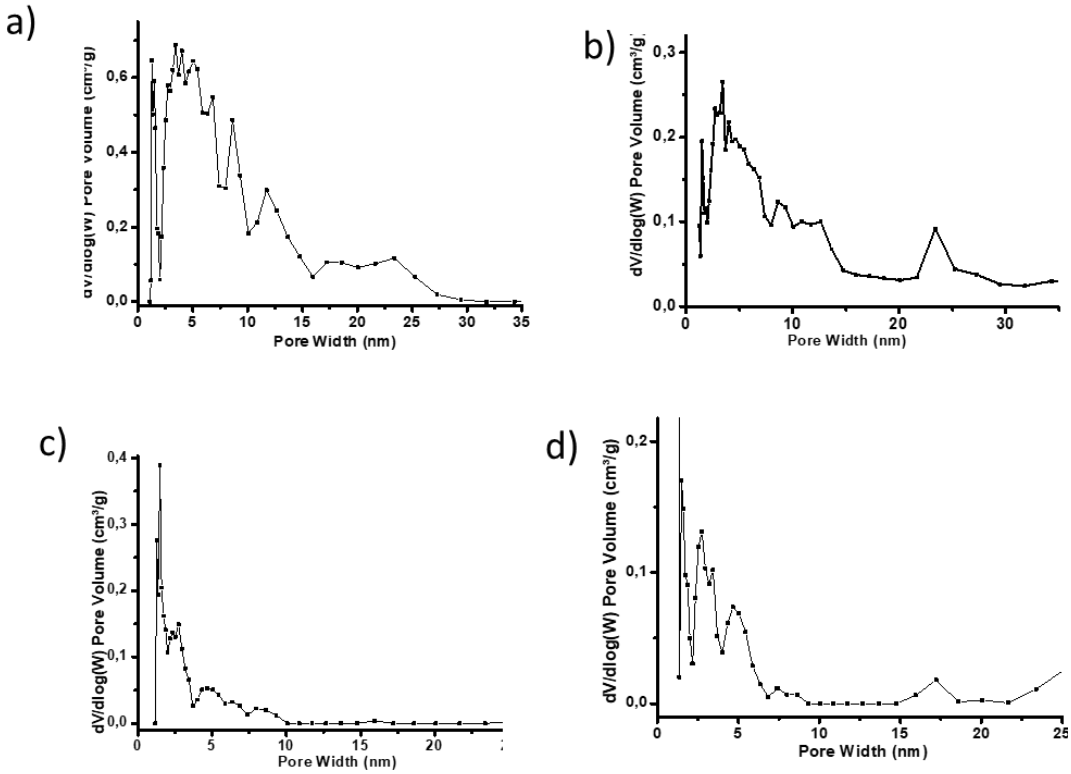

Figure S5. Pore size distribution of calculated by N_2-DFT methods for (a) **Tx2-CMP**, (b) **Tx3-CMP**, (c) **PhTx2-CMP** and (d) **PhTx3-CMP**.

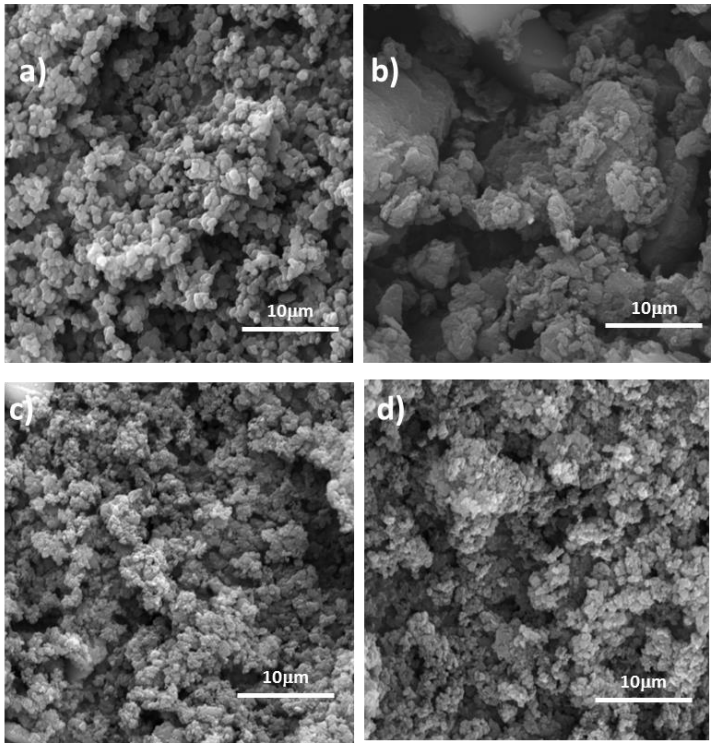

Figure S6. SEM images of (a) **Tx2-CMP**, (b) **Tx3-CMP**, (c) **PhTx2-CMP** and (d) **PhTx3-CMP**.

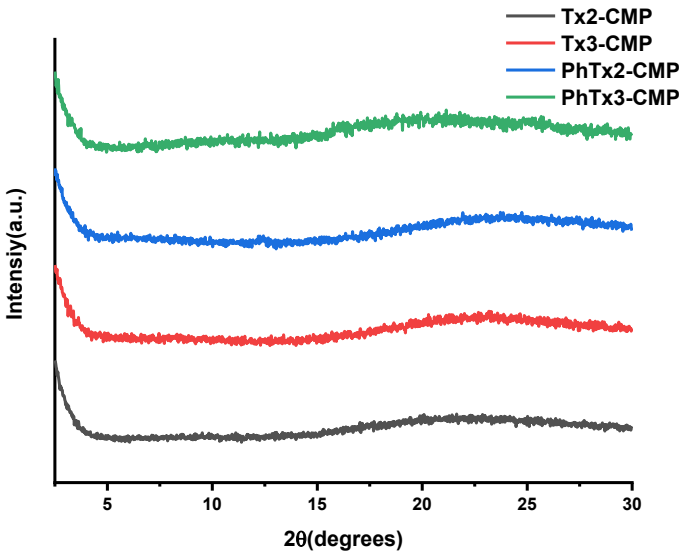

Figure S. Powder X-ray diffractograms of **Tx2-CMP**, **Tx3-CMP**, **PhTx2-CMP** and **PhTx3-CMP**.

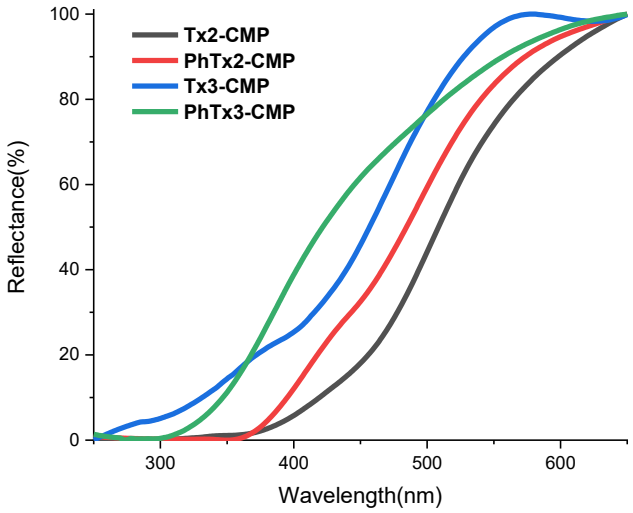

Figure S8. Normalized UV–Vis Diffuse reflectance spectra of **Tx2-CMP**, **Tx3-CMP**, **PhTx2-CMP** and **PhTx3-CMP**.

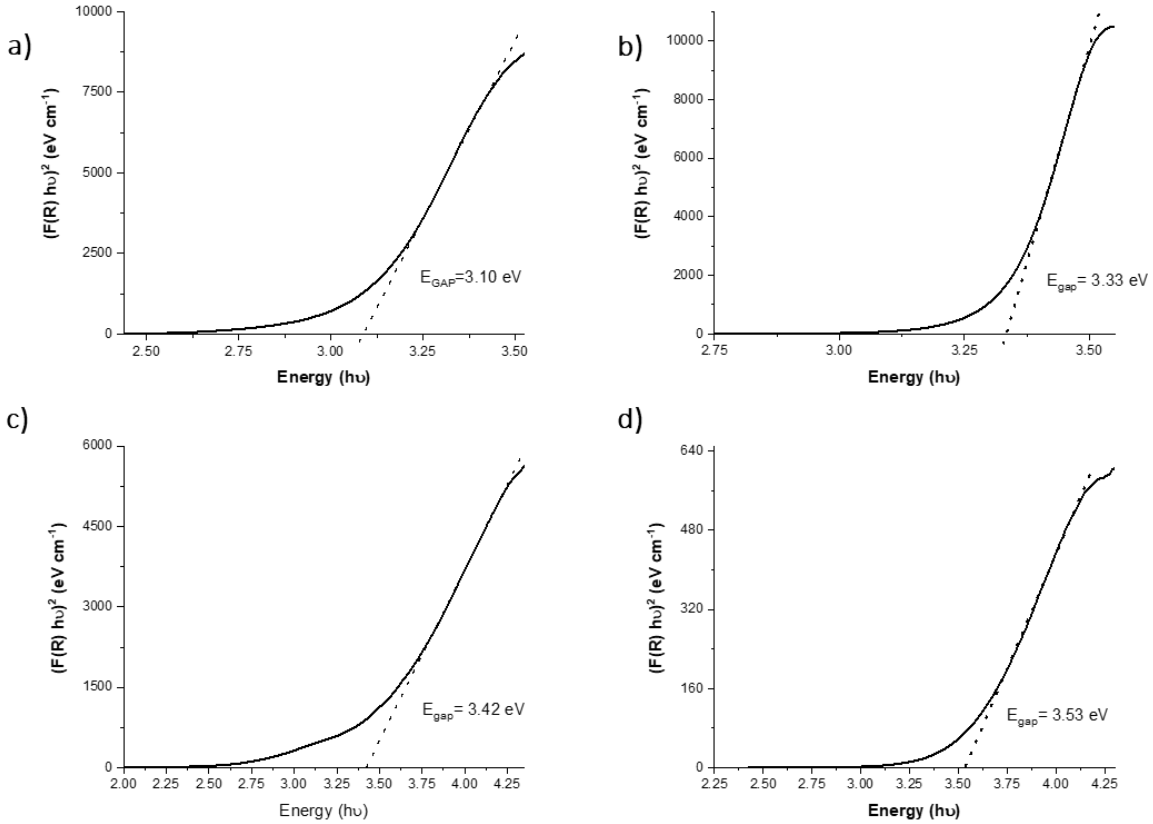

Figure S9. The tauc plot of the Kubelka-Munk function of (a) **Tx2-CMP**, (b) **PhTx2-CMP**, (c) **Tx3-CMP** and (d) **PhTx3-CMP.**

.

Table S1 Elemental analysis of the new truxene-based polymers.

	Yield (%)	**Calc.**		**Exp.**	
Polymer		**% C**	**%H**	**% C**	**%H**
Tx2-CMP	75	92.91	7.01	83.3	6.06
Tx3-CMP	82	92.91	7.01	85.3	6.65
PhTx3-CMP	80	93.81	6.19	82.80	6.28
PhTx2-CMP	78	93.81	6.19	83.37	6.01

S5. Sensing of nitroaromatic compounds

Dispersions of 50μg/mL of **PhTx2-CMP** and **PhTx3-CMP** in DCM were prepared for sensing experiments. The polymer powder (0.5mg) was grinded in a mortar, suspended in 10 mL of DCM and the suspension was well dispersed by using ultrasonic treatment (30 min). Upon this treatment, stable suspensions were obtained and no precipitate was discernible at the bottom of the vials. These polymers have a round shaped morphology, which is probably contributing to their easy dispersibility (see Figure S6). The photostability of the two polymers suspensions was estimated by subjecting them to continuous UV irradiation at a power of 15 mW/cm^2 for 30 min. Under these conditions variations of the fluorescence intensity lower than 3% loss was observed (which is within the experimental error).

The quenching efficiency (**QE**) was calculated by using the equation: $\mathbf{QE=(}I_0\mathbf{-}I\mathbf{)/}I_0 \times \mathbf{100\%}$, where I_0 is the initial fluorescence intensity and I is the fluorescence intensity in the presence of a constant concentration of the corresponding analyte (100μM).

Titration experiments were performed by adding to the suspension, the analytes under study at gradual intervals from 10^{-2} M and 10^{-3} stock solutions. The fluorescence spectra were recorded accordingly on an Aminco SLM 8000 spectrophotometer with excitation and the emission slit widths of 5.0 nm.

The quenching data were analysed using the **Stern–Volmer equation:** $\mathbf{I_0/I=1+K_{SV}[Q]}$, which provides a quantitative relationship between the changes in fluorescence intensity (I_0/I) and the concentration of added nitroaromatic compounds ([Q]). After the addition of each analyte, the samples were sonicated for 10 seconds, the measurements were repeated 3 times per addition, and the average values were selected in order to eliminate potential instrumental errors. In addition, every titration was repeated 3 times with different suspensions and we have obtained the standard deviation of $\mathbf{I_0/I-1}$ for each concentration used to calculate the Stern-Volmer constants.

The detection limit (**LOD**) was calculated using the equation: $\mathbf{LOD=3\sigma/\rho}$, where σ is the standard deviation of blank measurements of polymers suspension and ρ is slope of the calibration curve (relative fluorescent intensity versus sample concentration). The standard deviation of blank (n=10) was calculated for suspensions of **PhTx2-CMP** and **PhTx3-CMP** with values of σ=0.0068 and σ=0.009 respectively.

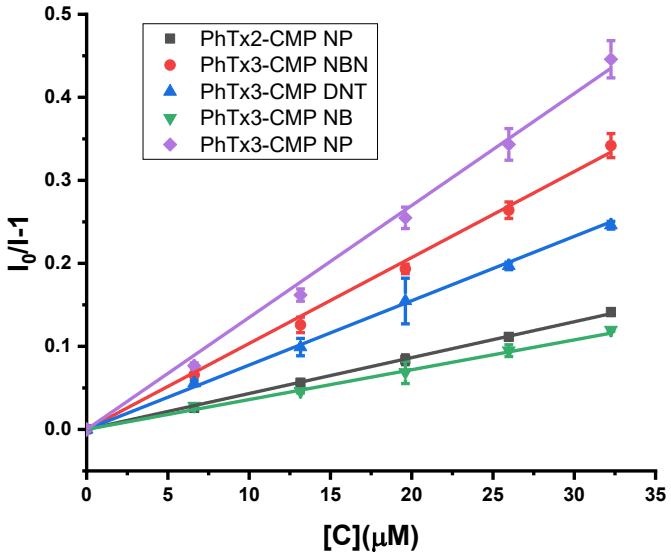

Figure S10. Stern-Volmer plots with standard deviation of **PhTx2-CMP** and **PhTx3-CMP** for *p*-nitrobenzonitrile (**NBN**), dinitrotoluene (**DNT**), *p*-nitrobencene (**NB**) and *p*-nitrophenol (**NP**).

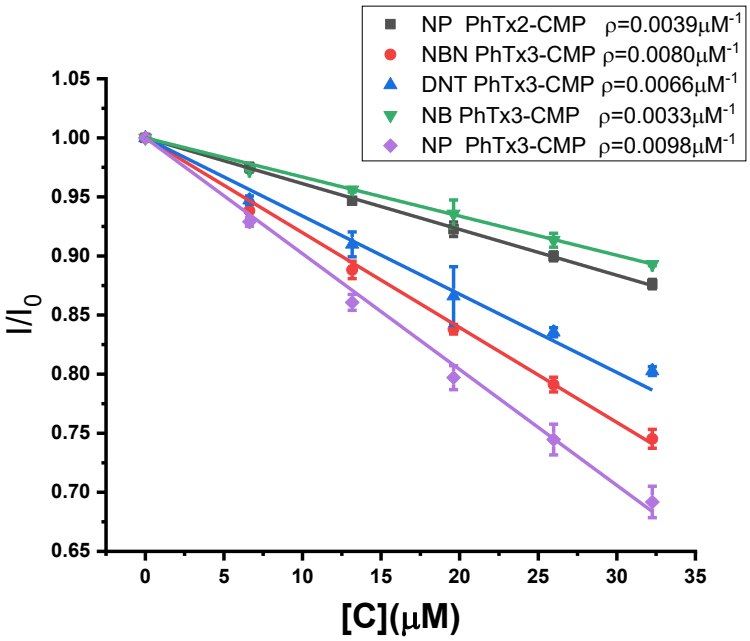

Figure S11. Calibration curve of relative fluorescent intensity versus sample concentration plots with standard deviation of **PhTx2-CMP** and **PhTx3-CMP** for *p*-nitrobenzonitrile (**NBN**), dinitrotoluene (**DNT**), *p*-nitrobencene (**NB**) and *p*-nitrophenol (**NP**).

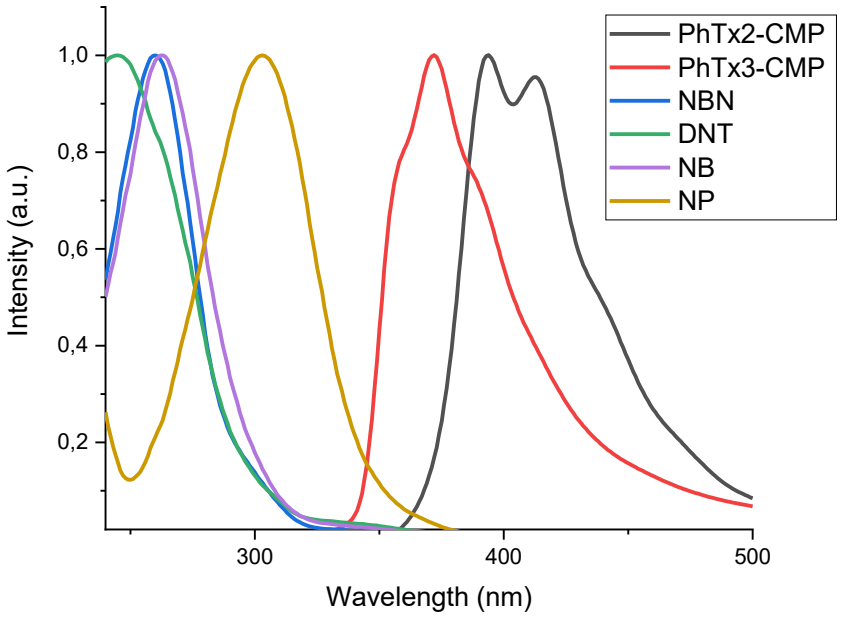

Figure S12. Spectral overlap between the abosrption of *p*-nitrobenzonitrile (**NBN**), dinitrotoluene (**DNT**), *p*-nitrobencene (**NB**) and *p*-nitrophenol (**NP**) and the emission espectra of **PhTx2-CMP** and **PhTx3-CMP**

S6. DFT Calculations.

Theoretical Methodology.

Simulations were performed in the framework of the density functional theory (DFT) using the Gaussian 09 program.[4] Fragments of molecules were considered as theoretical models for the truxene-based porous polymers with the aim of providing useful information about the trend of energy gaps, relative HOMO and LUMO energy levels, and nature of the electronic transitions as a function of the linkage position. It has been recently demonstrated that quantum chemical calculations of fragments of molecules provide relevant information about the molecular and electronic structure of porous polymeric networks.[5-7] In this work, four dimeric systems in which two truxene units are linked with or without a phenylene spacer have been considered as model systems for the truxene-based **Tx2-CMP**, **Tx3-CMP**, **PhTx2-CMP** and **PhTx3-CMP** porous polymers (see Figure S13). Geometry optimizations were performed for the four models of the porous polymers displayed in Figure S1 and for the hexamethyl truxene monomer **Tx** system. The calculations were performed by using the hybrid, generalized gradient approximation (GGA) functional B3LYP [8, 9] together with the 6-31G** basis set.[10, 11] Previous DFT calculations have shown that the popular B3LYP functional underestimate the optical band gap and overestimate the electron delocalization of large π-conjugated systems.[7, 12, 13] Therefore, the molecular geometries of the model systems were also calculated with the long-range corrected hybrid functional CAM-B3LYP[14] to check the long-range correction effects on the description of the electronic and molecular structure of the porous polymers. Interestingly, both CAM-B3LYP and B3LYP functionals give similar trends in the frontier molecular orbital energies, orbital description and energy gaps when comparing the polymers with the truxene connected through the 2,7,12 positions to those connected through the 3,8,13 positions. Note that all geometrical parameters were allowed to vary independently apart from planarity of the rings. Optimized geometries were confirmed as minima by frequency calculations. The calculated Raman frequencies at B3LYP level were scaled by 0.96 while a scaling factor of 0.98 was used for Raman frequencies at CAM-B3LYP level.

Time-dependent DFT (TDDFT)[15, 16] approach (in vacuo) was used to assess the excited state vertical transition energies. Molecular orbital contours were plotted using ChemCraft.[17]

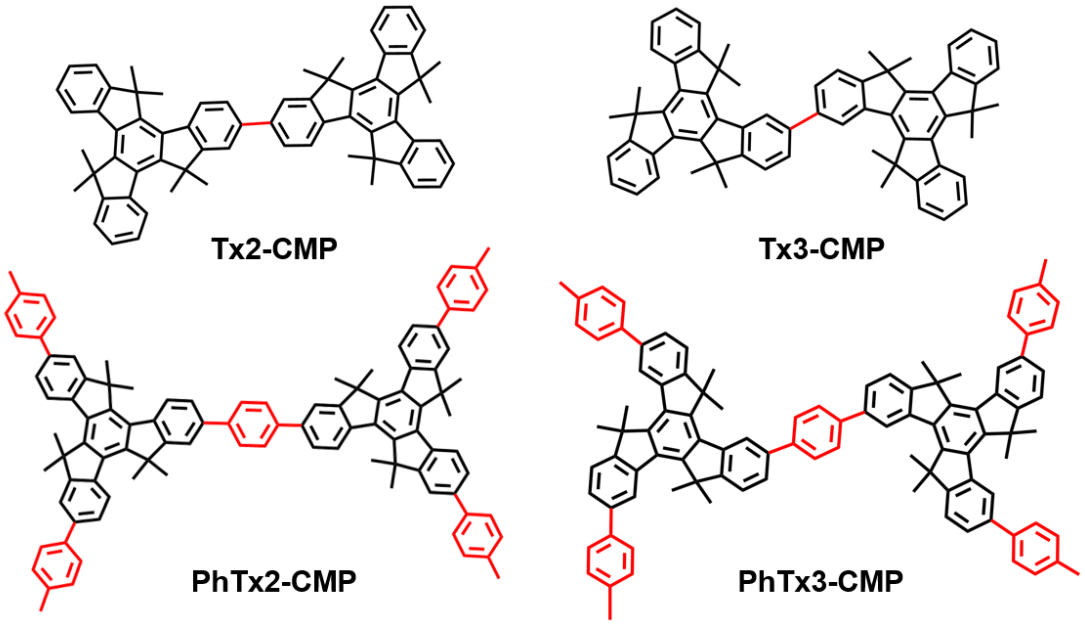

Figure S13. Chemical structures of the **Tx2-CMP**, **Tx3-CMP**, **PhTx2-CMP** and **PhTx3-CMP** model systems studied theoretically.

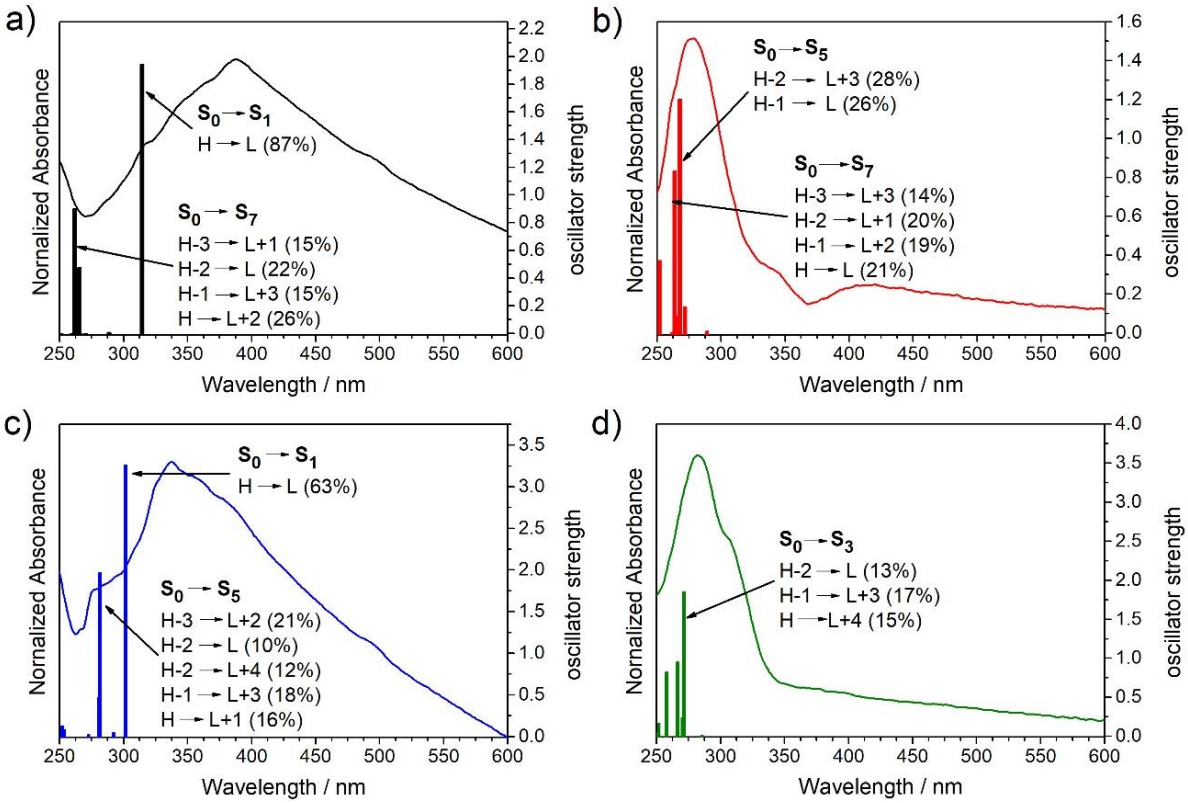

Figure S14. Comparison between the experimental UV-absorption spectra of (a) **Tx2-CMP**, (b) **Tx3-CMP**, (c) **PhTx2-CMP** and (d) **PhTx3-CMP** porous polymers and the vertical excited state transitions (solid bars) calculated at the TD-DFT//CAM-B3LYP/6-31G** level for their respective dimeric models. The composition of the frontier molecular orbitals involved in the main transitions are also shown.

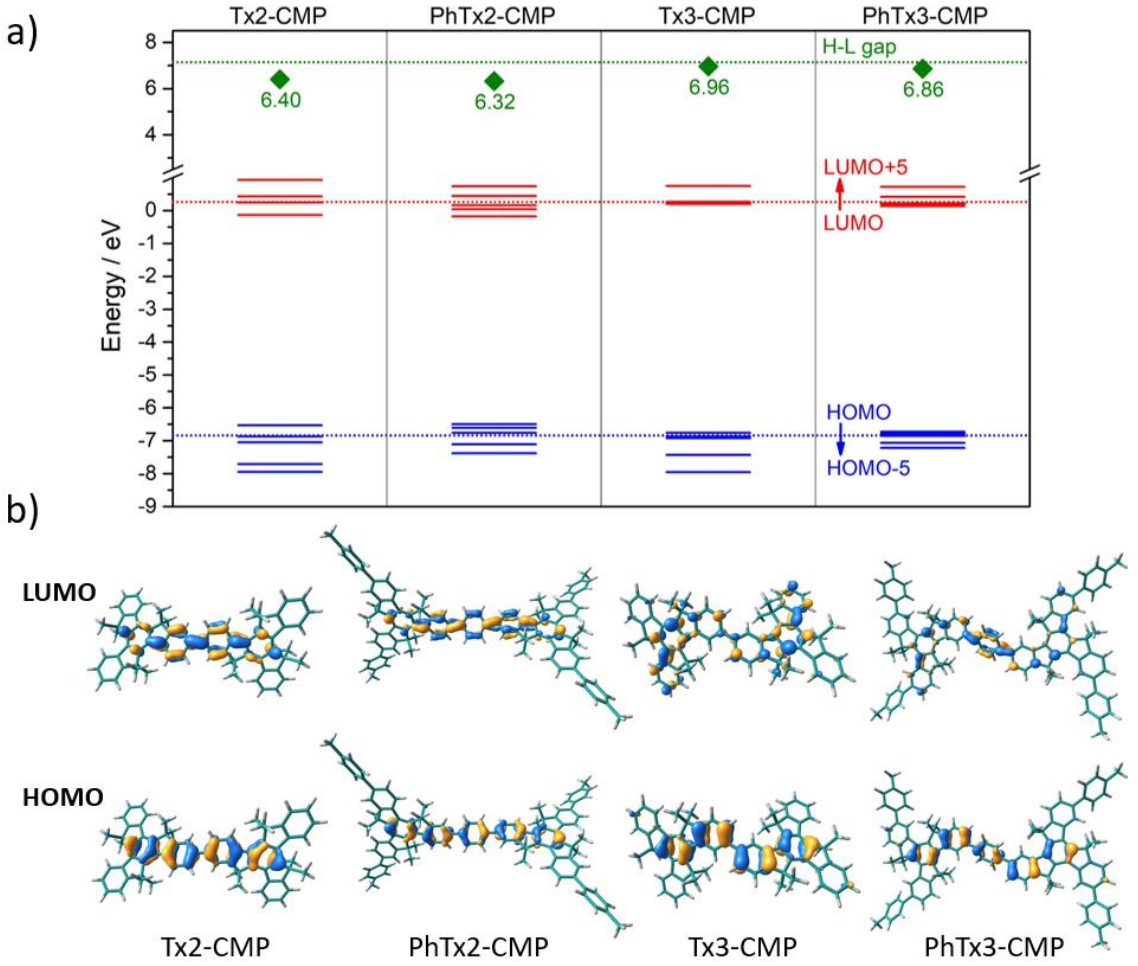

Figure S15. (a) DFT-calculated molecular orbital energies (CAM-B3LYP/6-31G** level) for the dimeric models of the truxene-based polymers, in comparison with those calculated for the hexamethyl truxene **Tx** system (dotted lines). (b) Topologies of the HOMO and LUMO orbitals.

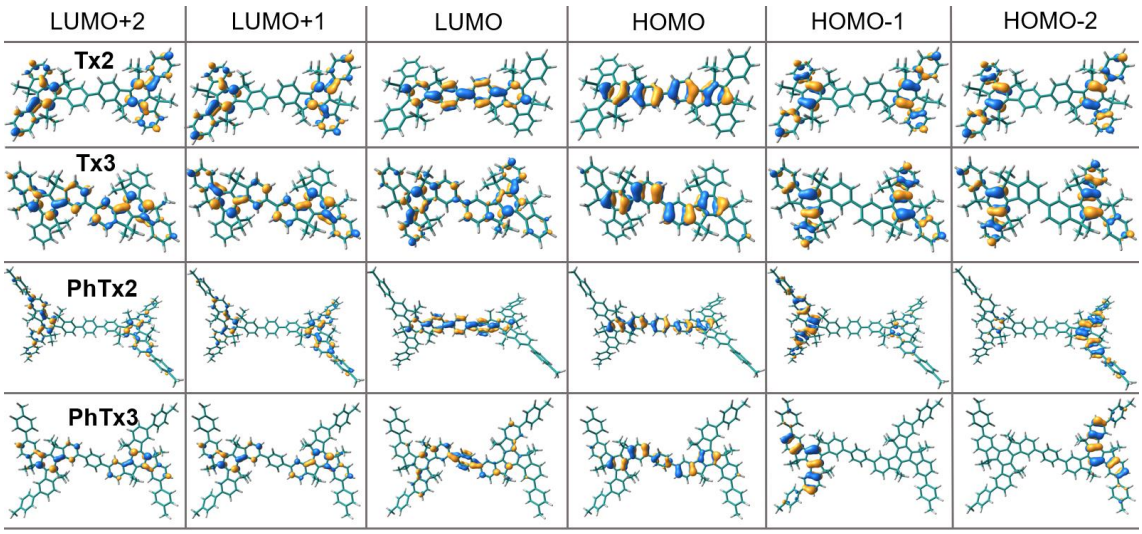

Figure S16. DFT-calculated frontier molecular orbitals (B3LYP/6-31G** level) for the dimeric models of the truxene-based polymers.

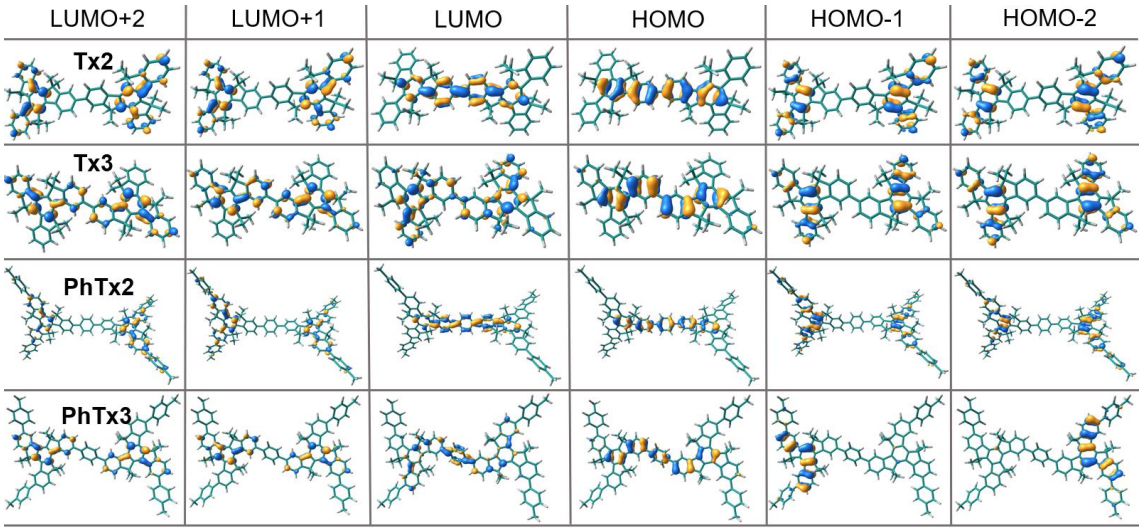

Figure S17. DFT-calculated frontier molecular orbitals (CAM-B3LYP/6-31G** level) for the dimeric models of the truxene-based polymers.

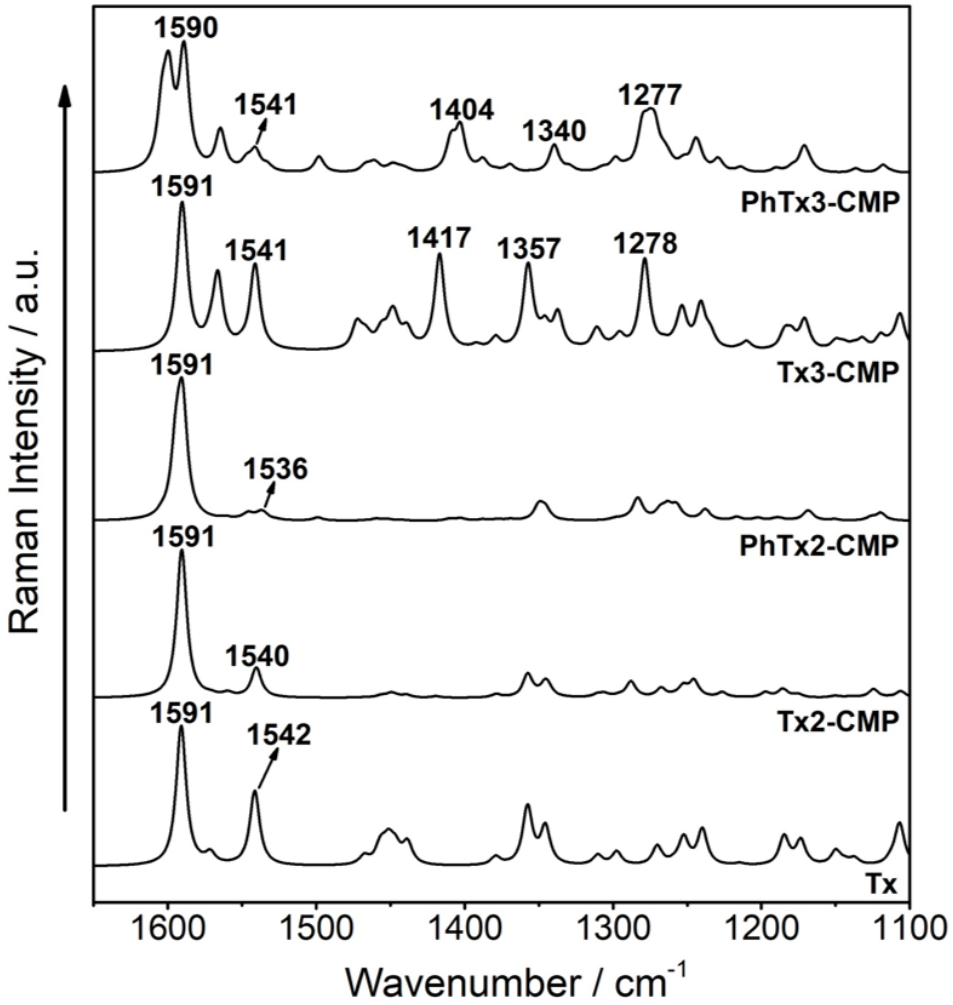

Figure S18. Theoretical Raman spectra (B3LYP/6-31G** level) for the dimeric models of the truxene-based polymers and for the hexamethyl truxene monomer **Tx**.

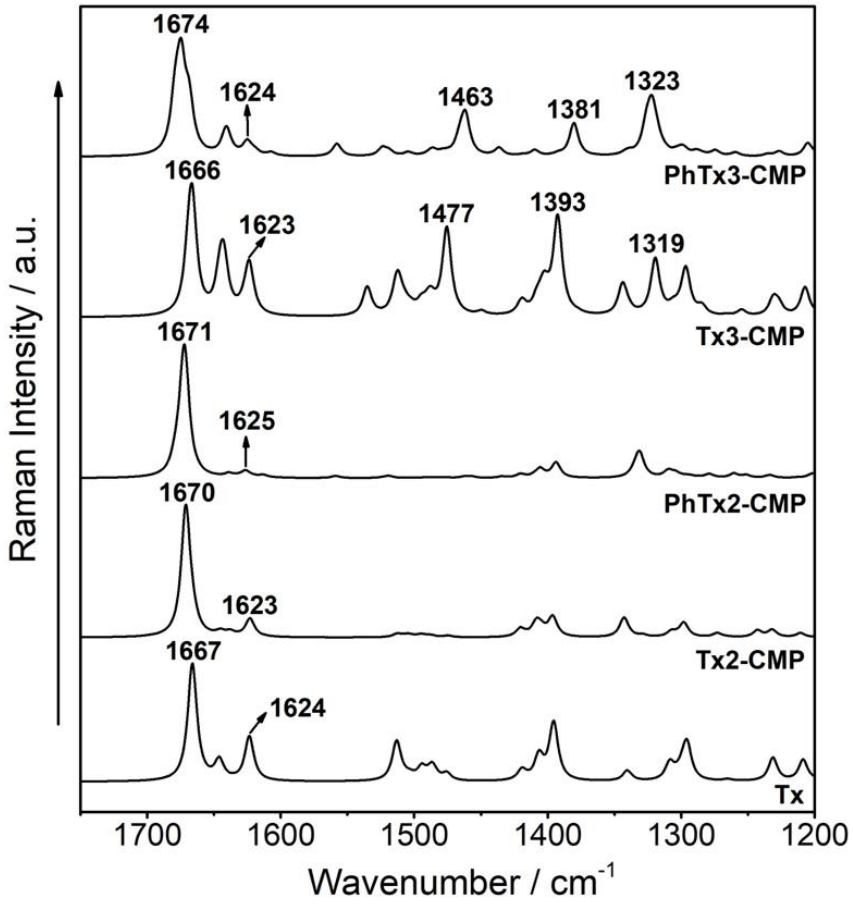

Figure S19. Theoretical Raman spectra (CAM-B3LYP/6-31G** level) for the dimeric models of the truxene-based polymers and for the hexamethyl truxene monomer **Tx**.

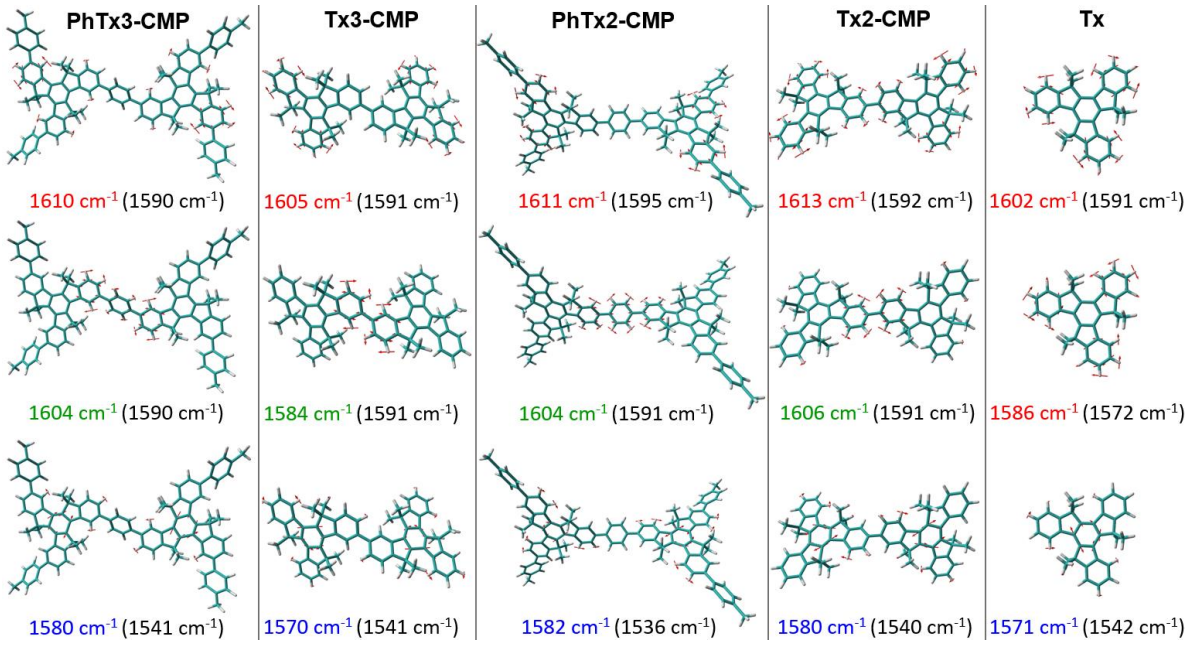

Figure S20. B3LYP/6-31G** vibrational eigenvectors associated with the most outstanding C=C/C-C Raman features for the dimeric models of the truxene-based polymers and for the hexamethyl truxene monomer **Tx**. The experimental and theoretical (in parentheses) wavenumbers are also shown.

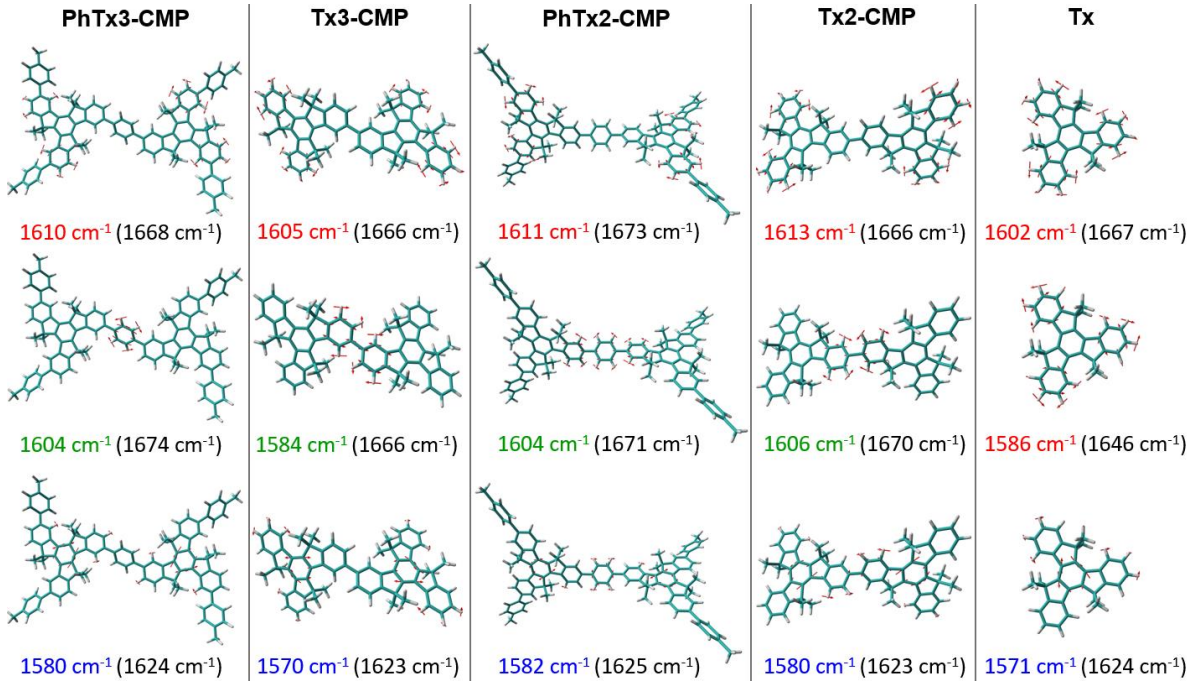

Figure S21. CAM-B3LYP/6-31G** vibrational eigenvectors associated with the most outstanding C=C/C-C Raman features for the dimeric models of the truxene-based polymers and for the hexamethyl truxene monomer **Tx**. The experimental and theoretical (in parentheses) wavenumbers are also shown.

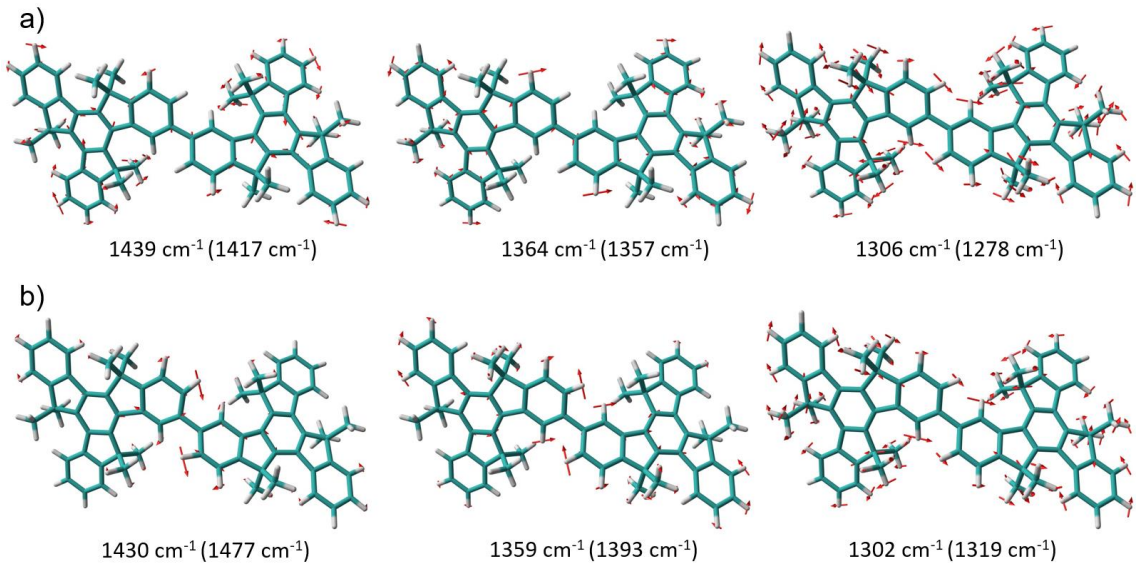

Figure S22. (a) B3LYP/6-31G** and (b) CAM-B3LYP/6-31G** vibrational eigenvectors associated with the most outstanding in plane CH deformation vibrations of the aromatic rings of the dimeric models of the truxene-based polymers and for the hexamethyl truxene monomer **Tx**. The experimental and theoretical (in parentheses) wavenumbers are also shown.

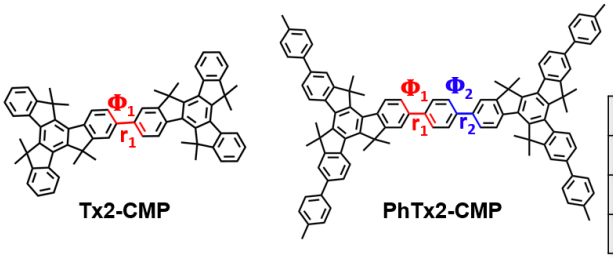

	Dihedral angles / °			
	B3LYP/6-31G**		CAM-B3LYP/6-31G**	
	Φ_1	Φ_2	Φ_1	Φ_2
Tx2-CMP	+36	-	+38	-
Tx3-CMP	+41	-	+41	-
PhTx2-CMP	-36	+36	-38	+38
PhTx3-CMP	-38	+38	-39	+39

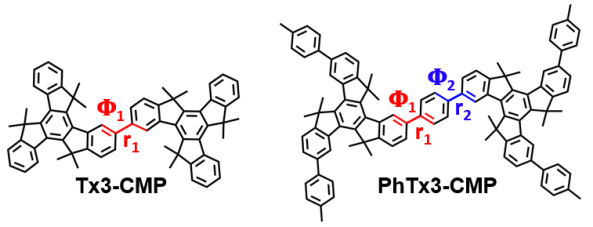

	Bond length / Å			
	B3LYP/6-31G**		CAM-B3LYP/6-31G**	
	r_1	r_2	r_1	r_2
Tx2-CMP	1.482	-	1.482	-
Tx3-CMP	1.488	-	1.486	-
PhTx2-CMP	1.482	1.482	1.482	1.482
PhTx3-CMP	1.485	1.485	1.484	1.484

Figure S23. DFT-calculated inter-ring dihedral angles and CC bond distances for the dimeric models of the truxene-based polymers.

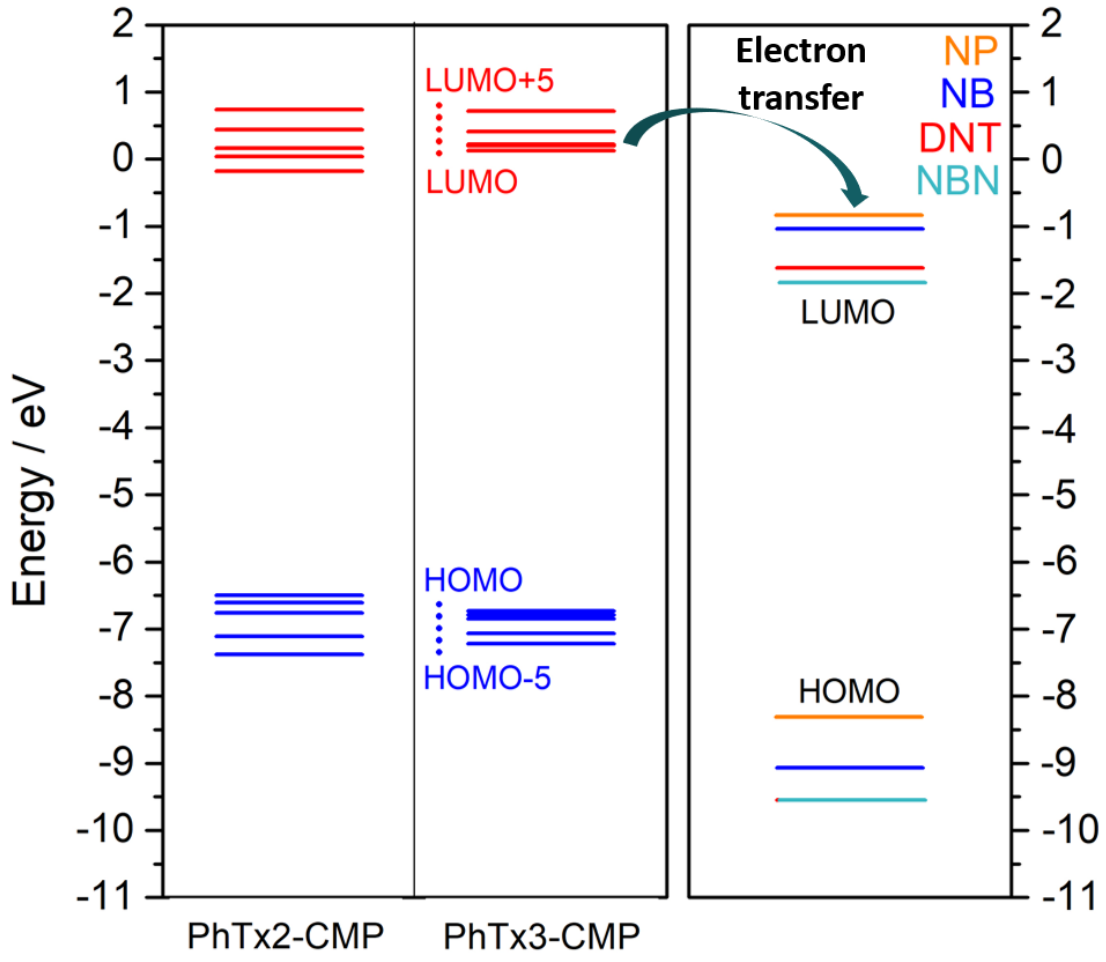

Figure S24. DFT-calculated molecular orbital energies (CAM-B3LYP/6-31G** level) for the dimeric models of the truxene-based polymers **PhTx2-CMP** and **PhTx3-CMP**, in comparison with the analytes orbital energies.

S7. References

1. Amick, A. W.; Scott, L. T., Trisannulated Benzene Derivatives by Acid Catalyzed Aldol Cyclotrimerizations of Cyclic Ketones. Methodology Development and Mechanistic Insight. *J. Org. Chem.* **2007,** 72, 3412-3418.
2. Gómez-Lor, B.; Frutos, Óscar d.; Ceballos, Plácido A.; Granier, T.; Echavarren, Antonio M., Synthesis of New C3h and C3v Truxene Derivatives. *Eur. J. Org. Chem.* **2001,** 2001, 2107-2114.
3. Kim, Y.; Das, S.; Bhattacharya, S.; Hong, S.; Kim, M. G.; Yoon, M.; Natarajan, S.; Kim, K., Metal-Ion Metathesis in Metal–Organic Frameworks: A Synthetic Route to New Metal–Organic Frameworks. *Chem. Eur. J.* **2012,** 18, 16642-16648.
4. Frisch, M. J., Trucks, G.W., Schlegel, H.B., et al. , Gaussian 09 Revision C 01 *Wallingford* **2009**
5. Li, L.; Cai, Z.; Wu, Q.; Lo, W.-Y.; Zhang, N.; Chen, L. X.; Yu, L., Rational Design of Porous Conjugated Polymers and Roles of Residual Palladium for Photocatalytic Hydrogen Production. *J. Am. Chem. Soc.* **2016,** 138, 7681-7686.
6. Li, L.; Lo, W.-y.; Cai, Z.; Zhang, N.; Yu, L., Donor–Acceptor Porous Conjugated Polymers for Photocatalytic Hydrogen Production: The Importance of Acceptor Comonomer. *Macromolecules* **2016,** 49, 6903-6909.
7. Wen, J.; Luo, D.; Cheng, L.; Zhao, K.; Ma, H., Electronic Structure Properties of Two-Dimensional π-Conjugated Polymers. *Macromolecules* **2016,** 49, 1305-1312.
8. Lee, C.; Yang, W.; Parr, R. G., Development of the Colle-Salvetti correlation-energy formula into a functional of the electron density. *Phys. Rev. B* **1988,** 37, 785-789.
9. Becke, A. D., Density‐functional thermochemistry. III. The role of exact exchange. *J. Chem. Phys* **1993,** 98, 5648-5652.
10. Hehre, W. J.; Ditchfield, R.; Pople, J. A., Self—Consistent Molecular Orbital Methods. XII. Further Extensions of Gaussian—Type Basis Sets for Use in Molecular Orbital Studies of Organic Molecules. *J. Chem. Phys* **1972,** 56, 2257-2261.
11. Francl, M. M.; Pietro, W. J.; Hehre, W. J.; Binkley, J. S.; Gordon, M. S.; DeFrees, D. J.; Pople, J. A., Self‐consistent molecular orbital methods. XXIII. A polarization‐type basis set for second‐row elements. *J. Chem. Phys* **1982,** 77, 3654-3665.
12. Körzdörfer, T.; Parrish, R. M.; Marom, N.; Sears, J. S.; Sherrill, C. D.; Brédas, J.-L., Assessment of the performance of tuned range-separated hybrid density functionals in predicting accurate quasiparticle spectra. *Phys. Rev. B* **2012,** 86, 205110.
13. Adamo, C.; Jacquemin, D., The calculations of excited-state properties with Time-Dependent Density Functional Theory. *Chem. Soc. Rev.* **2013,** 42, 845-856.
14. Yanai, T.; Tew, D. P.; Handy, N. C., A new hybrid exchange–correlation functional using the Coulomb-attenuating method (CAM-B3LYP). *Chem. Phys. Lett.* **2004,** 393, 51-57.
15. Runge, E.; Gross, E. K. U., Density-Functional Theory for Time-Dependent Systems. *Phys. Rev. Lett.* **1984,** 52, 997-1000.
16. Heinze, H. H.; Görling, A.; Rösch, N., An efficient method for calculating molecular excitation energies by time-dependent density-functional theory. *J. Chem. Phys* **2000,** 113, 2088-2099.
17. https://www.chemcraftprog.com, Chemcraft - graphical software for visualization of quantum chemistry computations. .

.

Supporting Information

In Silico Design of 2D Polymers Containing Truxene-Based Platforms: Insights into their Structural and Electronic Properties

Sergio Gámez-Valenzuela,[a] Marcelo Echeverri,[b] Berta Goḿez-Lor,[b*] José I. Martínez[b*] and M. Carmen Ruiz Delgado[a*]

[a] Dept. of Physical Chemistry, University of Málaga, Campus de Teatinos s/n, 29071, Málaga, Spain. [b] Dept. of Nanostructures and Low-dimensional Materials, Instituto de Ciencia de Materiales de Madrid (ICMM-CSIC), C/ Sor Juana Inés de la Cruz 3, Madrid 28049, Spain.

*Corresponding authors: bgl@icmm.csic.es; joseignacio.martinez@icmm.csic.es; carmenrd@uma.es

Page

S1. Theoretical Methods and Computational Details

Molecular fragments. First, molecular fragments of the 2D polymers under study (dimers for $\mathbf{T_2}$ and $\mathbf{T_3}$ and trimers for $\mathbf{T_{2,3}}$, see Figure S1) were performed in the framework of the density functional theory (DFT) using the Gaussian16 program.[1] Note that it has been recently demonstrated that calculations of molecular fragments provide important information about the molecular, electronic structure and charge-transport properties of 2D conjugated polymers.[2–9] To this end, two different hybrid functionals were used, such as the hybrid generalized gradient approximation (GGA) functional PBE0[10] and the long-range corrected hybrid functional CAM-B3LYP[11] together with the 6-31G**[12,13] and the cc-pVDZ[14] basis sets. All geometrical parameters were allowed to vary independently, and the calculated geometries were confirmed as minima by frequency calculations. The molecular orbitals were plotted using ChemCraft.[15] Interestingly, PBE0 and CAM-B3LYP functionals and the two different 6-31G** and cc-pVDZ basis sets predict the same trend in the description of the structural properties (*i.e.*, compare Fig. 2 in the main text and Fig S3 in the ESI with Fig. S4) and HOMO-LUMO gaps (*i.e.*, compare Fig. 3a in the main text with Fig. S5 in the SI) and topologies of the $\mathbf{T_2}$ an $\mathbf{T_3}$ dimeric models (*i.e.*, compare Fig. 3b in the main text and Fig. S6 with Fig. S7 in the SI).

NICS methodology. The NICS[16,17] values were calculated at the CAM-B3LYP/6-311++G(2df,p) level from the CAM-B3LYP/cc-pVDZ optimized structures by using the gauge-independent atomic orbital (GIAO)[18] method.

Intramolecular reorganization energies. We also carried out optimizations of the radical-ion states associated with the model dimers in order to analyze the intramolecular reorganization energies for holes (λ_h) and electron transfer (λ_e). The λ values were calculated directly from the relevant points on the potential energy surfaces by means of a standard procedure reported in the literature.[19,20]

Periodic calculations. In a step forward, we used periodic boundary conditions to obtain the geometry optimizations of 2D COF structures of all polymers under study. For that purpose, the preliminary optimized building blocks (at CAM-B3LYP/cc-pVDZ level) can be considered reasonable starting point geometries towards the assembling of the whole COF systems. Once the 2D COFs were constructed, they were fully optimized (simultaneous lattice/cell and structure optimizations) with the QUANTUM EXPRESSO plane- wave DFT code.[21] Within this implementation, the GGA-PBE[22] functional was used to account for the exchange-correlation (XC) effects, at the same time that we use the Grimme DFT-D3 semi-empirical efficient vdW correction to include dispersion forces and energies in conventional DFT functionals.[23] Ultra-soft pseudopotentials have been used to model the ion-electron interaction within the C, N, O and H atoms.[24,25] The Brillouin zones have been sampled by means of optimal Monkhorst-Pack grids.[26] In this regard, the one-electron wave-functions are expanded in a basis of plane-waves with a kinetic energy cutoff of 41 Ry for the kinetic energy and 260 Ry for electronic density. The energy cutoff values have been tested to achieve sufficient accuracy to guarantee a full convergence in total energy and electronic density. As mentioned, we have performed simultaneous full lattice/cell and structure optimizations for all the different periodic 2D systems. The atomic relaxations were carried out within a conjugate gradient minimization scheme until the maximum force acting on any atom was below 0.02 eV Å^{-}

[1]. Relaxations of cell shape and size have been double-checked with two different algorithms:a damped dynamics, and a Broyden–Fletcher–Goldfarb–Shanno-like relaxation.[27–29] These two approaches, tested thoroughly in the literature for different crystal bulk and molecular configurations, provide very similar and satisfactory results for cell-shape and lattice parameters.
Inter-layer distances have been fully-relaxed following the afore mentioned simultaneous lattice+structure relaxation protocol. Inter-layer cohesive energies for the crystal-bulks analyzed in the study have been obtained in their both AA and AB stacking fashions as the difference between the total energies of the crystal bulks (with one layer per unit cell) and the optimized corresponding single-layers.

Topologies of valence and conduction bands. 3D isosurfaces of the orbital electronic densities corresponding to the valence and conduction electronic states of the different extended 2D COF systems studied here ($||\Psi_{cond}(\mathbf{r})||^2$ and $||\Psi_{val}(\mathbf{r})||^2$) at the k-point corresponding to the direct band gap have been plotted using the the VMD 1.9.3 program.[30] The same program has been used in order to represent the surface charge distributions of the resulting 2D COFs. From these figures we can extract information about the spatial localization and delocalization degree of these states, which may directly connect with the transport performance of the systems, the homogeneity in the spatial distribution of the states, which is related to the spatial coherence of the electronic properties, as well as the preferential carrier transport paths across the compounds. All of them have been depicted with the same isosurface value (0.0003 e^-/A) for sake of comparison between them.

UV-Vis spectra. Photoexcitation (optical absorption) spectra of the periodic layers have been computed by the Time-dependent DFT formalism as implemented in the QUANTUM ESPRESSO simulation package.[31,32] Within this theoretical framework the excitation spectrum is obtained as:

$$I(\omega) \propto Im[\bar{\alpha}(\omega)], \qquad \text{eq. (3)}$$

where $I(\omega)$ is the absorption intensity, and $Im[\bar{\alpha}(\omega)]$ is the imaginary part of $\bar{\alpha}(\omega)$, the averaged (average of the diagonal elements) dipole polarizability. This dynamical polarizability is represented in terms of the resolvent of its Liouvillian super-operator within TD-DFT, and evaluated using a non-Hermitean Lanczos method, whose implementation does not require the calculation of virtual states.[31,32]

Effective masses. Effective hole and electron masses, m^*_h and m^*_e, have been evaluated for the top of the valence band and the bottom of the conduction band, respectively, for those systems with a significant electronic band dispersion via the following expression:

$$m^* = \hbar^2 \left\{ \frac{\partial^2 E}{\partial k^2} \right\}^{-1}, \qquad \text{eq. (4)}$$

The *E(k)* function has been parametrized and fitted by a quadratic anharmonical expression $E(k) = a_0 + a_1 \times k + a_2 \times k^2$ within a close region to the band-gap k-point, with the rest of quantities in atomic units to obtain the effective masses directly in m_e units.

S2. Study of Molecular Fragments

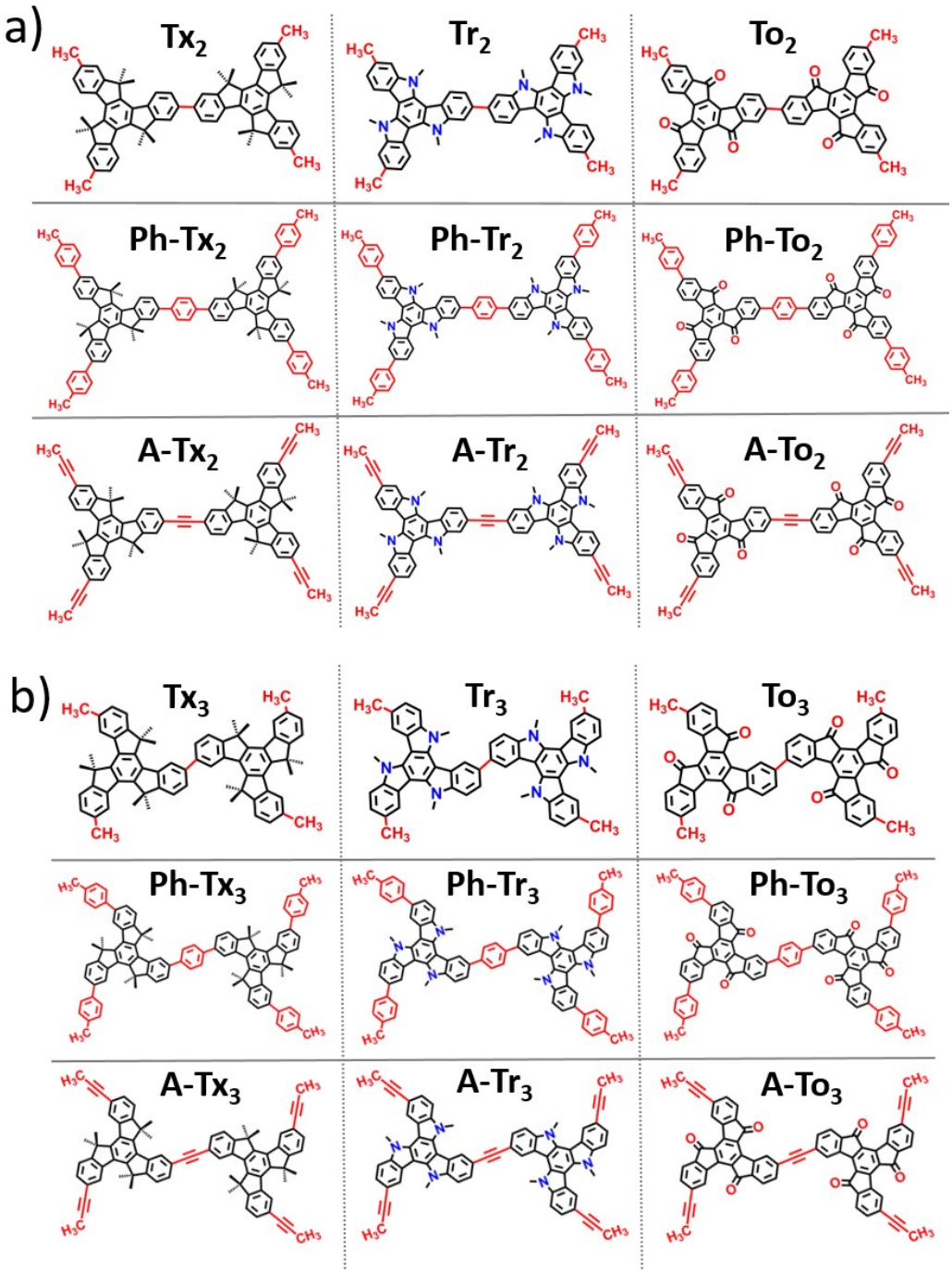

Figure S1. Chemical structures of $\mathbf{T_2}$ (a) and $\mathbf{T_3}$ (b) dimeric models studied theoretically.

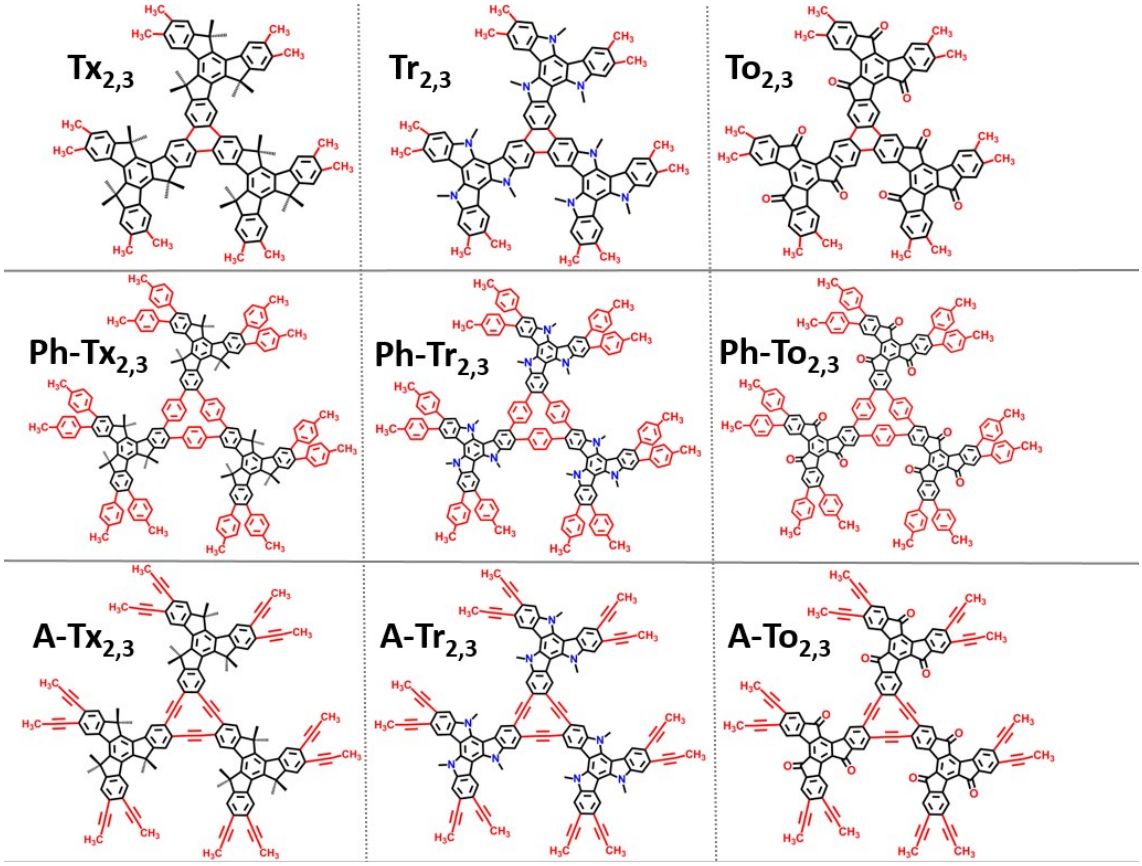

Figure S2. Chemical structures of $\mathbf{T_{2,3}}$ trimeric models studied theoretically.

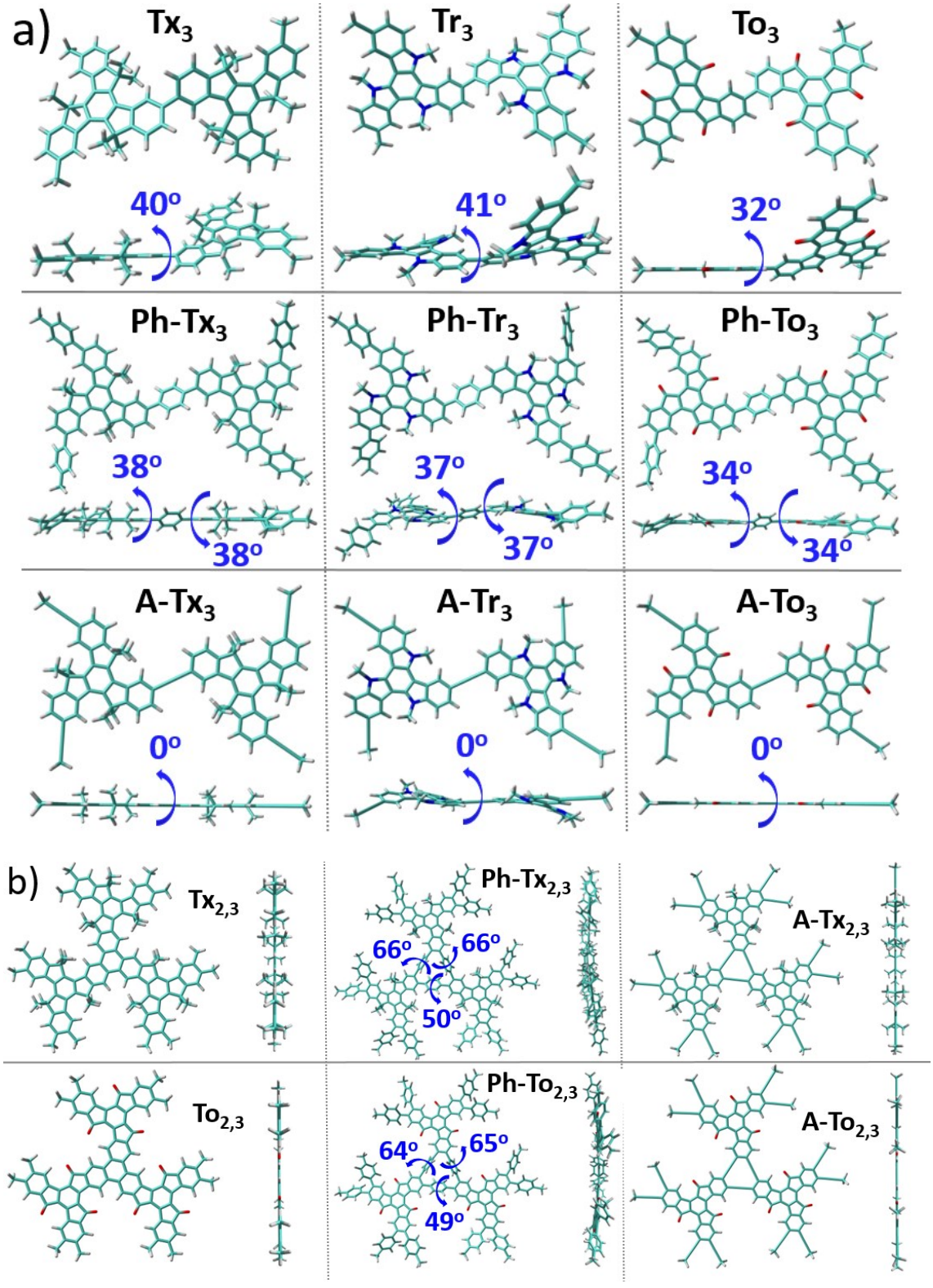

Figure S3. Top and lateral views of the DFT-optimized structures (PBE0/6-31G** level) for (a) $\mathbf{T_3}$ dimeric models and (b) $\mathbf{Tx_{2,3}}$ and $\mathbf{To_{2,3}}$ trimeric models. The dihedral angles between the conjugated cores and the π-bridges (in absolute values) are also shown.

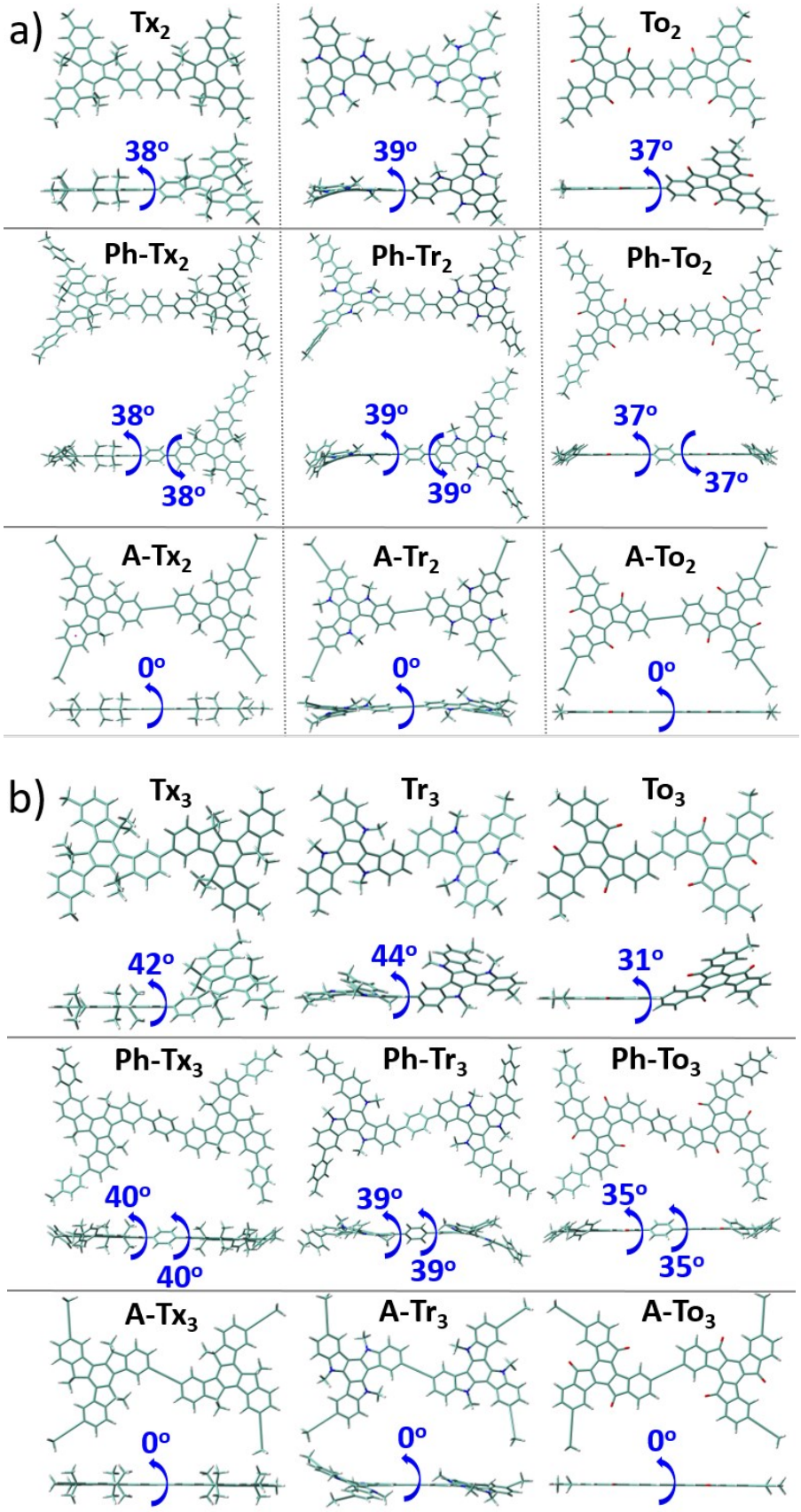

Figure S4. Top and lateral views of the DFT-optimized structures (CAM-B3LYP/cc-pVDZ level) for (a) $\mathbf{T_2}$ and (b) $\mathbf{T_3}$ dimeric models. The dihedral angles between the conjugated cores and the π-bridges (in absolute values) are also shown.

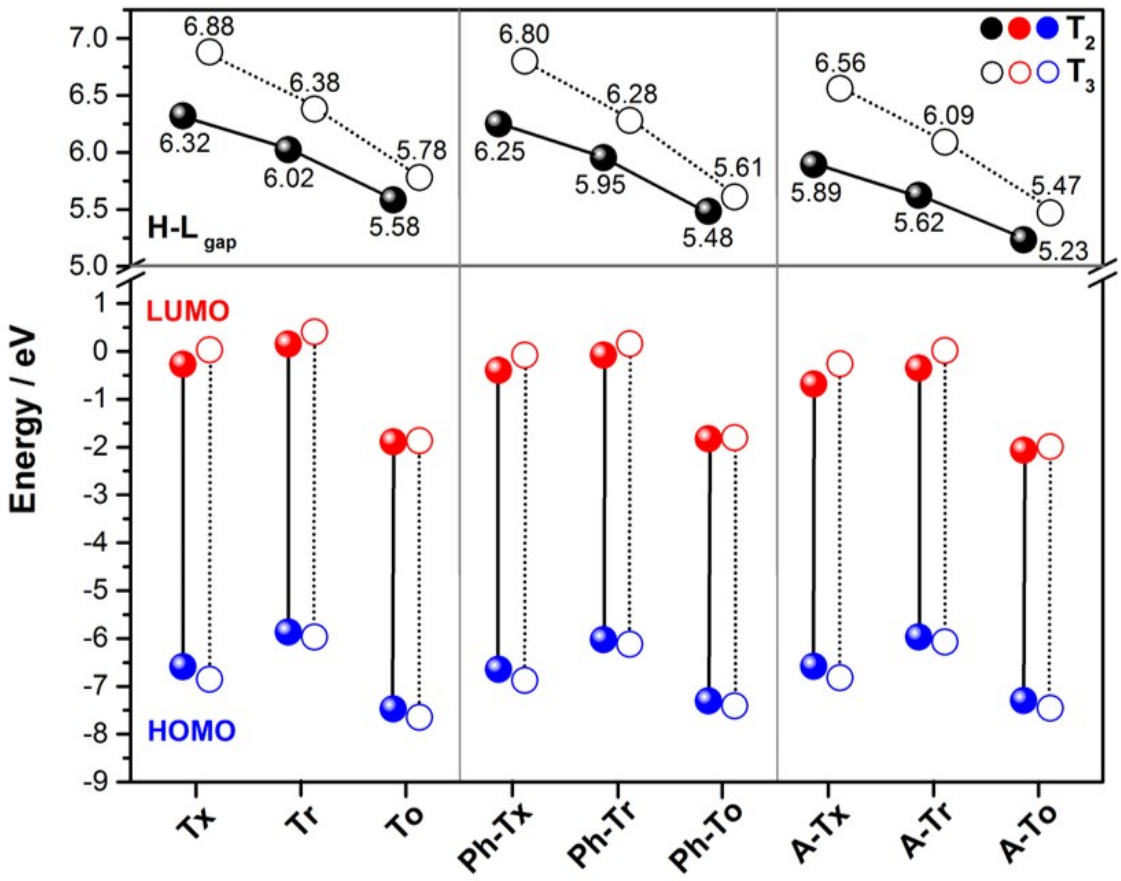

Figure S5. DFT-calculated (CAM-B3LYP/cc-pVDZ level) HOMO-LUMO gap (top) and frontier molecular orbital energies (bottom) for (a) $\mathbf{T_2}$ (solid circles) and $\mathbf{T_3}$ (open circles) dimeric models.

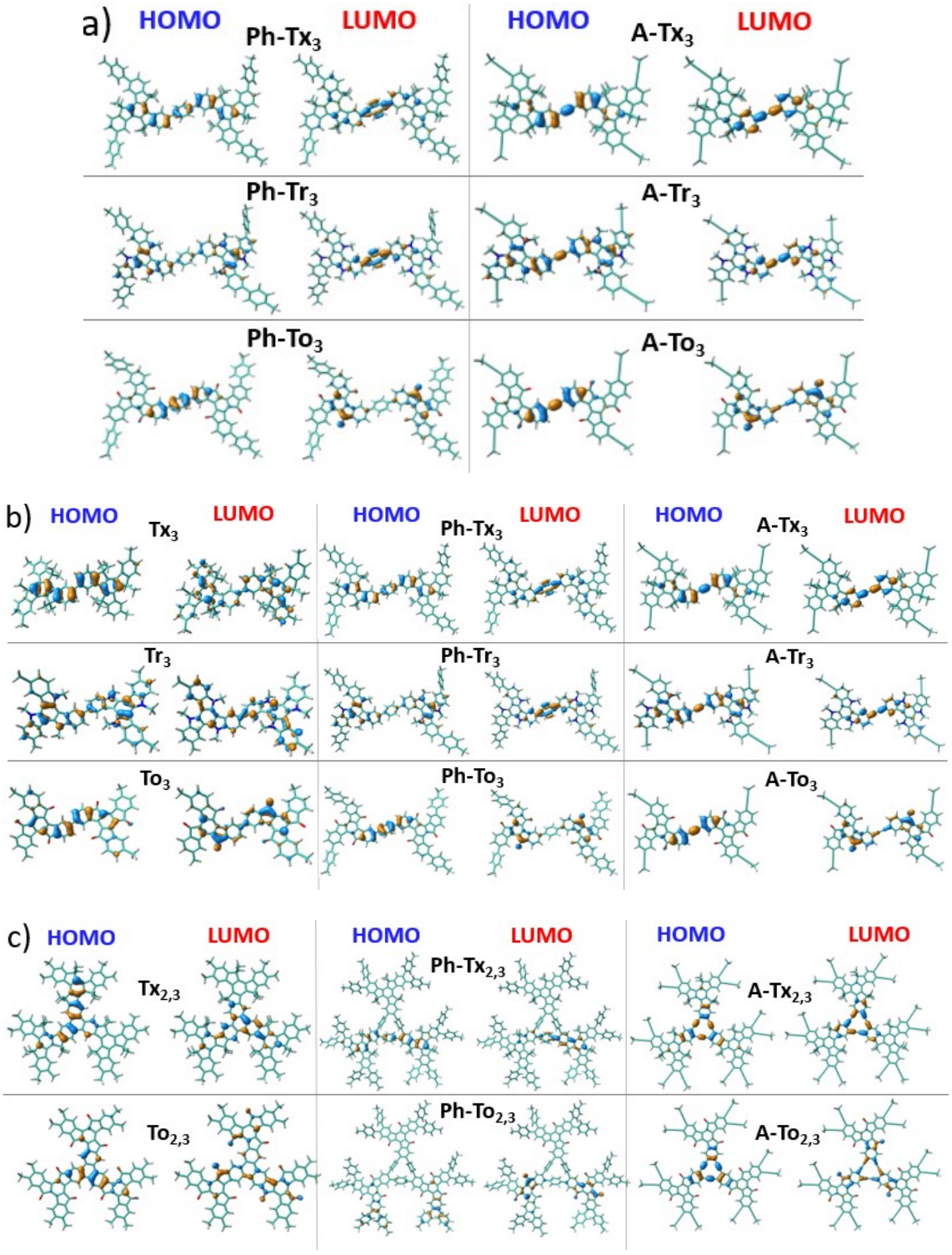

Figure S6. DFT-calculated (PBE0/6-31G** level) HOMO and LUMO topologies of (a) **Ph-T$_2$** and **A-T$_2$** dimeric models, (b) **T$_3$** dimeric models and (c) **Tx$_{2,3}$** and **To$_{2,3}$** trimeric models.

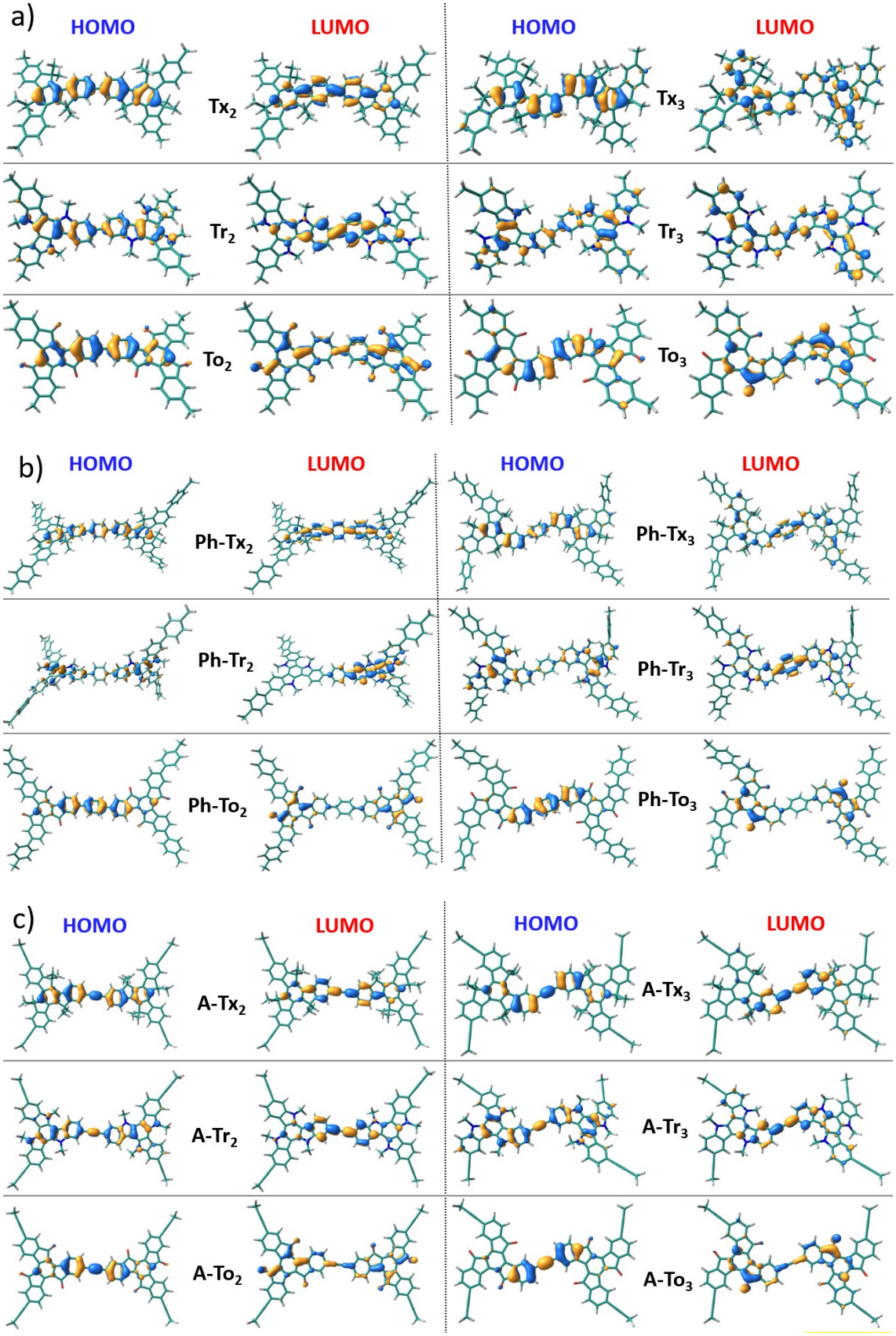

Figure S7. DFT-calculated (CAM-B3LYP/cc-pVDZ level) HOMO and LUMO topologies of (a) directly covalently linked, (b) phenylene-substituted and (c) alkyne-substituted $\mathbf{T_2}$ and $\mathbf{T_3}$ dimeric models.

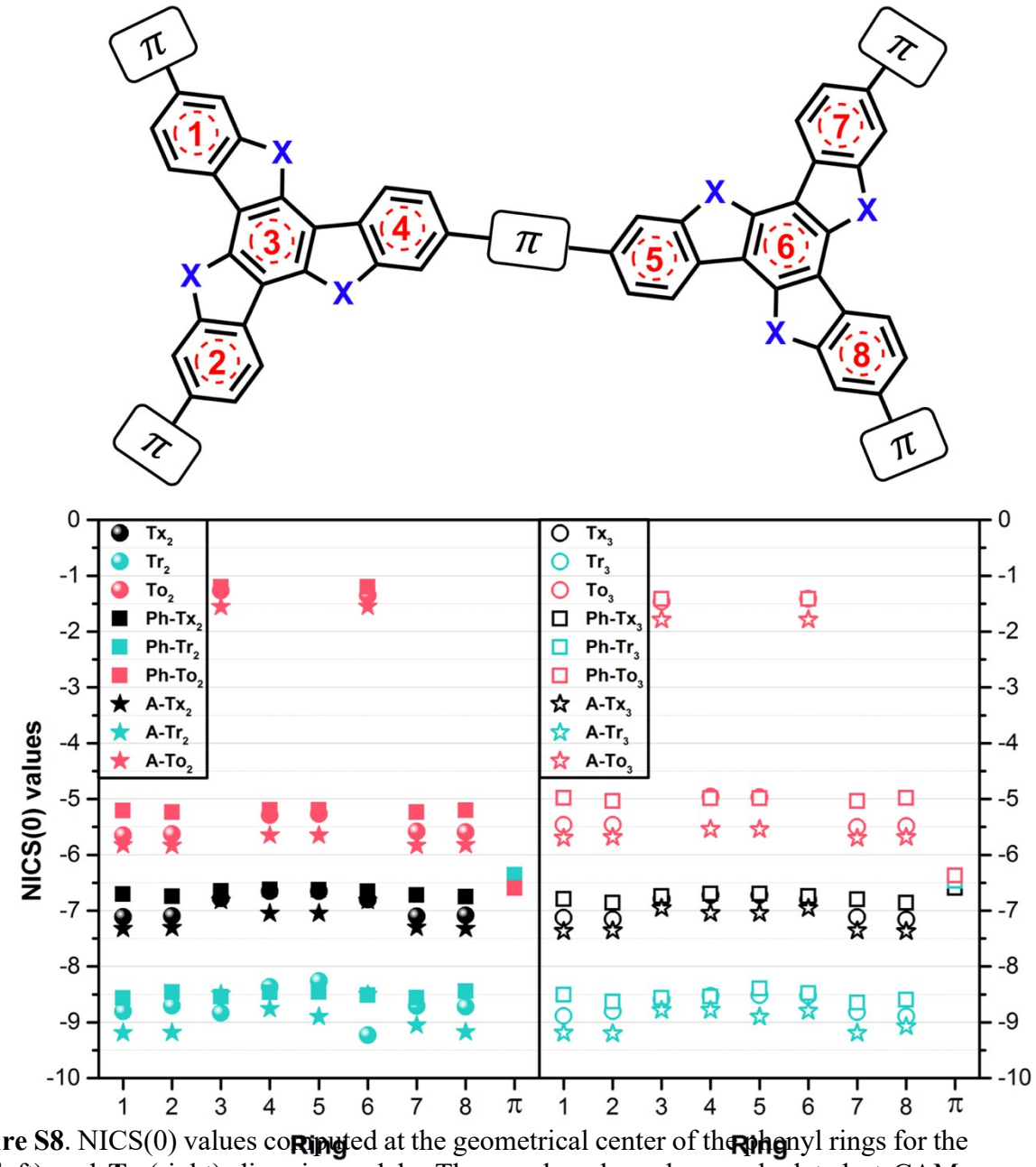

Figure S8. NICS(0) values computed at the geometrical center of the phenyl rings for the $\mathbf{T_2}$ (left) and $\mathbf{T_3}$ (right) dimeric models. These values have been calculated at CAM-B3LYP/6-311++G(2df,p)//CAM-B3LYP/cc-pVDZ level of theory and they are given in ppm.

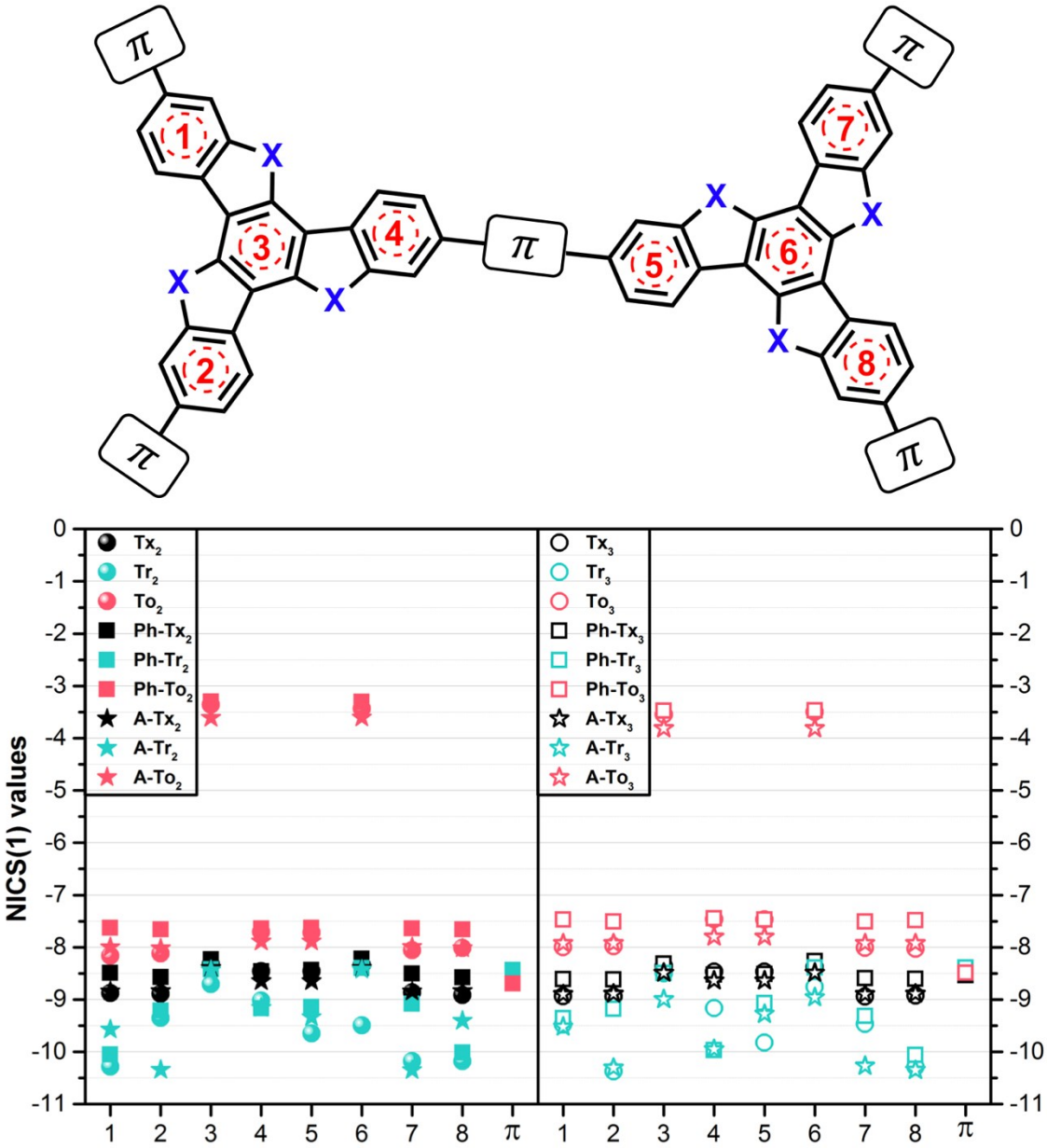

Figure S9. NICS(1) values computed at the geometrical center of the phenyl rings for the $\mathbf{T_2}$ (left) and $\mathbf{T_3}$ (right) dimeric models. These values have been calculated at CAM-B3LYP/6-311++G(2df,p)//CAM-B3LYP/cc-pVDZ level of theory and they are given in ppm.

S3. Study of 2D Conjugated Polymer Networks

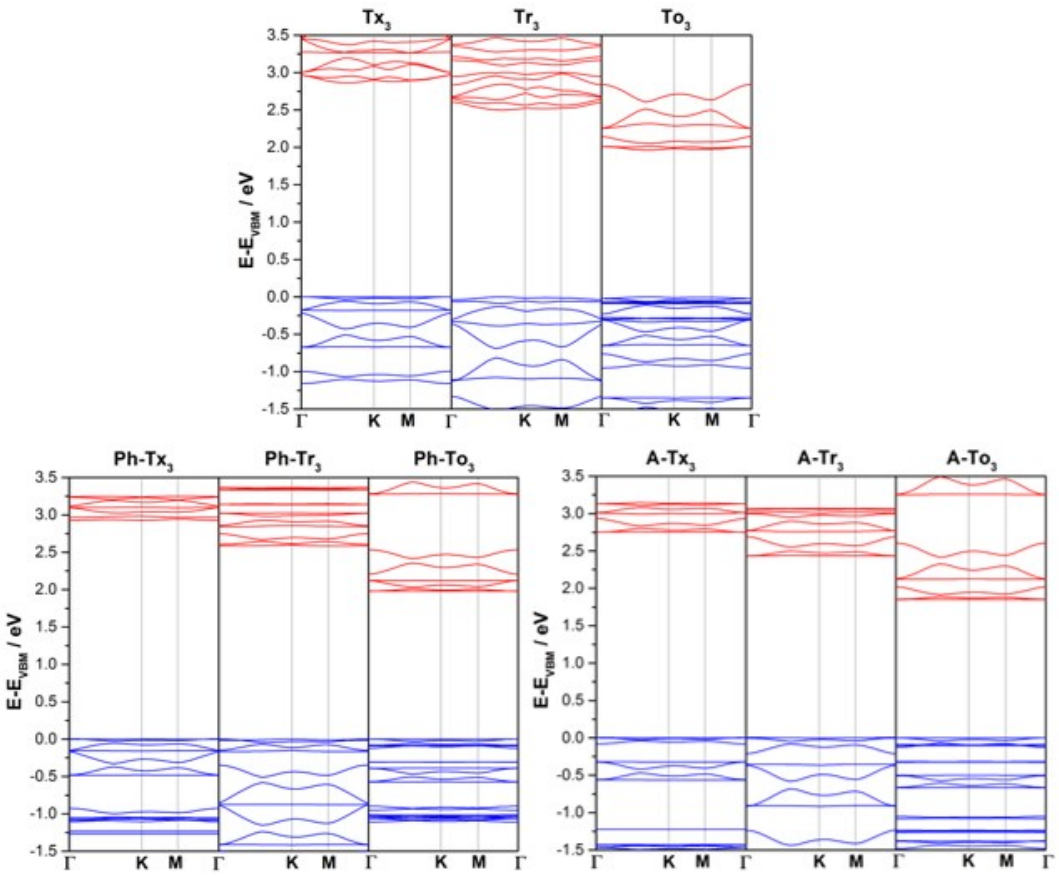

Figure S10. DFT-PBE-calculated electronic band structures of **Tx$_3$**, **Tr$_3$** and **To$_3$** (top), **Ph-Tx$_3$**, **Ph-Tr$_3$** and **Ph-To$_3$** (bottom, left) and **A-Tx$_3$**, **A-Tr$_3$**,and **A-To$_3$** (bottom, right) 2D-COFs. The valence and conduction bands are marked in blue and red, respectively. The zero energy is taken to correspond to the valence band maximum, E_{VBM}, while the x-axis labels denote a path through the 3D space of k-vectors. Points of high symmetry in the Brillouin zone are labeled as **Γ**(0, 0, 0), **M**(0, 1/2, 0) and **K**(1/3, 2/3, 0), all in reciprocal space crystal coordinates.

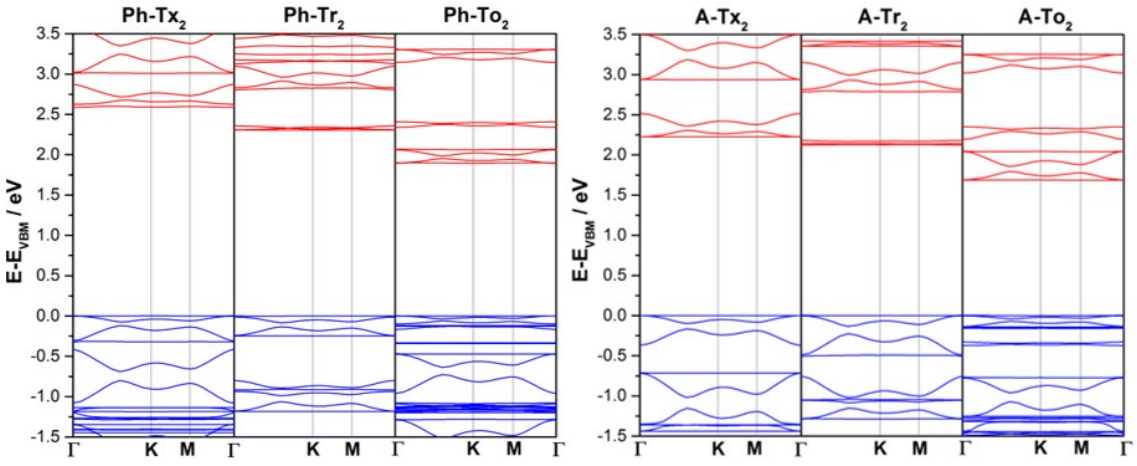

Figure S11. DFT-PBE-calculated electronic band structures of **Ph-Tx$_2$**, **Ph-Tr$_2$** and **Ph-To$_2$** (left) and **A-Tx$_2$**, **A-Tr$_2$** and **A-To$_2$** (right) 2D-COFs. The valence and conduction bands are marked in blue and red, respectively. The zero energy is taken to correspond to the valence band maximum, E_{VBM}, while the x-axis labels denote a path through the 3D space of k-vectors. Points of high symmetry in the Brillouin zone are labeled as **Γ**(0, 0, 0), **M**(0, 1/2, 0) and **K**(1/3, 2/3, 0), all in reciprocal space crystal coordinates.

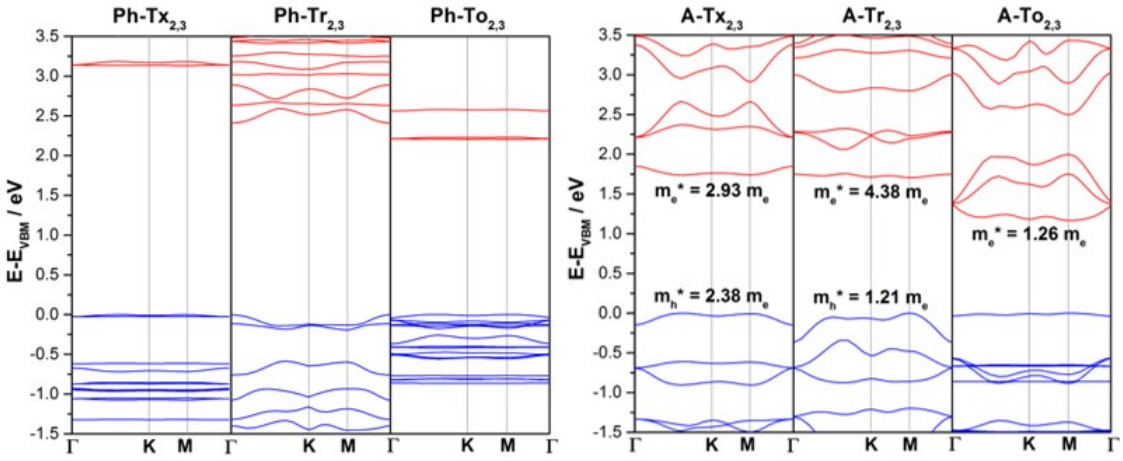

Figure S12. DFT-PBE-calculated electronic band structures of **Ph-Tx$_{2,3}$**, **Ph-Tr$_{2,3}$** and **Ph-To$_{2,3}$** (left) and **A-Tx$_{2,3}$**, **A-Tr$_{2,3}$** and **A-To$_{2,3}$** (right) 2D-COFs. The valence and

conduction bands are marked in blue and red, respectively. The zero energy is taken to correspond to the valence band maximum, E_{VBM}, while the x-axis labels denote a path through the 3D space of k-vectors. Points of high symmetry in the Brillouin zone are labeled as **Γ**(0, 0, 0), **M**(0, 1/2, 0) and **K**(1/3, 2/3, 0), all in reciprocal space crystal coordinates.

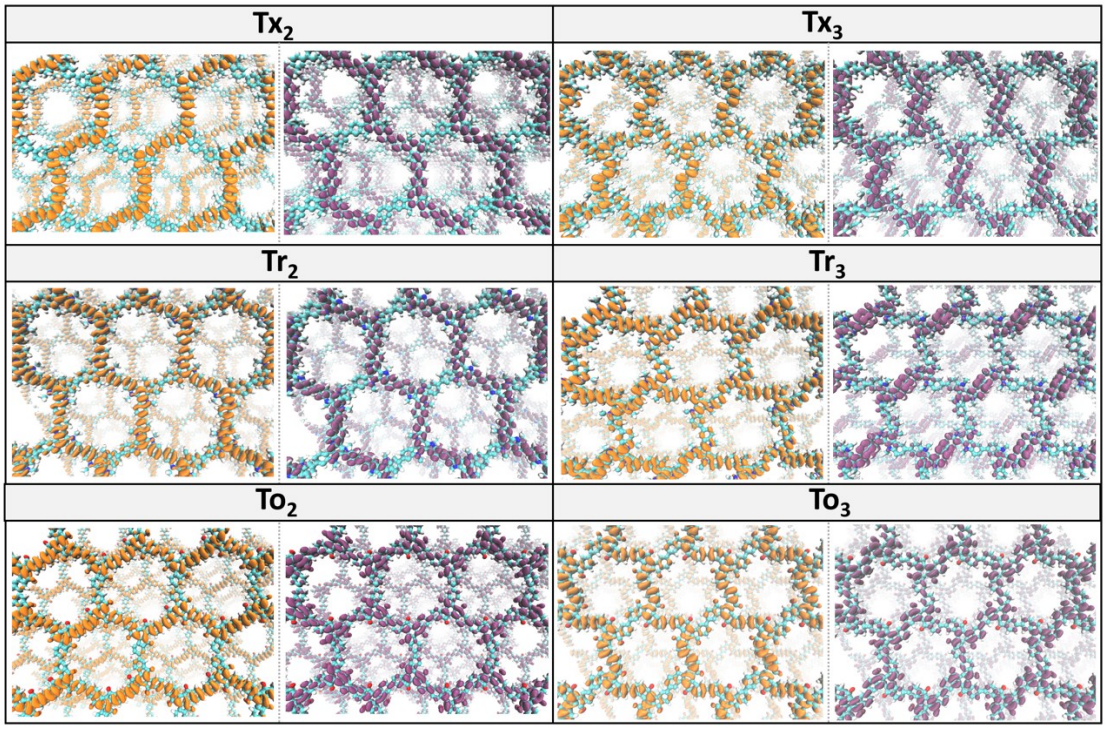

Figure S13. DFT-PBE-calculated topologies of the valence (orange) and conduction (purple) bands for directly connected **Tx-**, **Tr-** and **To**-based 2D COFs.

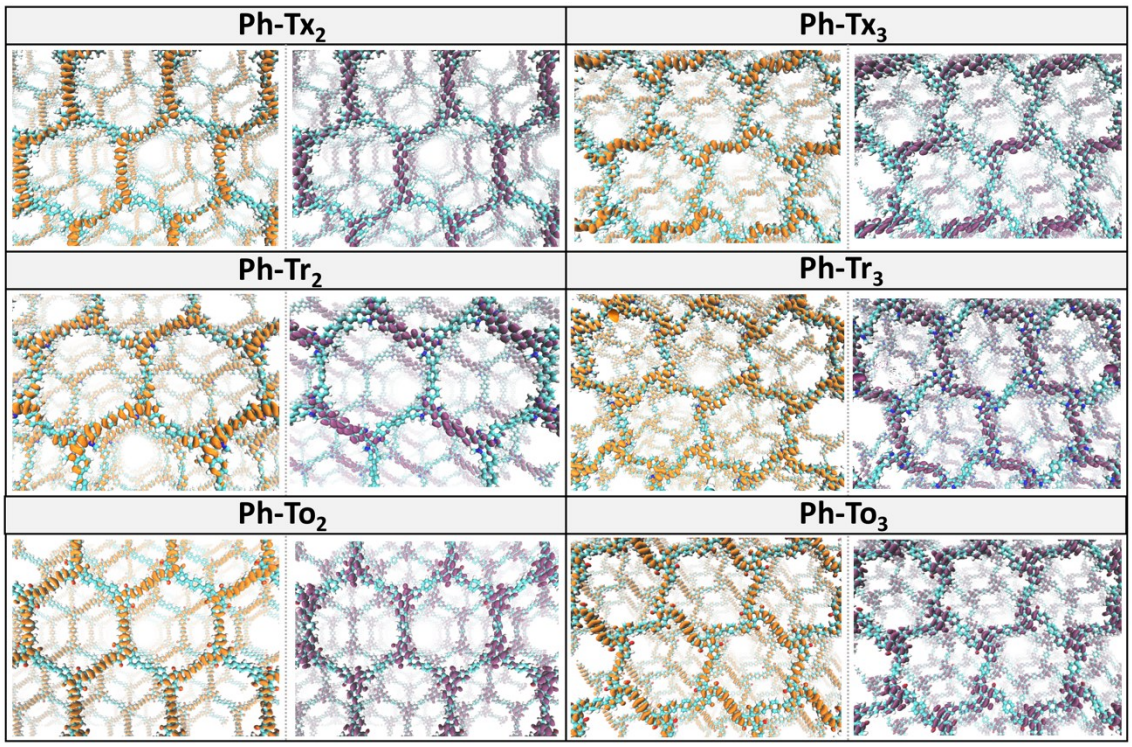

Figure S14. DFT-PBE-calculated topologies of the valence (orange) and conduction (purple) bands for phenylene-linked **Ph-Tx**, **Ph-Tr** and **Ph-To** 2D COFs.

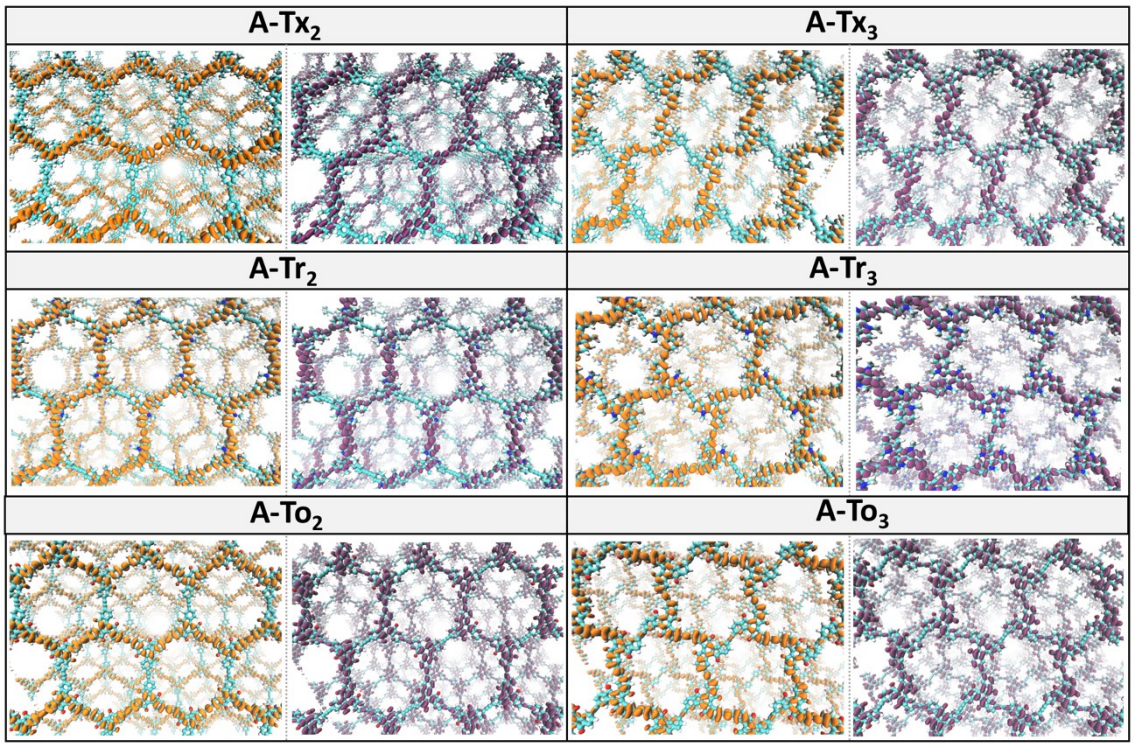

Figure S15. DFT-PBE-calculated topologies of the valence (orange) and conduction (purple) bands for alkyne-linked **A-Tx**, **A-Tr** and **A-To** 2D COFs.

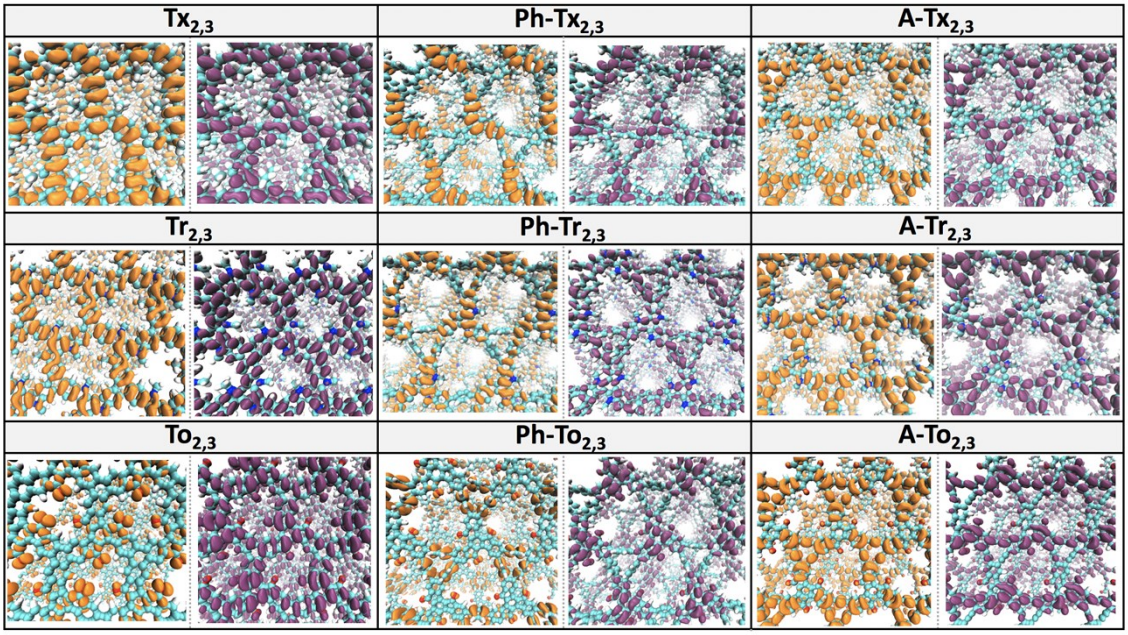

Figure S16. DFT-PBE-calculated topologies of the valence (orange) and conduction (purple) bands for $\mathbf{T_{2,3}}$ 2D COFs.

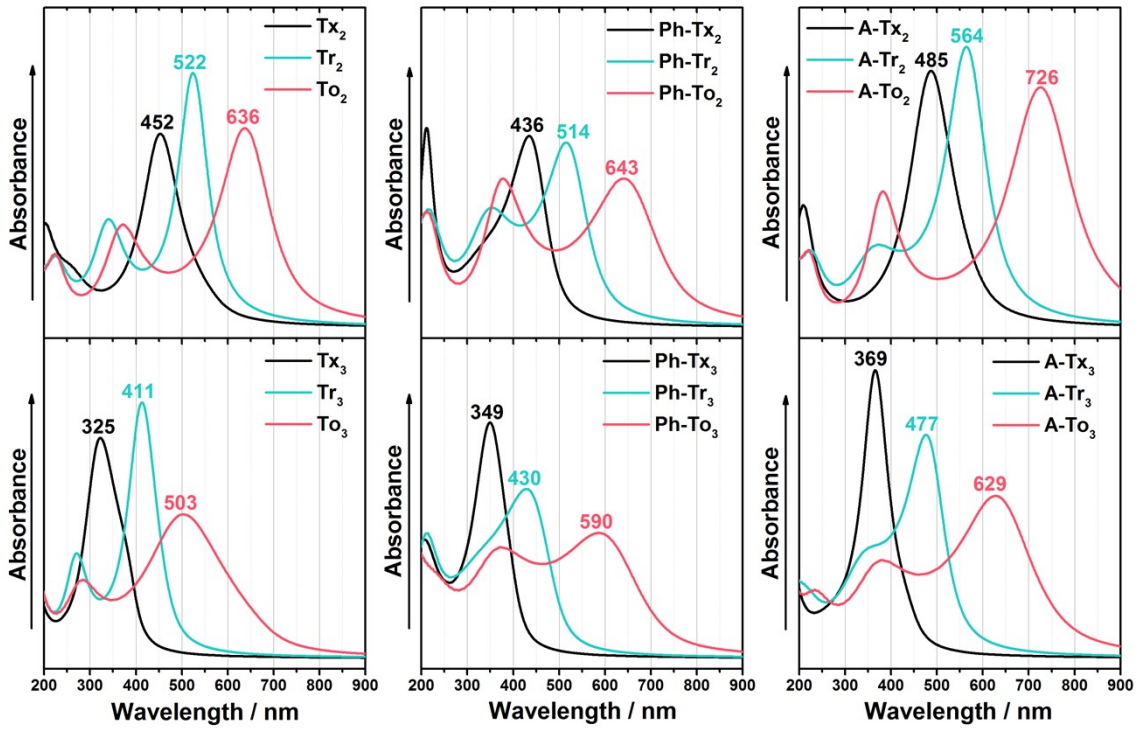

Figure S17. TD-DFT-PBE-calculated UV-Vis absorption spectra for the **Tx-** (black lines), **Tr-** (green lines) and **To**-based (red lines) $\mathbf{T_2}$ and $\mathbf{T_3}$ 2D COFs under study.

Discussion on the TD-DFT calculations for the **T_2** and **T_3** 2D COFs

The calculated spectra shown in Figure S17 are dominated by an intense band at lower energies, which corresponds to a $S_0 \rightarrow S_1$ transition assigned to one-electron promotion from the valence to the conduction band. An examination of the electronic absorption spectrum of **Tr_2** shows a strongly red-shifted band maximum (70 nm) when compared to those of **Tx_2**, being this effect even more important in the case of their **To_2** analogue (114 nm). This effect can be explained by a decrease in the band gap which is mainly ascribed to the stabilization of the conduction band minimum (CBM) in the following order: **Tx** > **Tr** > **To**. The conduction band wave functions of these compounds spread over one preferential direction along the conjugated framework, with higher contributions over other directions in **To_2**, resulting in an extension of the π-conjugation (see Figure S13). Interestingly, the electronic absorption band is red-shifted when the conjugated platforms are linked through phenylene or alkyne spacers; bathochromic shifts of 49 and 78 nm (79 and 162 nm) are observed for **Ph-Tr_2** (**A-Tr_2**) and **Ph-To_2** (**A-To_2**) respectively, in comparison with their directly linked analogues. The stronger effect played by the alkyne group can be explained by the higher planarity of alkyne-based COFs as compared to the moderately distorted phenylene-linked COFs , which facilities the extension of the π-conjugation over the whole framework allowing for large π-electron delocalization. On the other hand, the linkage position has a moderate influence on the optoelectronic properties of these 2D polymers. As a general trend, when the conjugated platforms are connected through *para* positions (**T_2** polymers), the absorption spectra are notably red-shifted when compared with those connected through *meta* positions (**T_3** polymers).

S4. References

1 M. J. Frisch, G. W. Trucks, H. B. Schlegel, G. E. Scuseria, M. a. Robb, J. R. Cheeseman, G. Scalmani, V. Barone, G. a. Petersson, H. Nakatsuji, X. Li, M. Caricato, a. V. Marenich, J. Bloino, B. G. Janesko, R. Gomperts, B. Mennucci, H. P. Hratchian, J. V. Ortiz, a. F. Izmaylov, J. L. Sonnenberg, Williams, F. Ding, F. Lipparini, F. Egidi, J. Goings, B. Peng, A. Petrone, T. Henderson, D. Ranasinghe, V. G. Zakrzewski, J. Gao, N. Rega, G. Zheng, W. Liang, M. Hada, M. Ehara, K. Toyota, R. Fukuda, J. Hasegawa, M. Ishida, T. Nakajima, Y. Honda, O. Kitao, H. Nakai, T. Vreven, K. Throssell, J. a. Montgomery Jr., J. E. Peralta, F. Ogliaro, M. J. Bearpark, J. J. Heyd, E. N. Brothers, K. N. Kudin, V. N. Staroverov, T. a. Keith, R. Kobayashi, J. Normand, K. Raghavachari, a. P. Rendell, J. C. Burant, S. S. Iyengar, J. Tomasi, M. Cossi, J. M. Millam, M. Klene, C. Adamo, R. Cammi, J. W. Ochterski, R. L. Martin, K. Morokuma, O. Farkas, J. B. Foresman and D. J. Fox, 2016, Gaussian 16, Revision C.01, Gaussian, Inc., Wallin.

2 S. Royuela, E. Martínez-Periñán, M. P. Arrieta, J. I. Martínez, M. M. Ramos, F. Zamora, E. Lorenzo and J. L. Segura, *Chem. Commun.*, 2020, **56**, 1267–1270.

3 P. Albacete, J. I. Martínez, X. Li, A. López-Moreno, S. Mena-Hernando, A. E. Platero-Prats, C. Montoro, K. P. Loh, E. M. Pérez and F. Zamora, *J. Am. Chem. Soc.*, 2018, **140**, 12922–12929.

4 L. Li, Z. Cai, Q. Wu, W. Y. Lo, N. Zhang, L. X. Chen and L. Yu, *J. Am. Chem. Soc.*, 2016, **138**, 7681–7686.

5 L. Li, W. Y. Lo, Z. Cai, N. Zhang and L. Yu, *Macromolecules*, 2016, **49**, 6903–

6909.
6 J. Wen, D. Luo, L. Cheng, K. Zhao and H. Ma, *Macromolecules*, 2016, **49**, 1305–1312.
7 R. Gutzler and D. F. Perepichka, *J. Am. Chem. Soc.*, 2013, **135**, 16585–16594.
8 S. Thomas, H. Li, R. R. Dasari, A. M. Evans, I. Castano, T. G. Allen, O. G. Reid, G. Rumbles, W. R. Dichtel, N. C. Gianneschi, S. R. Marder, V. Coropceanu and J. L. Brédas, *Mater. Horizons*, 2019, **6**, 1868–1876.
9 G. V. Baryshnikov, B. F. Minaev, N. N. Karaush and V. A. Minaeva, *RSC Adv.*, 2014, **4**, 25843–25851.
10 J. P. Perdew, M. Ernzerhof and K. Burke, *J. Chem. Phys.*, 1996, **105**, 9982–9985.
11 T. Yanai, D. P. Tew and N. C. Handy, *Chem. Phys. Lett.*, 2004, **393**, 51–57.
12 W. J. Hehre, K. Ditchfield and J. A. Pople, *J. Chem. Phys.*, 1972, **56**, 2257–2261.
13 M. M. Francl, W. J. Pietro, W. J. Hehre, J. S. Binkley, M. S. Gordon, D. J. DeFrees and J. A. Pople, *J. Chem. Phys.*, 1982, **77**, 3654–3665.
14 T. H. Dunning, *J. Chem. Phys.*, 1989, **90**, 1007–1023.
15 J. Oliver, *Hilos Tensados*, 2019, 1, 1–476.
16 P. V. R. Schleyer, C. Maerker, A. Dransfeld, H. Jiao and N. J. R. Van Eikema Hommes, *J. Am. Chem. Soc.*, 1996, **118**, 6317–6318.
17 T. K. Zywietz, H. Jiao, P. V. R. Schleyer and A. De Meijere, *J. Org. Chem.*, 1998, **63**, 3417–3422.
18 K. Wolinski, J. F. Hinton and P. Pulay, *J. Am. Chem. Soc.*, 1990, **112**, 8251–8260.
19 J. L. Brédas, D. Beljonne, V. Coropceanu and J. Cornil, *Chem. Rev.*, 2004, **104**, 4971–5003.
20 V. Coropceanu, J. Cornil, D. A. da Silva Filho, Y. Olivier, R. Silbey and J. L. Brédas, *Chem. Rev.*, 2007, 107, 926–952.
21 P. Giannozzi, S. Baroni, N. Bonini, M. Calandra, R. Car, C. Cavazzoni, D. Ceresoli, G. L. Chiarotti, M. Cococcioni, I. Dabo, A. Dal Corso, S. De Gironcoli, S. Fabris, G. Fratesi, R. Gebauer, U. Gerstmann, C. Gougoussis, A. Kokalj, M. Lazzeri, L. Martin-Samos, N. Marzari, F. Mauri, R. Mazzarello, S. Paolini, A. Pasquarello, L. Paulatto, C. Sbraccia, S. Scandolo, G. Sclauzero, A. P. Seitsonen, A. Smogunov, P. Umari and R. M. Wentzcovitch, *J. Phys. Condens. Matter*, 2009, **21**, 395502.
22 J. P. Perdew, K. Burke and M. Ernzerhof, *Phys. Rev. Lett.*, 1996, **77**, 3865–3868.
23 S. Grimme, *J. Comput. Chem.*, 2006, **27**, 1787–1799.
24 A. M. Rappe, K. M. Rabe, E. Kaxiras and J. D. Joannopoulos, *Phys. Rev. B*, 1990, **41**, 1227–1230.
25 N. Mounet and N. Marzari, *Phys. Rev. B - Condens. Matter Mater. Phys.*, 2005, **71**, 205214.
26 J. D. Pack and H. J. Monkhorst, *Phys. Rev. B*, 1977, 16, 1748–1749.
27 R. M. Wentzcovitch, *Phys. Rev. B*, 1991, **44**, 2358–2361.
28 M. Parrinello and A. Rahman, *J. Appl. Phys.*, 1981, **52**, 7182–7190.
29 M. Parrinello and A. Rahman, *Phys. Rev. Lett.*, 1980, **45**, 1196–1199.
30 W. Humphrey, A. Dalke and K. Schulten, *J. Mol. Graph.*, 1996, **14**, 33–38.
31 X. Ge, S. J. Binnie, D. Rocca, R. Gebauer and S. Baroni, *Comput. Phys. Commun.*, 2014, **185**, 2080–2089.
32 O. B. Malcioğlu, R. Gebauer, D. Rocca and S. Baroni, *Comput. Phys. Commun.*, 2011, **182**, 1744–1754.

7. CONCLUSIONES FINALES

La utilización de semiconductores orgánicos para el desarrollo de materiales inteligentes ha sido explorada satisfactoriamente en esta tesis doctoral. Estos resultados han dado a lugar a cinco publicaciones en revistas de alto impacto, en las que se aborda desde el diseño y síntesis de moléculas y polímeros ópticamente activos, hasta el desarrollo de aplicaciones en el campo de los materiales reescribibles y detección de explosivos.

Estos logros se han realizado desde dos enfoques distintos. Primero, mediante una aproximación molecular utilizando el benzotiadiazol (BTD) como plataforma para obtener materiales mecanocrómicos y termocrómicos; Segundo, por medio del diseño y síntesis de polímeros porosos basados en truxeno, capaces de reaccionar ante la presencia de compuestos nitro aromáticos y explosivos.

Las siguientes conclusiones han sido extraídas de esta tesis doctoral:

1. Se ha sintetizado una serie de derivados de BTD con los cuales se ha estudiado ampliamente como se organizan y como esto afecta a sus propiedades electrónicas y fotónicas, dilucidando claramente la relación estructura-propiedad de estos materiales. Esto ha demostrado que es posible modular las propiedades electrónicas cambiando los grupos funcionales terminales y como estos a su vez modifican las estructuras supramoleculares estructuras cristalinas y supramoleculares.
2. Se han logrado obtener materiales moleculares derivados del BTD con interesantes propiedades de mesomorfismo, mecanocrómismo y termocrómismo. Mediante el estudio de estas propiedades se ha logrado encontrar el origen de los cambios de emisión de estos derivados de BTD, donde un pequeño cambio en su organización genera un gran cambio supramolecular. Esto se ha logrado, por medio de estudios de difracción de rayos X, que han permitido dilucidar inequívocamente su estructura.
3. Teniendo en cuenta lo anterior, se ha desarrollado un material reescribible, el cual cambia sus propiedades fotoluminiscentes al aplicar temperatura, perfecto candidato para desarrollar termómetros, sensores, tintas inteligentes o marcas de seguridad. Esto se ha logrado mediante la incorporación de un derivado de BTD en una membrana de polivinil alcohol, el cual, en las condiciones optimizadas, forma estructuras micelares nanométricas dentro de la matriz del polímero (PVA),

permitiendo generar transformaciones reversibles, imposibles en otras condiciones.

4. Se han diseñado y sintetizado cuatro polímeros porosos basados en truxeno. Estos polímeros presentan altas porosidades (SA_{BET} 520-1167 $m^2.g^{-1}$) e interesantes propiedades emisoras. Se han estudiado mediante espectroscopia y cálculos teóricos sus propiedades electrónicas y ópticas. Este estudio demuestra la gran dependencia de estas propiedades a la conjugación de la plataforma, de modo que al modificar el punto de crecimiento del polímero cambia totalmente sus propiedades.
5. Se ha logado aplicar los polímeros obtenidos a la detección de explosivos y compuestos nitroaromáticos. Estos presentan una gran interacción con moléculas nitroaromaticas, causando el "quenching" de su fluorescencia. Esto permite su posible aplicación en el futuro para el desarrollo de sensores. El estudio además ha logrado establecer una clara tendencia entre la sensibilidad de detección y las estructuras de los polímeros, resaltando la importancia de la posición de funcionalización en los polímeros porosos.
6. Mediante un estudio computacional, se ha logrado predecir las propiedades electrónicas y estructurales de polímeros 2D formados por truxeno y sus derivados.

Apéndice

Durante el doctorado, además de las cinco publicaciones contenidas en esta tesis doctoral, se ha participado en otros dos trabajos que se recogen en los siguientes artículos:

- Aguirre Díaz, L. M.; Echeverri Muñoz, M.; Paredes-Gil, K.; Snejko, N.; Gómez-Lor, B.; Gutierrez-Puebla, E.; Monge, A. The Effect of Auxiliary Nitrogenated Linkers on the Design of New Cadmium Based Coordination Polymers as Sensors for Detection of Explosive Materials. *Chem. A Eur. J.* **2021**, 1–10.
- Cárdenas, J. C.; Aguirre-Diáz, L. M.; Galindo, J. F.; Alí-Torres, J.; Ochoa-Puentes, C.; Echeverri, M.; Gómez-Lor, B.; Monge, M. Á.; Gutiérrez-Puebla, E.; Sierra, C. A. Nature of Color Diversity in Phenylenevinylene-Based Polymorphs. *Cryst. Growth Des.* **2019**, *19*, 3913–3922.